UNIVERSITY OF OKLAHOMA

GRADUATE COLLEGE

PHOSPHINIMIDE COMPLEXES OF MOLYBDENUM: SYNTHESIS, AND REACTIVITY OF METAL-ELEMENT MULTIPLE BONDS

A DISSERTATION

SUBMITTED TO THE GRADUATE FACULTY

in partial fulfillment of the requirements for the

Degree of

DOCTOR OF PHILOSOPHY

By

CHRISTOPHER JOHN VARJAS
Norman, Oklahoma
2018

PHOSPHINIMIDE COMPLEXES OF MOLYBDENUM:
SYNTHESIS, AND REACTIVITY OF METAL-ELEMENT MULTIPLE BONDS

A DISSERTATION APPROVED FOR THE
DEPARTMENT OF CHEMISTRY AND BIOCHEMISTRY

BY

Dr. Robert K. Thomson, Chair

Dr. Michael T. Ashby

Dr. George B. Richter-Addo

Dr. Ian R. Sellers

Dr. Wai Tak Yip

Dedicated to those that endeavor to make their vision of the future a reality.

Acknowledgements

I would like to thank my advisor Dr. Robert Thomson for enabling me to contribute to the phenomenal world of organometallic chemistry, encouraging me to pursue innovative chemistry while always keeping me grounded in rigorous and well-characterized science; and his support of the diverse extracurricular events and projects that have contributed significantly to my current knowledge and capabilities, and aspirations for the future. I am grateful to my advisory committee for their advice and insight into the big picture of science and my career.

I would like to thank Dr. Susan Nimmo for enabling me to learn so much about the practical and technical aspects of nuclear magnetic resonance spectroscopy, and Dr. Douglas Powell for enabling me to learn so much about the practical and technical aspects of small-molecule crystallography. I would like to thank Dee Stone and the research stockroom for providing excellent access to the many chemicals and supplies used in my research. Access to research information was essential for my work and I would like to thank OU Libraries and the extended ILL network for connecting me with hard to access research from around the world. I am grateful to the Department of Chemistry and Biochemistry for funding my graduate research, and the College of Arts and Sciences and Graduate Student Senate for travel grants to present my research at international conferences.

I would also like to thank the Office of Technology Development, including Andrew Pollock, Jim Bratton, and Dr. Chris Corbett for an excellent

intellectual property internship and introducing me to the world of technology startups; and the Office of Strategic Initiatives and Center for Entrepreneurship for mentorship and technology innovation opportunities.

Finally, I would like to thank my parents, family, and friends for supporting me through all of my time and effort working on my graduate research.

Table of Contents

List of Tables

List of Figures

Abstract

Methods were developed to synthesize new high-oxidation state molybdenum complexes supported by phosphinimide ligands ($[R_3P{=}N]^-$) that incorporate ligands with metal-element multiple bonds. A series of imido, oxido, and chlorido complexes were synthesized and characterized, with phosphinimide ligand installation through σ-bond metathesis, salt metathesis, and protonolysis proligand reactivity. Molybdenum(VI) oxido-dichlorido and imido-dichlorido complexes were synthesized through selective hexamethyldisiloxane elimination. Synthesis of cationic phosphinimide complexes was achieved through ion exchange with non-coordinating sodium tetrakis[3,5-bis(trifluoromethyl)phenyl]borate.

An efficient synthetic route to access the first neutral oxido-alkylidene molybdenum complex $[(^tBu_3P{=}N)_2Mo(O)(=CHSi(CH_3)_3]$ (**3.1**) was defined by alkylation of the oxido-dichlorido complex $[(^tBu_3P{=}N)_2Mo(O)Cl_2]$ (**2.4**). Alkylidene complex **3.1** was shown to have lower activity than commercial catalysts towards catalytic ring-opening metathesis polymerization (ROMP) of norbornene.

Isolation and characterization of the tris(pentafluorophenyl)borane adduct $[(^tBu_3P{=}N)_2Mo(O\text{-}B(C_6F_5)_3)(=CHSi(CH_3)_3]$ (**3.3**) of the oxido-alkylidene complex showed improved catalytic ROMP performance due to Lewis acid activation of the oxido ligand. Comparison of the X-ray crystallographic structures of both oxido-alkylidene complexes revealed a molybdenum-oxygen bond length increase of 0.143(6) Å after borane coordination.

An efficient synthetic route was developed to isolate the first phosphinimide complex that contains an alkylidyne ligand (**4.6**), with a novel structure relative to known group VI alkylidyne species. Lewis acid activation of the alkylidyne complex, and preliminary reactivity studies with alkyne and nitrile substrates, indicate potential use as a metathesis catalyst.

Heteroallene cycloaddition with oxido ligands was evaluated as a general synthetic approach to access more valuable ligands. Aryl isocyanates (ArN=C=O) were shown to generate imido ligands through CO_2 elimination. Diphenyl ketene was observed to undergo [1,2] addition with an oxido ligand to generate a rare ene-diolate ligand. A new synthetic route to generate phosphaketenes (RP=C=O) was explored, which utilized less toxic reagents than known methods.

From this work, synthetic methods were developed to access molybdenum(VI) phosphinimide complexes that incoporate a diverse range of ligands with metal-element multiple bonds.

1 Introduction

1.1 Homogeneous Transition Metal Complex Design

Transition metals currently enable catalytic industrial processes[1–3] that are vital for modern civilization and offer immense potential for solving future challenges.[4–6] It is estimated that at the start of the 21st century, 80-90% of products used every day interacted with a catalyst at some point in production.[7,8] The large range of applications includes examples such as processes to create fine chemicals,[7,9–11] pharmaceuticals,[12–16] materials,[9,17–22] and fuels and energy systems.[7,23,24]

From this diverse range of applications, the use of lower molecular weight molecules that incorporate transition metals has become a prolific area of scientific research.[25,26] These smaller molecules are known as *transition metal complexes* (or *complexes)* and are often soluble in the same physical state (*homogeneous)* as the *substrate* molecules that they interact with.

Complexes consist of a central metal atom that is usually positively charged, which is coordinated by other small molecules (*ligands*). Ligands are usually neutral or negatively charged, and interact with the central metal atom through electron donation or electron acceptance.

Homogeneous complexes are often compared with *heterogeneous* transition metal systems, such as solid metal materials that liquid or gas phase substrates are passed over. Homogeneous systems can provide improved

reactivity and better selectivity for generating specific *product* molecules. These benefits are balanced with some limitations, such as lower long-term stability and separation difficulty of potentially toxic metals from products.[27] Heterogeneous systems have the opposite benefits and limitations to homogeneous systems, in that they are more stable and easy to separate from product molecules, but can be less reactive and more difficult to control.[28]

Methods of analysis for homogeneous complexes are more definitive than those available for heterogeneous systems.[29,30] The power of these techniques enables more rapid and directed development of homogeneous complexes, and has resulted in significant research progress in this domain during the past 60 years.

Improvement of transition metal complex properties can be realized through modification of the type of transition metal, the transition metal oxidation state, or the ligand framework of the complex.

1.2 Group VI Transition Metal Complexes

Transition metal complexes of the group VI metals that incorporate ligands with metal-element multiple bonds have established a field of high activity catalysts for a number of reactions.

Alkylidene, alkylidyne, and oxido complexes centered on molybdenum and tungsten are prototypical examples of group VI catalysts (Fig. 1.1).

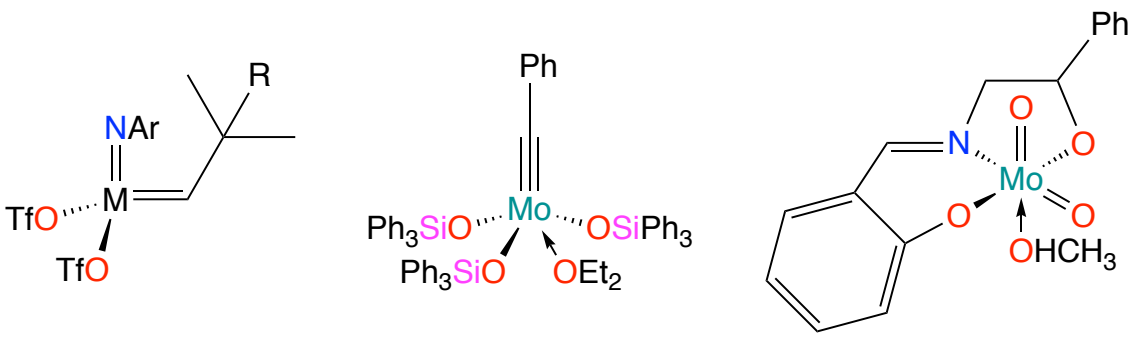

M = Mo or W
R = Ph or Me
Ar = 2,6(^{i}Pr)$_2$C$_6$H$_3$
OTf = [CF$_3$SO$_3$]$^-$

Figure 1.1: Representative alkylidene (left), alkylidyne (center), and oxido (right) group VI catalysts

Catalytic processes enabled by some of these alkylidene complexes include cross-metathesis, ring-opening metathesis polymerization (ROMP), and ring-closing metathesis (RCM).

Alkylidyne complexes of these types are capable of similar chemistry involving alkynes as substrates, such as ring-opening alkyne metathesis polymerization (ROAMP) and ring-closing alkyne metathesis (RCAM).

Oxido complexes of these types can be useful for oxygen atom transfer processes, such as the epoxidation of olefins.

The metal-carbon or metal-oxygen multiple bonds within the alkylidene and alkylidyne ligands enable these catalytic transformations. The other ligands within these catalysts modify the properties, with the intent of increasing catalytic performance or decreasing the rate of decomposition.

1.3 Phosphinimide Ligand Frameworks

1.3.1 Physicochemical Properties of Phosphinimides

Phosphinimide ligands (phosphinimides) provide a compelling framework for further research development (Fig. 1.2) because the synthetic methods available to generate phosphinimides allow for excellent structural diversity of the three functional (R) groups bonded to the phosphorus atom in the core P=N fragment. Variation of these groups enables control over specific steric and electronic ligand properties for use in tuning complex properties, and the phosphorus atom enables characterization of proligands and complexes by ^{31}P nuclear magnetic resonance (NMR) spectroscopy.

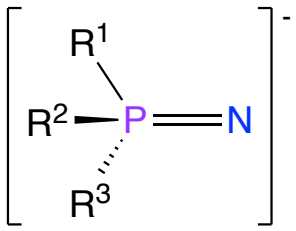

Figure 1.2: Generic anionic phosphinimide ligand

1.3.2 Coordination Modes

Phosphinimides can coordinate to transition metals by a number of different modes (Fig. 1.3).[31] The coordination mode is primarily influenced by the oxidation state of the metal center, with the non-bridging monodentate mode **A** common for high oxidation state metals, and increasingly bridged coordination modes (e.g. **E**) for metals in lower oxidation states. Metals with a

medium oxidation state can exhibit coordination modes in between the extremes, such as **B** or **D**.

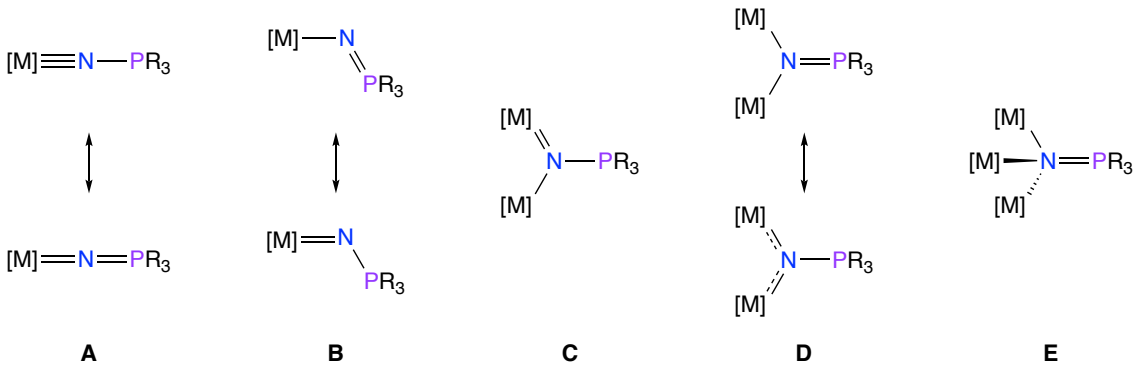

Figure 1.3: Phosphinimide coordination modes

The high +7 oxidation state $[ReO_3(NPEt_3)]$ complex is monomeric with the phosphinimide ligand coordinated in mode **A** (Fig. 1.4).[31–33] Low oxidation state complexes, such as manganese in the +2 oxidation state contain phosphinimide ligands in coordination mode **E** and form heterocubane structures to maintain the μ_3 coordination.[34]

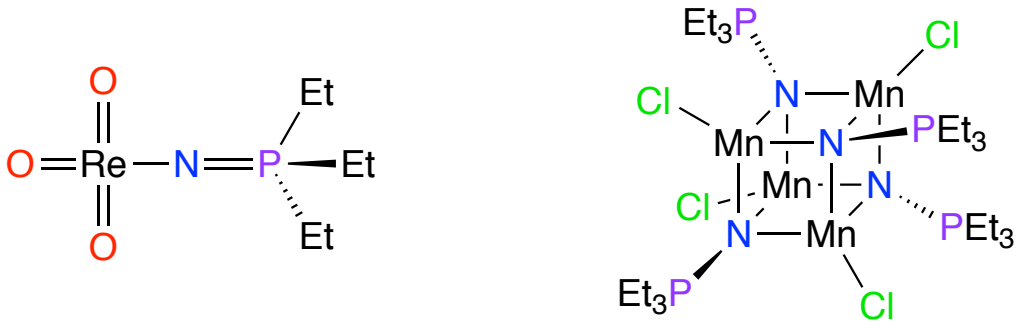

Figure 1.4: High oxidation state monomeric rhenium phosphinimide complex and low oxidation state heterocubane manganese phosphinimide complex

The coordination modes are also influenced by the steric and electronic properties of specific phosphinimide ligands. For instance, increased steric bulk can ensure non-bridging coordination of metals that are in lower oxidation states. These effects can be represented by comparison of trichlorido-titanium complexes in the +4 oxidation state that incorporate different phosphinimide ligands.

The complex $[TiCl_3(NPPh_3)]$ is a monomeric complex with the phosphinimide ligand coordinated by mode **A**, while the analogous triethyl phosphinimide complex exists as the $[TiCl_3(NPEt_3)]_2$ dimer complex where the phosphinimide ligands are in coordination mode **D** (Fig. 1.5).[35,36]

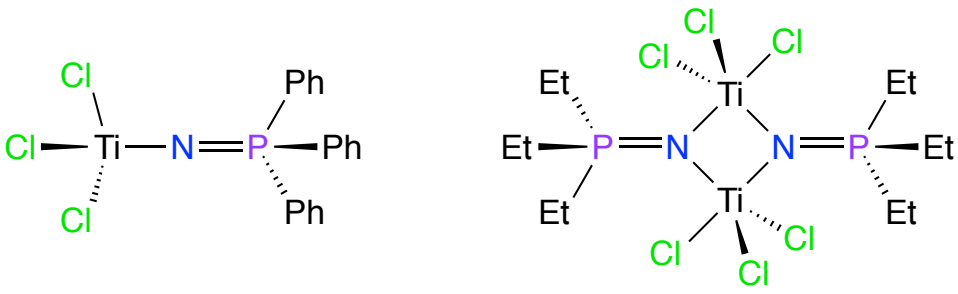

Figure 1.5: Monomeric non-bridging and dimeric bridging titanium phosphinimide complexes

At this intermediate point where both coordination modes are energetically accessible, other factors can influence the coordination mode as well. For instance, the dimeric complex $[TiCl_3(NPEt_3)]_2$ converts into the monomeric complex $[TiCl_3(NPEt_3)(THF)_2]$ when dissolved in tetrahydrofuran (THF), where the phosphinimide coordinates in mode **A** (Fig. 1.6).[36]

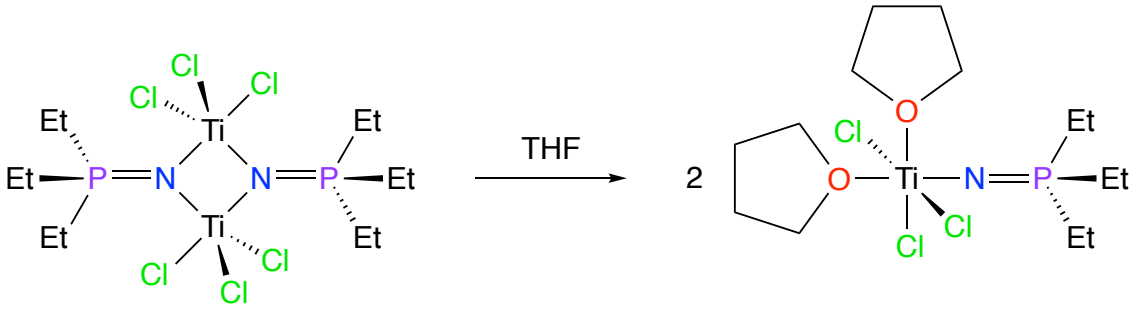

Figure 1.6: Conversion of dimeric bridging titanium phosphinimide complex into monomeric non-bridging complex through THF coordination

1.3.3 Steric Modification

Variation of functional groups bonded to the phosphinimide phosphorus can provide different amounts of steric protection, which impact the stability and reactivity of complexes.[37] Metrics to determine the steric bulk of a ligand can utilize different types of cone angle calculations, such as the Tolman[37], solid[38,39], or exact[40] cone angles. Fig. 1.7 depicts the right circular cone that contains all atoms in the trimethylphosphinimide ligand $[(CH_3)_3P{=}N]^-$, with the exact cone angle for this ligand indicated on the right.

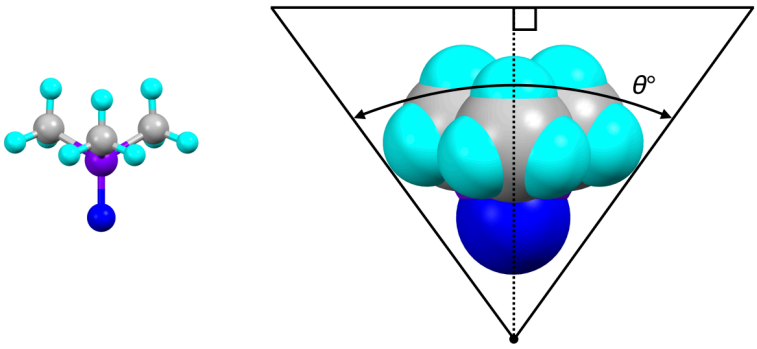

Figure 1.7: Diagram of cone angle for trimethylphosphinimide ligand superimposed over calculated geometry (ORCA[41], PBE0[42] density functional with D3BJ[43,44] correction, def2-TZVPP[45] basis set)

The cone angles for phosphinimide ligands have not been previously reported, but approximations of the steric bulk can be made by only considering the phosphane fragment of the ligands.

The exact cone angle values below for phosphanes show the extensive range of steric modification possible with these ligands when coordinated to a palladium metal ion (Table 1.1).[40] In these examples, the exact cone angle is the apex angle of the most acute right circular cone originating at the ion center and containing all ligand atoms. For this calculation, the size of ligand atoms are defined by the respective van der Waals radii. Increased steric bulk correlates with a larger exact cone angle.

Table 1.1: Calculated exact cone angles for monodentate phosphane ligands on palladium ions for minimum and maximum conformations[40]

Ligand (L)	θ° (minimum)	θ° (maximum)
$P(CH_3)_3$	120.4	–
PEt_3	136.0	168.7
$P(CH_3)_2{}^tBu$	146.0	–
PPh_2Et	149.9	169.3
$PPhEt_2$	153.1	172.8
$PClPh_2$	156.3	–
P^iPr_3	169.0	177.1
PPh_3	170.0	–
$P(p\text{-}FPh)_3$	170.8	–
$P(CH_3)^tBu_2$	174.4	–
P^tBu_3	187.6	–

A large range of exact cone angles is accessible with phosphane ligands, covering over 67° from trimethylphosphine to tris(*tert*-butyl)phosphine. Varied steric protection is also possible from phosphanes with functional groups that exhibit substantially different conformations. For instance, triethylphosphine represents a minimum exact cone angle of 136.0° and maximum of 168.7°, which covers a range of over 32°.

Variation of these functional groups that primarily influence the electronic structure of the ligand can help maintain steric protection while tuning the

electronic structure. As can be seen in Table 1.1, the exact cone angle minima for triphenylphosphine and tri(*para*-fluorophenyl)phosphine differ by less than one degree.

In addition to the range of steric protection available, the structure of phosphinimides provide another unique steric attribute. The majority of the steric bulk is slightly removed from the primary coordination sphere of the central ion due to the spacing provided by the linking nitrogen atom.

Shown below are two different XRD structures of tungsten complexes containing both phosphinimides and at least one structurally analogous phosphane (Fig. 1.8, Fig. 1.9).[46] In both structures the extent of steric bulk spacing provided by the nitrogen in the phosphinimide ligand can be clearly visualized.

The nitrogen of the phosphinimide ligands places the phosphorus atom approximately 3.36 Å from the tungsten center on average, which is an increase of 0.86 Å relative to the similar $P(CH_3)_3$ ligand within the same structures (Table 1.2, Table 1.3). This spacing is likely not consistent across a range of transition metal ions and different phosphinimide derivatives, but does exemplify this structural detail of the ligand framework.

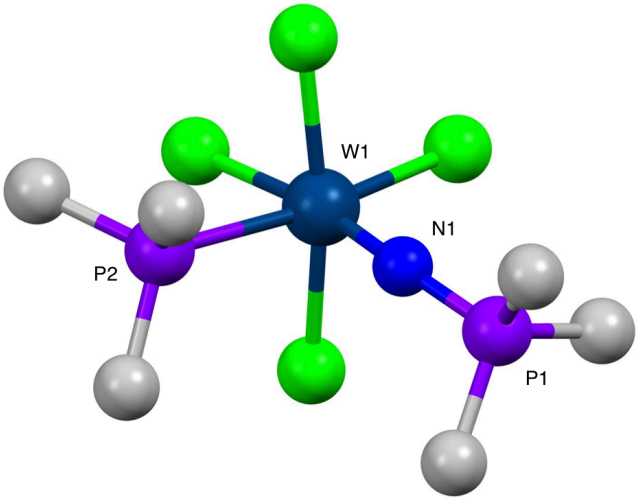

Figure 1.8: Tungsten V phosphinimide-phosphane complex; hydrogen atoms have been omitted for clarity

Table 1.2: Bond distances from tungsten V phosphinimide-phosphane complex

Atoms	**Length (Å)**	**Atoms**	**Length (Å)**
W1-P1	3.341	W1-P2	2.531
W1-N1	1.753	–	–

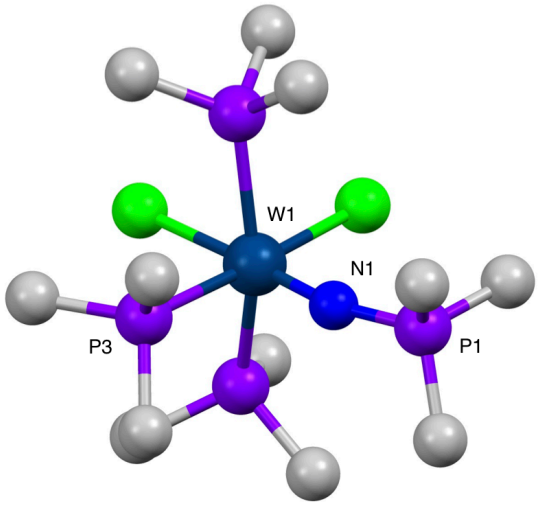

Figure 1.9: Tungsten IV phosphinimide-phosphane complex; chloride counterion and hydrogen atoms have been omitted for clarity

Table 1.3: Bond distances from tungsten IV phosphinimide-phosphane complex

Atoms	**Length (Å)**	**Atoms**	**Length (Å)**
W1-P1	3.385	W1-P3	2.470
W1-N1	1.788	–	–

This feature can provide improved substrate access to the central ion, which is often an important aspect of catalyst design by allowing better substrate access to the metal center for reactivity.[47]

1.3.4 Electronic Modification

Variation of functional groups bonded to the phosphinimide phosphorus can provide fine adjustment of the electronic character of the ligand. A common method to quantify the electronic differences between a class of ligand is to measure the IR bond stretching frequency of a carbonyl ligand *trans* to the varied ligand on the same central ion. As the amount of electron density imparted to the central ion increases, the IR stretching frequency for the trans carbonyl ligand will decrease due to increased back-bonding from the central ion.

As this type of study has not been reported specifically with phosphinimide ligands, the effect phosphanes exhibit can be used to approximate what the effect may be with phosphinimide ligands.

A number of phosphane carbonyl complexes centered on a common rhodium complex were used to study these effects (Table 1.4).[48] In these data, the more electron donating alkyl phosphanes, such as PCy_3 or PEt_3, cause the carbonyl stretching frequency to be lowered. The weaker electron donation from PPh_3 is observed to cause a more intermediate effect, and use of $P(C_6F_5)$ leads to a very limited effect. While the pentafluoroaryl groups of $P(C_6F_5)$ are electron withdrawing, the phosphane ligand as a whole still interacts with the rhodium center and does contribute some electron density to the central ion from this interaction.

Table 1.4: Carbonyl bond frequencies with varying phosphane ligands. Values are generally measured in CH_2Cl_2 solution.[48]

Ligand (L)	v(CO) for *trans*-$Rh(L)_2(CO)(Cl)$
$P(OPh)_3$	2022
$P(C_6F_5)_3$	2005
$PPh(C_6F_5)_2$	1996
$PClPh_2$	1993
$PPh_2(C_6F_5)$	1983
PPh_3	1979
PPh_2Et	1973
$PPhEt_2$	1964
PEt_3	1958
P^iPr_3	1950
PCy_3	1942

Extensive research on the effect of using different phosphanes in metal complexes has been reported previously, and it is clear that use of phosphane derivatives can have a profound effect on the reactivity, stability, and other properties of these systems.[14,48] It stands to reason that variation of the phosphane fragment of phosphinimides will also lead to similar effects when utilized as metal complex ligands, offering the potential for greater control over the reactivity and properties of these complexes.

Additional insight into the substituent effects on bonding within iminophosphorane proligands ($R_3P{=}N{-}H$) has been analyzed with computational methods.[49] In this work, the P=N bond length is impacted by electronic as well as steric influences from the substituents. In general, the results indicate electron donating groups (e.g. alkyl or aryl) lead to more ionic character in the iminophosphorane bonding $R_3P^+{-}N^-{-}H$ and longer P=N bond lengths, relative to the shorter and stronger P=N bonds with electron withdrawing groups as substituents (e.g. halogens). Larger substituents are also reported to lead to longer P=N bond lengths.

1.4 Transition Metal Phosphinimide Complexes

Phosphinimide complexes have been synthesized for most of the transition metals across a range of oxidation states. A variety of group VI transition metal complexes have been synthesized that were primarily centered on molybdenum or tungsten ions, with only two reported complexes centered on chromium (Fig. 1.10),[50,51] and no known complexes that incorporate the radioactive seaborgium ion.

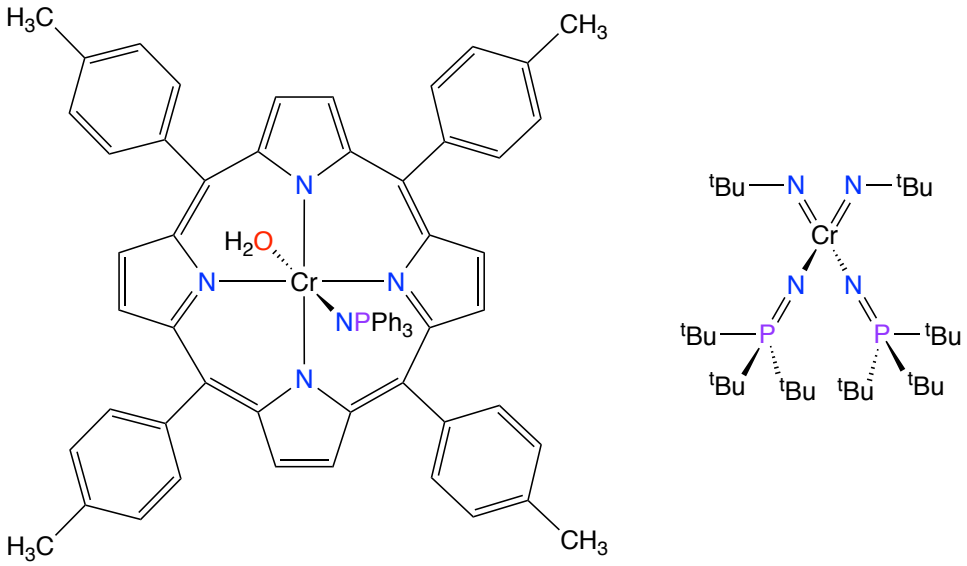

Figure 1.10: Two reported chromium phosphinimide complexes

Known tungsten phosphinimide complexes consist mostly of halide or homoleptic phosphinimide complexes (Fig. 1.11).[46,52–56] Literature reports of these complexes focus mostly on the methods of synthesis to generate these complexes and structural studies.

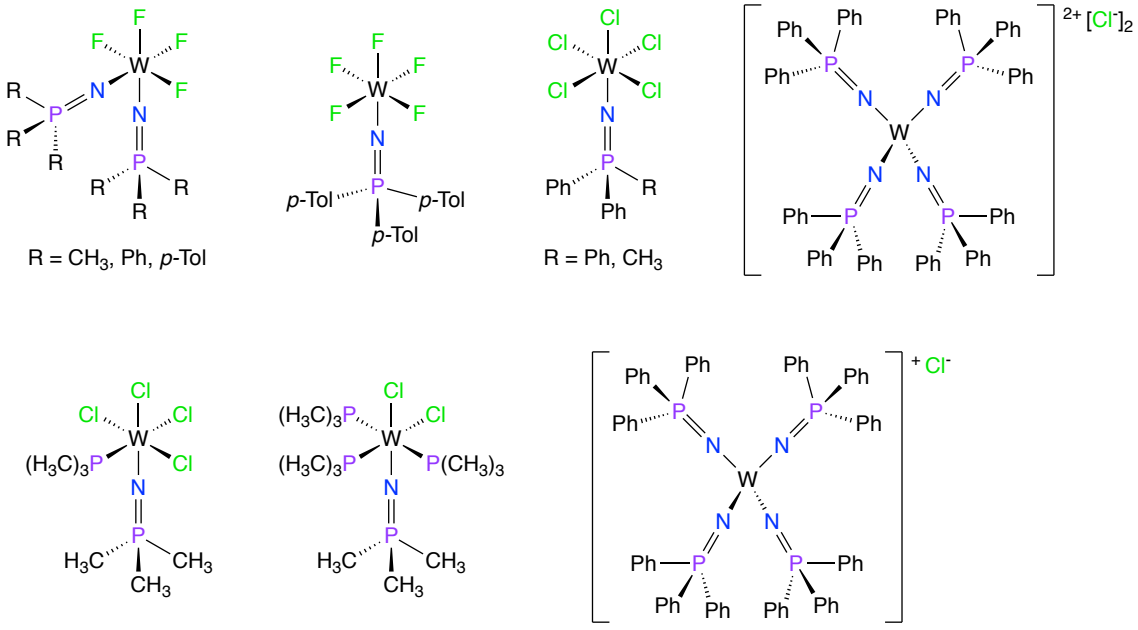

Figure 1.11: Tungsten halide and homoleptic phosphinimide complexes

There are some examples of more tungsten phosphinimide complexes that incorporate metal-element multiple bonds with nitrido, oxido, sulfido, and alkylidyne ligands (Fig. 1.12).[52,57–59]

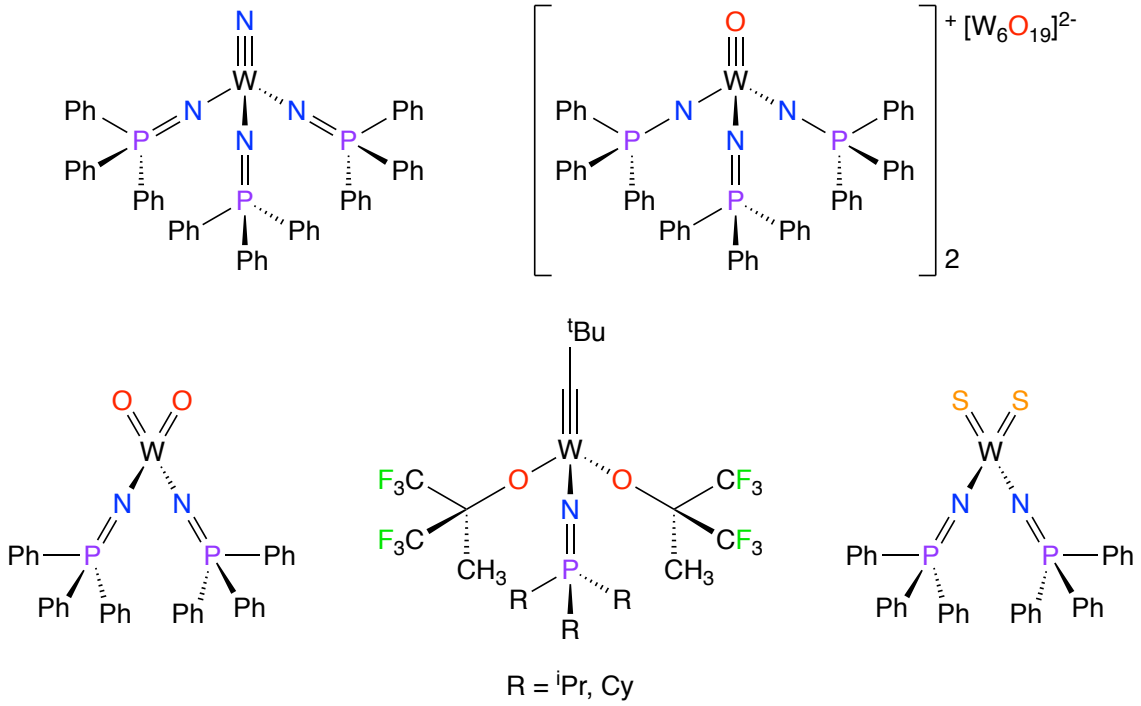

Figure 1.12: All reported tungsten phosphinimide complexes with metal-element multiple bonds

The tungsten alkylidyne complexes were evaluated for both catalytic alkyne cross-metathesis (ACM) and ring-closing alkyne metathesis (RCAM) at room temperature, and were shown to be effective catalysts for two test substrates.[57] For instance, catalyst loading as low as 0.1 mol% generated 85% yield of the ACM product within 6 hours. Optimization of conditions for these catalysts and expansion of the substrate scope is still pending.

Similar to the known tungsten complexes, molybdenum phosphinimide complexes also consist mostly of halide or homoleptic phosphinimide complexes (Fig. 1.13).

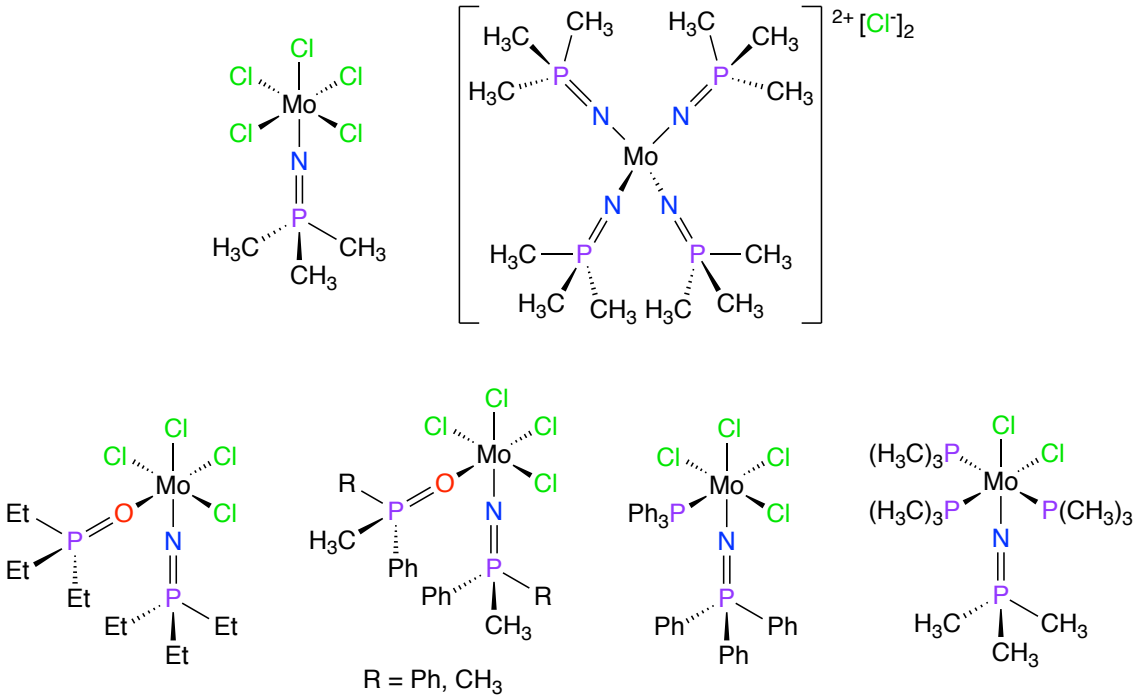

Figure 1.13: Molybdenum halide and homoleptic phosphinimide complexes

Similar to the tungsten complexes, there are only two known examples of molybdenum phosphinimide complexes that have metal-element multiple bonds, with incorporation of nitrido and oxido ligands (Fig. 1.14).[59,60] Reports on these complexes focused on structural assessment. There are no phosphinimide complexes reported that contain molybdenum-carbon bonds.

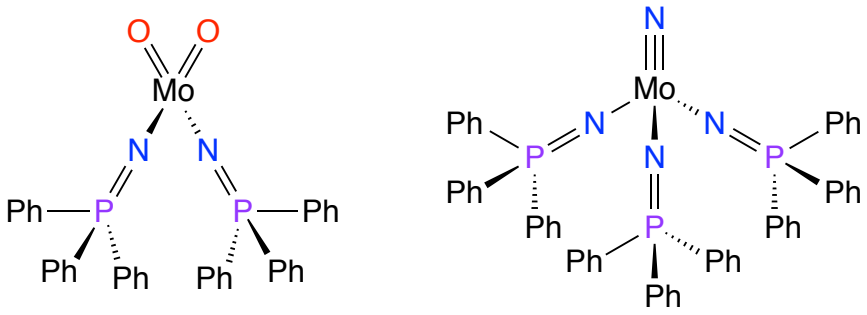

Figure 1.14: Molybdenum phosphinimide complexes with metal-element multiple bonds

While a number of group VI phosphinimide complexes have been reported, there is limited information about the reactivity and further synthetic use of these complexes. In addition, reports of group VI phosphinimide complexes that contain metal-element multiple bonds are also uncommon. Given this lack of knowledge about metal-element multiple bonds in complexes with phosphinimide ligands, and the prevalence of these ligands in many modern catalysts, there is a gap in knowledge of synthetic methods to build these types of complexes, and data on their properties and reactivity.

1.5 Main Group Phosphinimide Complexes

While not the focus of this research, phosphinimide ligands have also been coordinated to main group elements.[61] High-oxidation states are less common with the main-group elements, yet there is still diverse chemistry with these elements.

Monomeric homoleptic phosphinimide complexes such as $[(Ph_3P{=}N)_4Sn]$ have been reported,[62] as well as monomeric heteroleptic complexes such as $[(CH_3)_3P{=}N)GeCl_3]$ (Fig. 1.15).[63,64]

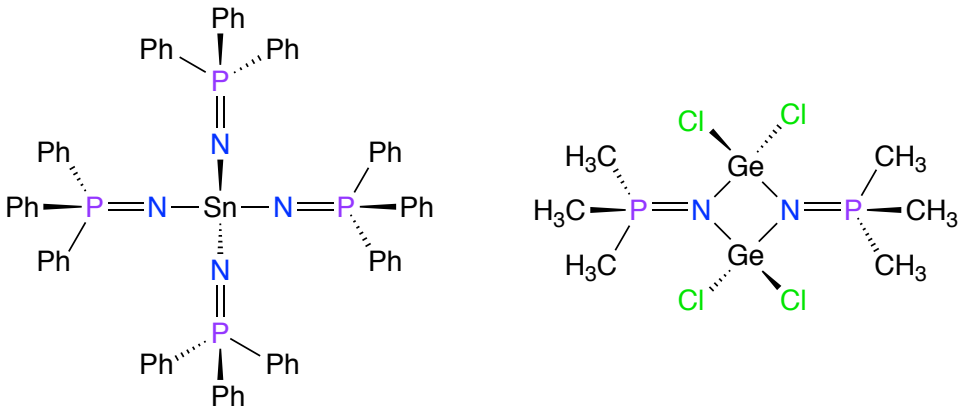

Figure 1.15: Tin and germanium phosphinimide complexes

One example of a higher oxidation state main-group complex is the dicationic sulfur complex $[(CH_3)_3P{=}N]_4S]Cl_2 \bullet 4\ CH_3CN$ (Fig. 1.16), where the SN bond distances are described as approximate double bonds.[65]

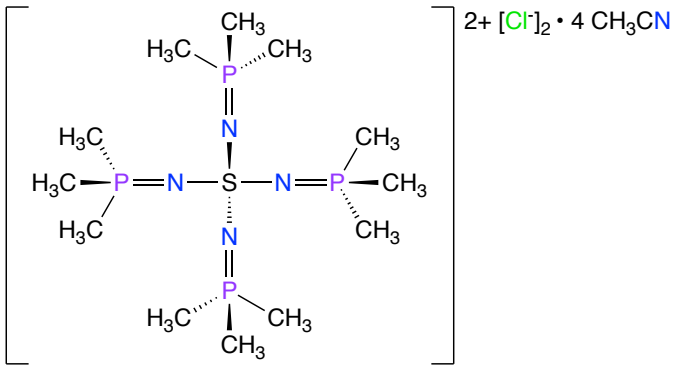

Figure 1.16: Tetraphosphinimide sulfur dicationic complex

Bridging species are also known with intervening chlorido ligands such as $[((CH_3)OC_6H_4)(Ph_3P{=}N)TeCl_2]_2$. Bridging through the phosphinimide nitrogen atom is also possible such as in the dimeric aluminum complex $[(Ph_3P{=}N]AlCl_2]_2$ (Fig. 1.17).[66]

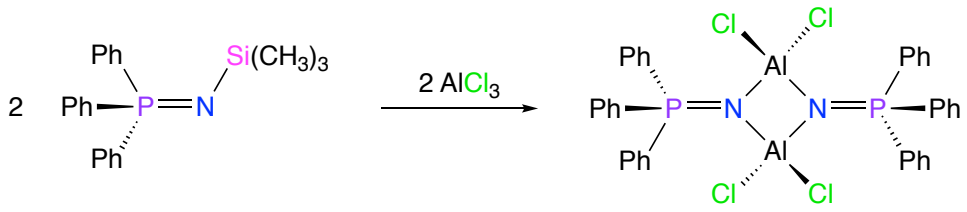

Figure 1.17: Dichlorido aluminum phosphinimide dimer complex

The similar tetramethyl aluminum complex $[(Ph_3P{=}N]AlMe_2]_2$ can also be synthesized, and can be converted to the cationic form by methyl abstraction by $B(C_6F_5)_3$ with further coordination of $P(CH_3)_3$ in the now open coordination site (Fig. 1.18).[67]

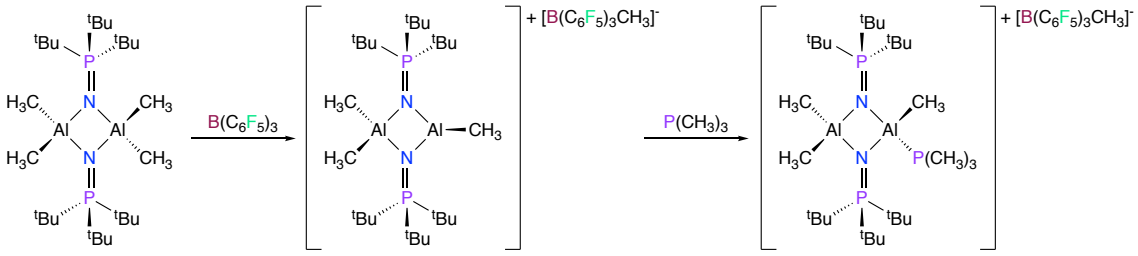

Figure 1.18: Dimethyl aluminum phosphinimide dimer complex reactivity

Some of the synthetic methods to generate main-group phosphinimide complexes are analogous to methods used for the transition metals.

Future research in developing main group phosphinimide complexes further can potentially apply some of the results from later chapters of this dissertation.

1.6 References

1. J. N. Armor, *Catal. Today*, 2011, **163**, 3–9.
2. I. Fechete, Y. Wang and J. C. Védrine, *Catal. Today*, 2012, **189**, 2–27.
3. B. Cornils and W. A. Herrmann, *J. Catal.*, 2003, **216**, 23–31.
4. J. R. Rostrup-Nielsen, *Catal. Today*, 1993, **18**, 125–145.
5. J. F. Roth, *Appl. Catal. Gen.*, 1994, **113**, 131–140.
6. G. J. P. Britovsek, V. C. Gibson and D. F. Wass, *Angew. Chem. Int. Ed.*, 1999, **38**, 428–447.
7. C. Marcilly, *J. Catal.*, 2003, **216**, 47–62.
8. J. N. Armor, *Catal. Today*, 2014, **236**, 171–181.
9. J. Mol, *J. Mol. Catal. Chem.*, 2004, **213**, 39–45.
10. C. E. Tucker, *Top. Catal.*, 2002, **19**, 111–118.
11. A. S. K. Hashmi, *Chem. Rev.*, 2007, **107**, 3180–3211.
12. C. C. C. Johansson Seechurn, M. O. Kitching, T. J. Colacot and V. Snieckus, *Angew. Chem. Int. Ed.*, 2012, **51**, 5062–5085.
13. S. H. Cho, J. Y. Kim, J. Kwak and S. Chang, *Chem. Soc. Rev.*, 2011, **40**, 5068–5083.
14. D. S. Surry and S. L. Buchwald, *Angew. Chem. Int. Ed.*, 2008, **47**, 6338–6361.

15. A. Dondoni and A. Massi, *Angew. Chem. Int. Ed.*, 2008, **47**, 4638–4660.
16. G. Beck, *Synlett*, 2002, **6**, 837–850.
17. S. Dworakowska, D. Bogdał, F. Zaccheria and N. Ravasio, *Catal. Today*, 2014, **223**, 148–156.
18. G. Wegener, M. Brandt, L. Duda, J. Hofmann, B. Klesczewski, D. Koch, R.-J. Kumpf, H. Orzesek, H.-G. Pirkl, C. Six, C. Steinlein and M. Weisbeck, *Appl. Catal. Gen.*, 2001, **221**, 303–335.
19. K. Matyjaszewski and J. Xia, *Chem. Rev.*, 2001, **101**, 2921–2990.
20. M. Kamigaito, T. Ando and M. Sawamoto, *Chem. Rev.*, 2001, **101**, 3689–3746.
21. R. R. Schrock and A. H. Hoveyda, *Angew. Chem. Int. Ed.*, 2003, **42**, 4592–4633.
22. C. W. Bielawski and R. H. Grubbs, *Prog. Polym. Sci.*, 2007, **32**, 1–29.
23. A. P. S. Chouhan and A. K. Sarma, *Renew. Sustain. Energy Rev.*, 2011, **15**, 4378–4399.
24. A. Singh and L. Spiccia, *Coord. Chem. Rev.*, 2013, **257**, 2607–2622.
25. G. W. Parshall, *J. Mol. Catal.*, 1978, **4**, 243–270.
26. K. Sakai and H. Ozawa, *Coord. Chem. Rev.*, 2007, **251**, 2753–2766.
27. D. J. Cole-Hamilton, *Science*, 2003, **299**, 1702–1706.
28. C. E. Garrett and K. Prasad, *Adv. Synth. Catal.*, 2004, **346**, 889–900.
29. J. M. Thomas, R. Raja and D. W. Lewis, *Angew. Chem. Int. Ed.*, 2005, **44**, 6456–6482.

30. P. Weightman and D. S. Martin, in *Surfaces and Interfaces for Biomaterials*, Elsevier Science & Technology, Cambridge, 2005, pp. 3–28.
31. K. Dehnicke, M. Krieger and W. Massa, *Coord. Chem. Rev.*, 1999, **182**, 19–65.
32. H. W. Roesky, D. Hesse, M. Rietzel and M. Noltemeyer, *Z. Naturforschung*, 1990, **45b**, 72–76.
33. A. Diefenbach and F. M. Bickelhaupt, *Z. Anorg. Allg. Chem.*, 1999, **625**, 892–900.
34. U. Riese, B. Neumüller, N. Faza, W. Massa and K. Dehnicke, *Z. Anorg. Allg. Chem.*, 1997, **623**, 351–356.
35. T. Rübenstahl, F. Weller, K. Harms, K. Dehnicke, D. Fenske and G. Baum, *Z. Anorg. Allg. Chem.*, 1994, **620**, 1741–1749.
36. M. M. Stahl, N. Faza, W. Massa and K. Dehnicke, *Z. Anorg. Allg. Chem.*, 1998, **624**, 209–214.
37. C. A. Tolman, *Chem. Rev.*, 1977, **77**, 313–348.
38. D. White, B. C. Taverner, P. G. L. Leach and N. J. Coville, *J. Comput. Chem.*, 1993, **14**, 1042–1049.
39. T. L. Brown and K. J. Lee, 28.
40. J. A. Bilbrey, A. H. Kazez, J. Locklin and W. D. Allen, *J. Comput. Chem.*, 2013, **34**, 1189–1197.
41. F. Neese, *Wiley Interdiscip. Rev. Comput. Mol. Sci.*, 2012, **2**, 73–78.
42. C. Adamo and V. Barone, *J. Chem. Phys.*, 1999, **110**, 6158–6170.

43. S. Grimme, J. Antony, S. Ehrlich and H. Krieg, *J. Chem. Phys.*, 2010, **132**, 154104.
44. S. Grimme, S. Ehrlich and L. Goerigk, *J. Comput. Chem.*, 2011, **32**, 1456–1465.
45. F. Weigend and R. Ahlrichs, *Phys. Chem. Chem. Phys.*, 2005, **7**, 3297.
46. J. D. Lichtenhan, J. W. Ziller and N. M. Doherty, *Inorg. Chem.*, 1992, **31**, 2893–2900.
47. D. W. Stephan, *Organometallics*, 2005, 2548–2560.
48. M. L. Clarke and J. R. Frew, *Organomet Chem*, 2009, **35**, 19–46.
49. W. C. Lu and C. C. Sun, *J. Mol. Struct. Theochem*, 2002, **593**, 1–7.
50. A. A. Danopoulos, W.-H. Leung and G. Wilkinson, *Polyhedron*, 1990, **9**, 2625–2634.
51. J. W. Buchler, C. Dreher and K.-L. Lay, *Chem. Ber.*, 1984, **117**, 2261–2274.
52. A. Dietrich, B. Neumüller and K. Dehnicke, *Z. Anorg. Allg. Chem.*, 2000, 1837–1844.
53. E. Rentschler, D. Nußhär, F. Weller and K. Dehnicke, *Z. Anorg. Allg. Chem.*, 1993, **619**, 999–1003.
54. H. W. Roesky, K. V. Katti, U. Seseke, U. Scholz, R. Herbst, E. Egert and G. M. Sheldrick, *Z. Naturforschung*, 1986, 1509–1512.
55. A. Dietrich and K. Dehnicke, *Z. Anorg. Allg. Chem.*, 2007, **633**, 705–708.
56. H. W. Roesky, T. Tojo, M. Ilemann and D. Westhoff, *Z. Naturforschung*, 1987, **42b**, 877–880.

57. X. Wu, C. G. Daniliuc, C. G. Hrib and M. Tamm, *J. Organomet. Chem.*, 2011, **696**, 4147–4151.

58. S. Beer, K. Brandhorst, C. G. Hrib, X. Wu, B. Haberlag, J. Grunenberg, P. G. Jones and M. Tamm, *Organometallics*, 2009, **28**, 1534–1545.

59. A. Dietrich, B. Neumüller and K. Dehnicke, *Z. Anorg. Allg. Chem.*, 1999, 1321–1326.

60. A. Dietrich, B. Neumüller and K. Dehnicke, *Z. Anorg. Allg. Chem.*, 1998, **624**, 1247–1249.

61. K. Dehnicke and F. Weller, *Coord. Chem. Rev.*, 1997, **158**, 103–169.

62. M. Veith and V. Huch, *J. Organomet. Chem.*, 1985, **293**, 161–176.

63. W. Wolfsberger, *Z. Naturforschung*, 1977, **32b**, 152–156.

64. W. Wolfsberger and H. H. Pickel, *J. Organomet. Chem.*, 1973, **54**, C8–C10.

65. H. Folkerts, W. Hiller, M. Herker, S. F. Vyboishchikov, G. Frenking and K. Dehnicke, *Angew. Chem. Int. Ed. Engl.*, 1995, **34**, 1362–1363.

66. F. Heshmatpour, D. Nußhär, R. Garbe, S. Wocadlo, W. Massa, K. Dehnicke, H. Goesmann and D. Fenske, *Z. Anorg. Allg. Chem.*, 1995, **621**, 443–450.

67. C. M. Ong, P. McKarns and D. W. Stephan, *Organometallics*, 1999, **18**, 4197–4204.

2 General Complex Synthesis and Reactivity

2.1 Introduction

Phosphinimide ligands have been structurally studied in transition metal complexes that primarily incorporate halide ligands or neutral solvent donor ligands.[1,2] A diverse range of metal ions and oxidation states have been studied with these complexes. Despite the wide range of phosphinimide complexes reported, evaluation of further reactivity or catalytic use of these complexes has been limited. The only class of phosphinimide complexes studied more extensively are group IV (primarily titanium) based complexes, which were developed to be effective catalysts for ethylene polymerization under commercial conditions by the Stephan research group (Fig. 2.1),[3–5] and may be utilized in industry.[6]

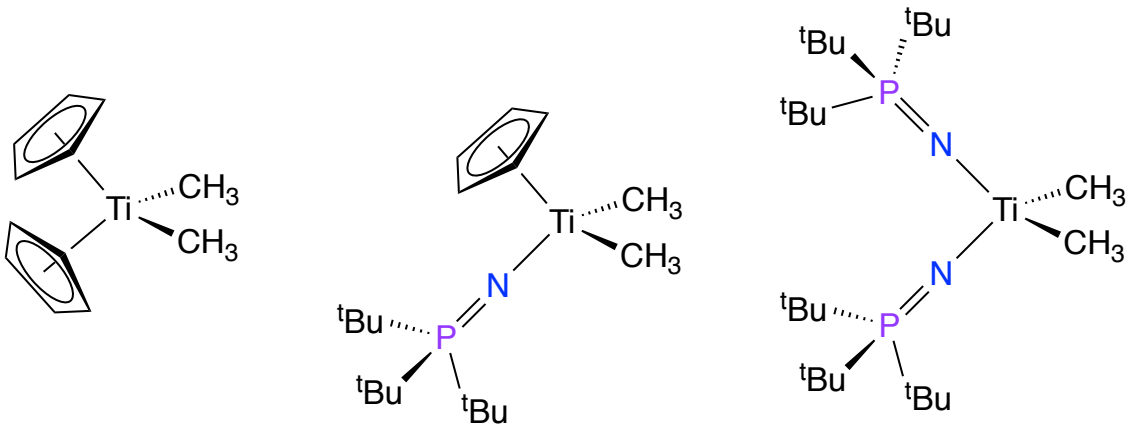

Figure 2.1: Selection of titanium ethylene polymerization catalysts from Stephan research group

Given the precedence of successful phosphinimide group IV catalysts, and the beneficial attributes of phosphinimide ligands described in Chapter 1, a large potential exists for further research in the use of phosphinimide ligands. In addition to these catalytic metathesis applications, the +6 oxidation state of group VI metals was the focus of this research, as knowledge of phosphinimide complexes of high oxidation state group VI metals was limited, with only a few previously reported Mo(VI) phosphinimide complexes, three of which are neutral molecules.

In 1992, $[((CH_3)_3P{=}N)MoCl_5]$ was the first Mo(VI) phosphinimide complex reported. This complex was generated through oxidation of $[Mo(NSi(CH_3)_3)Cl_2(P(CH_3))_3]$ with chlorine gas and subsequent ligand rearrangement to eliminate trimethylsilylchloride and $PCl_2(CH_3)_3$ (Fig 2.2).

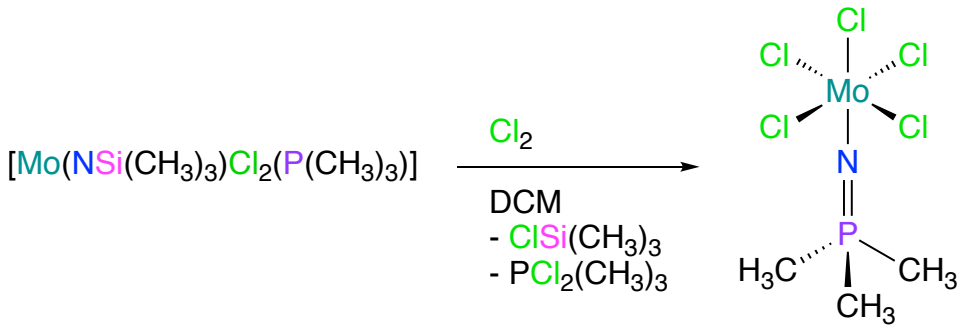

Figure 2.2: First neutral Mo(VI) phosphinimide complex

The first ionic Mo(VI) phosphinimide complexes were reported in 1993, as the ions of $[(Ph_3P{=}N)_4Mo][(Ph_3P{=}N)Mo(N)Cl_3]_2$ (Fig. 2.3),[7] and the related $[Mo(NP(CH_3)_3)_4]Cl_2$ has also been reported.[8]

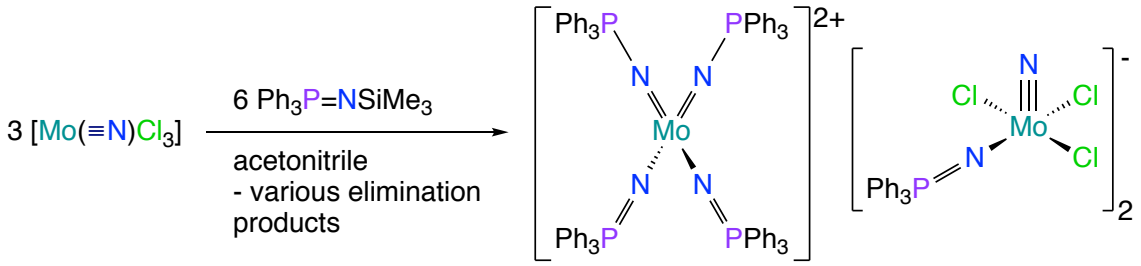

Figure 2.3: First ionic Mo(VI) phosphinimide complexes

In 1998, a neutral nitrido Mo(VI) phosphinimide complex $[(Ph_3P{=}N)_3Mo(N)]$ was reported.[9] This complex was generated by salt metathesis of a lithiated phosphinimide proligand with $[Mo(N_3S_2)Cl_3]_2$ to generate the nitride fragment (Fig. 2.4). In a later report, crystals of $[Mo(NPPh_3)_4][BF_4]_2$ were obtained through exposure of $[(Ph_3P{=}N)_3Mo(N)]$ to boron trifluoride etherate.[10]

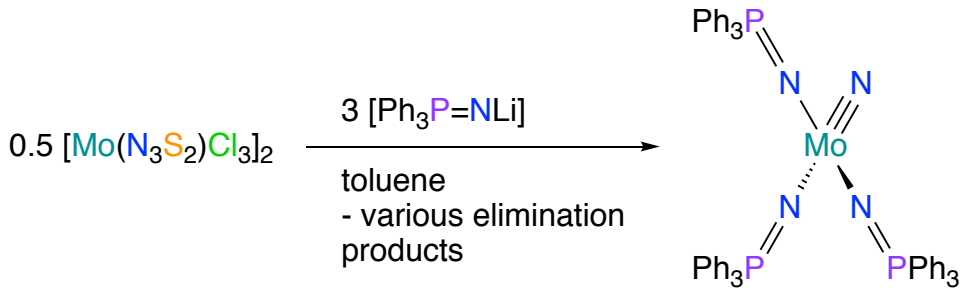

Figure 2.4: Synthesis of a neutral nitrido Mo(VI) phosphinimide complex

The dioxido Mo(VI) complex $[(Ph_3P{=}N)_3Mo(O)_2]$ was reported in 1999, and can be generated through reaction of $[(Ph_3P{=}N)_3Mo(N)]$ with water, or by salt metathesis with $[Mo(O)_2Cl_2]$ (Fig. 2.5).[11]

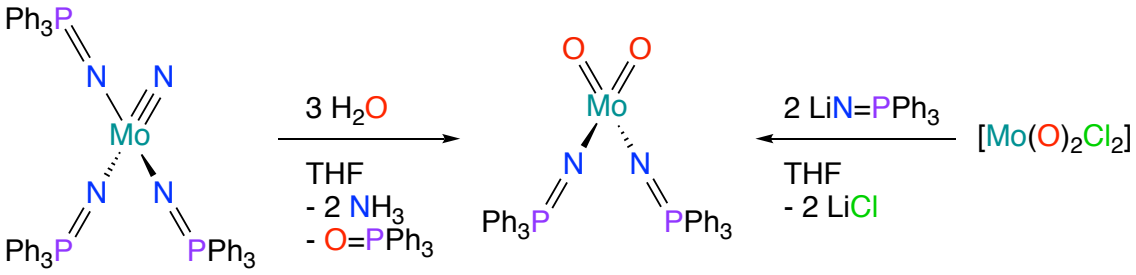

Figure 2.5: Synthesis of a dioxido Mo(VI) phosphinimide complex

Building on these reported results, the initial sequence of complexes selected to study were derived from the readily prepared group VI synthons [(DME)Mo(O)$_2$Cl$_2$] (**2.1**), [(DME)Mo(O)(N^{t}Bu)Cl$_2$] (**2.2**), and [(DME)Mo(N^{t}Bu)$_2$Cl$_2$] (**2.3**) (Fig 2.6). These precursor complexes provide oxido and chlorido ligands that can be used for installation of phosphinimide ligands. Complexes **2.1-2.3** also contain metal-element multiple bonds in the form of oxido and imido ligands, removing the need to incorporate these functionalities at a later point.

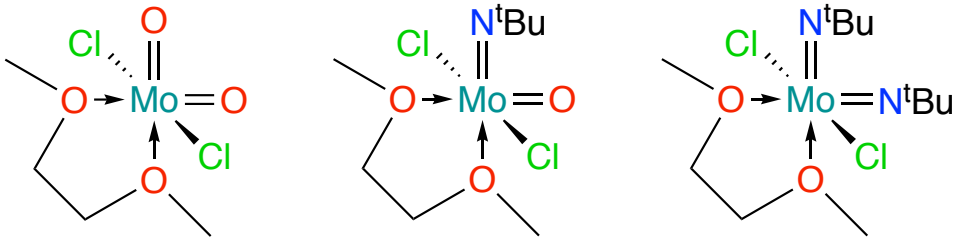

2.1 **2.2** **2.3**

Figure 2.6: Oxido and imido molybdenum dichloride dimethoxyethane starting materials

2.2 Results and Discussion

2.2.1 Phosphinimide Proligand Syntheses

Initial efforts focused primarily on the use of *tert*-butyl phosphane derived phosphinimide ligands. Three forms of the proligand were utilized for different synthetic approaches to complex formation.

2.2.1.1 Trimethylsilyl Phosphinimide Proligand Syntheses

The generic trimethylsilyl substituted phosphinimine species ($R_3P{=}N{-}Si(CH_3)_3$) can be synthesized by a Staudinger reaction between a phosphane derivative and azido trimethylsilane ($N_3Si(CH_3)_3$).[4]

Specifically, $^tBu_3P{=}N{-}Si(CH_3)_3$ (**L1**) was generated by the combination of tris(*tert*-butyl)phosphane with a three-fold excess of azido trimethylsilane (Fig 2.7) in a sealed vessel at elevated temperature for 6 hours.

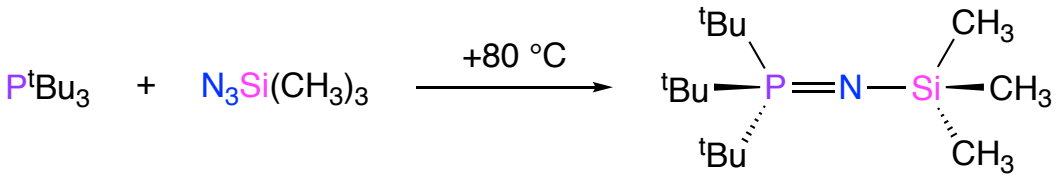

Figure 2.7: Synthesis of $^tBu_3P{=}N{-}Si(CH_3)_3$ (**L1**)

Removal of the remaining azido trimethylsilane and volatile byproducts under reduced pressure results in the isolation of the target product **L1**. ^1H and $^{31}P\{^1H\}$ nuclear magnetic resonance (NMR) spectroscopic analysis at ambient temperature (~25 °C) indicates pure isolation of **L1** in 98% yield, with both

spectra matching previously reported data.[4] The ^{1}H NMR spectrum contains a long-range ^{31}P coupled doublet for the *tert*-butyl protons at 1.16 ppm ($^{3}J_{PH}$ = 12.7 Hz) in C_6D_6, and a singlet for the trimethylsilyl protons at 0.41 ppm in C_6D_6 (Fig. 2.8). Finally, the ^{31}P{^{1}H} NMR spectrum contains a singlet for the single phosphorus nucleus in **L1** at 32.31 ppm in C_6D_6 (Fig 2.9).

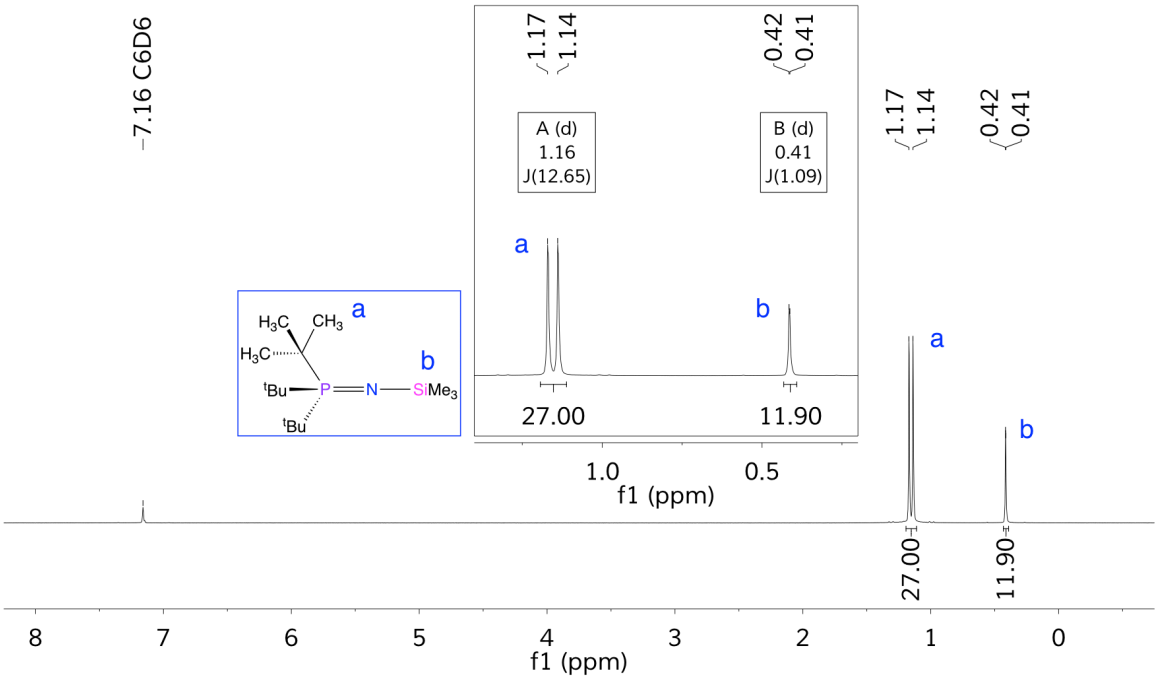

Figure 2.8: ^{1}H NMR spectrum of **L1** in C_6D_6 (400 MHz)

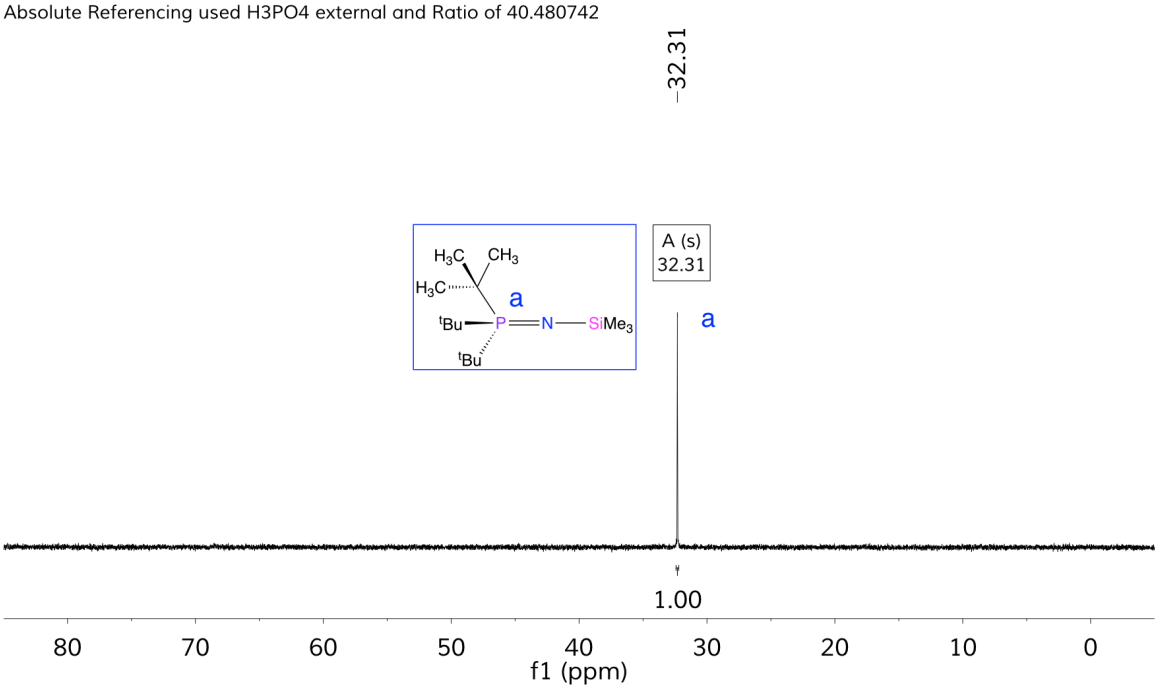

Figure 2.9: $^{31}P\{^{1}H\}$ NMR spectrum of **L1** in C_6D_6 (162 MHz)

This trimethylsilyl-substituted phosphinimine can be used directly as proligands for metal complexes through elimination reactions involving the $Si(CH_3)_3$ fragment, which is described in more detail in Section 2.2.2. Alternately, the trimethylsilyl-substituted phosphinimines, can be further elaborated to alternative proligand forms as described in Section 2.2.1.2.

2.2.1.2 Protonated Phosphinimine Proligand Syntheses

The trimethylsilyl-substituted phosphinimines ($R_3P{=}NSi(CH_3)_3$) can generally be protonated through reaction with alcohols to eliminate alkylsilylethers. Specifically, $^{t}Bu_3P{=}NH$ (**L2**) was formed through combination of L1 with methanol in toluene, which was allowed to react at elevated

temperatures (+100 °C) for 18 hours (Fig 2.10), using a modified literature procedure.[12]

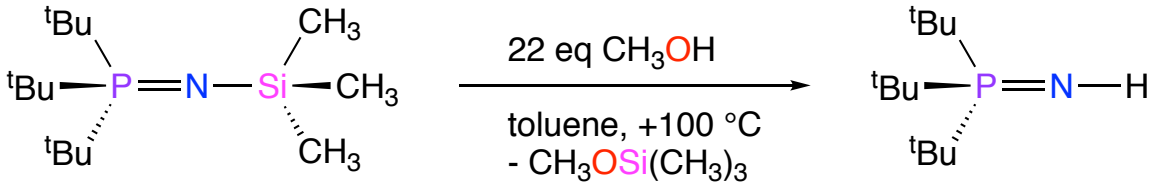

Figure 2.10: Synthesis of protonated phosphinimine **L2**

Removal of volatile byproducts, solvent, and excess methanol under reduced pressure allows for clean isolation of the target product **L2**. ^{1}H, $^{13}C\{^{1}H\}$, and $^{31}P\{^{1}H\}$ NMR spectra collected at ambient temperature (~25 °C) indicated pure isolation of **L2** in 96% yield.[13] The ^{1}H NMR spectrum contains the expected ^{31}P coupled doublet for the *tert*-butyl protons at 1.22 ppm ($^{3}J_{PH}$ = 11.9 Hz) in C_6D_6, and a singlet for the N-H proton at 0.19 ppm in C_6D_6 (Fig 2.11). The $^{13}C\{^{1}H\}$ NMR spectrum exhibits the ^{31}P coupled quaternary *tert*-butyl carbons at 38.96 ppm ($^{1}J_{PC}$ = 45.6 Hz), and a single peak for the *tert*-butyl methyl carbons at 29.29 ppm (Fig. 2.12). The $^{31}P\{^{1}H\}$ NMR spectrum contains the expected singlet for the lone phosphorus nucleus in **L2** at 56.13 ppm in C_6D_6 (Fig. 2.13).

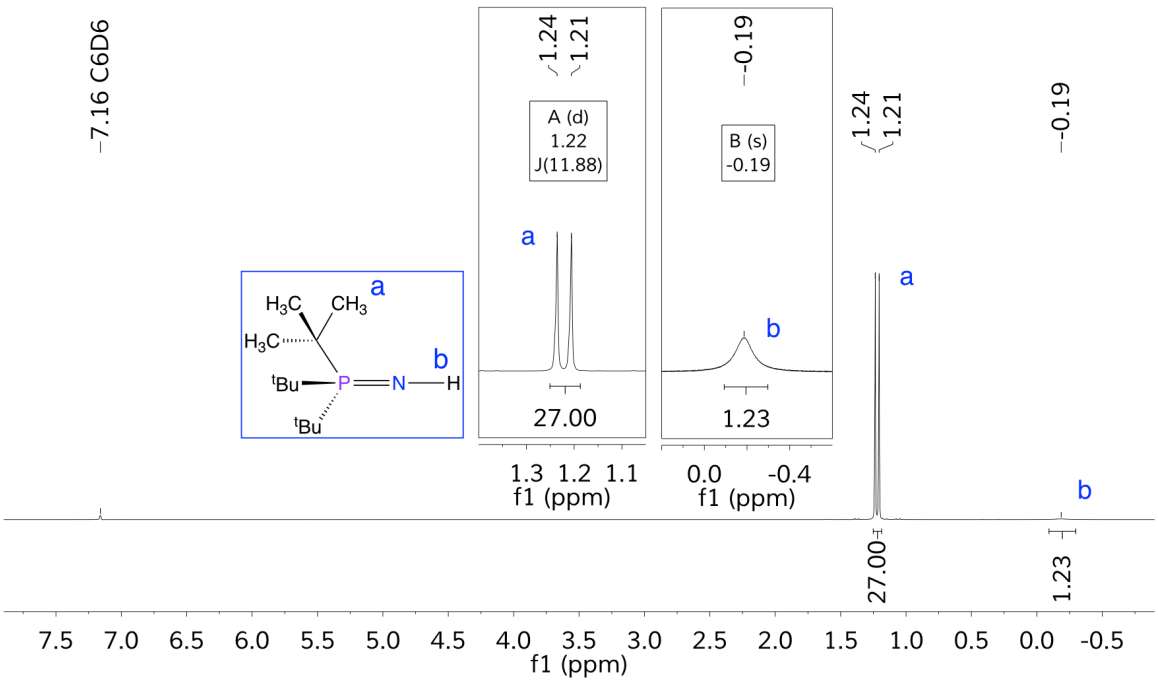

Figure 2.11: ^{1}H NMR spectrum of **L2** in C_6D_6 (400 MHz)

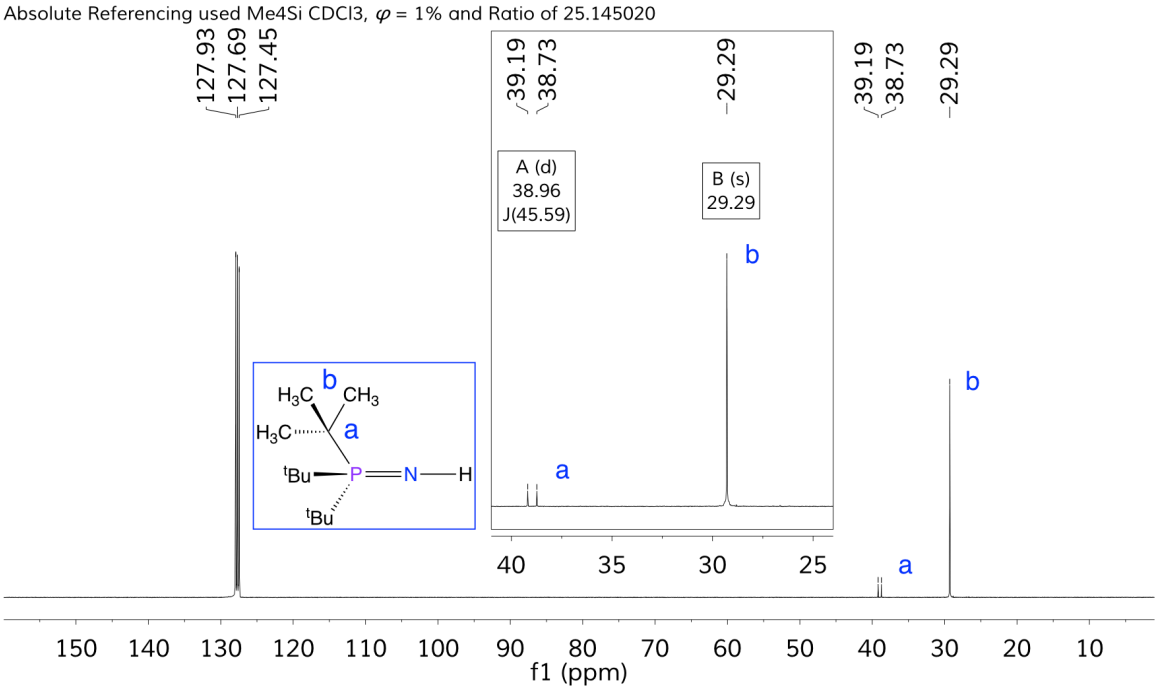

Figure 2.12: $^{13}C\{^{1}H\}$ NMR spectrum of **L2** in C_6D_6 (101 MHz)

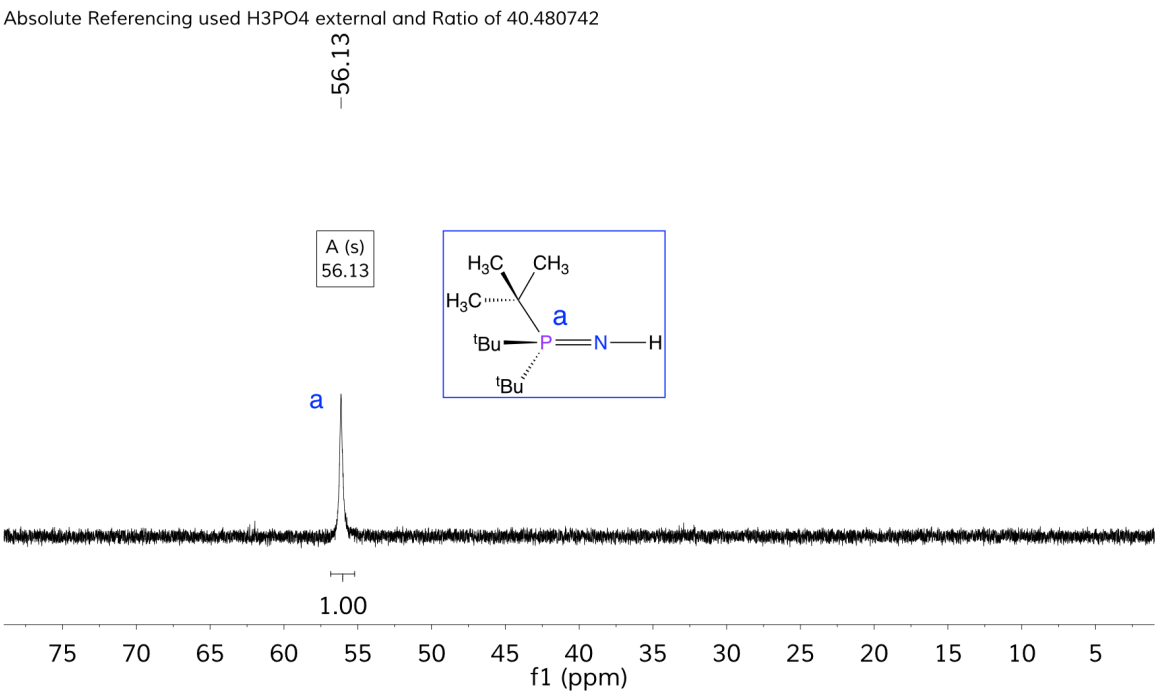

Figure 2.13: $^{31}P\{^{1}H\}$ NMR spectrum of **L2** in C_6D_6 (162 MHz)

2.2.1.3 Lithiated Phosphinimide Proligand Syntheses

The free phosphinimines ($R_3P{=}NH$) can generally be deprotonated through reaction with alkyllithium reagents to eliminate the corresponding alkane and form lithio salts. Specifically, $^{t}Bu_3P{=}NLi$ (**L3**) was formed by combination of **L2** with methyllithium in THF, initially below -100 °C and equilibrated to ambient temperature over 1 hour.[12] While **L3** could be isolated by removal of solvent and volatile byproducts, the solid form of **L3** has been reported to form tetrameric aggregates with a cubic Li-N core (Fig. 2.14).[14]

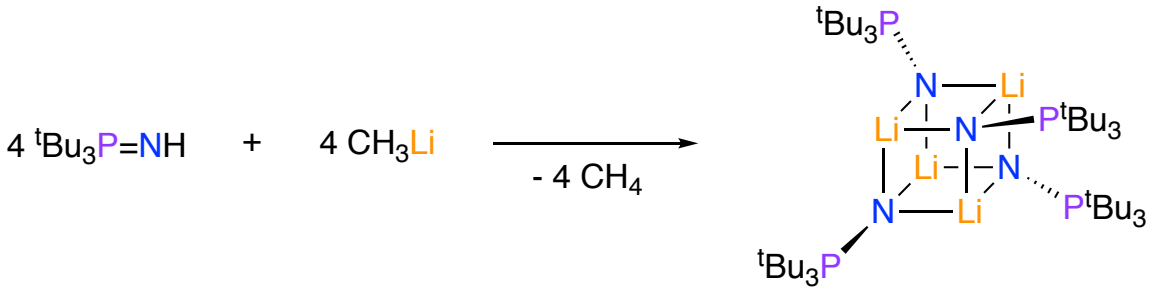

Figure 2.14: Synthesis of a tetrameric lithium phosphinimide complex

The large steric volume of the $^{t}Bu_3P$ fragments make this aggregated form of the proligand difficult to dissolve back into the monomeric form for further synthetic use. Given these concerns, an *in situ* methodology was utilized with **L3**, where it was not explicitly isolated, but used soon after formation to generate phosphinimide complexes. Higher yields and better purity were observed for isolated metal complexes that were formed through *in situ* generation of **L3** rather than use of isolated **L3**. Due to the *in situ* usage of **L3**, this proligand and related derivatives were not isolated specifically for characterization as the data for the aggregates have been previously reported.[14]

2.2.2 Me_3Si-X Elimination Methodology

Elimination reactions of trimethylsilyl containing compounds have been previously reported as a synthetic approach to install phosphinimide ligands when using $R_3P{=}N{-}Si(CH_3)_3$ derivatives. Reaction of this proligand with metal nitrido, oxido, or chlorido ligands can generate silylated byproducts such as

$N(Si(CH_3)_3)_3$, $O(Si(CH_3)_3)_2$, or $ClSi(CH_3)_3$ (Fig. 2.15), which can be easily separated by vacuum from metal complex products.

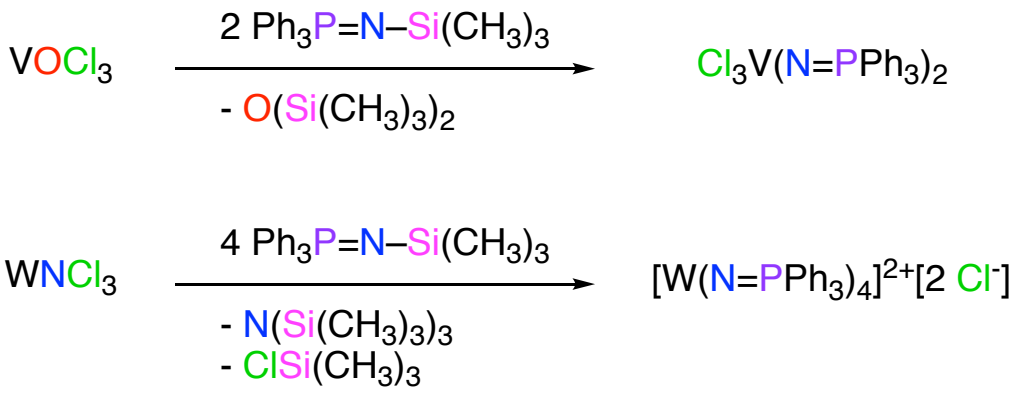

Figure 2.15: Previously reported trimethylsilyl elimination reactions

These elimination reactions were commonly used to generate phosphinimide complexes, but have never been shown to generate heteroleptic complexes containing metal-element multiple bonds.

With this type of reactivity it was possible that complexes **2.1** and **2.2** could eliminate $O(Si(CH_3)_3)_2$, $ClSi(CH_3)_3$, or both, given the presence of both oxido and chlorido ligands. Complex **2.3** however was only anticipated to eliminate $ClSi(CH_3)_3$ due to a lack of oxido ligands in the complex. Complexes **2.1** and **2.2** interestingly undergo chemospecific elimination of $O(Si(CH_3)_3)_2$ when combined with two equiv. of $^tBu_3P{=}N{-}Si(CH_3)_3$ despite the presence of chlorido groups in the starting complexes. This selective elimination leads to complexes $[(^tBu_3P{=}N)_2Mo(O)Cl_2]$ (**2.4**) in 99% yield and $[(^tBu_3P{=}N)_2Mo(N^tBu)Cl_2]$ (**2.5**) in 97% yield (Fig. 2.16).

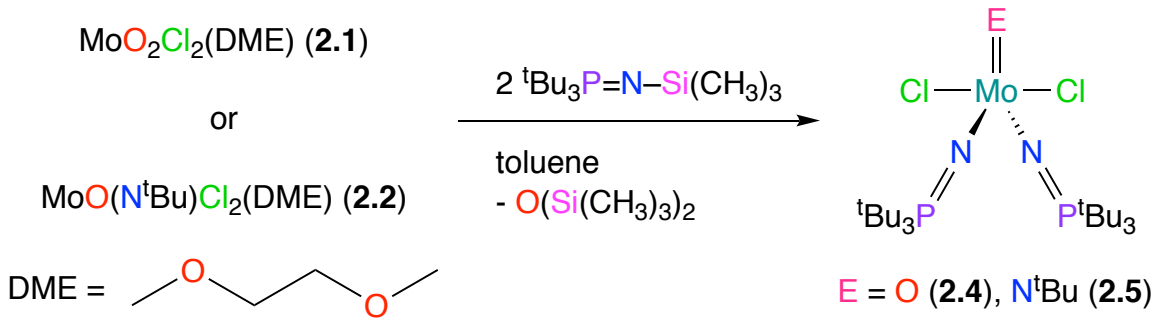

Figure 2.16: Bis(trimethylsilyl)ether elimination reaction to generate bis(phosphinimide) Mo(VI) dichlorido complexes

The elimination reaction in Fig. 2.16 appears to be general, as variation of the phosphinimide proligand gives similar results in reactions with $Cy_3P{=}N{-}Si(CH_3)_3$, $Ph_3P{=}N{-}Si(CH_3)_3$, *p*-$Tol_3P{=}N{-}Si(CH_3)_3$, and $^tBu_2CH_3P{=}N{-}(CH_3)_3$ which also result in the generation of analogous $MoOCl_2L_2$ type complexes $[(Cy_3P{=}N)_2Mo(O)Cl_2]$ (**2.6**) in 99% yield, $[(Ph_3P{=}N)_2Mo(O)Cl_2]$ (**2.7**) in 95% yield, $[((p\text{-}Tol)_3P{=}N)_2Mo(O)Cl_2]$ (**2.8**) in 90% yield, and $[(^tBu_2CH_3P{=}N)_2Mo(O)Cl_2]$ (**2.9**) in 89% yield. The reaction temperature for the synthesis of **2.4** was optimized (+70 °C) to minimize total reaction time, and decrease byproduct formation that was observed when the reaction was performed at higher temperatures (+90 °C).

Complex **2.4** can be cleanly isolated as a yellow solid, and is readily characterized by multinuclear NMR spectroscopy, X-Ray Diffraction (XRD), and elemental analysis. Based on the XRD structure, **2.4** is pseudo C_{2v} symmetric with a trigonal bipyramidal (τ_5 = 0.89) ligand geometry around the metal center (Fig. 2.17). Both phosphinimide ligands exhibit nearly linear (Mo-N-P) bond

angles (Table 2.2) to the molybdenum center, indicative of π-electron donation from the phosphinimide nitrogen lone pairs to the high oxidation-state molybdenum ion. Visualization of the space-filling model of the XRD structure of **2.4** (Fig. 2.18) reveals good steric protection of the metal center where the phosphinimide ligands are located, with minimal steric protection along the dichlorido-oxido region of the molecule.

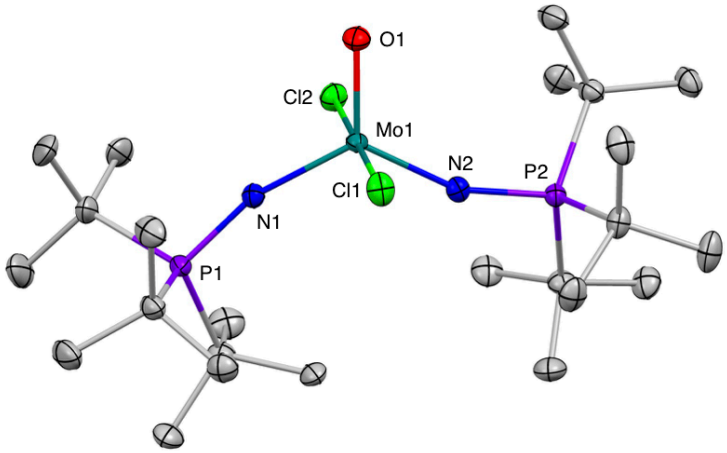

Figure 2.17: Thermal ellipsoid plot (50% probability) of complex **2.4**; hydrogen atoms have been omitted for clarity

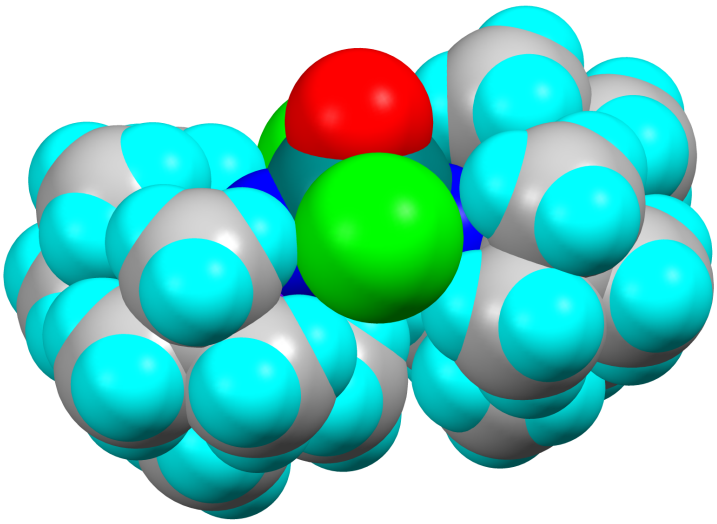

Figure 2.18: Space-filling model of complex **2.4** (van der Waals radii)

The molybdenum-oxido bond distance (Table 2.1) is within the distribution of previously reported Mo(VI) mono-oxido fragments.[15] It is relatively longer, by approximately 0.029 Å, than the average of this distribution. This longer oxido bond length is proposed to be the result of the phosphinimide ligands bonding with vacant metal *d* orbitals that have partial antibonding character with the oxido fragment. The increased electron density at the metal center from the strongly electron donating [$^{t}Bu_3P=N$] ligands also has a net effect of increasing the Mo-O bond length slightly, but is likely not the dominant effect behind the oxido bond length, as changes in metal oxidation state have been shown to not dramatically impact metal-oxido bond lengths.[15]

The bond lengths between the molybdenum and phosphinimide nitrogen atoms (Mo1-N1 and Mo1-N2) are comparable to previously reported molybdenum phosphinimide complexes and can be evaluated as molybdenum-nitrogen double bonds.

Table 2.1: Selected XRD Bond Distances for Complex **2.4**

Atoms	**Distance (Å)**	**Atoms**	**Distance (Å)**
Mo1-Cl1	2.4545(8)	Mo1-O1	1.707(2)
Mo1-Cl2	2.4826(9)	P1-N1	1.609(3)
Mo1-N1	1.836(3)	P2-N2	1.612(3)
Mo1-N2	1.838(3)	–	–

The molecular motif exemplified by **2.4**, with a single oxido ligand and two chlorido ligands, is relatively rare for molybdenum. To date, only four molybdenum complexes that are 5-coordinate have been reported with this type of metal-ligand core structure, with a single example containing molybdenum in the +6 oxidation state (Fig. 2.19).[16–18] While structurally related to **2.4**, this Mo(VI) complex contains two monodentate aryloxide ligands oriented much closer to a *trans* coordination conformation with a O-Mo-O bond angle of more than 157°. This ligand geometry generates a molybdenum coordination environment that is closer to square-pyramidal (τ_5 = 0.89).

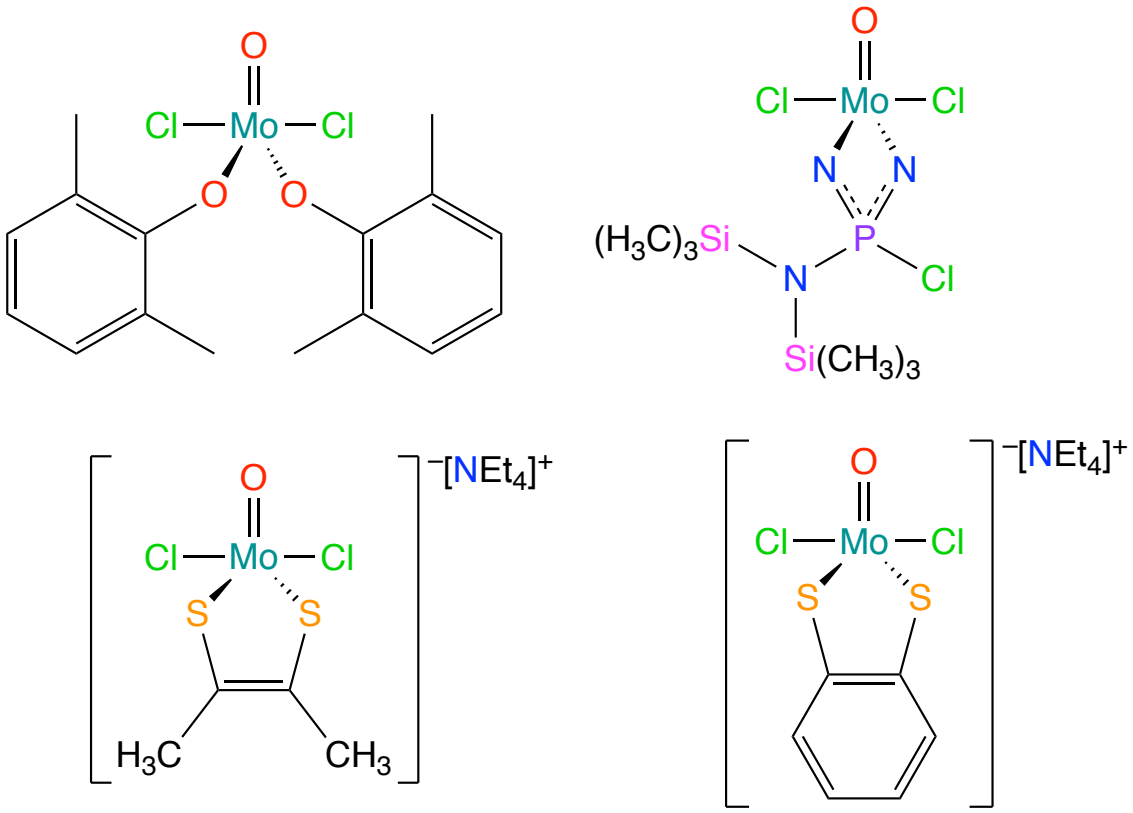

Figure 2.19: Reported 5-coordinate Mo(VI) and Mo(V) complexes that are structurally similar to **2.4**

The 2,6-dimethylphenyloxide ligands have less steric bulk than the tris(*tert*-butyl)phosphinimide ligands in **2.4** and do not adopt the *cis* coordination geometry observed with the phosphinimide ligands. This difference in coordination geometry is structural evidence of the strong donor properties of phosphinimides, such that while a *trans* coordination for the phosphinimides would minimize steric interactions in **2.4**, *cis* coordination geometry is observed to presumably minimize electronic interactions between the phosphinimide ligands bonding to the same *d*-orbitals.

The oxido and chlorido ligand bond lengths are all shorter in this related complex by approximately 0.1 Å, which is another indication of a less electron rich molybdenum center than in **2.4**.

The other 5-coordinate molybdenum complexes similar to **2.4** all contain bidentate ligand systems that preclude evaluation of relative ligand coordination angles. There are four additional 6-coordinate molybdenum complexes (Fig. 2.20) known in lower oxidation states, which contain neutral sulfur and phosphorus ligands.[19,20]

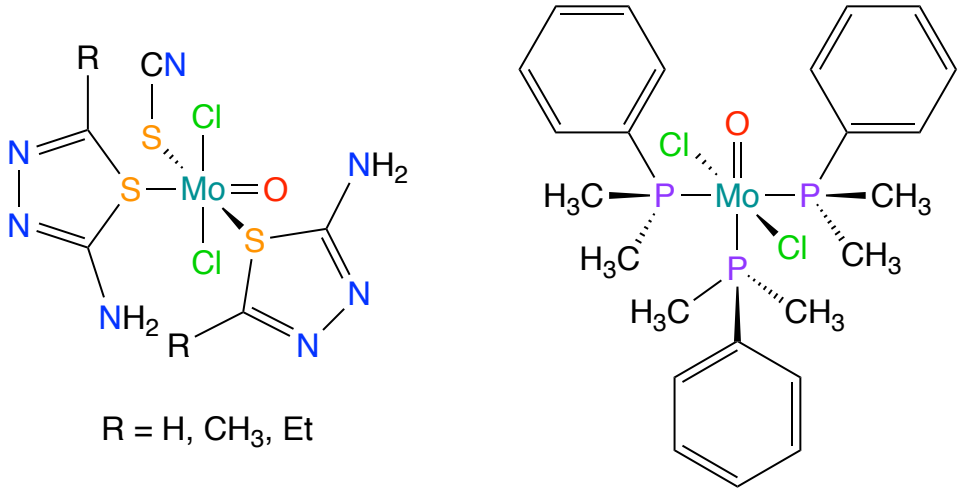

Figure 2.20: Reported 6-coordinate Mo(V) and Mo(IV) complexes that are structurally similar to **2.4**

As mentioned previously, the bond angles (Table 2.2) at each of the phosphinimide nitrogen atoms (Mo1-N1-P1 and Mo1-N2-P2) are relatively linear, which is indicative of more multiple bond character between the molybdenum and nitrogen atoms.

Table 2.2: Selected XRD Bond Angles for Complex **2.4**

Atoms	**Angle (°)**	**Atoms**	**Angle (°)**
Mo1-N1-P1	162.2(2)	N1-Mo1-N2	125.7(1)
Mo1-N2-P2	159.6(2)	Cl1-Mo1-Cl2	179.12(3)
O1-Mo1-N1	115.9(1)	Cl1-Mo1-O1	90.44(8)
O1-Mo1-N2	118.3(1)	Cl2-Mo1-O1	90.40(8)

In the solid-state XRD model, it is clear that the phosphinimide ligands are not identical to one another. While the molybdenum-nitrogen bond lengths are very similar, and the bond angles only differ by a few degrees, the torsion angles that describe the larger orientation of the ligands to the core oxido-dichlorido fragment are distinct (Table 2.3). One phosphinimide ligand binds to the core tilted downwards, while the other is tilted upwards resulting in a 190° difference in torsion angles between the two ligands.

Table 2.3: Selected XRD Torsion Angles for Complex **2.4**

Atoms	**Angle (°)**	**Atoms**	**Angle (°)**
O1-Mo1-N1-P1	176.5(5)	N1-Mo1-N2-P2	163.3(4)
O1-Mo1-N2-P2	-14.0(5)	N2-Mo1-N1-P1	-0.8(6)

The differences in the solid-state XRD structure are likely an artifact of crystal packing effects, rather than fundamental bonding differences in the ligands. The very similar molybdenum-nitrogen bond lengths are the best

evidence for the bonding similarity in the solid-state structure, and solution phase data support the existence of two equivalent phosphinimide ligands in solution (*vide infra*).

In solution, **2.4** is interpreted to be C_{2v} symmetric due to increased motion of the phosphinimide ligands, which can be observed in the ^{1}H, $^{13}C\{^{1}H\}$, and $^{31}P\{^{1}H\}$ NMR spectra at ambient temperature (~25 °C). A diagnostic doublet in the ^{1}H NMR spectrum (Fig. 2.21) is observed at 1.43 ppm ($^{3}J_{PH}$ = 13.9 Hz) from the ^{31}P coupled *tert*-butyl protons. The $^{13}C\{^{1}H\}$ NMR spectrum (Fig 2.22) presents both ^{31}P coupled quaternary *tert*-butyl carbons at 42.73 ppm ($^{1}J_{PC}$ = 42.8 Hz), and a single peak for the methyl carbons at 29.71 ppm. A single peak is observed in the $^{31}P\{^{1}H\}$ spectrum (Fig. 2.23) at 58.64 ppm for the chemically equivalent phosphorus atoms.

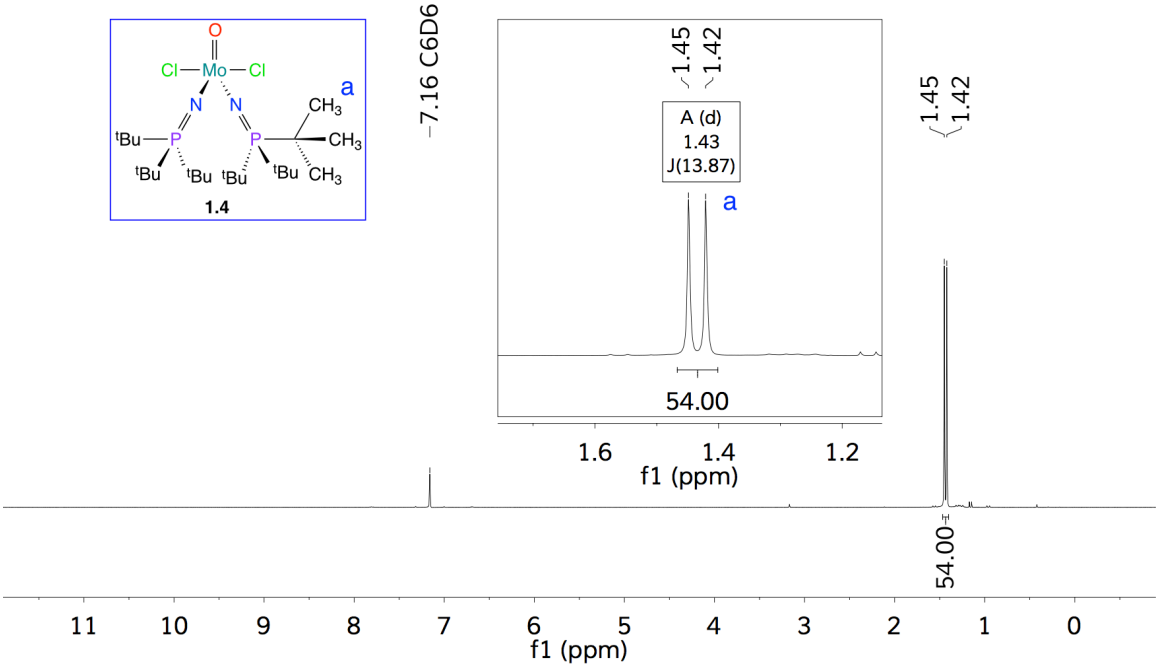

Figure 2.21: ^{1}H NMR spectrum of **2.4** in C_6D_6 (500 MHz)

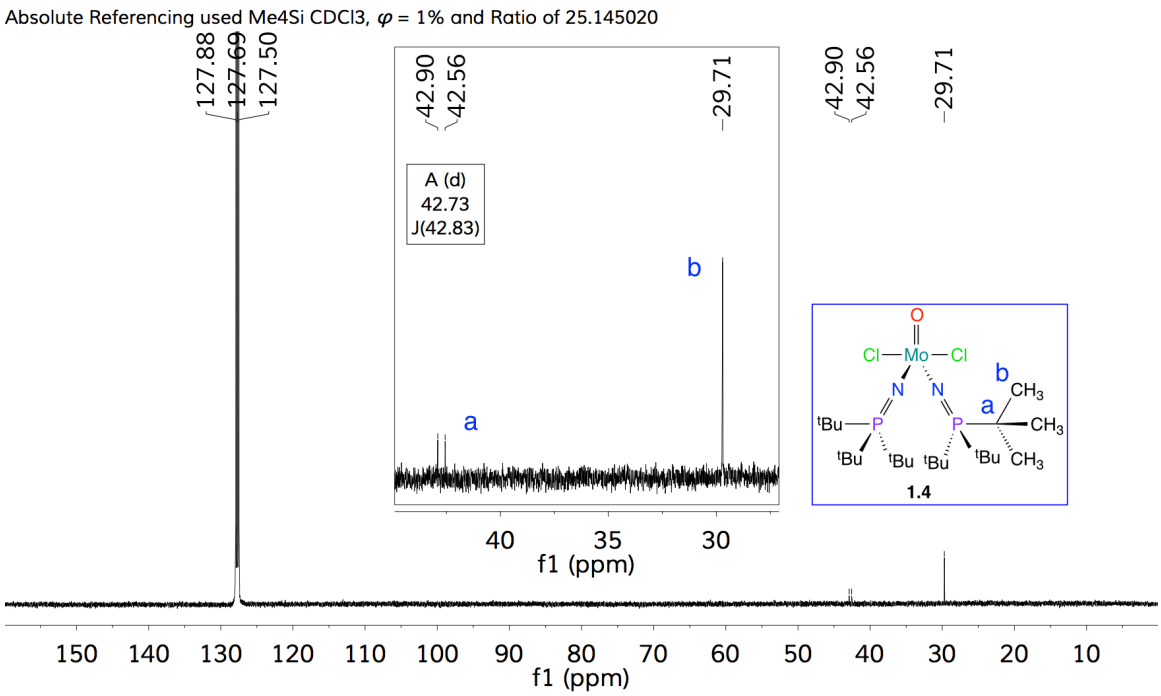

Figure 2.22: $^{13}C\{^{1}H\}$ NMR spectrum of **2.4** in C_6D_6 (126 MHz)

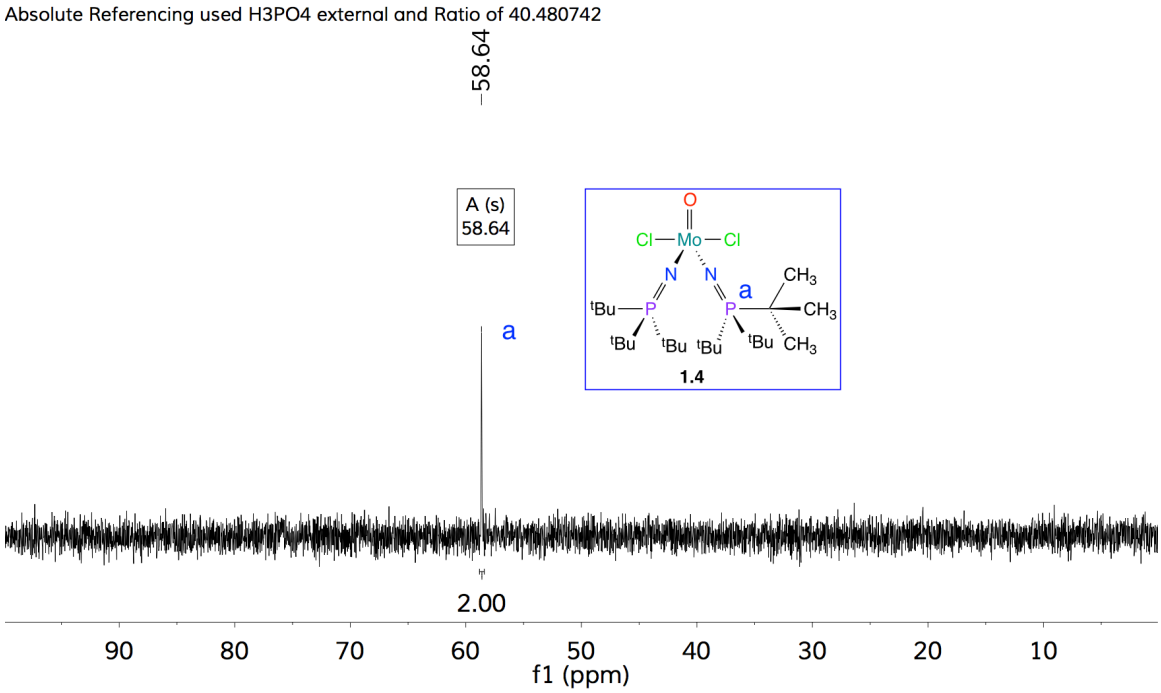

Figure 2.23: $^{31}P\{^{1}H\}$ NMR spectrum of **2.4** in C_6D_6 (202 MHz)

The analogous reaction to generate the imido complex **2.5** results in a product that is more challenging to isolate in high purity, due to the presence of starting material impurities and longer reaction times necessary for the synthesis. However, the major product has been characterized by NMR spectroscopy and XRD.

The solid-state structure of complex **2.5** (Fig. 2.24) determined by XRD analysis reveals a very similar structure to complex **2.4**. Both phosphinimide ligands exhibit nearly linear (Mo-N-P) bond angles to the molybdenum center, indicative of π-electron donation from the phosphinimide nitrogen lone pair to the high oxidation-state molybdenum ion. Visualization of the space-filling model of the XRD structure of **2.5** (Fig. 2.25) shows a more protected metal center than in **2.4** due to the steric bulk of the *tert*-butylimido fragment in the complex.

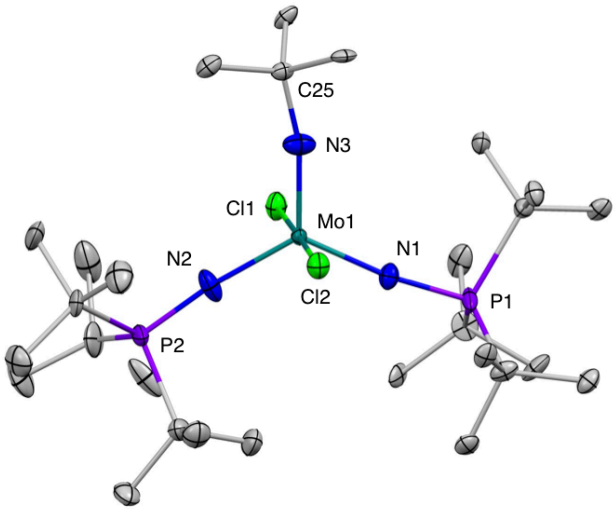

Figure 2.24: Thermal ellipsoid plot (50% probability) of complex **2.5**; hydrogen atoms and disordered tert-butyl groups have been omitted for clarity

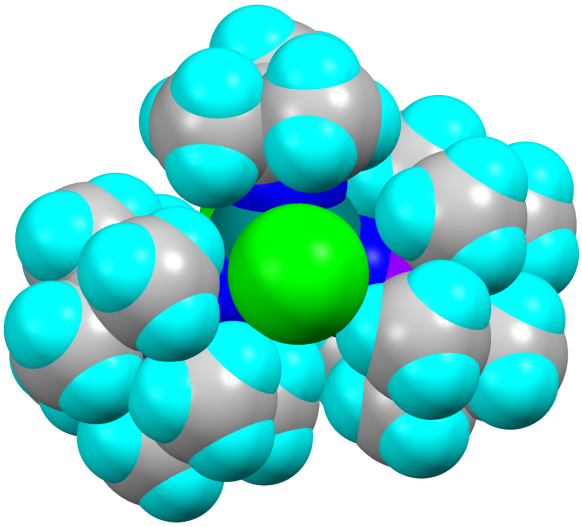

Figure 2.25: Space-filling model of complex **2.5** (van der Waals radii); disordered tert-butyl groups have been omitted for clarity

Comparison of the bond distances between **2.4** (Table 2.1) and **2.5** (Table 2.4) shows that **2.5** has slightly longer ligand bond distances to the

molybdenum center, indicating a more electron rich molybdenum ion or steric pressure between the phosphinimide and imido ligands. The molybdenum-chlorido bond distances increase by an average of 0.019 Å in **2.5**, and the molybdenum-nitrogen (phosphinimide) bond distances increase by a similar average of 0.018 Å.

Table 2.4: Selected XRD Bond Distances for Complex **2.5**

Atoms	**Length (Å)**	**Atoms**	**Length (Å)**
Mo1-Cl1	2.478(2)	Mo1-N3	1.728(8)
Mo1-Cl2	2.497(2)	P1-N1	1.572(8)
Mo1-N1	1.855(7)	P2-N2	1.571(8)
Mo1-N2	1.855(8)	N3-C25	1.435(11)

Comparison of the bond angles between **2.5** and **2.4** shows more linear phosphinimide Mo-N-P angles (average difference of 11.8°) to the molybdenum center in **2.5** (Table 2.5). More linear coordination of phosphinimide ligands usually indicates stronger binding, and increased donation of electron density from the phosphinimide ligands. In this case, the more linear coordination is proposed to be more strongly influenced by steric repulsion between the phosphinimide *tert*-butyl groups and the *tert*-butyl imido fragment.

The *tert*-butyl imido ligand bond angle is relatively linear at 166.6(5)°, which indicates the imido fragment coordinates with closer to triple-bond

character versus double-bond character. This is a common characteristic of imido ligands when coordinated to high oxidation state metals.

Table 2.5: Selected XRD Bond Angles for Complex **2.5**

Atoms	**Angle (°)**	**Atoms**	**Angle (°)**
Mo1-N1-P1	172.4(5)	N1-Mo1-N2	126.1(4)
Mo1-N2-P2	173.0(6)	Cl1-Mo1-Cl2	178.58(8)
N1-Mo1-N3	115.8(4)	Cl1-Mo1-N3	90.6(3)
N2-Mo1-N3	118.0(4)	Cl2-Mo1-N3	89.0(3)
Mo1-N3-C25	166.6(7)	–	–

Comparison of the torsion angles between **2.5** (Table 2.6) and **2.4** show a minimal difference between these metrical parameters. Given the close to linear core bond angles of **2.5**, the torsion angles of these groups do not significantly impact the structure of the complex.

One detail to point out in the selected torsion angles for **2.5** is that the values are close to absolute values of 0° or 180°. This indicates that all of the core fragments of the complex are located close to the same plane (containing all three nitrogen donors to the molybdenum center), with minimal twisting of the phosphinimide ligands out of the plane. The close to centered torsion angles are perhaps an indication of a complex that is more strongly affected by steric repulsions than electronic effects.

While the steric interactions of **2.4** are quite similar to **2.5**, the presence of the oxido ligand allows for more flexibility in the phosphinimide torsion angles. One of the phosphinimide fragments in **2.4** is nearly 17° out of plane, versus the approximate maximum of 8° observed in **2.5**.

Table 2.6: Selected XRD Torsion Angles for Complex **2.5**

Atoms	**Angle (°)**	**Atoms**	**Angle (°)**
N3-Mo1-N1-P1	4.0(4)	N1-Mo1-N2-P2	-8.0(5)
N3-Mo1-N2-P2	171.0(4)	N2-Mo1-N1-P1	-177.0(4)

Synthesis of $[(^{t}Bu_2CH_3P{=}N)_2Mo(O)Cl_2]$ (**2.9**) was achieved using analogous methodology to **2.4** by reaction of $^{t}Bu_2CH_3P{=}NSi(CH_3)_3$ (**L4**) with **2.1**.

Complex **2.9** can be cleanly isolated as a yellow solid, and was characterized by multinuclear variable-temperature and multidimensional NMR spectroscopy. In solution, **2.9** is interpreted to be C_1 symmetric and exhibit asymmetric binding of the phosphinimide ligands to the molybdenum center, which can be observed using a variety of NMR spectroscopic techniques.

At 20 °C, the ^{1}H NMR spectrum (Fig. 2.26) shows a pair of overlapping doublets at 1.05 ppm ($^{3}J_{PH}$ = 14.8 Hz), and 1.09 ppm ($^{3}J_{PH}$ = 14.7 Hz), for the two different ^{31}P coupled *tert*-butyl environments, and two separate doublets for the ^{31}P coupled methyl groups at 1.40 ppm ($^{2}J_{PH}$ = 11.1 Hz), and 1.96 ppm ($^{2}J_{PH}$ = 10.6 Hz).

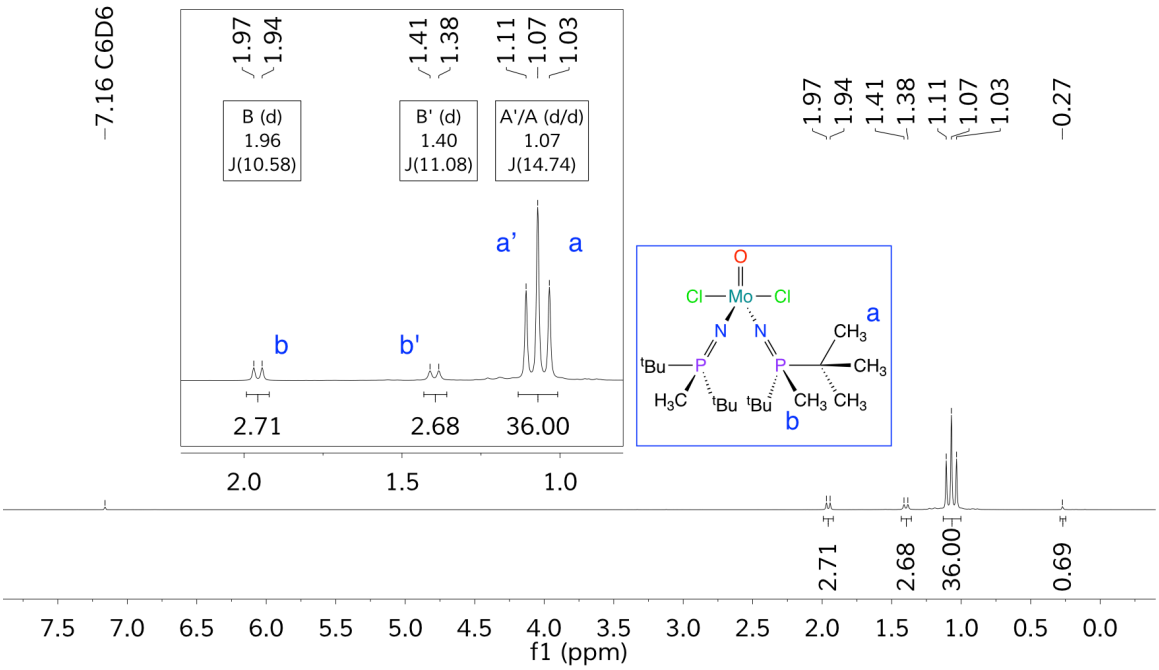

Figure 2.26: ^{1}H NMR spectrum of **2.9** in C_6D_6 (400 MHz)

The $^{31}P\{^{1}H\}$ NMR spectrum (Fig. 2.27) exhibits the two expected singlets for the different phosphinimide environments at 58.03 ppm and 77.59 ppm. The relative integrations of the ^{31}P NMR signals are nearly equivalent, which is interpreted as a 1:1 ratio of phosphinimide environments within complex **2.9** and not two separate molecular species.

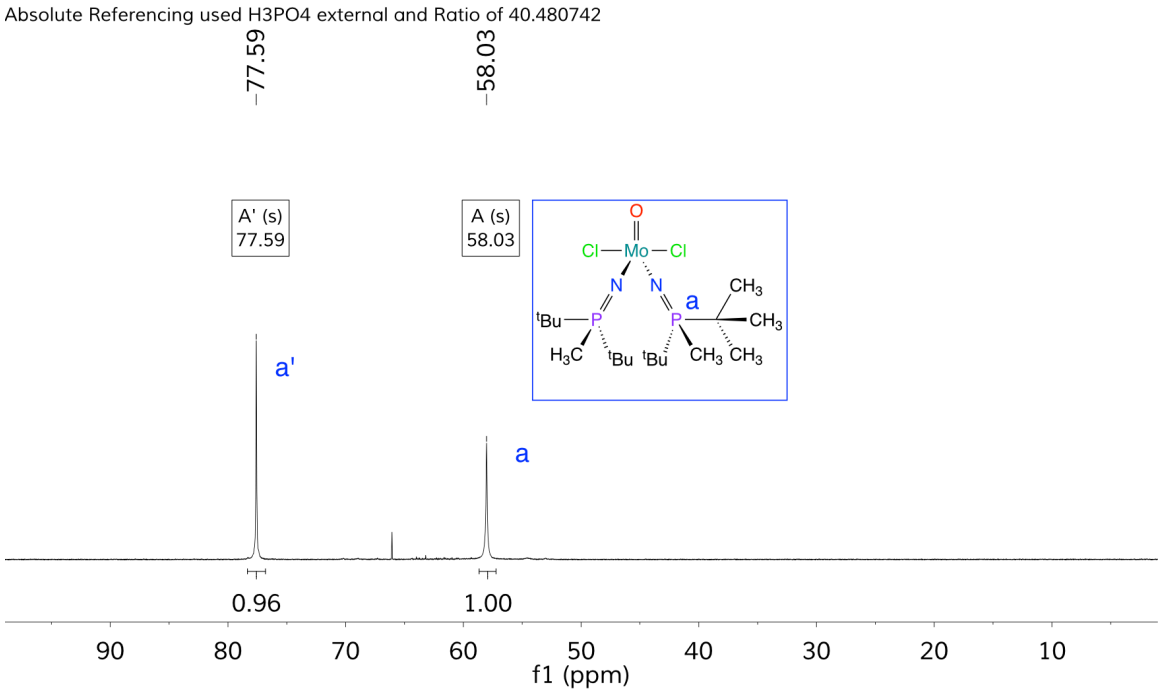

Figure 2.27: $^{31}P\{^{1}H\}$ NMR spectrum of **2.9** in C_6D_6 (162 MHz)

The $^{13}C\{^{1}H\}$ NMR spectrum (Fig. 2.28) contains *tert*-butyl methyl singlets at 26.08 and 26.41 ppm, ^{31}P coupled *tert*-butyl quaternary carbon doublets at 35.37 ppm ($^{1}J_{PC}$ = 61.8 Hz) and 36.28 ppm ($^{1}J_{PC}$ = 57.4 Hz), and ^{31}P coupled methyl doublets at 0.59 ppm ($^{1}J_{PC}$ = 50.7 Hz) and 5.59 ppm ($^{1}J_{PC}$ = 58.1 Hz).

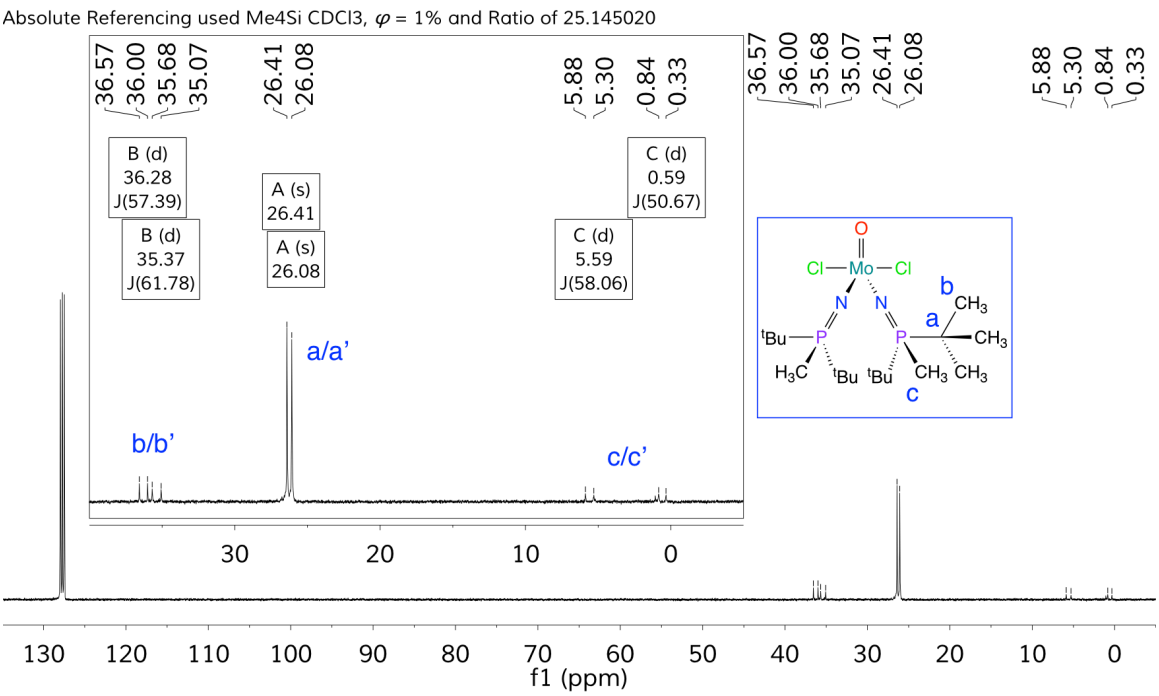

Figure 2.28: $^{13}C\{^{1}H\}$ NMR spectrum of **2.9** in C_6D_6 (101 MHz)

Synthesis of **2.9** within a sealed J. Young NMR tube allows the observation of $O(Si(CH_3)_3)_2$ elimination and decoordination of DME by ^{1}H NMR spectroscopy. Fig. 2.29 shows the peaks corresponding to these byproducts, with minimal generation of $ClSi(CH_3)_3$.

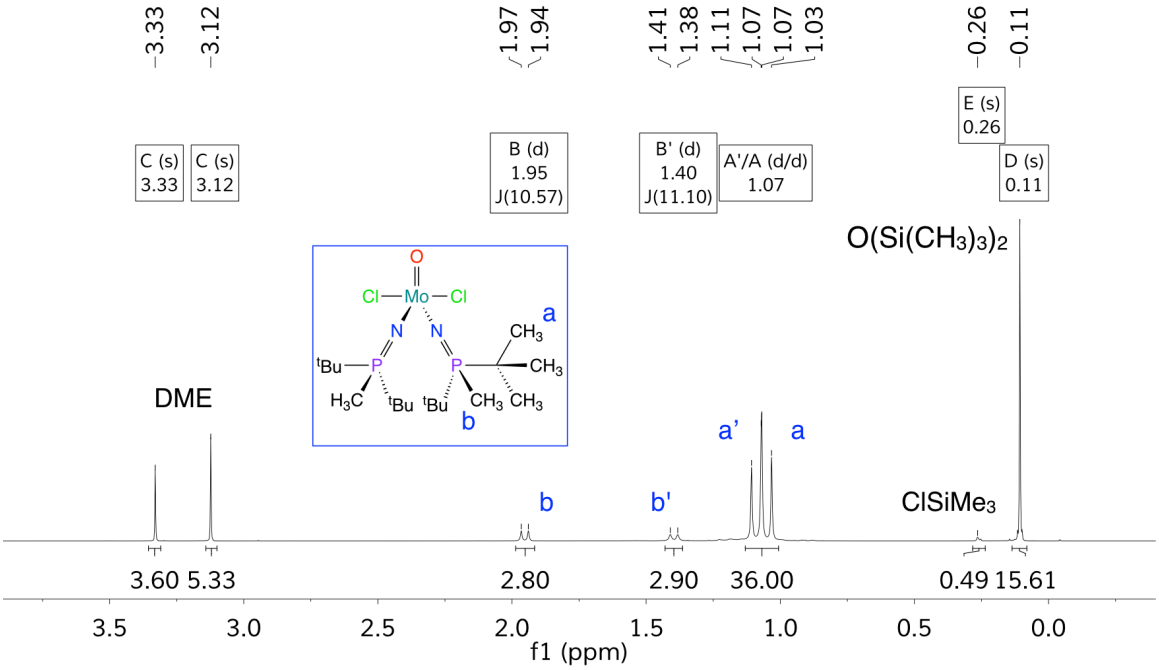

Figure 2.29: ^{1}H NMR spectrum of **2.9** generated in a J. Young NMR tube in C_6D_6 (400 MHz)

Further evaluation of the phosphinimide ligands was achieved through a two-dimensional ^{1}H-^{31}P gradient heteronuclear multiple bond coherence (gHMBC) NMR experiment. The gHMBC NMR spectrum (Fig. 2.30, and more detailed sections in Fig. 2.31 and Fig. 2.32) shows diagnostic cross peaks between pairs of methyl and *tert*-butyl ^{1}H signals and the associated neighboring ^{31}P signals.

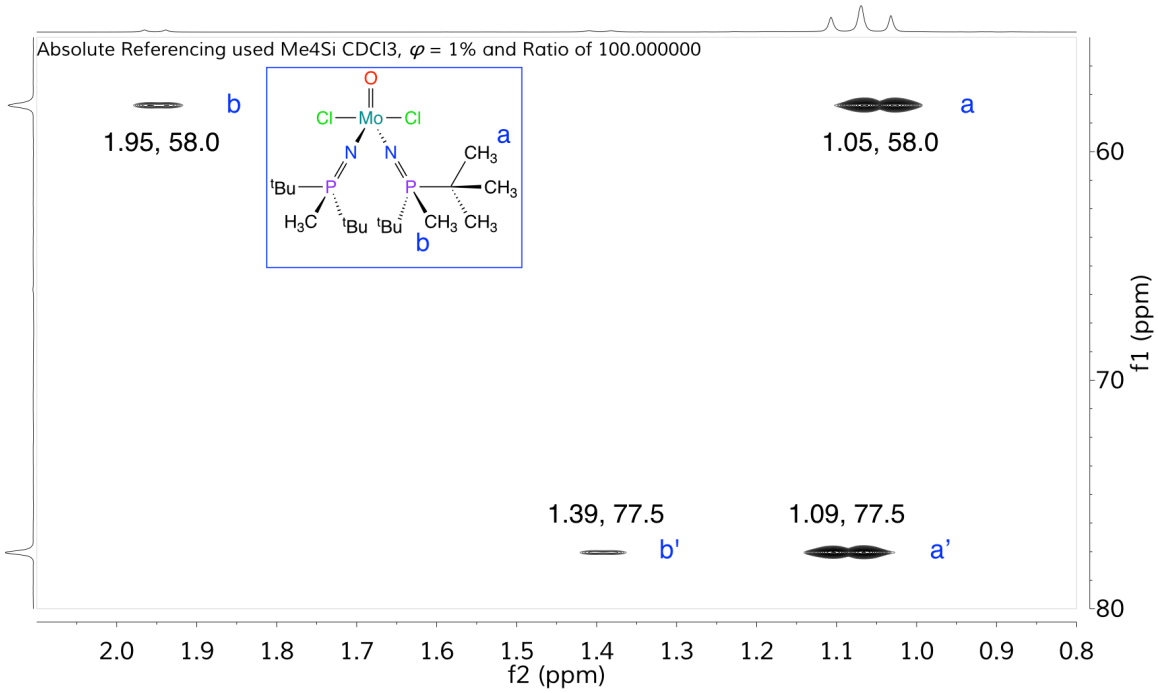

Figure 2.30: ^{1}H-^{31}P gHMBC NMR spectrum of **2.9** in C_6D_6 (400 MHz, 162 MHz)

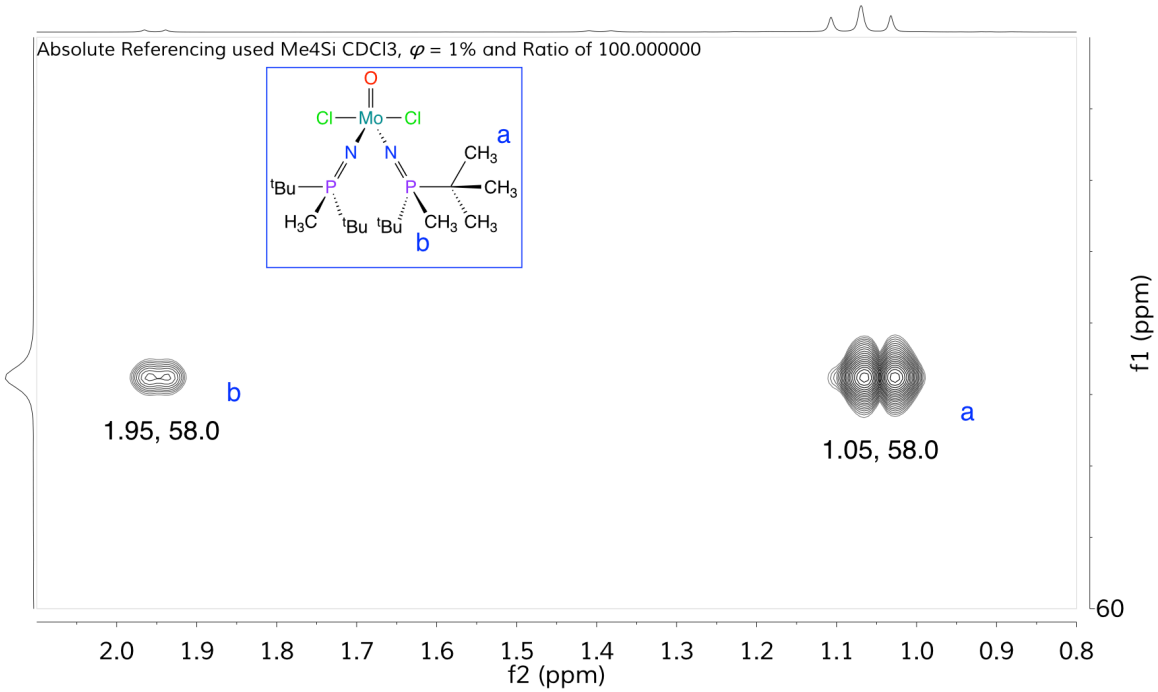

Figure 2.31: ^{1}H-^{31}P gHMBC NMR spectrum of **2.9** in C_6D_6 (detail between tert-butyl **a** and methyl **b**) (400 MHz, 162 MHz)

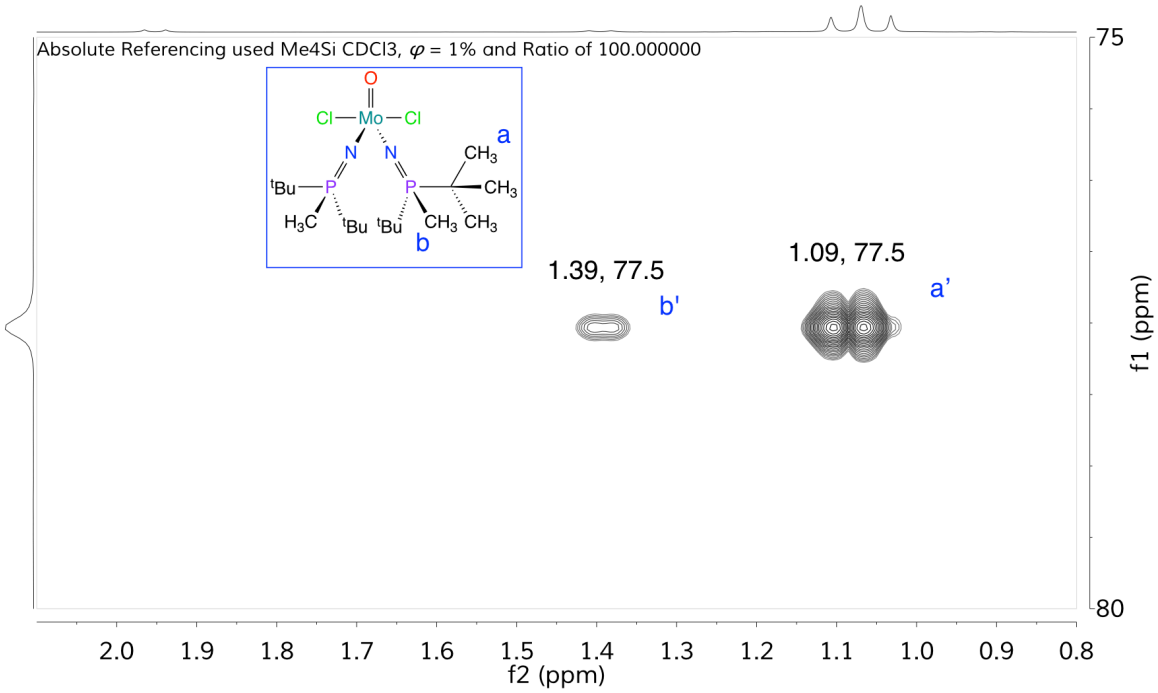

Figure 2.32: ^{1}H-^{31}P gHMBC NMR spectrum of **2.9** in C_6D_6 (detail between tert-butyl **a'** and methyl **b'**) (400 MHz, 162 MHz)

To my knowledge, asymmetric phosphinimide coordination has not been previously described in the chemical literature. Variable-temperature NMR experiments were performed to determine if increased temperature would lead to equilibration of the two different phosphinimide chemical environments. Both ^{1}H and $^{31}P\{^{1}H\}$ NMR spectra were monitored up to 70 °C, with no definitive equilibration of the two different ligand environments observed (Fig. 2.33, Fig. 2.34). The higher chemical shift signal broadened as temperature increased, which may be due to increased motion of that ligand or decoordination of the ligand, while the other signal remained sharp and appears to remain in a single coordination conformation. Relative integrations of the signals did not vary significantly from a 1:1 ratio.

It is possible these different signals arise from *cis* and *trans* isomers of the five-coordinate complex, but the large difference in ^{31}P NMR chemical shifts is not expected for these potential isomers and *trans* isomers have not been observed for five-coordinate complexes in this research.

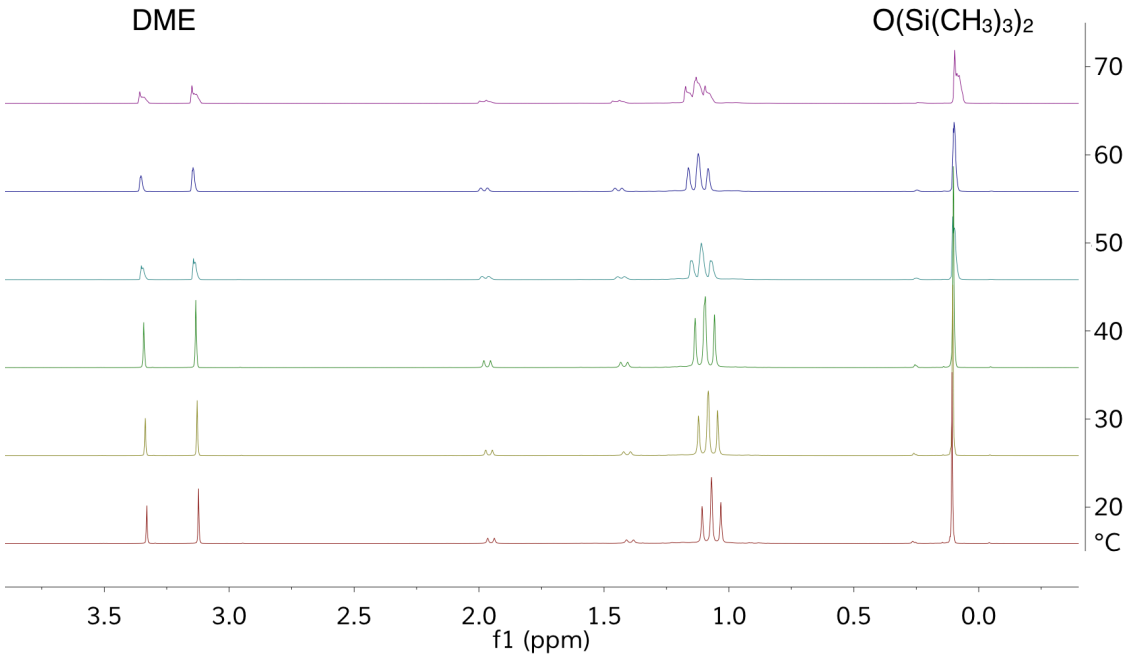

Figure 2.33: Variable temperature (20-70 °C) ^{1}H NMR spectrum of **2.9** in C_6D_6 (400 MHz)

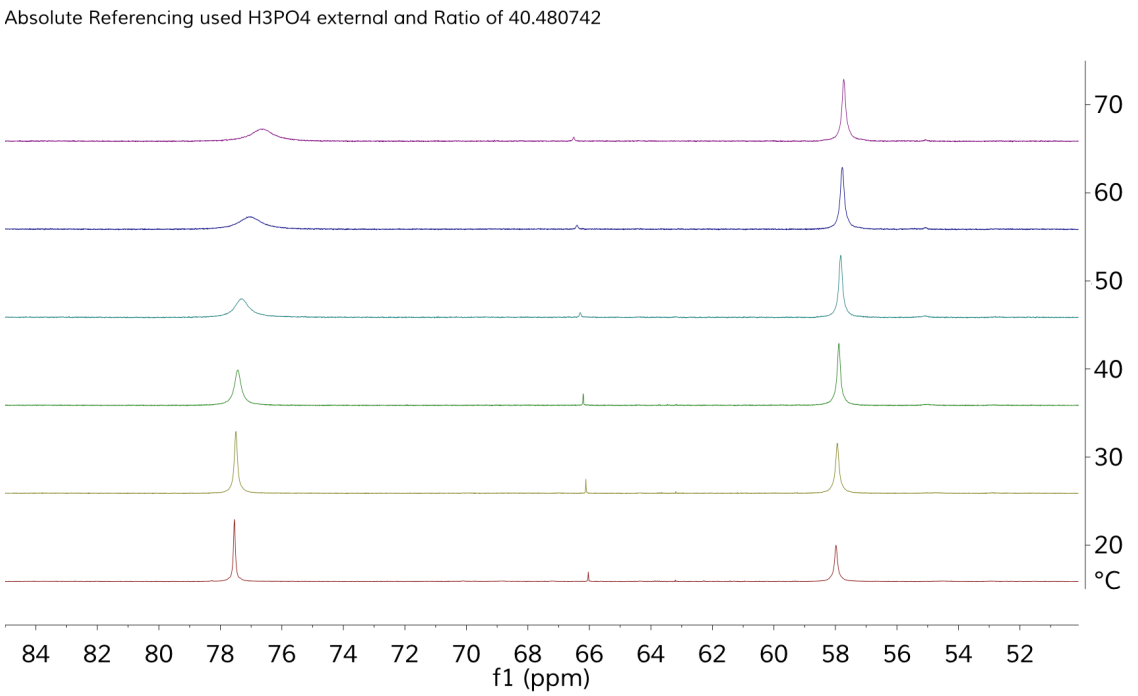

Figure 2.34: Variable temperature (20-70 °C) $^{31}P\{^{1}H\}$ NMR spectrum of **2.9** in C_6D_6 (162 MHz)

The spectroscopic data suggests that the phosphinimide ligands are asymmetrically coordinated in solution; however, an XRD structure was not obtained for **2.9** to confirm this in the solid-state.

Similar to **2.9**, $[(Cy_3P{=}N)_2Mo(O)Cl_2]$ (**2.6)** also exhibits asymmetric phosphinimide coordination. This feature is primarily observed in the $^{31}P\ \{^{1}H\}$ NMR spectrum of **2.6** (Fig. 2.36), and is difficult to discern in the ^{1}H NMR spectrum due to overlapping signals (Fig. 2.35). As such, 2D NMR experiments were not performed to evaluate asymmetric coordination of this particular complex.

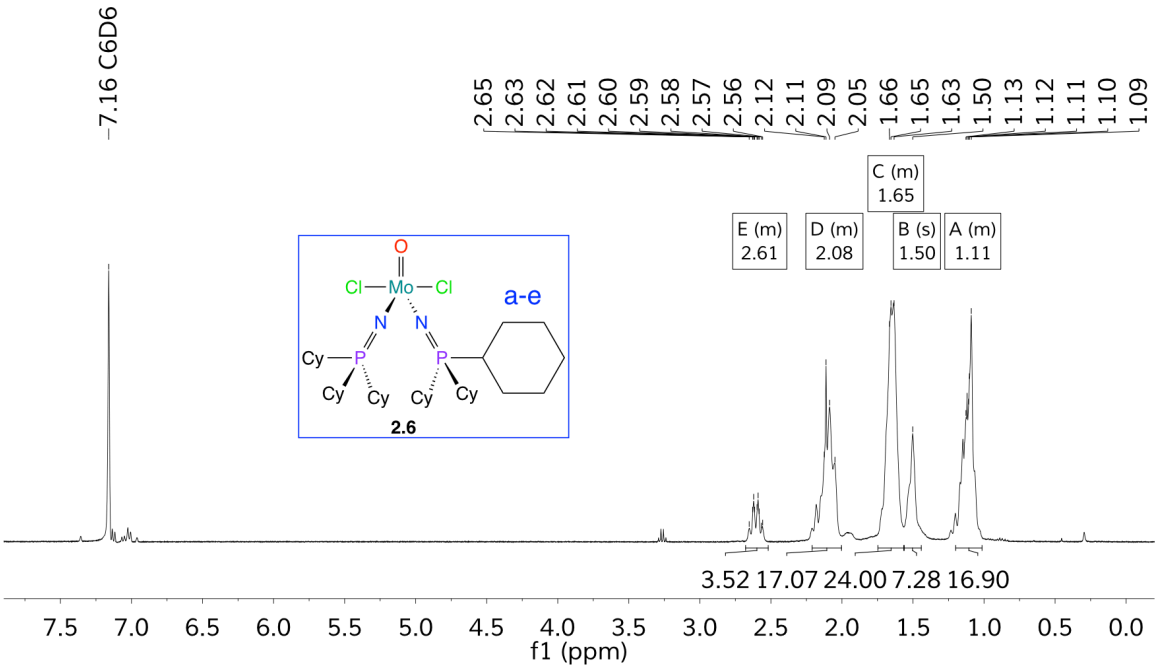

Figure 2.35: ^{1}H NMR spectrum of **2.6** in C_6D_6 (400 MHz)

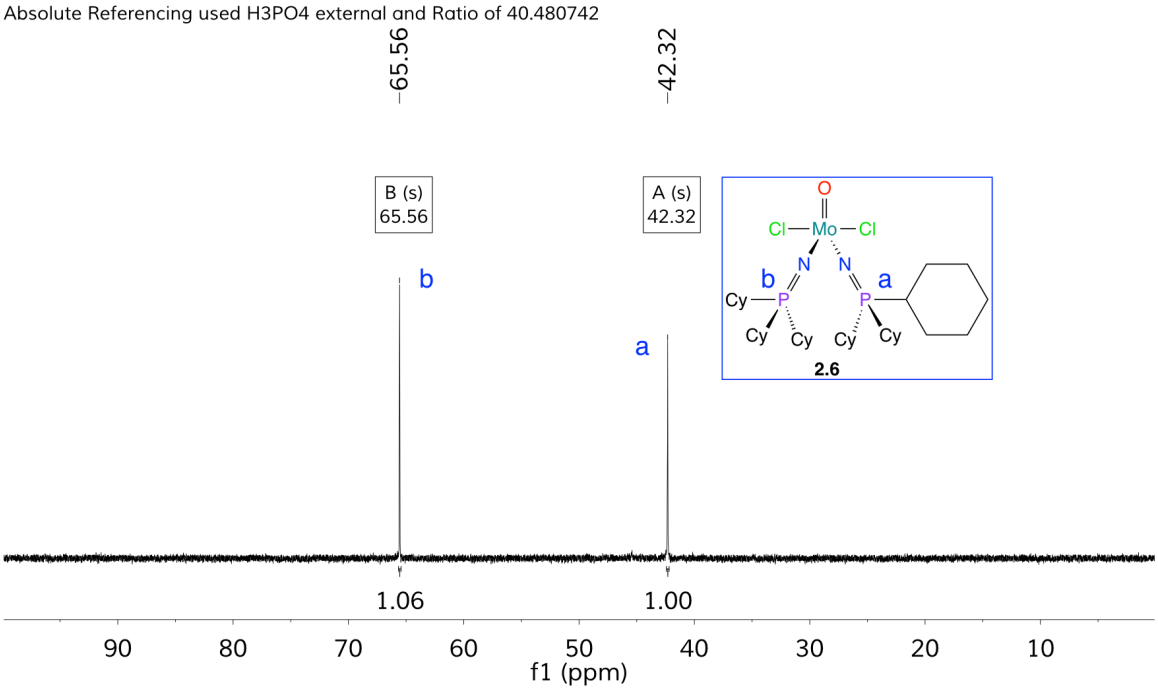

Figure 2.36: $^{31}P\{^{1}H\}$ NMR spectrum of **2.6** in C_6D_6 (162 MHz)

2.6 also exhibited similar coordination dynamics to **2.9** when monitored by variable-temperature NMR experiments. The two phosphinimide signals in the $^{31}P\{^{1}H\}$ NMR spectra (Fig. 2.37) remained distinct within the 25-70 °C range, and the higher chemical shift signal also broadened as temperature increased. The relative integrations of the two signals remained effectively 1:1 for each spectrum. These observations indicate that each phosphinimide ligand is coordinated differently to the molybdenum center, and this coordination difference is not simply a transient lower energy conformation. Variable-temperature NMR experiments to higher temperatures could perhaps observe the phosphinimide signals equilibrate to a shared average chemical environment, or 2D NMR experiments could show exchange between these two chemical environments.

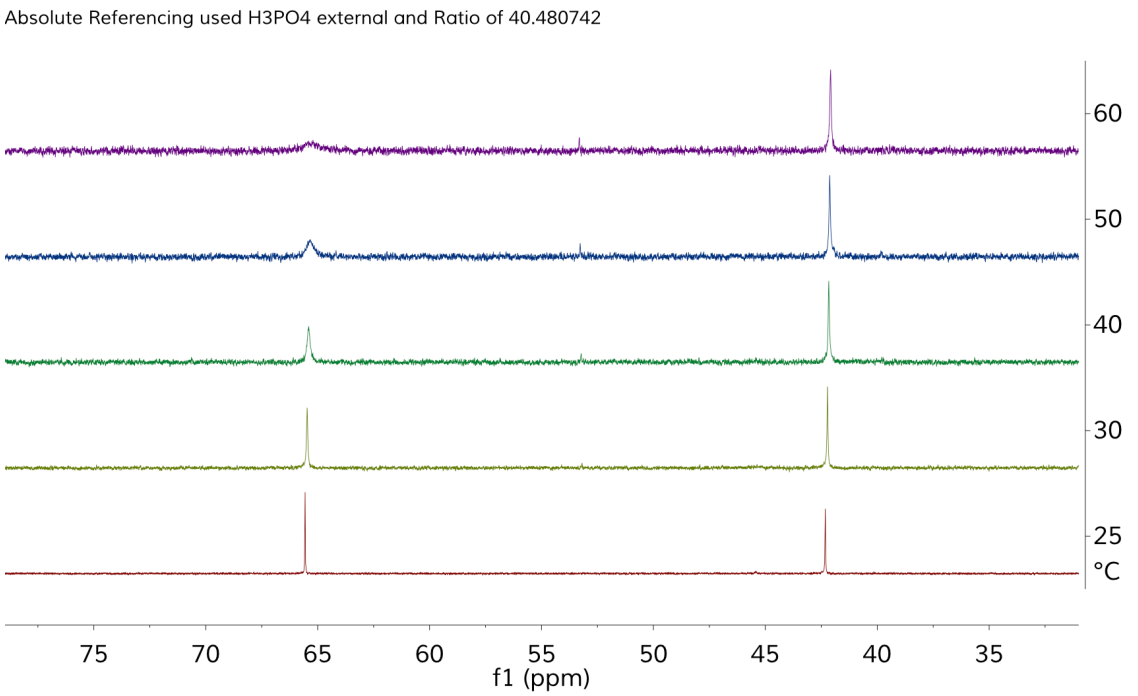

Figure 2.37: Variable temperature (25-60 °C) $^{31}P\{^{1}H\}$ NMR spectrum of **2.6** in C_6D_6 (162 MHz)

While a high quality XRD structure was not obtained for **2.6** due to significant overlap of disordered molecules, a sufficient model was determined to indicate structural connectivity (Fig. 2.38). Qualitative analysis of the two models of **2.6** in the unit cell indicates that the phosphinimide ligands are coordinated differently. One phosphinimide is oriented in a more linear coordination mode with a Mo-N-P bond angle between 156-164°, while the other phosphinimide has an angle between 141-143°.

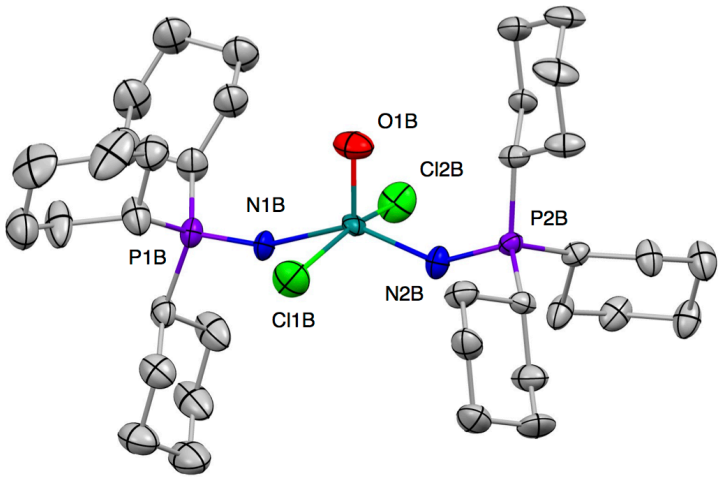

Figure 2.38: Thermal ellipsoid plot (50% probability) of complex **2.6**; hydrogen atoms have been omitted for clarity

The chlorido ligands are also shifted toward the more linearly coordinated phosphinimide, with Cl-Mo-N bond angles varying between 84-94°. In contrast, the XRD structures of **2.4** and **2.5** had Cl-Mo-N bond angles within two degrees of 90°. This difference is attributed to stronger steric interactions from the less linear phosphinimide cyclohexyl groups on the chlorine atoms.

Complex **2.7**, the triphenylphosphinimide derivative of **2.4**, can be generated using similar synthetic methodology, and was characterized by ^{1}H and $^{31}P\{^{1}H\}$ NMR. In solution, **2.7** was interpreted to be C_{2v} symmetric from the signals observed in the ^{1}H, and $^{31}P\{^{1}H\}$ NMR spectra at ambient temperature (~25 °C). Multiplets for the aryl protons are observed in the ^{1}H NMR spectrum (Fig. 2.39) at 7.87 and 6.99 ppm. A single peak is observed in the $^{31}P\{^{1}H\}$ spectrum (Fig. 2.40) at 32.48 ppm for the chemically equivalent phosphorus atoms.

While the steric bulk of the phosphinimide ligands in **2.7** is less than the cyclohexyl variant (**2.6**), both phosphinimide ligand chemical environments are interpreted to be equivalent in the ^{1}H and $^{31}P\{^{1}H\}$ NMR spectra at ambient temperature (~25 °C) when dissolved in C_6D_6. The lack of asymmetry between the phosphinimide ligands suggests that the tri(phenyl)phosphinimide ligands are fluctional in solution, or possibly that limited interaction with the solvent (low solubility) prevents significant conformational changes within the structure, leading to resolution of a single peak in the $^{31}P\{^{1}H\}$ NMR spectrum. Analysis of the related tri(tolyl)phosphinimide complex **2.8** suggests that limited solubility is the main influence on the apparent symmetric phosphinimide coordination in **2.7**.

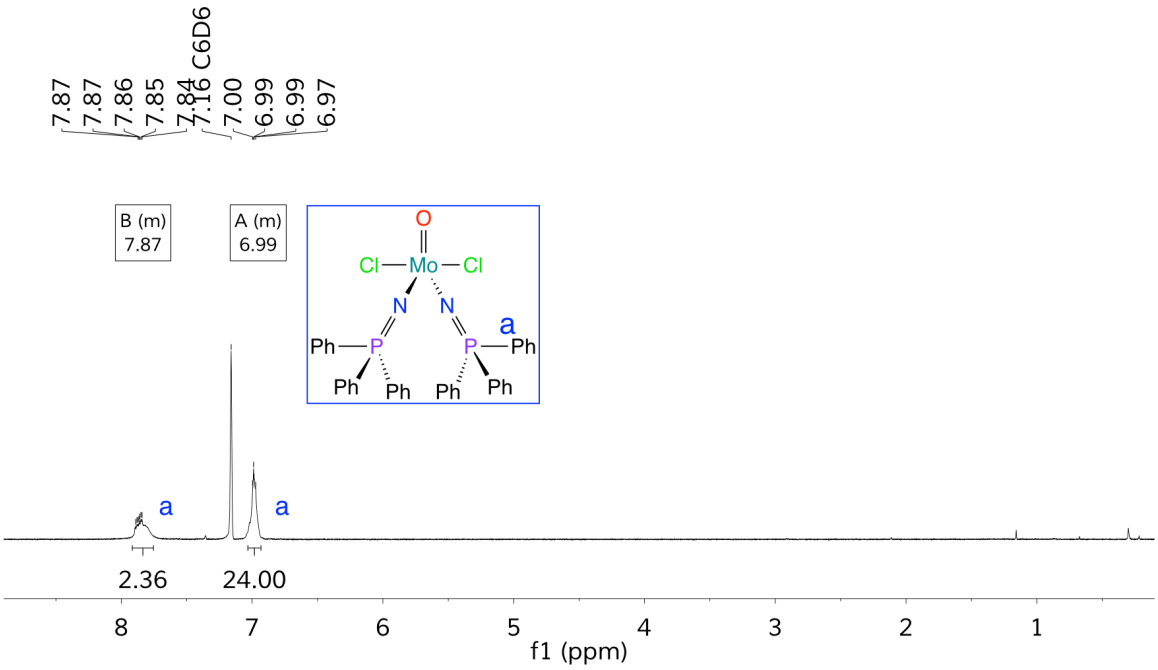

Figure 2.39: ^{1}H NMR spectrum of **2.7** in C_6D_6 (400 MHz)

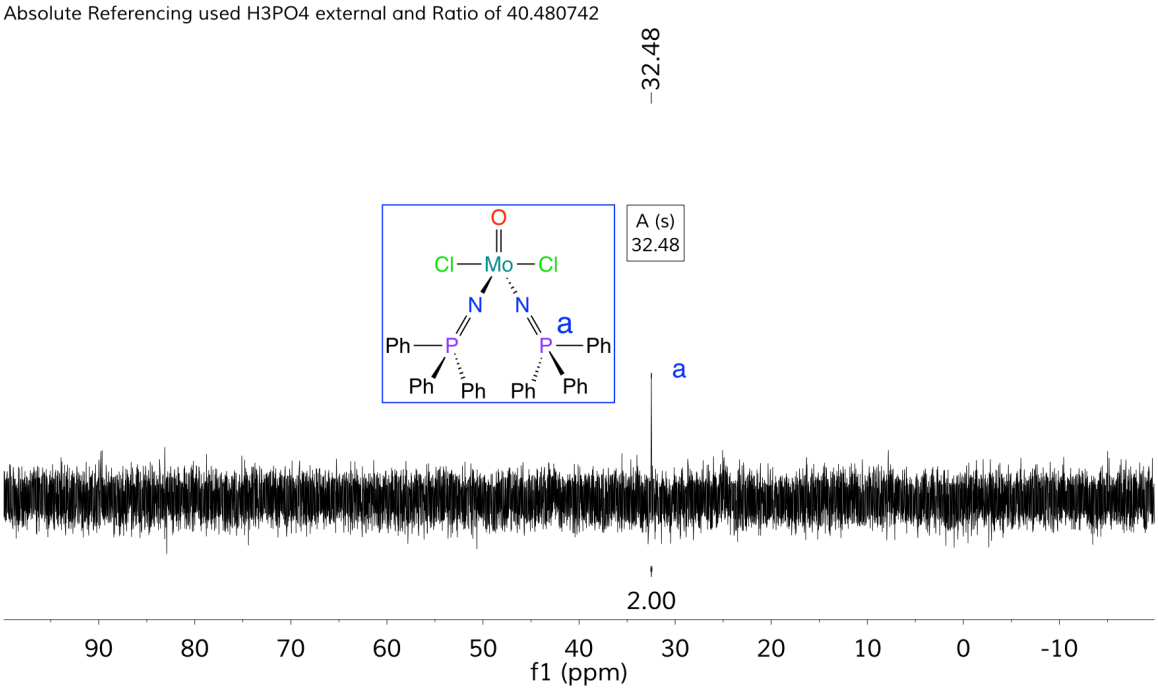

Figure 2.40: $^{31}P\{^{1}H\}$ NMR spectrum of **2.7** in C_6D_6 (162 MHz)

Complex **2.8**, the tri(tolyl)phosphinimide derivative of **2.4**, can be generated using an analogous approach, and was characterized by ^{1}H and $^{31}P\{^{1}H\}$ NMR spectroscopy. When dissolved in benzene-d_6, **2.8** was interpreted to be a mixture of a C_{2v} symmetric conformer (main component), with a smaller amount of a C_1 symmetric conformer, based on the signals observed in the ^{1}H, and $^{31}P\{^{1}H\}$ NMR spectra.

At 25 °C, the ^{1}H NMR spectrum shows a major singlet at 1.94 ppm (CH_3) with lower intensity nearby peaks, and broader aryl singlets at 6.87 ppm and 7.82 ppm (Fig. 2.41). The ^{31}P channel is not decoupled and no clear splitting of the signal at 1.94 is observed, which indicates that the bond separation between the phosphorus nuclei and the *para*-methyl groups of the tri(tolyl)phosphinimide ligands is sufficient for negligible ^{1}H-^{31}P coupling.

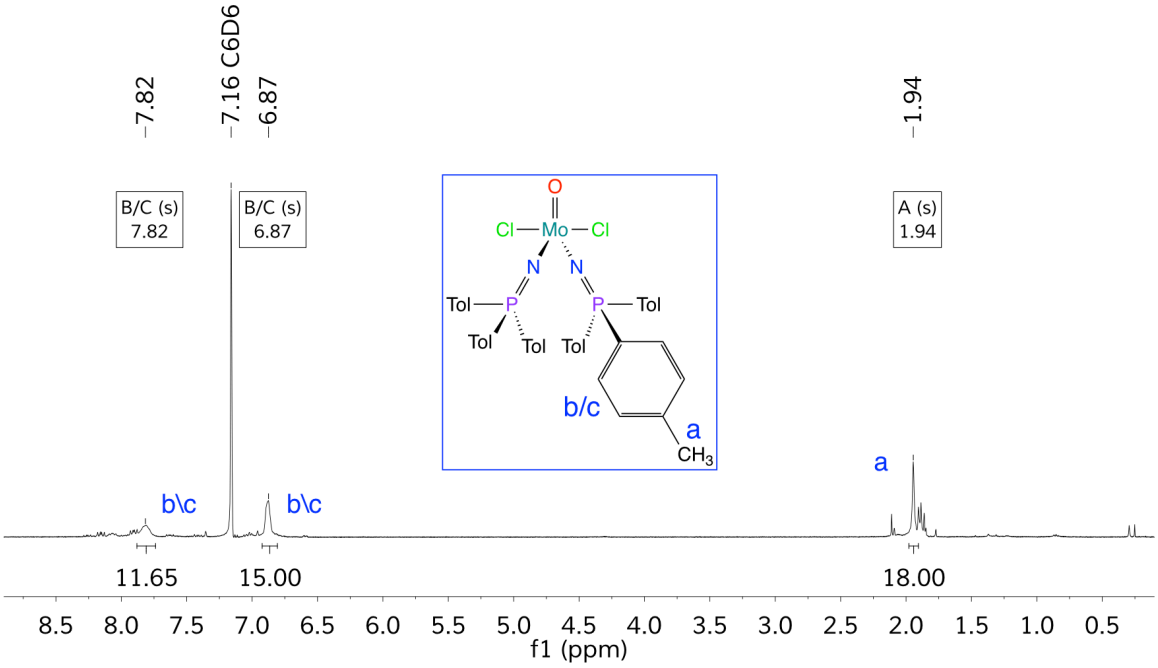

Figure 2.41: ^{1}H NMR spectrum of **2.8** in C_6D_6 (400 MHz)

The $^{31}P\{^{1}H\}$ NMR spectrum exhibits a major component singlet at 24.83 ppm, with smaller singlets at 32.81, 44.06, and 73.18 ppm (Fig. 2.42). The relative integrations of the ^{31}P NMR signals at 32.81 and 44.06 ppm are 1:1, which is interpreted as the presence of a small amount of complex **2.8** in the C_1 symmetric conformation. The identity of the ^{31}P signal at 73.18 ppm is unknown, although intermediate complexes within this family of compounds have been observed at higher chemical shifts than the major products and starting materials, which are evaluated as monophosphinimide complexes that have not been isolated.

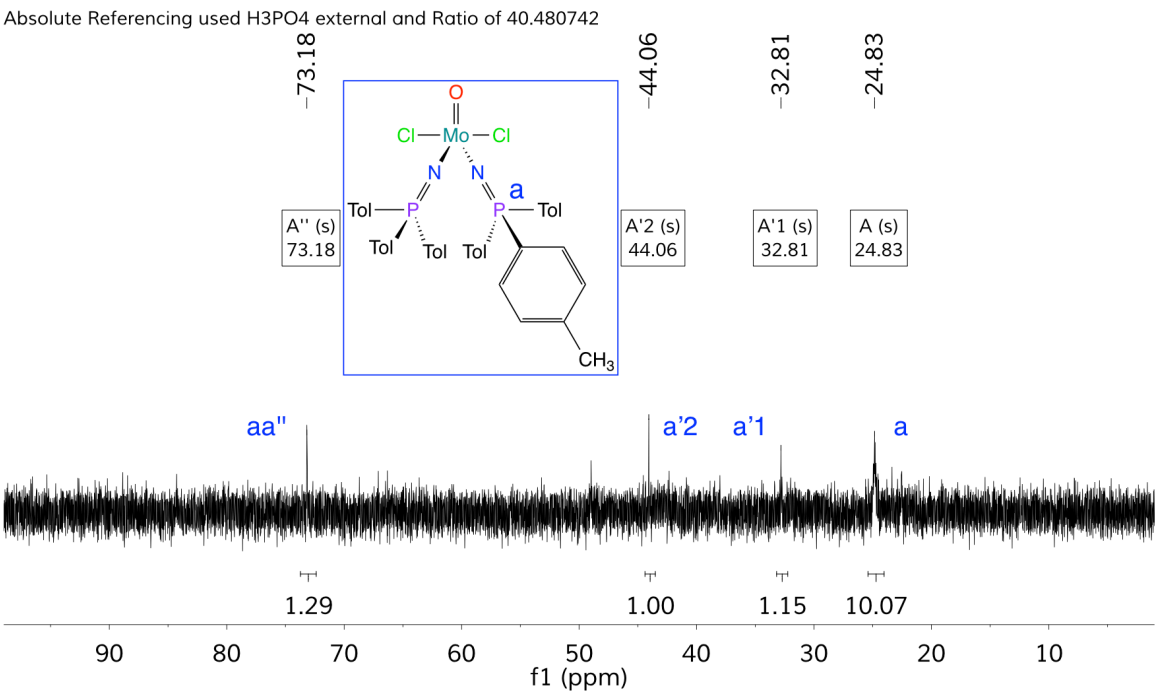

Figure 2.42: $^{31}P\{^{1}H\}$ NMR spectrum of **2.8** in C_6D_6 (162 MHz)

Interestingly, when **2.8** was dissolved in chloroform-*d*, the NMR spectra indicated that the complex is C_1 symmetric with asymmetric coordination of the phosphinimide ligands and no indication of a C_{2v} symmetric conformer present in solution.

At 15 °C, the ^{1}H NMR spectrum (Fig. 2.43) shows a pair of overlapping singlets at 2.37 and 2.38 ppm, which indicates two subtly different chemical environments for the CH_3 groups of the phosphinimide ligands. As mentioned previously, no measureable long-range 6-bond ^{1}H-^{31}P coupling was observed in this ligand. Aryl C-H signals are observed at 7.26 ppm (coincident with the residual $CHCl_3$ signal) that are evaluated as the *ortho*-hydrogens of both phosphinimide ligands, 7.63 ppm ($^{3}J_{PH}$ = 12.4 Hz, $^{3}J_{HH}$ = 8.1 Hz) for the *meta*-

hydrogens of one phosphinimide ligand, and 7.71 ppm (broad) for the remaining hydrogens of the other phosphinimide ligand.

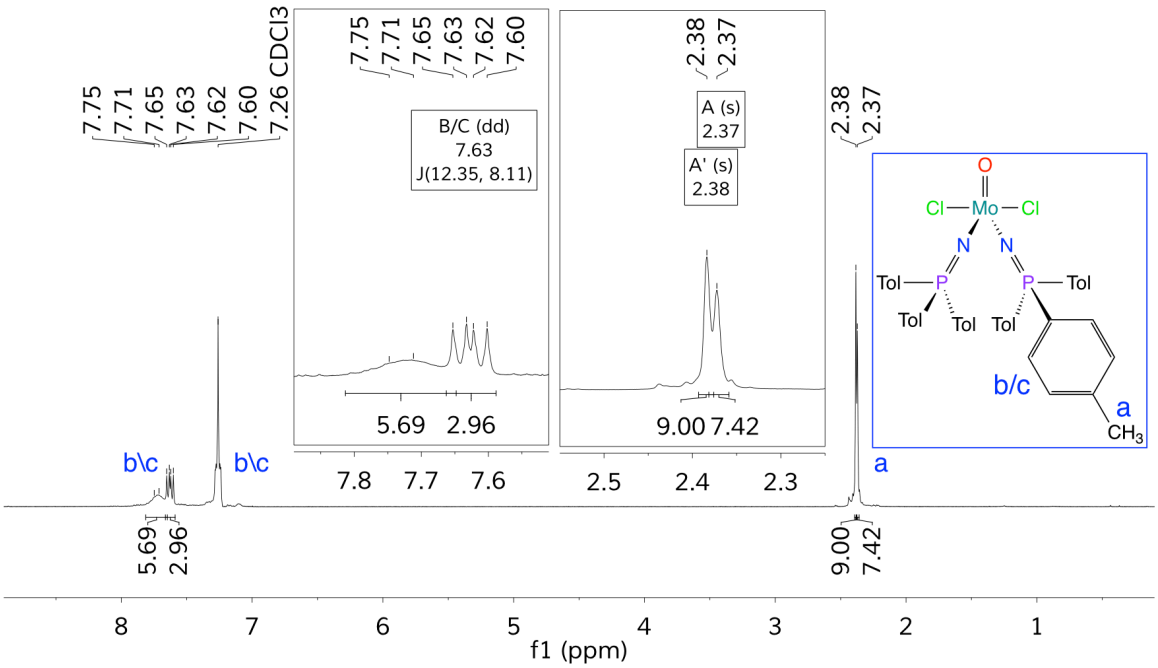

Figure 2.43: ^{1}H NMR spectrum of **2.8** in $CDCl_3$ (400 MHz)

Analysis of the ^{1}H NMR spectra of **2.8** in CD_2Cl_2 at various temperatures shows a similar distribution of peaks when at 20 °C. The aryl signals combine into similar chemical environments at 40 °C, with good correlation of relative integrations between both *ortho* and *meta* positions. At -40 °C, the aryl signals separate out further to more well defined doublets of doublets, which are evaluated to arise entirely from ^{31}P and ^{1}H coupling rather than restrained rotation, as similar coupling is observed in the free proligand.

The $^{31}P\{^{1}H\}$ NMR spectrum (Fig. 2.44) exhibits only two singlets at 34.19 and 43.67 ppm with an exact 1:1 integration ratio. The chemical shifts of these signals correlate closely to the $^{31}P\{^{1}H\}$ signals when measured in benzene-d6 that were the minor components in that spectrum.

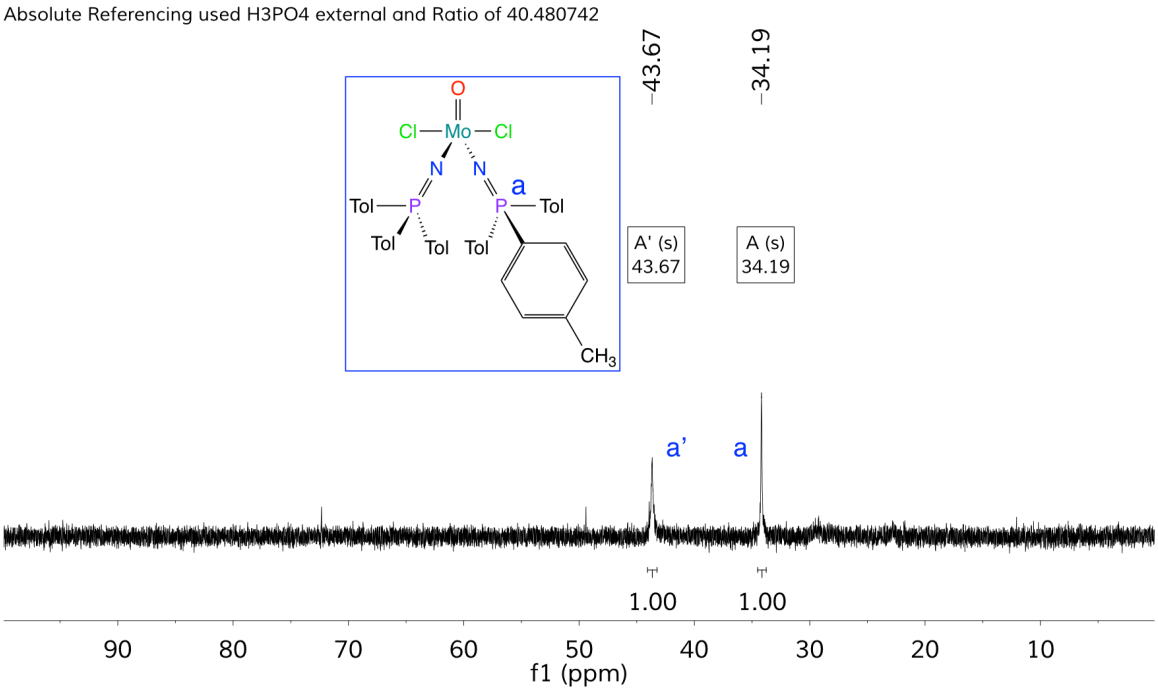

Figure 2.44: $^{31}P\{^{1}H\}$ NMR spectrum of **2.8** in $CDCl_3$ (162 MHz)

2.2.3 Salt Metathesis Methodology

Salt metathesis is another synthetic route that has been used to generate phosphinimide complexes (Fig. 2.45), as discussed in Chapter 1. The versatile Mo(VI) oxido and imido complexes **2.1-2.3** can be used as starting materials for salt metathesis reactivity to install the phosphinimide ligands while retaining both imido and oxido fragments.

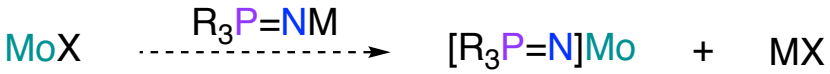

Figure 2.45: General salt metathesis methodology

Trimethylsilyl iminophosphoranes ($R_3P{=}N{-}Si(CH_3)_3$) can be converted into the corresponding phosphinimide ($R_3P{=}NH$), which can be deprotonated for use in salt metathesis reactions. Two equiv. of $^tBu_3P{=}NLi$, prepared using the synthetic protocol described in Section 2.2.1.3, cleanly generate [($^tBu_3P{=}N)_2Mo(O)(N^tBu)$] (**2.10**) (83% yield) when combined with precursor **2.2**, presumably through elimination of two equiv. of lithium chloride (Fig. 2.46).

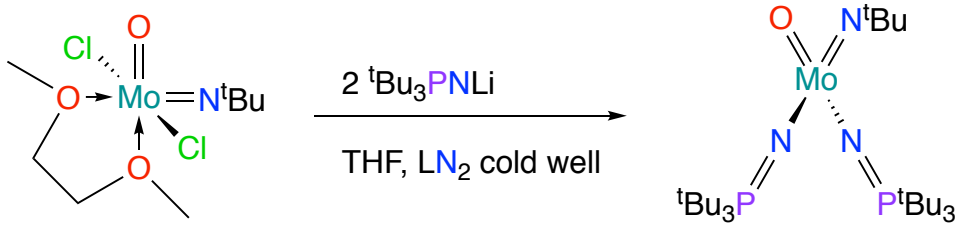

Figure 2.46: Synthesis of **2.10** by salt metathesis

Complex **2.10** is soluble in non-polar solvents, and can be cleanly separated from the salt byproducts by filtration. The same methodology can be used with precursor complex **2.3** to generate [($^tBu_3P{=}N)_2Mo(N^tBu)_2$] (**2.11**). Attempts to synthesize [($^tBu_3P{=}N)_2Mo(O)_2$] (**2.12**) by this same approach appears to work based on monitoring of the reaction by ^1H and $^{31}P\{^1H\}$ NMR spectroscopy. However, the product complex cannot be isolated cleanly by

filtration due to the similar solubility properties with the salt byproducts. The next section describes an alternative approach to generate complex **2.12**.

Complex **2.10** has been characterized by multinuclear NMR spectroscopy, XRD, and EA. Based on the XRD structure, **2.10** is approximately C_s symmetric with a mirror plane that contains the Mo atom and the oxido and imido ligands, with a pseudo-tetrahedral (τ'_4 = 0.98) core about the molybdenum atom (Fig. 2.47). Visualization of the space-filling model of the XRD structure of **2.10** reveals extensive steric protection around the metal center provided by the various *tert*-butyl fragments, with only the expected exposure of the oxido ligand (Fig. 2.48).

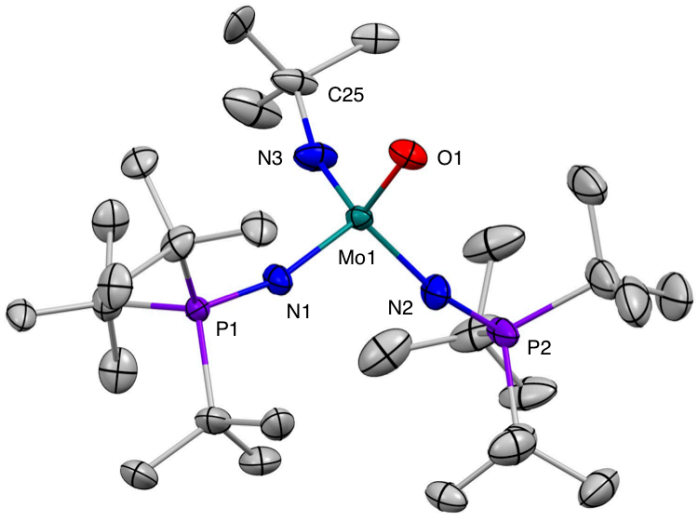

Figure 2.47: Thermal ellipsoid plot (50% probability) of complex **2.10**; hydrogen atoms and disordered tert-butyl groups have been omitted for clarity

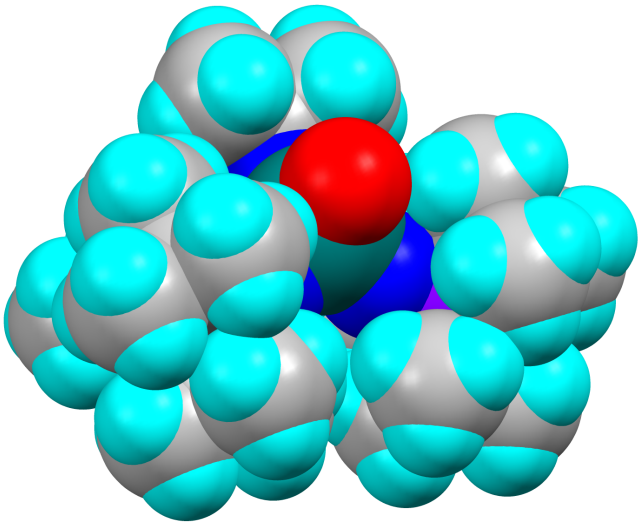

Figure 2.48: Space-filling model for **2.10** (van der Waals radii); disordered tert-butyl groups removed for clarity

The molybdenum-oxido bond length (Table 2.7) is comparable to other reported Mo(VI) oxido fragments.[15] The molybdenum-nitrogen (phosphinimide) bond lengths in **2.10** are slightly longer than complex **2.4** by less than 0.046(4) Å on average, and **2.5** by less than 0.028(6) Å on average. The corresponding oxido-molybdenum or imido-molybdenum bond lengths are also longer than observed in **2.4** by 0.026(3) Å for the oxido fragment, or **2.5** by 0.029(9) Å for the imido fragment. These bond lengths are not directly comparable, as complex **2.10** is four-coordinate and contains both oxido and imido ligands, yet indicates that the phosphinimide coordination to the molybdenum atom is not drastically different in terms of bond lengths.

Table 2.7: Selected XRD Bond Distances for Complex **2.10**

Atoms	**Length (Å)**	**Atoms**	**Length (Å)**
Mo1-O1	1.733(3)	P1-N1	1.557(3)
Mo1-N1	1.887(3)	P2-N2	1.565(3)
Mo1-N2	1.879(4)	N3-C25	1.458(5)
Mo1-N3	1.757(3)	–	–

Complex **2.10** is very close to a tetrahedral geometry, which is clear from the combined tau parameter, or the 108.93(8)° average of the bond angles centered on the molybdenum atom that are very close to the 109.5° expected for a perfect geometric tetrahedron. The bond angles for **2.10** (Table 2.8) centered on the phosphinimide nitrogen atoms are slightly more linear than **2.4** by an average of 2.9(3)°, yet less linear than **2.5** by an average of 8.9(4)°.

The *tert*-butyl imido ligand bond angle at 157.1(3)° is less linear than the imido fragment in **2.5**, and is quite different than the very linear imido ligands coordinated to high oxidation state metals, where bond angles are commonly greater than 170° for molybdenum imido ligands.[21] This difference in angle suggests that there is less triple-bond character in the imido bond than normal. The phosphinimide ligands in **2.10** are oriented similarly (Table 2.9), almost a reflection across the plane that contains the O1-Mo1-N3 atoms.

Table 2.8: Selected XRD Bond Angles for Complex **2.10**

Atoms	**Angle (°)**	**Atoms**	**Angle (°)**
Mo1-N1-P1	164.9(2)	N1-Mo1-N2	107.71(15)
Mo1-N2-P2	162.7(3)	N1-Mo1-N3	110.36(17)
O1-Mo1-N1	109.49(14)	N2-Mo1-N3	110.73(19)
O1-Mo1-N2	109.53(16)	Mo1-N3-C25	157.1(3)
O1-Mo1-N3	109.01(16)	–	–

Table 2.9: Selected XRD Torsion Angles for Complex **2.10**

Atoms	**Angle (°)**	**Atoms**	**Angle (°)**
P1-N1-Mo1-O1	78.0(9)	P2-N2-Mo1-O1	-89.7(8)
P1-N1-Mo1-N3	-42.0(9)	P2-N2-Mo1-N3	30.5(9)
N1-Mo1-N2-P2	151.3(8)	N2-Mo1-N1-P1	-163.0(8)

At 25 °C, the ^{1}H NMR spectrum (Fig. 2.49) of **2.10** shows a ^{31}P coupled doublet for the phosphinimide *tert*-butyl protons at 1.36 ppm ($^{3}J_{PH}$ = 12.8 Hz), and a singlet for the imido *tert*-butyl group at 1.73 ppm.

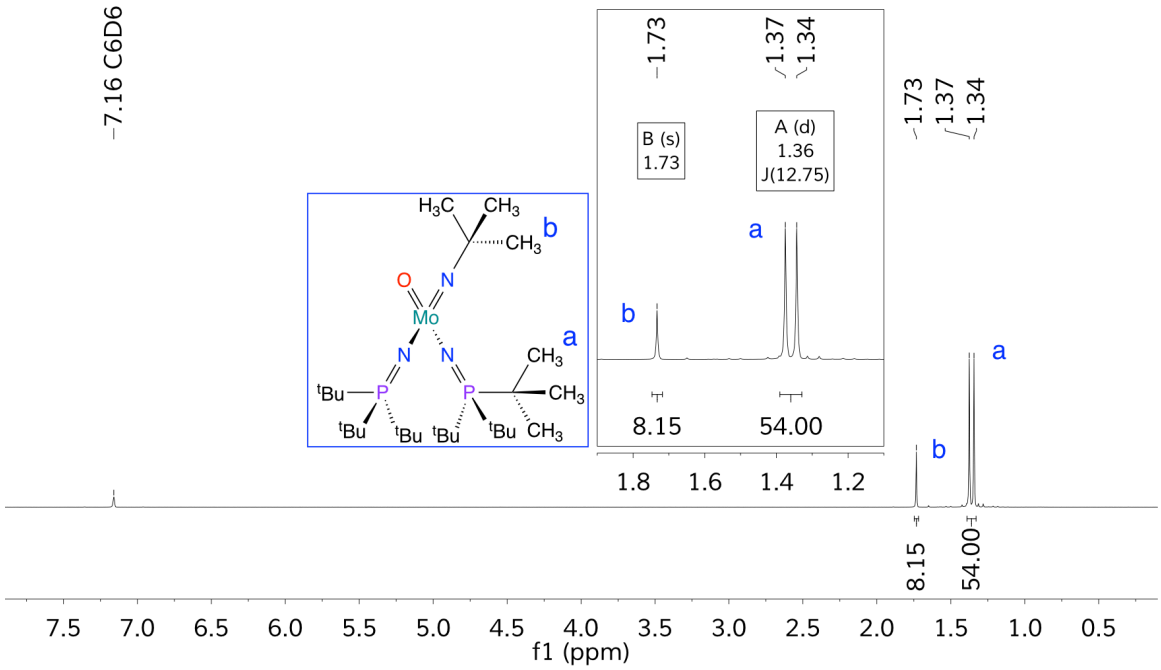

Figure 2.49: ^{1}H NMR spectrum of **2.10** in C_6D_6 (400 MHz)

The $^{31}P\{^{1}H\}$ NMR spectrum (Fig. 2.50) exhibits one singlet for the equivalent chemical environments of both phosphinimide ligands at 44.82 ppm.

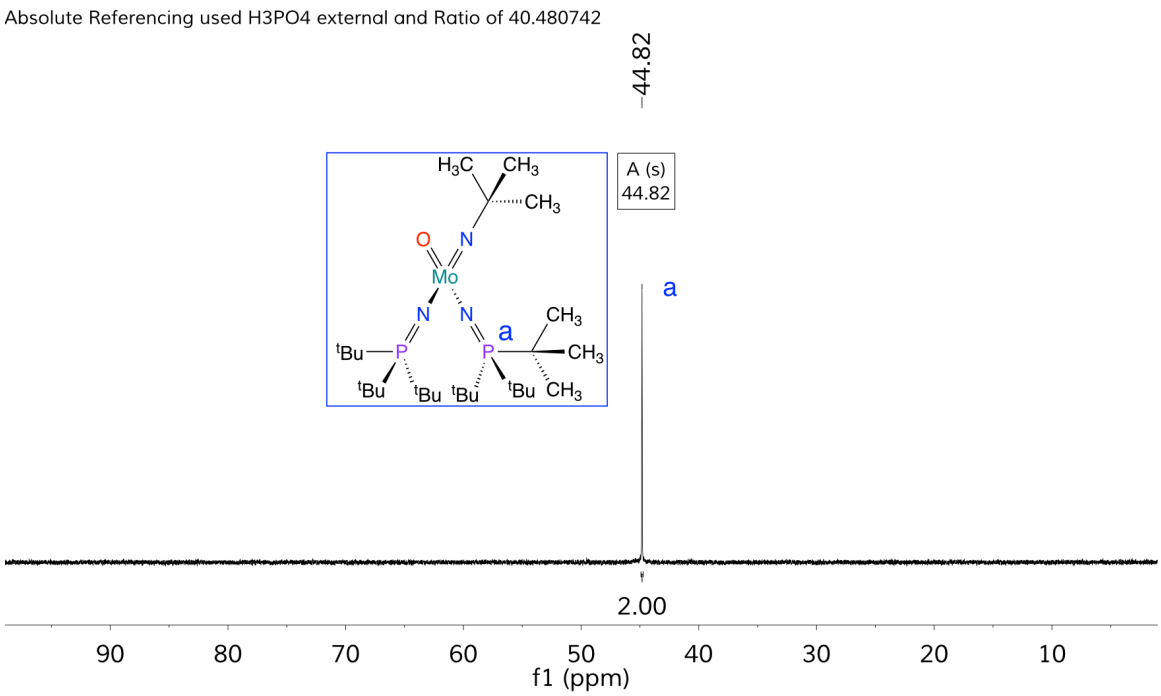

Figure 2.50: $^{31}P\{^{1}H\}$ NMR spectrum of **2.10** in C_6D_6 (162 MHz)

The $^{13}C\{^{1}H\}$ NMR spectrum (Fig. 2.51) contains a singlet for the phosphinimide *tert*-butyl methyl carbons at 29.65 ppm, and a ^{31}P coupled *tert*-butyl quaternary carbon doublet at 41.41 ppm ($^{1}J_{PC}$ = 47.8 Hz). Singlets are also observed for the imido *tert*-butyl methyl carbons at 32.44 ppm, and the *tert*-butyl quaternary carbon at 66.33 ppm.

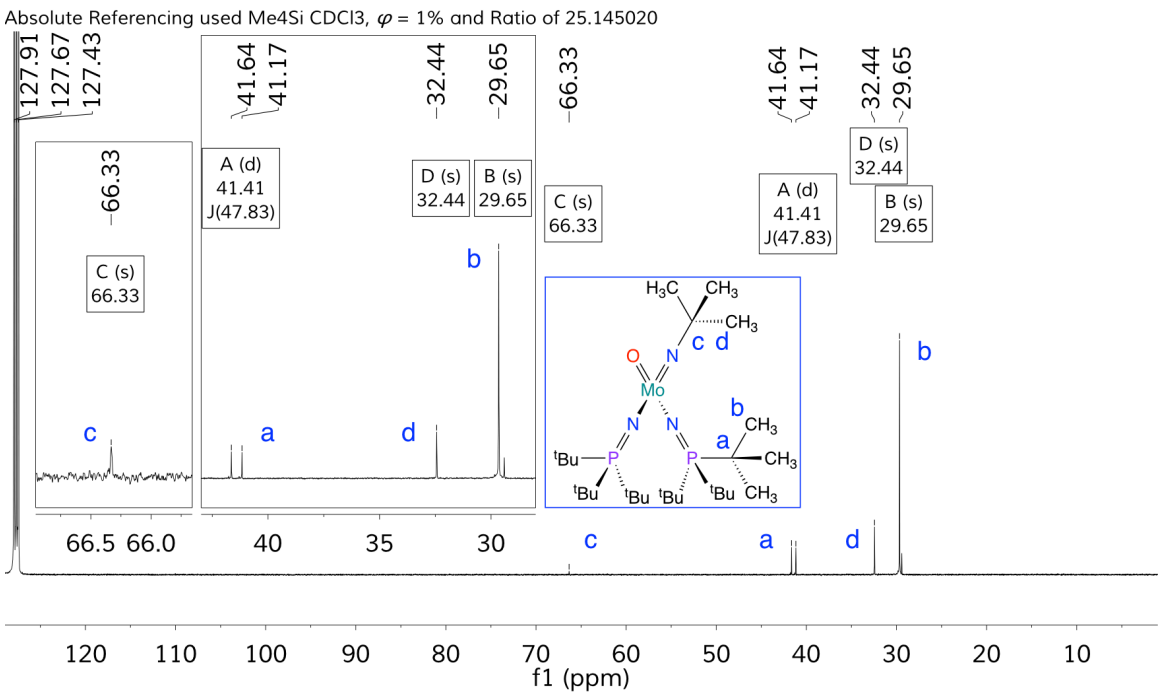

Figure 2.51: $^{13}C\{^{1}H\}$ NMR spectrum of **2.10** in C_6D_6 (101 MHz)

Synthesis of $[(^tBu_3P{=}N)_2Mo(N^tBu)_2]$ **(2.11)** (84% yield) is possible through an analogous reaction to the synthesis of **2.10** using **2.3** as the molybdenum reagent (Fig. 2.52).

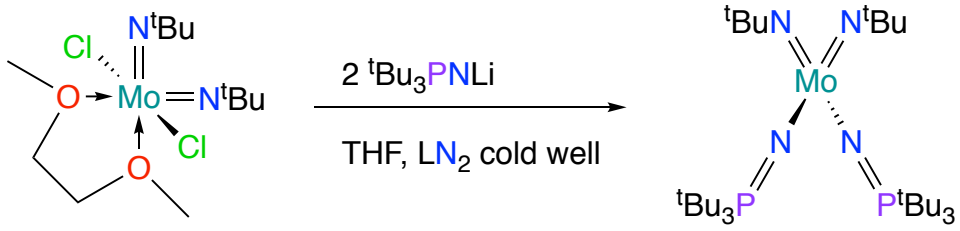

Figure 2.52: Synthesis of **2.11** by salt metathesis

Complex **2.11** has been characterized by multinuclear NMR spectroscopy, XRD, and EA. The high symmetry pseudo-tetrahedral (τ'_4 = 0.98) geometry, and increased steric bulk around the molybdenum ion, results in a

solid-state structure with very similar metrical parameters between equivalent fragments of the molecule (Fig. 2.53).

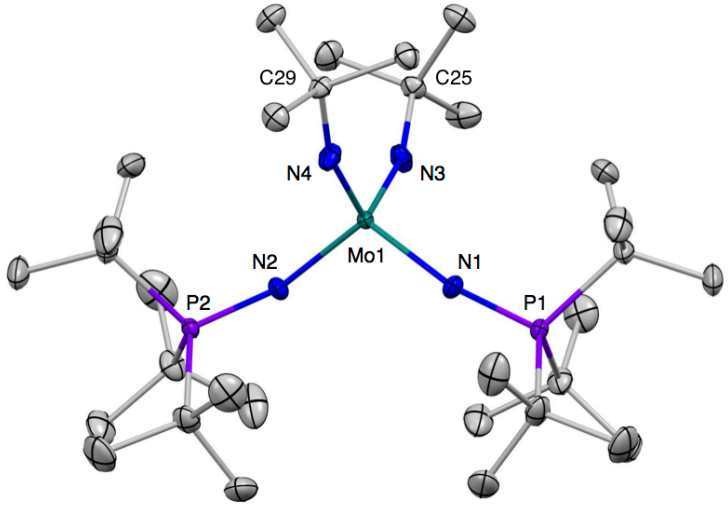

Figure 2.53: Thermal ellipsoid plot (50% probability) of complex **2.11**; hydrogen atoms have been omitted for clarity

The phosphinimide P-N and Mo-N bonds are effectively identical between both ligands, and the same bond length similarity is observed for the pair of imido ligands (Table 2.10). The bond lengths between the molybdenum and phosphinimide nitrogen atoms (Mo1-N1 and Mo1-N2) are longer than those in complex **2.10** by an average of 0.033(2) Å. These differences are understood as the effect of a more electron rich metal center than **2.10** from the additional imido ligand, and more significant steric interactions between the bulky ligands.

Table 2.10: Selected XRD Bond Distances for Complex **2.11**

Atoms	Length (Å)	Atoms	Length (Å)
Mo1-N1	1.9161(8)	P1-N1	1.5597(8)
Mo1-N2	1.9134(8)	P2-N2	1.5611(8)
Mo1-N3	1.7638(8)	N3-C25	1.4463(11)
Mo1-N4	1.7599(8)	N4-C29	1.4459(11)

Bond angles (Table 2.11) within the core of the molecule are very similar, with the largest difference between pairs of fragments below 1.5°. The phosphinimide coordination angles (Mo-N-P) in **2.11** are more acute than in **2.10**, which suggests a more electron rich metal center and weaker phosphinimide coordination. More acute imido ligand (Mo-N-C) bond angles are also observed in **2.11**, which again indicate a more electron rich metal center and weaker imido ligand coordination.

Table 2.11: Selected XRD Bond Angles for Complex **2.11**

Atoms	Angle (°)	Atoms	Angle (°)
Mo1-N1-P1	155.93(5)	N2-Mo1-N3	107.90(4)
Mo1-N2-P2	157.28(6)	N2-Mo1-N4	110.77(4)
N1-Mo1-N2	110.29(3)	N3-Mo1-N4	110.26(4)
N1-Mo1-N3	110.59(4)	Mo1-N3-C25	160.51(7)
N1-Mo1-N4	107.06(4)	Mo1-N4-C29	161.32(7)

Compared to the more sterically open structures, such as the oxido-dichlorido complex **2.4**, the phosphinimide ligands in **2.11** are coordinated in a very similar manner to the molybdenum center. There is some variance between the selected torsion angle pairs in Table 2.12, yet overall the mode of binding for both ligands is the same. This similarity is expected given the significant steric size of all ligands in the complex. There simply isn't enough flexibility in the structure to allow for different angles of coordination for the ligands. The space-filling visualization of this structure supports this analysis with all external *tert*-butyl groups in effectively direct contact with the adjacent ligands (Fig. 2.54).

Table 2.12: Selected XRD Torsion Angles for Complex **2.11**

Atoms	**Angle (°)**	**Atoms**	**Angle (°)**
P1-N1-Mo1-N3	-15.74(14)	P2-N2-Mo1-N4	-5.83(15)
P1-N1-Mo1-N4	-135.89(12)	P2-N2-Mo1-N3	-126.6(14)
N1-Mo1-N2-P2	112.51(14)	N2-Mo1-N1-P1	103.52(13)

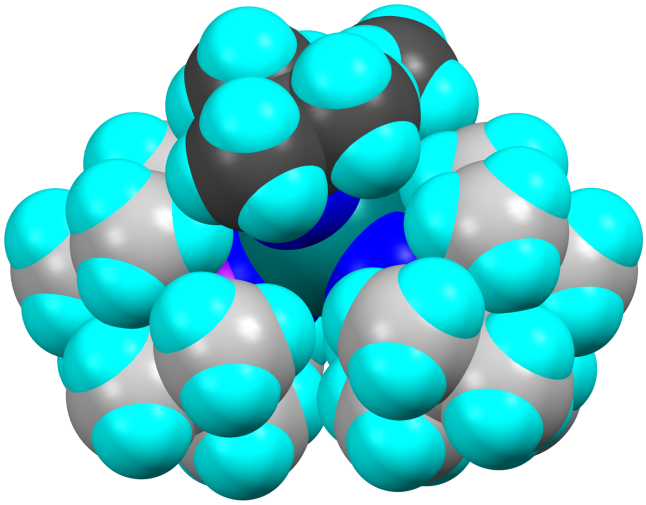

Figure 2.54: Space-filling model of complex **2.11** (van der Waals radii), imido carbon atoms indicated in dark grey

In solution, complex **2.11** exhibits C_{2v} symmetry due to the equivalence between pairs of imido and phosphinimide ligands and thermal motion, which can be observed in the ^{1}H, $^{13}C\{^{1}H\}$, and $^{31}P\{^{1}H\}$ NMR spectra at ambient temperature (~25 °C). A diagnostic doublet in the ^{1}H NMR spectrum (Fig. 2.55) is observed at 1.41 ppm ($^{3}J_{PH}$ = 12.5 Hz) from the ^{31}P coupled *tert*-butyl protons, along with a single peak at 1.65 ppm for the *tert*-butyl imido protons. The $^{13}C\{^{1}H\}$ NMR spectrum presents a ^{31}P coupled quaternary *tert*-butyl carbon peak at 41.31 ppm ($^{1}J_{PC}$=48.0 Hz), a single peak for the imido methyl carbons at 33.59 ppm, and a single peak for the phosphinimide methyl carbons at 29.85 ppm (Fig. 2.56). A single peak is observed in the $^{31}P\{^{1}H\}$ spectrum (Fig. 2.57) at 40.61 ppm for the chemically equivalent phosphorus atoms.

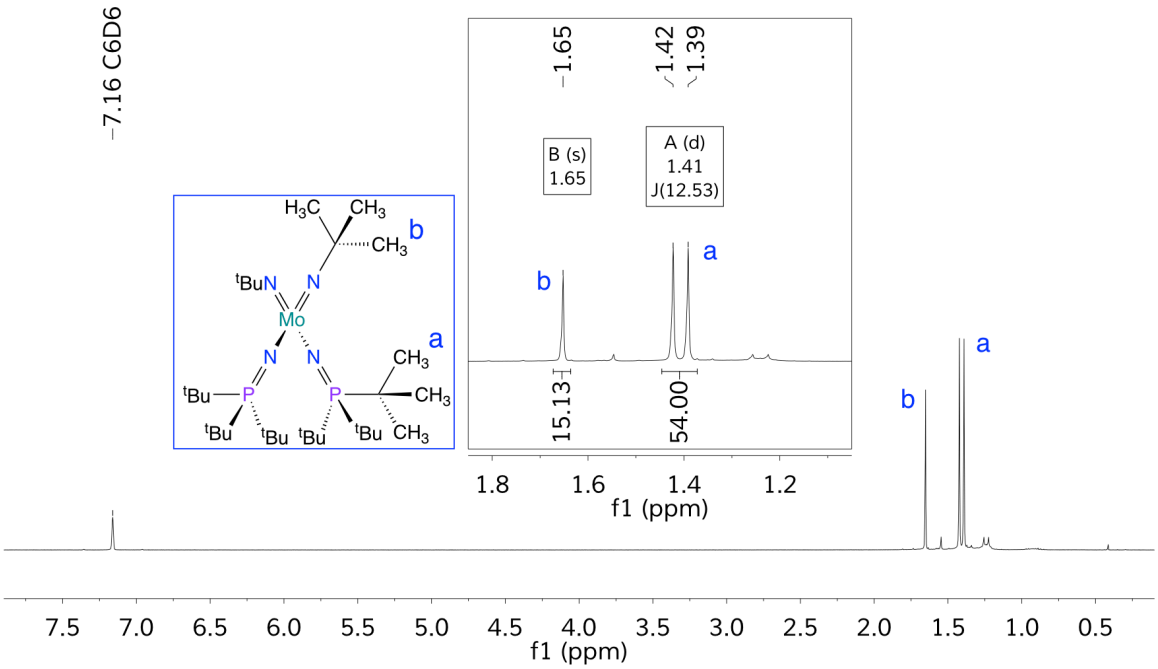

Figure 2.55: ^{1}H NMR spectrum of **2.11** in C_6D_6 (400 MHz)

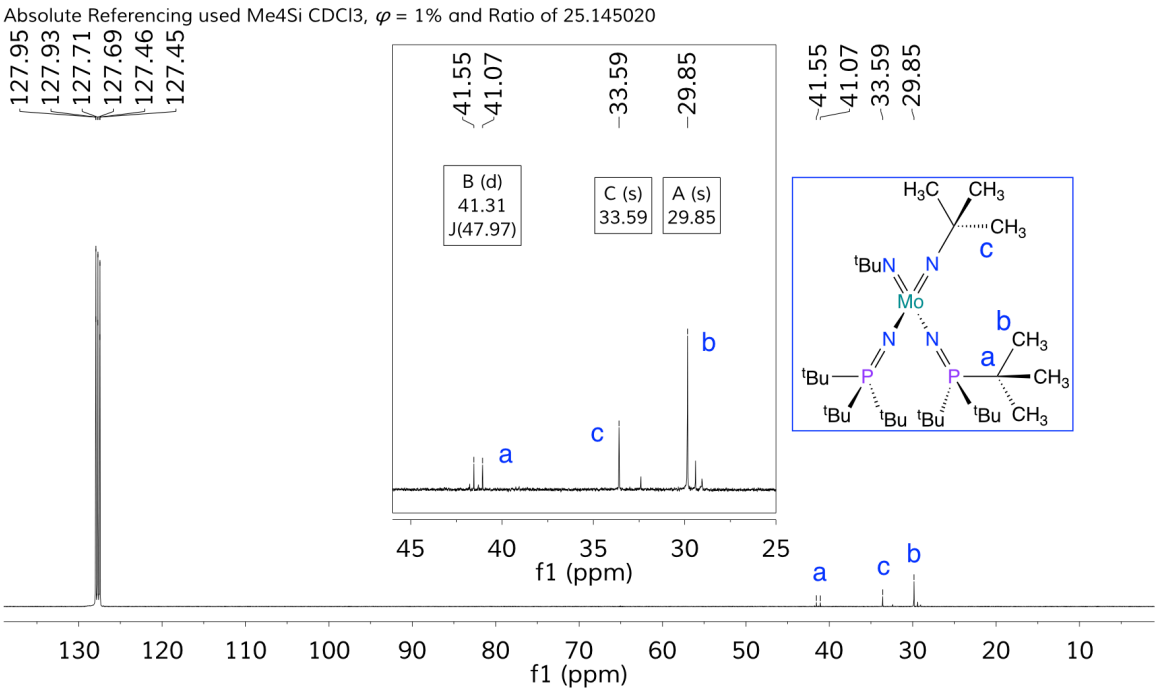

Figure 2.56: $^{13}C\{^{1}H\}$ NMR spectrum of **2.11** in C_6D_6 (101 MHz)

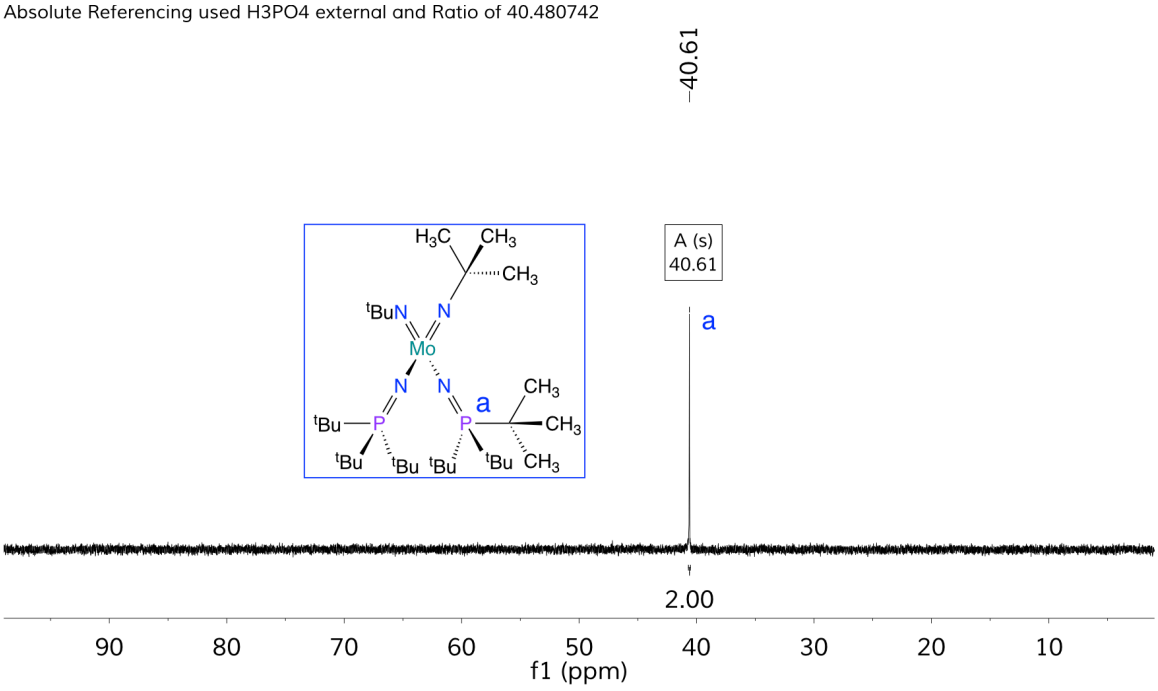

Figure 2.57: $^{31}P\{^{1}H\}$ NMR spectrum of **2.11** in C_6D_6 (162 MHz)

2.2.4 Protonolysis Methodology

As mentioned previously, use of the salt metathesis methodology described in section 2.2.3 appears to work based on NMR spectral data when starting with the dioxido-dichlorido starting material (**2.1**), to generate the bis(phosphinimide)-dioxido species [(^{t}Bu$_3$P=N)$_2$Mo(O)$_2$] (**2.12**); however, isolation of **2.12** can not be achieved using the same filtration approach. Despite the presence of six *tert*-butyl groups within the phosphinimide ligand framework, **2.12** has poor solubility in non-polar solvents, and is only soluble in the same polar solvents as the salt reaction byproducts. As such, an alternative synthetic approach was necessary to access this dioxido complex.

Conversion of oxido-dichlorido **2.4** to **2.12** through reaction with bis(trimethylsilyl)ether to eliminate trimethylsilylchloride also does not proceed, even at elevated temperatures (+80°C).

The R_3P=N–H derivative **L2** used as a precursor for salt metathesis offers the potential to be used as a proligand through protonolysis approaches. A metal starting material incorporating ligands that are more basic than R_3P=NH could eliminate the protonated form of the basic ligand and install the phosphinimide ligand (Fig. 2.58). Using this approach, the volatile protonated byproduct could be more easily separated from the target dioxido complex **2.12**.

Figure 2.58: General protonolysis methodology

A potentially suitable initial complex for this type of reactivity is $(acac)_2Mo(O)_2$ (acac = acetylacetonate) (**2.13**), a readily synthesized and commercially available metal starting material. The pK_a difference between the phosphinimine proligand and acetylacetonate is not substantial, and reaction between these two reagents is not expected to proceed if only the proligand and acetylacetonate ion were present in solution (Fig. 2.59).

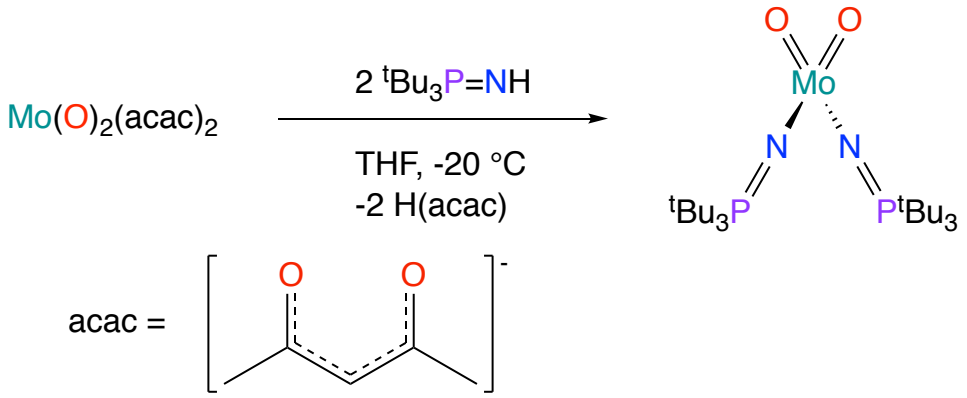

Figure 2.59: Synthesis of **2.12** by protonolysis

Substituted phosphinimines are known to function as neutral ligands through electron donation from the nitrogen lone pair to metal ions.[22–27] If this characteristic is taken into consideration, it is plausible that initial dative coordination of the protonated phosphinimine could occur. Upon coordination, the more electropositive nitrogen atom can lead to a decrease in pK_a for the nitrogen bound hydrogen atom, which is then capable of deprotonation by even weak bases, such as acetylacetonate. Steric pressure of the relatively bulky phosphinimine ligands could also factor into elimination of the protonated byproduct pentane-2,4-dione (acetylacetone), and may drive the conversion

forward by preventing subsequent coordination of pentane-2,4-dione and formation of an equilibrium mixture of products.

The combination of two equivalents of $^{t}Bu_3P{=}NH$ with **2.13** results in rapid elimination of pentane-2,4-dione and generation of the intended dioxido complex **2.12**. Pentane-2,4-dione formed as a byproduct is volatile enough to be removed along with the solvent under vacuum, allowing for pure isolation of complex **2.12** in quantitative yield. To my knowledge this protonolysis approach to synthesize phosphinimide complexes has not been previously reported.

Complex **2.12** has been characterized by NMR spectroscopy, and elemental analysis. The ^{1}H NMR spectrum of **2.12** in $CDCl_3$ (Fig. 2.60) shows the expected doublet for the ^{31}P split tert-butyl groups, located at 1.49 ppm ($^{3}J_{PH}$ = 13.3 Hz). The $^{13}C\{^{1}H\}$ NMR spectrum contains a ^{31}P coupled peak at 41.97 ppm ($^{1}J_{PC}$ = 46.9 Hz) for the quaternary phosphinimide carbons, and a singlet at 29.67 ppm for the phosphinimide methyl carbons (Fig. 2.61). The proton decoupled ^{31}P NMR spectrum presents a lone singlet resonance at 51.98 ppm (Fig. 2.62), These NMR peaks correlate well with crystallographically characterized complexes **2.11** and **2.10**, suggesting that complex **2.12** is similar in structure.

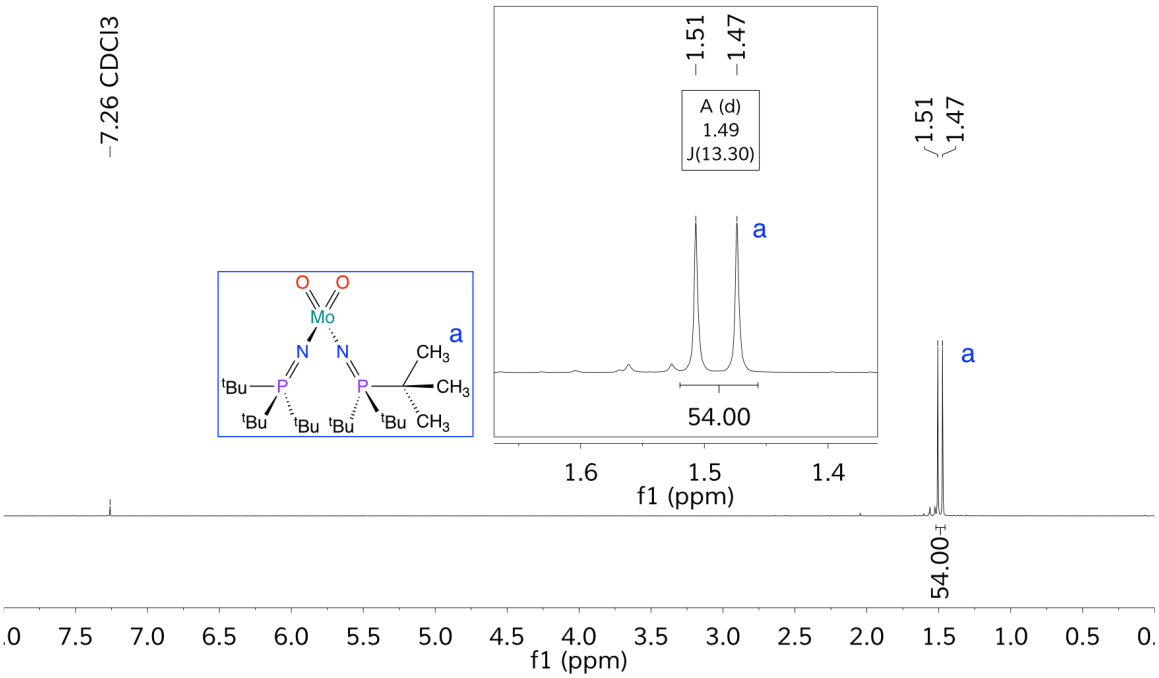

Figure 2.60: ^{1}H NMR spectrum of **2.12** in $CDCl_3$ (400 MHz)

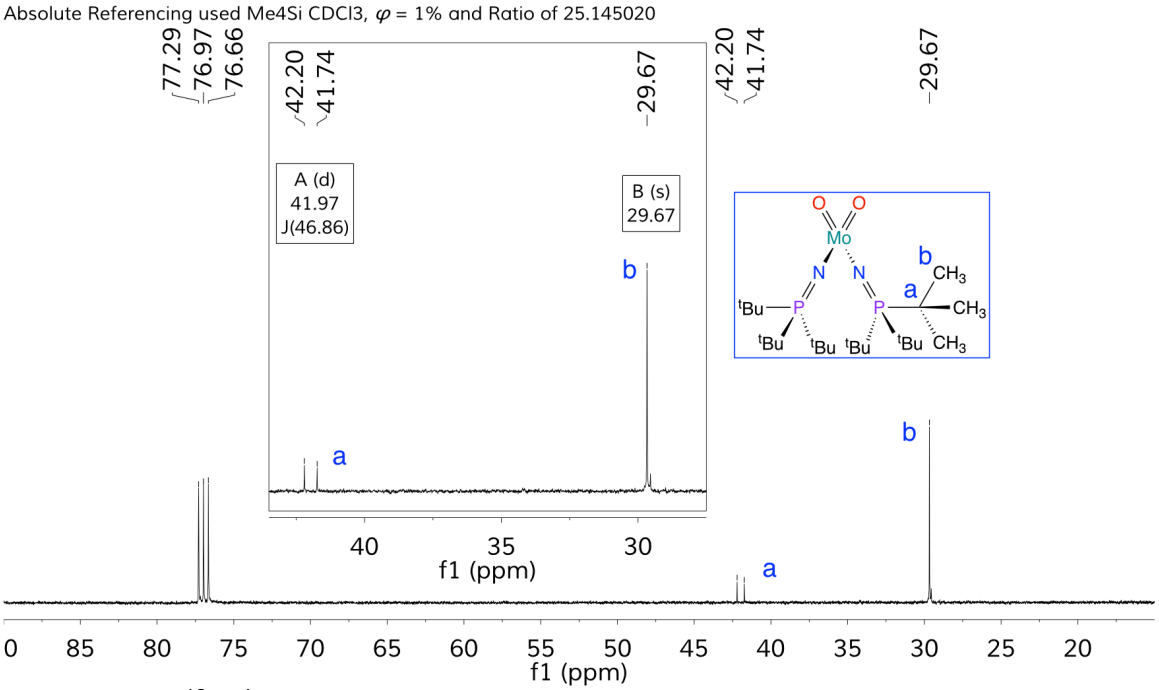

Figure 2.61: $^{13}C\{^{1}H\}$ NMR spectrum of **2.12** in $CDCl_3$ (101 MHz)

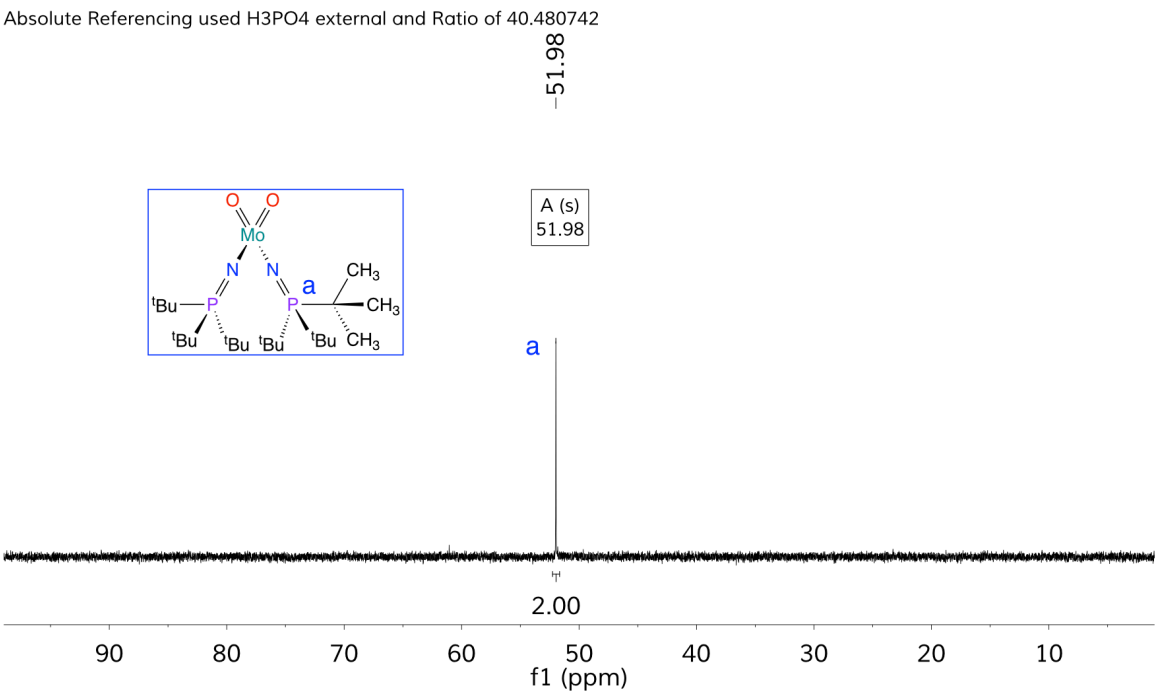

Figure 2.62: $^{31}P\{^{1}H\}$ NMR spectrum of **2.12** in $CDCl_3$ (162 MHz)

The effectiveness of this reaction is further corroborated by a negative observation of acetylacetone derivatives in the NMR spectral data, indicating that no alternative reaction products are generated. A single peak in the ^{31}P NMR spectrum supports this assessment of formation of a single product. Further, the elemental analysis of complex **2.12** matches the chemical formula of the target complex **2.12** very closely.

Single crystals of **2.12** suitable for XRD analysis could not be obtained, due to the limited solubility of the complex even in very polar solvents. The previously reported complex $[(Ph_3P{=}N)_2Mo(O)_2]$ was characterized by XRD and exhibited a pseudo-tetrahedral geometry.[11] Given the NMR spectroscopic data, complex **2.12** is expected to have a similar geometry to this previously reported complex, and to the structures determined for complexes **2.11** and **2.10**.

2.2.5 General Discussion

It is notable that the syntheses of $[(^tBu_3P{=}N)_2Mo(O)Cl_2]$ (**2.4**), $[(^tBu_3P{=}N)_2Mo(N^tBu)Cl_2]$ (**2.5**), and related derivatives proceed cleanly without additional side reactions involving the chloride ligands, which would lead to impurities and decreased formation of the intended products. Monitoring the synthesis of **2.4** over time by NMR spectroscopy provides no evidence for the formation of any $ClSi(CH_3)_3$ even as an intermediate byproduct in the reaction. Synthesis of complex **2.9** within a closed system indicates minimum formation of $ClSi(CH_3)_3$, with $O(Si(CH_3)_3)_2$ as the major byproduct. Due to these reaction characteristics, the relatively unique complexes **2.4** and **2.5** can be accessed. These complexes are unique due to the presence of the highly configurable supporting phosphinimide ligands, with an imido or oxido fragment, as well as two chlorido ligands that can be utilized for further reactivity, such as the installation of additional ligands by salt metathesis (see Chapter 3).

Alternative synthetic methodologies, including salt metathesis and protonolysis, enabled the synthesis of the series of related alkylimido and oxido complexes **2.11-2.12** (Fig. 2.63).

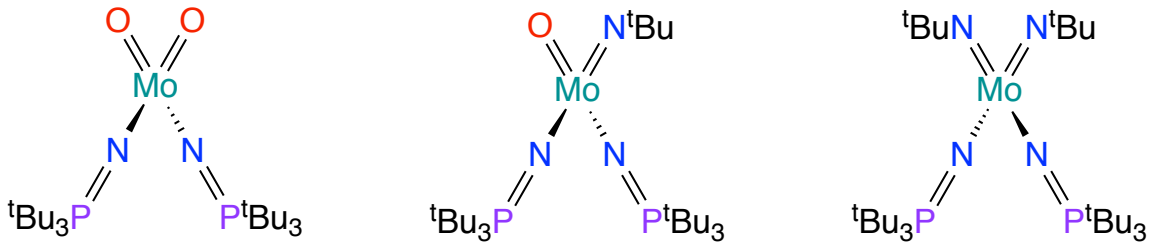

Figure 2.63: Sequence of bisphosphinimide imido and oxido complexes

Comparison of the ^{31}P NMR chemical shifts of the singlets for complexes **2.11-2.12** when measured in benzene-d_6 reveals a consistent change in the chemical shift values as the oxido ligands are changed to tert-butylimido ligands (Figure 2.64).

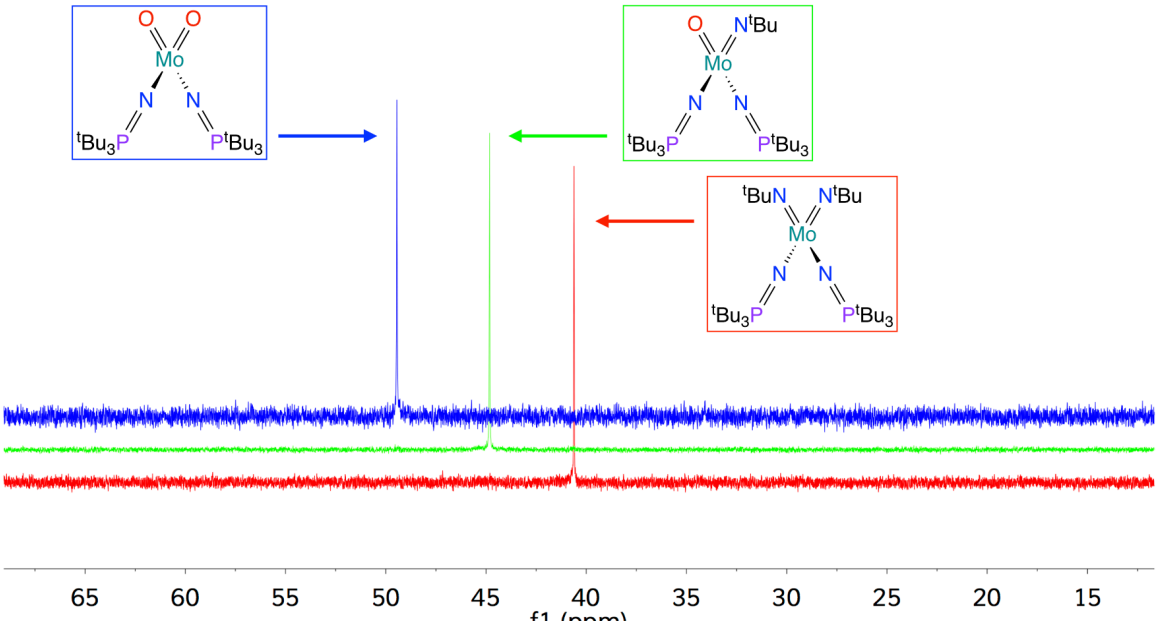

Figure 2.64: Superimposed $^{31}P\{^1H\}$ NMR spectra of **2.11** (red/bottom), **2.10** (green/middle), and **2.12** (blue/top) in C_6D_6 (162 MHz)

This variation in the chemical shift can primarily be attributed to a change in electron donation to the molybdenum center. The presence of more electron withdrawing oxido ligands reduces the electron density at the phosphorus nuclei leading to a more positive chemical shift. This effect is reduced as the oxido ligands are replaced by the more electron donating *tert*-butylimido ligands.

Similarly, the same type of effect can be seen through comparison of the ^{1}H NMR spectra of complexes **2.11-2.12** (Figure 2.65). For complexes **2.11** and **2.10**, the ^{1}H NMR peaks for the *tert*-butylimido protons follow the same trend as the ^{31}P NMR trend. As electron donation from the imido ligands increases to the metal center due to the presence of an oxido fragment in complex **2.10**, the *tert*-butylimido methyl peak shifts slightly downfield, indicating a less electron rich environment around the protons.

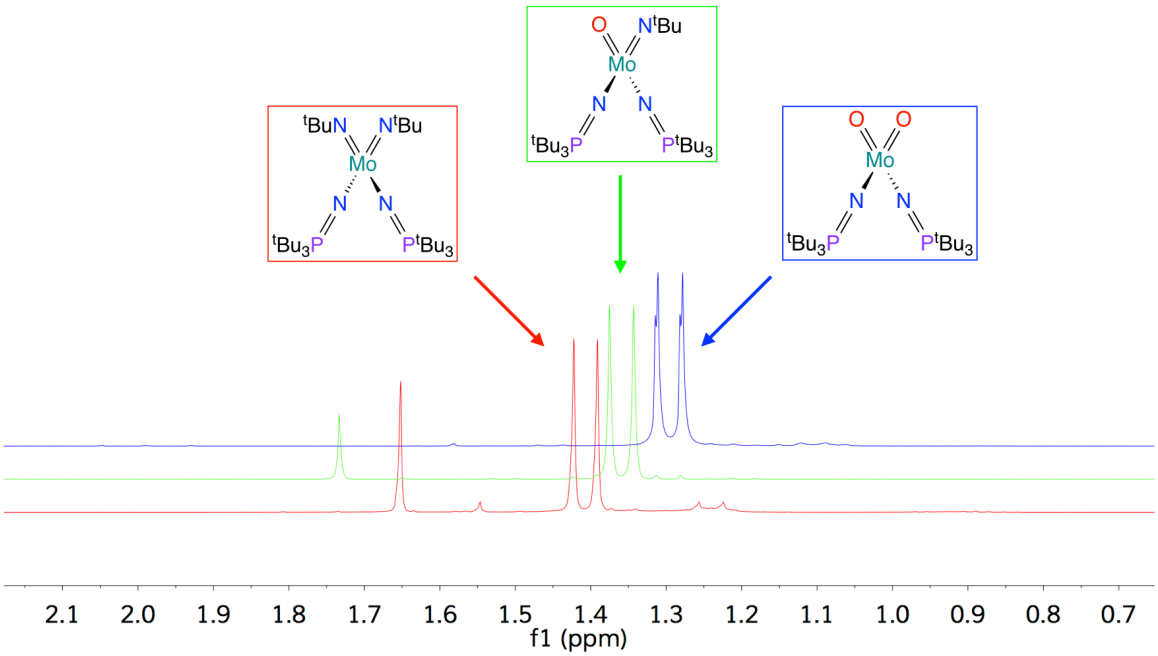

Figure 2.65: ^{1}H NMR superimposed spectra of **2.11** (red/bottom), **2.10** (green/middle), and **2.12** (blue/top) in C_6D_6 (400 MHz)

While the *tert*-butyl imido fragments follow the same trend as the ^{31}P NMR spectroscopic trend, the *tert*-butyl fragments of the phosphinimide ligands follow an inverse trend. Decreasing electron density at the molybdenum center

from **2.11** to **2.12** causes the phosphinimide ligand *tert*-butyl fragments to decrease in chemical shift, indicating a more electron rich environment near the *tert*-butyl fragments. This opposite trend can be attributed to slightly weaker coordination of the phosphinimide ligands.

Many of the complexes studied, exhibited asymmetric phosphinimide ligand coordination in solution. These coordination differences appear to be influenced by the steric size of the ligand, the surrounding solvent environment, and temperature. Lower steric bulk phosphinimide ligand derivatives are more likely to exhibit asymmetric coordination. Increased solubility of the complexes has shown they are more prone to asymmetric ligand coordination. Asymmetric coordination is also observed to have a more consistently coordinated phosphinimide ligand, while the coordination of the other phosphinimide ligand fluctuates more readily, which is interpreted as a weaker coordination interaction. Increased temperature causes the more weakly coordinated phosphinimide ligands to fluctuate more significantly in solution, while the more strongly coordinated phosphinimide ligands do not appear to be effected by temperature changes.

2.3 Conclusions

A range of group VI bisphosphinimide complexes have been synthesized and characterized, none of which have been previously reported in the literature. Synthetic routes to access these complexes have been developed through expansion of previously reported methods and new approaches,

including efficient ligand installation through selective $O(Si(CH_3)_3)_2$ elimination, salt metathesis, and protonolysis. These synthetic approaches provide foundational knowledge that will facilitate future study of phosphinimide complexes of group VI metals and other transition metals.

2.4 Future Work

A more in-depth comparison of derivative forms of **2.7** could explain whether asymmetric coordination of phosphinimide ligands is primarily an electronic or steric effect. Density functional theory (DFT) calculations of the geometry and electronic structure of these derivative complexes could help assess the factors involved in asymmetric coordination. DFT NMR property calculations could also be utilized to better support the trends observed in the series of complexes **2.10** to **2.12**, along with related derivatives.

2.5 Experimental

General Experimental Procedures

Unless otherwise specified, all reactions and manipulations were performed under a dry oxygen-free atmosphere of dinitrogen in either a Vacuum Atmospheres NEXUS model drybox equipped with a 40CFM Dual Purifier NI-Train, or by using standard Schlenk techniques. Glassware was dried in an oven at 150 ºC overnight prior to use.

NMR spectra were collected using a Varian Inova 600 MHz NMR spectrometer with a 5 mm indirect detection probe, Varian VNMRS 500 MHz

NMR spectrometer with a tunable 5 mm $^{1}H\{^{15}N\text{-}^{31}P\}$ PFG probe, Varian VNMRS 400 MHz spectrometer with an auto-tunable 5 mm Dual Broadband $^{15}N\text{-}^{31}P$ $\{^{1}H\}$ PFG probe optimized for broadband detection, or Oxford Mercury VX-300 300 MHz NMR spectrometer with a 5 mm 4-nuclei ($^{1}H/^{13}C/^{19}F/^{31}P$) auto-switchable PFG probe. Chemical shifts for ^{1}H, ^{11}B, ^{13}C, ^{19}F, ^{29}Si, and ^{31}P NMR spectra are reported in parts per million (ppm), and were referenced to residual solvent impurities, or when stated on the spectra with the absolute unified scale corresponding to the following standards using the relevant Ξ / % frequency ratios: ^{11}B, 32.083974 ($BF_3{\bullet}Et_2O$ $CDCl_3$, ϕ = 15 %); ^{13}C, 25.145020 ($Si(CH_3)_4$ $CDCl_3$, ϕ = 1 %); ^{19}F, 94.094011 ($FCCl_3$); ^{29}Si, 19.867187 ($Si(CH_3)_4$ $CDCl_3$, ϕ = 1 %); ^{31}P, 40.480742 (H_3PO_4 external).[28,29] All NMR spectral data were processed with the MestReNova 11.0.2 software package.

Elemental analyses were performed at Midwest Microlab LLC. Single crystal X-ray diffraction data were collected using a Bruker APEX2 diffractometer with a CCD area detector and graphite-monochromated Mo Kα radiation (λ = 0.71073 Å). Structural solution and refinement were accomplished using the APEX2, SAINT, SADABS, TWINABS, and SHELXL programs.[30–32] Details regarding data collection for each structure are provided in the individual CIF files.

Except where otherwise noted, reagents were purchased from commercial suppliers and used without further purification. Benzene-d_6, chloroform-d, dichloromethane-d_2, and toluene-d_8, were purchased from Cambridge Isotope Laboratories (99.9%D) and were purified by storage over 4

Å molecular sieves under N_2 prior to use. Celite (Aldrich) and 4 Å molecular sieves (Aldrich) were dried under dynamic vacuum at 250 ºC for 48 h prior to use. All solvents were purchased from commercial suppliers and dried and deoxygenated with the appropriate VAC Atmospheres Solvent Purifier modules and stored over activated 4 Å molecular sieves prior to use. The following compounds were prepared according to literature procedures: [(DME)Mo(O)$_2$Cl$_2$] (**2.1**), [(DME)Mo(O)(N^{t}Bu)Cl$_2$] (**2.2**), and [(DME)Mo(N^{t}Bu)$_2$Cl$_2$] (**2.3**).[33]

Synthesis of ^{t}Bu$_3$P=N–Si(CH$_3$)$_3$ (L1): In a 20 mL scintillation vial, ^{t}Bu$_3$P (3.71 mmol, 750 mg) was combined with neat (CH$_3$)$_3$Si-N$_3$ (11.12 mmol, 1.281 g) at ambient temperature. The vial was sealed, and the colorless transparent reaction mixture was stirred with a magnetic stir bar while heated to +90 °C for 6 hours. Any N_2 pressure generated in the headspace was released by briefly venting the reaction after 1 and 3 hours. The reaction was cooled to ambient temperature and volatiles were removed under vacuum. 1.058 g (98% yield by mass) of **L1** was isolated as a white solid. This is a modified synthesis based on a previously reported synthesis.[4] ^{1}H NMR (400 MHz, benzene-d_6, 25.0 °C) δ = 0.41 (d, 9H, $^4J_{PH}$ = 1.1 Hz, NSi(CH_3)$_3$), 1.16 (d, 27H, $^3J_{PH}$ = 12.7 Hz, PC(CH_3)$_3$). ^{31}P{^{1}H} NMR (162 MHz, benzene-d_6, 25.0 °C) δ = 32.31 (s, 1P, *P*C(CH$_3$)$_3$). ^{1}H NMR (400 MHz, chloroform-*d*, 25.0 °C) δ = 0.01 (s, 9 H, NSi(CH_3)$_3$), δ = 1.29 (d, $^3J_{PH}$ = 12.6 Hz, 27 H, PC(CH_3)$_3$). ^{31}P{^{1}H} NMR (162 MHz, chloroform-*d*, 25.0

°C) δ = 32.35 (s, 1 P, PC$(CH_3)_3$). ^{13}C NMR data was not collected on this compound as it was previously reported.[34]

Synthesis of ^{t}Bu$_3$P=NH (L2): ^{t}Bu$_3$P=N–Si$(CH_3)_3$ (3.02 mmol, 874 mg) was dissolved in 10 mL of toluene and added to a 50 mL Schlenk tube. The Schlenk tube was connected to a Schlenk line and unpurified standard grade CH_3OH (62 mmol, 2.5 mL) was added to the reaction flask while purging with dinitrogen. The Schlenk tube was sealed and the colorless transparent reaction was stirred using a magnetic stir bar and heated at +100 °C for 18 hours. The system was cooled, and solvent and volatiles were removed under vacuum, leaving behind a white solid. The white solid was transferred out of the Schlenk tube with hexanes in a glovebox, and the hexanes were removed under vacuum. 627 mg (96 % yield) of ^{t}Bu$_3$P=NH was isolated as a white powder. This is a modified synthesis based on a related synthesis.[35] ^{1}H NMR (500 MHz, benzene-d_6, 25.0 °C) δ = 0.19 (s, 1H, NH), δ = 1.22 (d, 27 H, $^3J_{PH}$ = 11.9 Hz, PC(C$H_3)_3$). ^{31}P{^{1}H} NMR (162 MHz, benzene-d_6, 25.0 °C) δ = 56.13 (s, 1P, PC$(CH_3)_3$). ^{13}C NMR data was not collected on this compound as it was previously reported.[13]

Synthesis (*in situ*) of ^{t}Bu$_3$P=NLi (L3): ^{t}Bu$_3$P=NH (**L2**) (0.906 mmol, 197.0 mg) was dissolved in ~10 mL of THF and was then cooled thoroughly in a LN_2 cooled cold well. While stirring and warming to ambient temperature, a methyl lithium solution (0.912 mmol, 0.57 mL) was added dropwise. The solution rapidly clarifies to give a colorless transparent solution, along with generation of

gas bubbles. After one hour, the solution was used in the next synthetic step and not isolated.

Synthesis of $Cy_3P{=}NSi(CH_3)_3$ (L4): L4 was synthesized using the same conditions as the synthesis of **L1**. ^{1}H NMR (400 MHz, benzene-d_6, 25.0 °C) δ = 0.45 (s, 9H, NSi(CH_3)$_3$), (P(C$_6H_{11}$)$_3$) 1.10, 1.34, 1.59, 1.63, 1.70, 1.88. ^{31}P{^{1}H} NMR (162 MHz, benzene-d_6, 25.0 °C) δ = 17.09 (s, 1P, *P*C(CH$_3$)$_3$). ^{13}C NMR data was not collected on this compound as it was previously reported.[4]

Synthesis of $Ph_3P{=}NSi(CH_3)_3$ (L5): In a 20 mL scintillation vial, Ph_3P (6.55 mmol, 1.72 g) was combined with neat Me_3Si-N_3 (26.1 mmol, 3.00 g) at ambient temperature. The vial was sealed, and the colorless transparent reaction mixture was stirred using a magnetic stir bar while heated at 80 °C for 15 hours. Any N_2 pressure generated in the headspace was released by briefly venting the reaction after 1 hour. The reaction was cooled to ambient temperature and volatiles were removed under vacuum. 2.06 g (90% yield by mass) of **L5** was isolated as a white crystalline solid. ^{1}H NMR (400 MHz, benzene-d_6, 25.0 °C) δ = 0.39 (s, 9H, NSi(CH_3)$_3$), 7.04 (m, 9H, P(o-Ph)/P(p-Ph)), 7.74 (m, 6H, P(m-Ph)). ^{31}P{^{1}H} NMR (162 MHz, benzene-d_6, 25.0 °C) δ = -1.02 (s, 1P, *P*C(CH$_3$)$_3$). ^{13}C NMR data was not collected on this compound as it was previously reported.[4]

Synthesis of *p*-Tol$_3$P=NSi(CH$_3$)$_3$ (L6): In a 20 mL scintillation vial, (*p*-Tol)$_3$P (3.28 mmol, 1.000 g) was combined with neat (CH$_3$)$_3$Si-N$_3$ (4.85 mmol, 1.136 g) at ambient temperature and generated a slightly opaque colorless solution. The reaction mixture was stirred with a magnetic stir bar while heated to +80 °C for 6.5 hours. The reaction was cooled to ambient temperature, hexanes were added to precipitate product out of solution, and volatiles were removed under vacuum. 1.279 g (98% yield by mass) of **L6** was isolated as white solid. ^{1}H NMR (400 MHz, benzene-d_6, 25.0 °C) δ = 0.43 (s, 9H, NSi(C*H*$_3$)$_3$), 1.99 (s, 9H, *p*-C*H*$_3$), 6.93 (d, $^{3}J_{HH}$ = 7.2 Hz, 6H, *o*-*H*), 7.76 (dd, $^{3}J_{PH}$ = 12.6 Hz, $^{3}J_{HH}$ = 7.5 Hz, 6H, *m*-*H*). ^{31}P{^{1}H} NMR (162 MHz, benzene-d_6, 25.0 °C) δ = -0.63 (s, 1P, N*P*). ^{13}C{^{1}H} NMR (101 MHz, benzene-d_6, 25.0 °C) δ = 4.26 (d, $^{3}J_{PC}$ = 3.4 Hz, NSi(*C*H$_3$)$_3$), 20.89 (d, $^{5}J_{PC}$ = 1.5 Hz, *p*-*C*H$_3$), 133.17 (d, $^{1}J_{PC}$ = 104.3 Hz, P*C*), 128.73 (d, $^{2}J_{PC}$ = 12.3 Hz, *o*-*C*H), 132.15 (d, $^{3}J_{PC}$ = 10.6 Hz, *m*-*C*H), 140.59 (d, $^{4}J_{PC}$ = 2.8 Hz, *p*-*C*CH$_3$).

Synthesis of (CH$_3$)^{t}BuP=NSi(CH$_3$)$_3$ (L7): In a 20 mL scintillation vial, ^{t}Bu$_2$(CH$_3$)P (5.80 mmol, 929 mg) was combined with neat (CH$_3$)$_3$Si-N$_3$ (18.3 mmol, 2.11 g) at ambient temperature and generated a slightly opaque colorless solution. The vial was sealed, and the reaction mixture was stirred with a magnetic stir bar while heated to +80 °C for 7 hours. Any N$_2$ pressure generated in the headspace was released by briefly venting the reaction after 1 hour. The reaction was cooled to ambient temperature and volatiles were removed under vacuum. 1.403 g (98% yield by mass) of **L7** was isolated as an

opaque colorless liquid. ^{1}H NMR (400 MHz, benzene-d_6, 20.0 °C) δ = 0.24 (d, 9H, $^{4}J_{PH}$ = 1.8 Hz, NSi(CH_3)$_3$), 0.91 (d, $^{2}J_{PH}$ = 10.5 Hz, P(C(CH$_3$)$_3$)$_2$CH_3), 1.02 (d, $^{3}J_{PH}$ = 13.6 Hz, P(C(CH_3)$_3$)$_2$CH$_3$). ^{31}P{^{1}H} NMR (162 MHz, benzene-d_6, 20.0 °C) δ = 25.50 (s, 1P, P^{t}Bu$_2$CH$_3$). ^{13}C{^{1}H} NMR (101 MHz, benzene-d_6, 20.0 °C) δ = 4.4 (d, $^{3}J_{PC}$ = 2.3 Hz, NSi(*C*H$_3$)$_3$), 8.59 (d, $^{1}J_{PC}$ = 51.4 Hz, P(C(CH$_3$)$_3$)$_2$*C*H$_3$), 26.55 (s, P(C(*C*H$_3$)$_3$)$_2$CH$_3$), 34.99 (d, $^{3}J_{PC}$ = 67.7 Hz, P(*C*(CH$_3$)$_3$)$_2$CH$_3$).

Synthesis of [(tBu$_3$P=N)$_2$MoOCl$_2$] (2.4): In a 20 mL scintillation vial, ^{t}Bu$_3$P=N–Si(CH$_3$)$_3$ (**L1**) (75.2 mg, 0.260 mmol) and [(DME)MoO$_2$Cl$_2$] (**2.1**) (171 mg, 0.591 mmol) were combined as solids. 8 mL of toluene was added to the vial, which generated a yellow/green suspension at ambient temperature (~21 °C). The vial was capped and the suspension was stirred using a magnetic stir bar and heated at 70 °C for 16 hours. After cooling to room temperature, volatiles were removed under reduced pressure from the yellow/orange suspension, resulting in 361 mg (0.587 mmol, 99% yield) of [(^{t}Bu$_3$P=N)$_2$MoOCl$_2$] (**2.4**) as a yellow powder. Single crystals suitable for X-ray diffraction were obtained from a concentrated solution of benzene-d_6 at ambient temperature. ^{1}H NMR (500 MHz, benzene-d_6, 25.0 °C) δ = 1.44 (d, 54H, $^{3}J_{PH}$ = 13.9 Hz, PC(CH_3)$_3$). ^{31}P{^{1}H} NMR (202 MHz, benzene-d_6, 25.0 °C) δ = 58.64 (s, 2P, *P*C(CH$_3$)$_3$). ^{13}C{^{1}H} NMR (126 MHz, benzene-d_6, 25.0 °C) δ = 29.71 (s, PC(*C*H$_3$)$_3$), 42.73 (d, $^{1}J_{PC}$ = 42.8 Hz, P*C*(CH$_3$)$_3$). Elemental analysis found: C, 46.56; H, 8.66; N, 4.54. C$_{24}$H$_{54}$Cl$_2$MoN$_2$OP$_2$ requires: C, 46.83; H, 8.84; N, 4.55.

Synthesis of [(^{t}Bu$_3$P=N)$_2$Mo(N^{t}Bu)Cl$_2$] (2.5): [(DME)Mo(N^{t}Bu)OCl$_2$] (**2.2**) (144.9 mg, 0.421 mmol) was transferred with 10 mL of toluene into a 20 mL scintillation vial containing ^{t}Bu$_3$P=N–Si(CH$_3$)$_3$ (**L1**) (243.5 mg, 0.841 mmol) as a solid, which generated a dark brown/orange suspension at ambient temperature (~21 °C). The vial was capped and the suspension stirred using a magnetic stir bar and heated at +90 °C for 21 hours. After cooling to room temperature, volatiles were removed under reduced pressure from the dark red/orange transparent solution, resulting in 275.0 mg (0.410 mmol, 97% yield) of [(^{t}Bu$_3$P=N)$_2$Mo(N^{t}Bu)Cl$_2$] (**2.5**) as an orange powder. Single crystals suitable for X-ray diffraction analysis were obtained from a concentrated solution of pentane and DCM (1:3) at -30 °C. ^{1}H NMR (400 MHz, benzene-d_6, 20.0 °C) δ = 1.50 (d, 54H, $^3J_{PH}$ = 13.4 Hz, PC(CH_3)$_3$), 1.69 (s, 9H, MoN(C(CH_3)$_3$)). ^{31}P{^{1}H} NMR (162 MHz, benzene-d_6, 20.0 °C) δ = 52.40 (s, 2P, *P*C(CH$_3$)$_3$). ^{13}C{^{1}H} NMR (101 MHz, benzene-d_6, 20.0 °C) δ = 29.98 (s, PC(*C*H$_3$)$_3$), 42.13 (d, $^1J_{PC}$ = 44.4 Hz, P*C*(CH$_3$)$_3$).

Synthesis of [(Cy$_3$P=N)$_2$MoOCl$_2$] (2.6): [Cy$_3$P=N–Si(CH$_3$)$_3$] (**L4**) (249.1 mg, 0.678 mmol) was transferred with 10 mL of toluene into a 20 mL scintillation vial containing [(DME)MoO$_2$Cl$_2$] (**2.1**) (97.3 mg, 0.337 mmol) as a solid, which generated a light green suspension at ambient temperature (~21 °C). The vial was capped and the suspension stirred using a magnetic stir bar and heated at 85 °C for 23 hours. After cooling to room temperature, volatiles were removed under reduced pressure from the red/orange suspension, resulting in 257.8 mg

(0.334 mmol, 99% yield) of [($Cy_3P{=}N)_2MoOCl_2$] **2.6** as a pale orange solid. ^{1}H NMR (400 MHz, benzene-d_6, 25.0 °C)δ = ($P(C_6H_{11})_3$) 1.11, 1.50, 1.65, 2.08, 2.61, 3.26. $^{31}P\{^1H\}$ NMR (162 MHz, benzene-d_6, 25.0 °C)δ = 42.32 (s, 1P, $PC(CH_3)_3$), 65.56 (s, 1P, $PC(CH_3)_3$).

Synthesis of [($Ph_3P{=}N)_2MoOCl_2$] (2.7): In a 20 mL scintillation vial, [(DME)MoO_2Cl_2] (**2.1**) (106.0 mg, 0.367 mmol) was suspended in 5 mL of toluene, and $Ph_3P{=}N{-}Si(CH_3)_3$ (**L5**) (256.4 mg, 0.734 mmol) was transferred into the vial with 5 mL of toluene, which generated a green/blue suspension at ambient temperature (~21 °C). The vial was capped and the suspension was stirred using a magnetic stir bar and heated at 90 °C for 18 hours. After cooling to room temperature, volatiles were removed under reduced pressure from the orange suspension, resulting in 255.2 mg (0.347 mmol, 95% yield) of [($Ph_3P{=}N)_2MoOCl_2$] (**2.7**) as a pale yellow solid. ^{1}H NMR (400 MHz, benzene-d_6, 20.0 °C)δ = 6.99 (m, 24H, $P(C_6H_5)_3$), 7.87 (m, 6H, $P(C_6H_5)_3$). $^{31}P\{^1H\}$ NMR (162 MHz, benzene-d_6, 20.0 °C)δ = 32.48 (s, 2P, $P(C_6H_5)_3$).

Synthesis of [(*p*-$Tol_3P{=}N)_2MoOCl_2$] (2.8): In a 20 mL scintillation vial, *p*-$Tol_3P{=}N{-}Si(CH_3)_3$ (**L6**) (258 mg, 0.659 mmol) was dissolved in 5 mL of toluene. A 5 mL toluene suspension of [(DME)MoO_2Cl_2] (**2.1**) (95 mg, 0.329 mmol) was added to the **L6** solution, generating a dark green solution at ambient temperature (~21 °C). The vial was capped and the solution was stirred using a magnetic stir bar and heated at 90 °C for 72 hours. After cooling to room

temperature, volatiles were removed under reduced pressure from the orange/red suspension, providing 242 mg (0.295 mmol, 90% yield) of [(*p*-$Tol_3P{=}N)_2MoOCl_2$] (**2.8**) as a pale tan/orange solid. ^{1}H NMR (400 MHz, chloroform-*d*, 15.0 °C δ = 2.37 (s, 9H, $P((C_6H_4)CH_3)_3$), 2.38 (s, 9H, $P((C_6H_4)CH_3)_3$), 7.26 (m, 12H, $P((C_6H_4)CH_3)_3$), 7.63 (dd, $^3J_{PH}$ = 12.4 Hz, $^3J_{HH}$ = 8.1 Hz, 6H, $P((C_6H_4)CH_3)_3$), 7.71 (b, 6H, $P((C_6H_4)CH_3)_3$). $^{31}P\{^1H\}$ NMR (162 MHz, chloroform-*d*, 15.0 °C) δ = 34.19 (s, 1P, $P((C_6H_4)CH_3)_3$), 43.67 (s, 1P, $P((C_6H_4)CH_3)_3$).

Synthesis of [$((CH_3)^tBu_2P{=}N)_2MoOCl_2$] (2.9): In a 20 mL scintillation vial, [$(DME)MoO_2Cl_2$] (**2.1**) (100 mg, 0.346 mmol) was suspended in 1 mL of toluene, and $(CH_3)^tBuP{=}N{-}Si(CH_3)_3$ (**L7**) (171 mg, 0.691 mmol) was transferred into the vial with 3 mL of toluene, which generated a yellow/green suspension at ambient temperature (~21 °C). The vial was capped and the suspension was stirred using a magnetic stir bar and heated at 80 °C for 20 hours. After cooling to room temperature, volatiles were removed under reduced pressure from the orange suspension, resulting in 163 mg (0.307 mmol, 89% yield) of [$((CH_3)^tBu_2P{=}N)_2MoOCl_2$] (**2.9**) as a pale yellow solid. ^{1}H NMR (400 MHz, benzene-d_6, 20.0 °C) δ = 1.05 (d, 18H, $^3J_{PH}$ = 14.8 Hz, $P(C(CH_3)_3)_2CH_3$), 1.09 (d, 18H, $^3J_{PH}$ = 14.7 Hz, $P(C(CH_3)_3)_2CH_3$), 1.40 (d, 3H, $^3J_{PH}$ = 11.1 Hz, $P(C(CH_3)_3)_2CH_3$), 1.96 (d, 3H, $^3J_{PH}$ = 10.6 Hz, $P(C(CH_3)_3)_2CH_3$). $^{31}P\{^1H\}$ NMR (162 MHz, benzene-d_6, 20.0 °C) δ = 58.03 (s, 1P, $P^tBu_2CH_3$), 77.59 (s, 1P, $P^tBu_2CH_3$). $^{13}C\{^1H\}$ NMR (101 MHz, benzene-d_6, 20.0 °C) δ = 0.59 (d, $^1J_{PC}$ =

50.7 Hz, P(C(CH_3)$_3$)$_2$*C*H$_3$), 5.59 (d, $^1J_{PC}$ = 58.1 Hz, P(C(CH_3)$_3$)$_2$*C*H$_3$), 26.08 (s, P(C(*C*H$_3$)$_3$)$_2$CH$_3$), 26.41 (s, P(C(*C*H$_3$)$_3$)$_2$CH$_3$), 35.37 (d, $^3J_{PC}$ = 61.8 Hz, P(*C*(CH$_3$)$_3$)$_2$CH$_3$), 36.28 (d, $^3J_{PC}$ = 57.4 Hz, P(*C*(CH$_3$)$_3$)$_2$CH$_3$). ^{1}H-^{31}P gHMBC NMR (benzene-d_6, 20.0 °C) [(^{1}H, 400 MHz), (^{31}P, 162 MHz)] δ = [1.05, 58.0] (d, *P*(C(*C*H$_3$)$_3$)$_2$CH$_3$), [1.95, 58.0] (d, *P*^{t}Bu$_2$C*H*$_3$), [1.09, 77.5] (d, *P*(C(*C*H$_3$)$_3$)$_2$CH$_3$), [1.39, 77.5] (d, *P*^{t}Bu$_2$C*H*$_3$). The ^{1}H-^{31}P gHMBC NMR experiment used a ^{1}H spectral window of 1000.0 Hz, centered at 1.10 ppm, with a 0.256 s acquisition time (256 data points), and a 1.097 s relaxation delay; a ^{31}P spectral window of 6474.6 Hz, centered at 70.05 ppm; and 4 scans per time increment, 512 time increments, a J_{nxh} of 12 Hz, and non-uniform sampling density of 50%.

Synthesis of [(^{t}Bu$_3$P=N)$_2$Mo(O)(N^{t}Bu)] (2.10): ^{t}Bu$_3$P=NH (**L2**) (0.32 mmol, 70 mg) was dissolved in ~10 mL of THF and was then cooled thoroughly in a LN_2 cooled cold well. While stirring and warming to ambient temperature, a methyl lithium solution (0.33 mmol, 0.21 mL) was added dropwise. The solution rapidly clarifies to give a colorless transparent solution, along with generation of gas bubbles. After one hour, the solution was cooled thoroughly in a cold well. A dark green THF solution of the molybdenum starting material [(DME)Mo(N^{t}Bu)OCl$_2$] (**2.2**) (0.16 mmol, 55 mg) was added slowly to the lithium salt solution. The resulting solution rapidly changed from opaque white to brown/yellow. After 13 hours, the solution was transparent gold in color, and solvent was removed under vacuum. The solid residue was dissolved in hexane and filtered through Celite to remove salt byproducts. A pale yellow/orange oil

was isolated from the filtrate (81 mg, 83% yield). Transparent tan crystals for XRD analysis were generated out of a slowly evaporating hexane solution at –20 °C. ^{1}H NMR (500 MHz, benzene-d_6, 25.0 °C) δ = 1.36 (d, 54H, $^{3}J_{PH}$ = 12.8 Hz, PC(CH_3)$_3$), 1.73 (s, 9H, MoN(C(CH_3)$_3$)). ^{31}P{^{1}H} NMR (202 MHz, benzene-d_6, 25.0 °C) δ = 44.82 (s, 2P, *P*C(CH$_3$)$_3$). ^{13}C{^{1}H} NMR (126 MHz, benzene-d_6, 30.0 °C) δ = 29.65 (s, PC(*C*H$_3$)$_3$), 32.44 (s, MoN(C(*C*H$_3$)$_3$)), 41.41 (d, $^{1}J_{PC}$ = 47.8 Hz, P*C*(CH$_3$)$_3$), 66.33 (s, MoN(*C*(CH$_3$)$_3$)). Elemental analysis found: C, 54.58; H, 10.41; N, 6.60. $C_{28}H_{63}MoN_3OP_2$ requires: C, 54.62; H, 10.31; N, 6.82.

Synthesis of [(^{t}Bu$_3$P=N)$_2$Mo(N^{t}Bu)$_2$] (2.11): ^{t}Bu$_3$P=NH (**L2**) (1.00 mmol, 217.6 mg) was dissolved in ~10 mL of THF and cooled thoroughly in a LN_2 cold well. While stirring and warming to ambient temperature, methyl lithium solution (1.02 mmol, 0.64 mL) was added dropwise. The solution rapidly clarified to give a colorless transparent solution, and generate gas bubbles. After one hour, solvent was removed under vacuum. The resulting white material was dissolved in ~10 mL of THF and then cooled in a cold well. In a second flask, a transparent yellow THF solution of the molybdenum starting material [(DME)Mo(N^{t}Bu$_2$)$_2$Cl$_2$] (**2.3**) (0.50 mmol, 199.5 mg) was cooled in a cold well. The *in situ* generated lithium salt suspension was added slowly to molybdenum starting material solution while warming. After 30 minutes, the solution slowly changes to a transparent golden yellow color. After 14 hours, the solvent was removed under vacuum. The resulting material was dissolved in hexane and filtered through Celite to remove salt byproducts. The solvent was then

removed from the filtrate (281 mg, 84% yield). Transparent tan crystals for XRD analysis were generated out of a slowly evaporating diethyl ether solution at –20 °C. ^{1}H NMR (400 MHz, benzene-d_6, 20.0 °C) δ = 1.41 (d, 54H, $^{3}J_{PH}$ = 12.5 Hz, PC(CH_3)$_3$), 1.65 (s, 18H, MoN(C(CH_3)$_3$)). ^{31}P{^{1}H} NMR (162 MHz, benzene-d_6, 20.0 °C) δ = 40.61 (s, 2P, *P*C(CH$_3$)$_3$). ^{13}C{^{1}H} NMR (101 MHz, benzene-d_6, 25.0 °C) δ = 29.65 (s, PC(*C*H$_3$)$_3$), 32.44 (s, MoN(*C*(CH$_3$)$_3$)), 41.41 (d, $^{1}J_{PC}$ = 47.8 Hz, P*C*(CH$_3$)$_3$), 65.01 (s, MoN(*C*(CH$_3$)$_3$)). Elemental analysis found: C, 57.17; H, 10.63; N, 7.60. $C_{32}H_{72}MoN_4P_2$ requires: C, 57.29; H, 10.82; N, 8.35.

Synthesis of (^{t}Bu$_3$P=N)$_2$Mo(O)$_2$ (2.12): A light orange suspension of $MoO_2(acac)_2$ (**2.13**) (0.23 mmol, 75 mg) in 1 mL of THF was cooled to -20 °C and was added to a colorless transparent 3 mL THF solution of ^{t}Bu$_3$P=NH (**L2**) (0.46 mmol, 99 mg) at -30 °C. The reaction solution rapidly darkened to opaque red while stirring and warming to ambient temperature. After 1.5 hours, solvent and volatiles were removed under vacuum from the orange/red solution. After drying under vacuum, 152 mg of (^{t}Bu$_3$P=N)$_2$Mo(O)$_2$ **(2.12)** was isolated as a light orange solid (128 mg, quantitative). ^{1}H NMR (400 MHz, chloroform-*d*, 25.0 °C) δ = 1.49 (d, 54H, $^{3}J_{PH}$ = 13.3 Hz, PC(CH_3)$_3$). ^{31}P{^{1}H} NMR (162 MHz, chloroform-*d*, 25.0 °C) δ = 51.98 (s, 2P, *P*C(CH$_3$)$_3$). No ^{13}C NMR data was obtained due to poor solubility. Elemental analysis found: C, 51.95; H, 9.58; N, 4.55. $C_{24}H_{54}MoN_2O_2P_2$ requires: C, 51.42; H, 9.71; N, 5.00.

2.6 References

1. K. Dehnicke and J. Strähle, *Polyhedron*, 1989, **8**, 707–726.
2. K. Dehnicke, M. Krieger and W. Massa, *Coord. Chem. Rev.*, 1999, **182**, 19–65.
3. D. W. Stephan, J. C. Stewart, F. Guérin, R. E. v. H. Spence, W. Xu and D. G. Harrison, *Organometallics*, 1999, **18**, 1116–1118.
4. D. W. Stephan, J. C. Stewart, S. Courtenay, J. Kickham, E. Hollink, C. Beddie, A. Hoskin, T. Graham, P. Wei, R. E. H. Spence, W. Xu, L. Koch, X. Gao and D. G. Harrison, 2003, 1937–1947.
5. D. W. Stephan, *Organometallics*, 2005, 2548–2560.
6. M. C. Baier, M. A. Zuideveld and S. Mecking, *Angew. Chem. Int. Ed.*, 2014, **53**, 9722–9744.
7. D. Nußhär, F. Weller and K. Dehnicke, *Z. Anorg. Allg. Chem.*, 1993, **619**, 507–512.
8. M. Rhiel, S. Wocadlo, W. Massa and K. Dehnicke, *Z. Naturforschung*, 1996, **51b**, 1419–1422.
9. A. Dietrich, B. Neumüller and K. Dehnicke, *Z. Anorg. Allg. Chem.*, 1998, **624**, 1247–1249.
10. A. Dietrich, B. Neumüller and K. Dehnicke, *Z. Anorg. Allg. Chem.*, 2000, 1837–1844.
11. A. Dietrich, B. Neumüller and K. Dehnicke, *Z. Anorg. Allg. Chem.*, 1999, 1321–1326.
12. W. Wolfsberger, *Z. Naturforschung*, 1978, **33b**, 1452–1456.

13. B. Ross and K.-P. Reetz, *Chem. Ber.*, 1979, **112**, 1756–1762.
14. S. Courtenay, P. Wei and D. W. Stephan, *Can. J. Chem.*, 2003, **81**, 1471–1476.
15. J. M. Mayer, *Inorg. Chem.*, 1988, **27**, 3899–3903.
16. T. A. Hanna, A. K. Ghosh, C. Ibarra, L. N. Zakharov, A. L. Rheingold and W. H. Watson, *Inorg. Chem.*, 2004, **43**, 7567–7569.
17. B. S. Lim, M. W. Willer, M. Miao and R. H. Holm, *J. Am. Chem. Soc.*, 2001, **123**, 8343–8349.
18. V. V. Trachevsky, A. I. Brusilovets, I. V. Korendovich, V. G. Bdzhola and I. G. Ryabokon, *Ukr.Khim.Zh*, 2002, **68**, 14.
19. E. Carmona, A. Galindo, C. Guille-Photin, R. Lai, A. Monge, C. Ruiz and L. Sanchez, *Inorg. Chem.*, 1988, **27**, 488–492.
20. O. A. Azizkulova and A. A. Amindzhanov, *Zhurnal Neorganicheskoi Khimii*, 2001, **46**, 444–448.
21. R. A. Eikey and M. M. Abu-Omar, *Coord. Chem. Rev.*, 2003, 42.
22. H. Bock and H. Tom Dieck, *Z. Anorg. Allg. Chem.*, 1966, **345**, 9–22.
23. H. Bock and H. T. Dieck, *Z. Naturforschung*, 1966, **21b**, 739–746.
24. R. E. Cramer, S. Roth and J. W. Gilje, *Organometallics*, 1989, **8**, 2327–2330.
25. M. J. Sarsfield, I. May, S. M. Cornet and M. Helliwell, *Inorg. Chem.*, 2005, **44**, 7310–7312.
26. L. J. L. Häller, N. Kaltsoyannis, M. J. Sarsfield, I. May, S. M. Cornet, M. P. Redmond and M. Helliwell, *Inorg. Chem.*, 2007, **46**, 4868–4875.

27. M. P. Redmond, S. M. Cornet, S. D. Woodall, D. Whittaker, D. Collison, M. Helliwell and L. S. Natrajan, *Dalton Trans.*, 2011, **40**, 3914.
28. R. K. Harris, E. D. Becker, S. M. Cabral de Menezes, R. Goodfellow and P. Granger, *Pure Appl. Chem.*, 2001, **73**, 1795–1818.
29. R. K. Harris, E. D. Becker, S. M. Cabral de Menezes, P. Granger, R. E. Hoffman and K. W. Zilm, *Pure Appl. Chem.*, 2008, **80**, 59–84.
30. G. M. Sheldrick, *Acta Crystallogr. Sect. A*, 2015, **71**, 3–8.
31. G. M. Sheldrick, *Acta Crystallogr. Sect. C*, 2015, **71**, 3–8.
32. L. Krause, R. Herbst-Irmer, G. M. Sheldrick and D. Stalke, *J. Appl. Crystallogr.*, 2015, **48**, 3–10.
33. K. A. Rufanov, D. N. Zarubin, N. A. Ustynyuk, D. N. Gourevitch, J. Sundermeyer, A. V. Churakov and J. A. K. Howard, *Polyhedron*, 2001, **20**, 379–385.
34. S. Courtenay, C. M. Ong and D. W. Stephan, *Organometallics*, 2003, **22**, 818–825.
35. I. Ghesner, A. Fenwick and D. W. Stephan, *Organometallics*, 2006, **25**, 4985–4995.

3 Metal-Carbon Bond Containing Complex Synthesis and Reactivity

3.1 Introduction

Alkylidene complexes of the group 6 metals are highly effective catalysts for olefin metathesis reactivity, including cross-metathesis, ring-opening metathesis polymerization (ROMP) and ring-closing metathesis (RCM) applications.[1] The earliest group 6 alkylidene complexes generated were oxido-alkylidene tungsten complexes,[2–5] yet most subsequent alkylidene research in this area has focused on imido-alkylidene complexes.[1] The presence of an imido ligand allows for steric and electronic tuning of the catalysts, and helps prevent catalyst deactivation through dimerization by providing greater steric protection. A renewed interest in the study of oxido-alkylidene species has been seen recently, as these complexes are postulated to be the active moieties in heterogeneous surface-supported W catalysts.[6–8] A recent study by Trunschke and coworkers evaluated Mo oxide dispersed on the surface of mesoporous silica for catalytic olefin metathesis, and it was shown through IR spectroscopy that surface-bound Mo(VI) oxido-alkylidene species are generated *in situ* for catalytic cross-metathesis reactions.[9]

Despite the importance of Mo oxido-alkylidene complexes in such metathesis processes, they have not been widely studied. Prior to this research, the only Mo oxido-alkylidene complex (**A**) to be characterized is the

phosphonium adduct shown in (Fig. 3.1), which is in resonance with a σ-vinyl species (**B**).[10,11] The alkylidene fragment in this complex is formed through alkyne insertion into a Mo-P bond, while the oxido ligand is likely derived from hydrolysis by adventitious water.

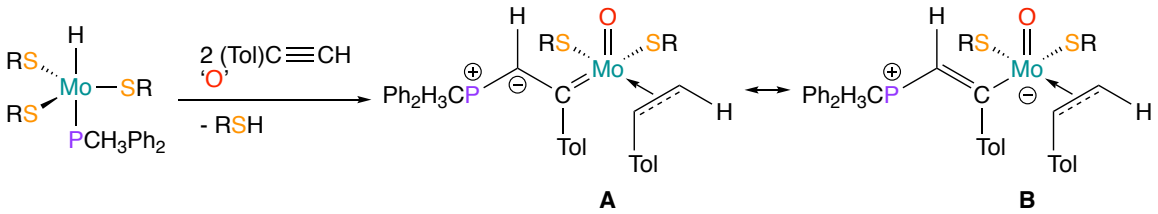

Figure 3.1: First reported molecular molybdenum oxido-alkylidene complex

Unlike imido-alkylidene species that are typically prepared through salt metathesis with a "universal starting material," such as [(DME)Mo(=CH(CH_3)$_3$)(NAr)(OTf)$_2$],[12] analogous established routes to oxido-alkylidene complexes of Mo do not exist. The Schrock group has reported a general synthesis of W oxido-alkylidene species of the type $L_2W(=CH(CH_3)_3)(O)Cl_2$ (L = phosphine) through ligand exchange with a Ta alkylidene derivative[13] (Fig. 3.2), and have since reported a more convenient approach using a W dioxido dialkyl precursor[5] (Fig.3.3), but a comparable synthesis on Mo is not known.

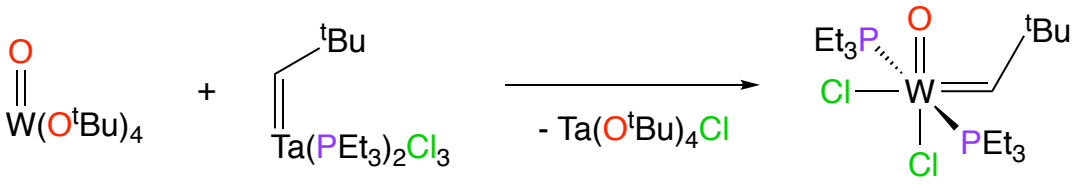

Figure 3.2: Synthesis of tungsten oxido-alkylidene through ligand exchange

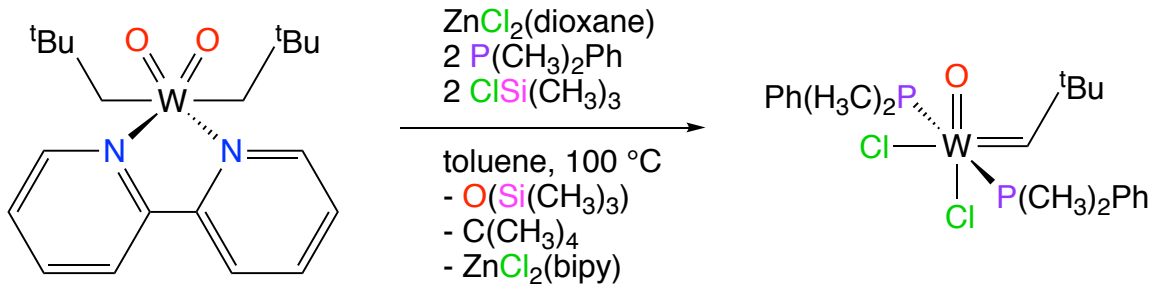

Figure 3.3: Synthesis of tungsten oxido-alkylidene from dioxido precursor

In Chapter 2, it was shown that phosphinimide ligands could be used to support both oxygen and nitrogen-metal multiple bonds in the form of oxido and imido ligands on molybdenum centers. Given these encouraging results and the importance of group 6 alkylidene complexes, the phosphinimide ligand platform was examined as a supporting ancillary framework for supporting metal-carbon multiple bonds.

3.2 Results and Discussion

Alkylidene complexes are conventionally synthesized by time-consuming and atom-inefficient processes, which require multiple synthetic steps and a significant number of atoms lost as byproducts (Fig. 3.4).[1] Here, generation of the imido alkylidene species is accomplished through salt metathesis to form a

bis(alkyl) species (**C**), which then undergoes protonolysis chemistry with triflic acid to produce the imido-alkylidene complex (**D**), liberating both an alkane, and an ammonium salt in the process. In effect, one of the imido ligands acts as a sacrificial proton acceptor. The laborious synthesis of related derivatives of these imido-alkylidene complexes represents the current state of the art in terms of group VI metathesis catalysts. As such, a more atom-economic process involving less waste would be beneficial.

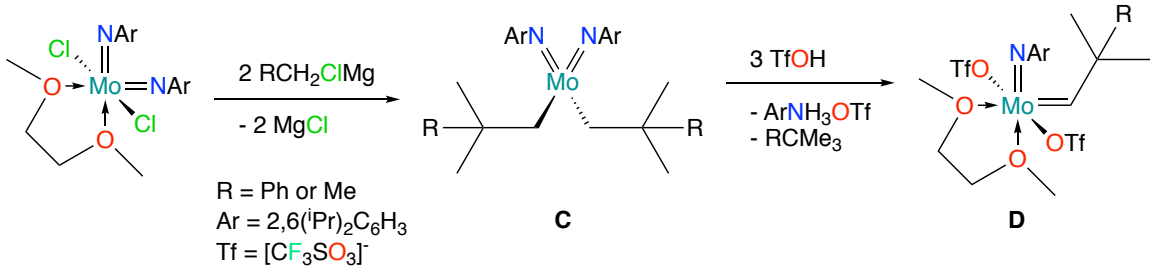

Figure 3.4: Conventional synthesis of imido-alkylidene molybdenum complexes

The syntheses of (^{t}Bu$_3$P=N)$_2$Mo(O)Cl$_2$ (**2.4**) and (^{t}Bu$_3$P=N)$_2$Mo(N^{t}Bu)Cl$_2$ (**2.5**) described in Chapter 2 provide a new platform for the synthesis of alkylidene complexes through a more efficient process. These complexes each incorporate two chlorido ligands, which are ideal functionalities for further salt metathesis reactivity.

Alkylidene fragments have been previously introduced by methods that involve salt metathesis reactions. These reactions generate intermediate polyalkyl complexes, which can undergo thermal α-hydrogen abstraction that can either occur spontaneously (Fig. 3.5), or can be promoted through steric

pressure introduced by a coordinating ligand (Fig. 3.6), resulting in formation of an alkylidene fragment and elimination of one equivalent of alkane.[1]

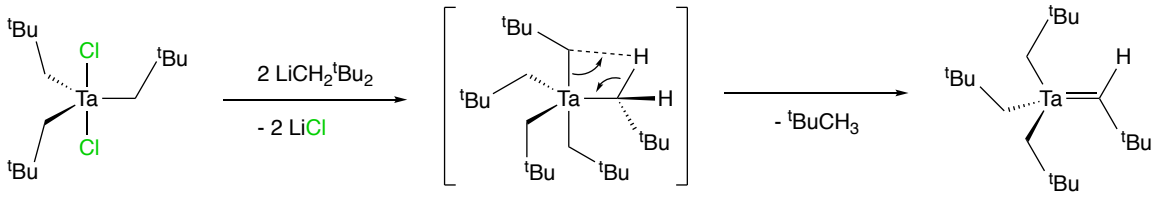

Figure 3.5: Generation of the first high-oxidation state alkylidene complex by α-hydrogen abstraction

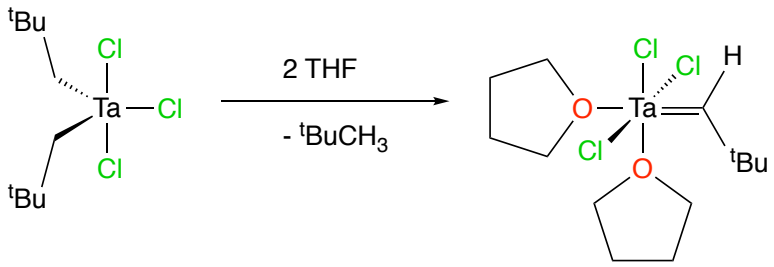

Figure 3.6: Generation of an alkylidene complex by α-hydrogen abstraction induced by coordination of tetrahydrofuran

3.2.1 Oxido-Alkylidene Complex

In a fashion analogous to that shown in Fig 3.7, two equiv. of $LiCH_2Si(CH_3)_3$ can be combined with **2.4** at low temperature to generate a transient bis(neosilyl) complex. While this reactive intermediate was not isolated, it is presumed to form based on reaction precedent[1] and ^1H NMR spectroscopic evidence. At room temperature, the bisalkyl complex converts cleanly into the red oxido-alkylidene complex $[(tBu_3P{=}N)_2Mo(O)(=CHSi(CH_3)_3)]$ (**3.1**).

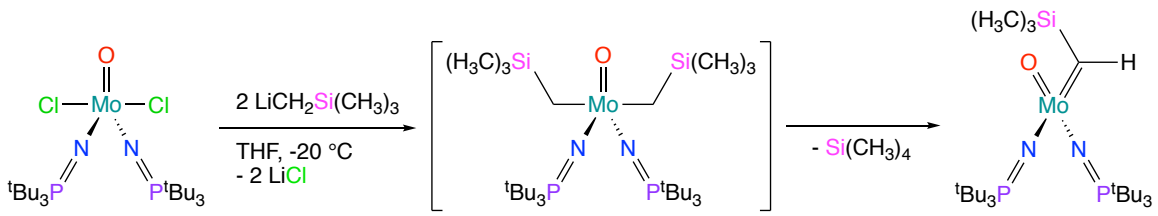

Figure 3.7: Synthesis of **3.1** by salt metathesis and alkane elimination

Complex **3.1** has been characterized by NMR spectroscopy, XRD, and EA. Based on the XRD structure, **3.1** is pseudo C_s symmetric with a plane of symmetry that contains the O-Mo-C fragment, and exhibits a pseudo-tetrahedral core around the molybdenum atom, with a τ'_4 value of 0.94 (Fig. 3.8).

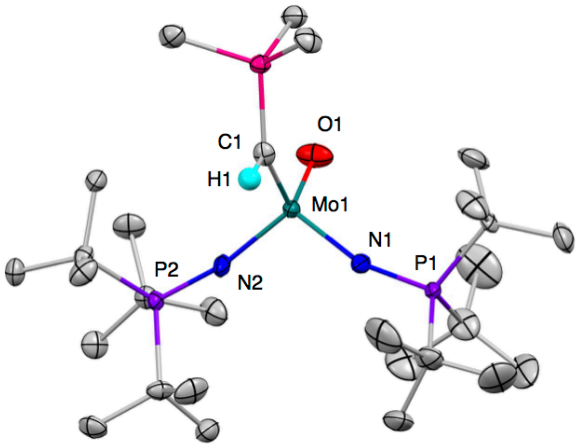

Figure 3.8: Thermal ellipsoid plot (50% probability) of complex **3.1**; non-alkylidene hydrogen atoms have been omitted for clarity

Visualization of the space-filling model of **3.1**, derived from the XRD structure, reveals highly exposed alkylidene and oxido fragments (Fig. 3.9), with significant access to the molybdenum center.

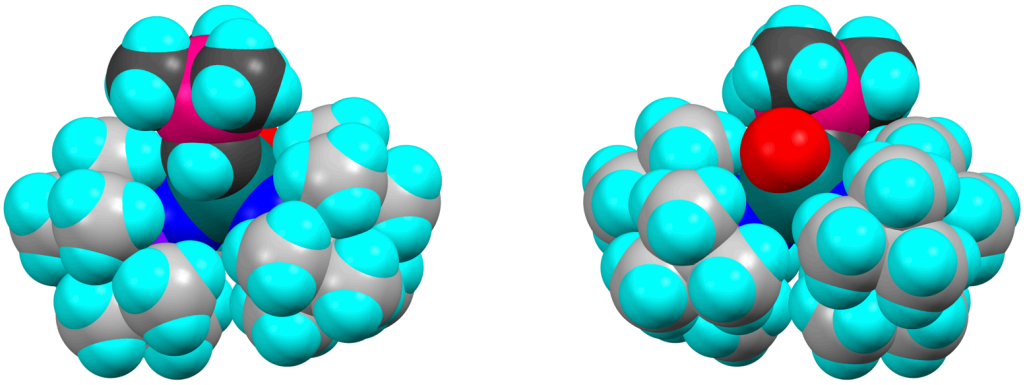

Figure 3.9: Space-filling model of complex **3.1** focused on alkylidene ligand (left), focused on oxido-ligand (right), alkylidene carbon atoms indicated in dark grey

The molybdenum-oxido bond length (Table 3.1) is within the distribution of previously reported Mo(VI) mono-oxido fragments, and is slightly longer (+0.026 Å) than the average of this distribution.[14] This bond length is more comparable to Mo(VI) *cis*-dioxido fragments, given the presence of a *cis*-alkylidene fragment, and the oxido ligand in this complex exhibits a negligible difference from the average value for *cis*-dioxido species (-0.004 Å).

Comparison of the metrical parameters for **3.1** with the oxido-imido complex **2.10** reveals a shorter oxido-molybdenum bond length for **3.1** (-0.033 Å). This difference is reasonable since the alkylidene carbon atom is less

electronegative than the nitrogen of the imido ligand, resulting in a weaker bond with less ionic character. This is compensated for by the increased bond strength of the oxido ligand in **3.1**.

Table 3.1: Selected XRD Bond Distances for Complex **3.1**

Atoms	**Length (Å)**	**Atoms**	**Length (Å)**
Mo1-C1	1.920(5)	C1-Si1	1.832(5)
Mo1-O1	1.700(4)	P1-N1	1.560(4)
Mo1-N1	1.887(4)	P2-N2	1.563(4)
Mo1-N2	1.877(4)	-	-

The bond angles (Table 3.2) at each of the phosphinimide nitrogen atoms are both relatively linear (greater than 158°). Comparison of **3.1** with **2.10** reveals a larger bond angle difference between the ligands in **3.1**, varying across a range of 11°, while the ligands in **2.10** vary by less than 3°. This difference between ligand bonding angles in **3.1** indicates ligand asymmetry, at least in the solid state, as has been observed with complexes with less bulky phosphinimide substituents described in Chapter 2. The average phosphinimide bond angles for **3.1** (163.55°) compared with those for **2.10** (163.80°) indicate a negligible difference of less than 1 degree.

Table 3.2: Selected XRD Bond Angles for Complex **3.1**

Atoms	Angle (°)	Atoms	Angle (°)
Mo1-N1-P1	158.0(3)	N1-Mo1-N2	106.57(18)
Mo1-N2-P2	169.1(3)	O1-Mo1-C1	105.29(18)
O1-Mo1-N1	113.9(2)	Si1-C1-Mo1	134.7(3)
O1-Mo1-N2	113.89(19)	-	-

The torsion angles of **3.1** (Table 3.3) indicate that the phosphinimide ligands are oriented in different directions relative to the oxido ligand. While the phosphinimide containing N2 and P2 is oriented almost orthogonal to the oxido ligand, the linearity of the Mo-N2-P2 bond makes the impact of this torsion angle negligible on the overall structure. The phosphinimide ligand containing the N1-P1 bond is less linear and points more towards the oxido ligand, perhaps a consequence of reduced steric bulk in that area of the molecule.

The alkylidene ligand is oriented in the *syn* configuration, where the oxido ligand and the $Si(CH_3)_3$ group of the ligand are on the same side of the M=C bond, with an almost perfectly aligned torsion angle of -0.73°. This geometry is likely driven by the lower steric bulk around the oxido ligand, as the *trans* isomer would have greater steric interactions with the bulky phosphinimide ligands. Studies have also suggested an electronic component for the greater stability of the *syn* configuration due to an agostic interaction between the alkylidene C-H bond and the metal center.[1,15]

Table 3.3: Selected XRD Torsion Angles for Complex **3.1**

Atoms	Angle (°)	Atoms	Angle (°)
O1-Mo1-N1-P1	7.0(8)	N1-Mo1-N2-P2	163.5(17)
O1-Mo1-N2-P2	-70.1(18)	N2-Mo1-N1-P1	133.4(8)
O1-Mo1-C1-Si1	-0.7(4)	-	-

Analysis of **3.1** by ^{1}H NMR spectroscopy (Fig.3.10) reveals diagnostic resonances for all protons within the structure, including a higher field singlet at 0.67 ppm for the trimethylsilyl fragment and a ^{31}P-coupled doublet at 1.31 for the phosphinimide protons, which is comparable to other compounds with this ligand, as discussed in Chapter 2. The alkylidene proton is identified as the resonance at a much higher chemical shift of 10.33 ppm.

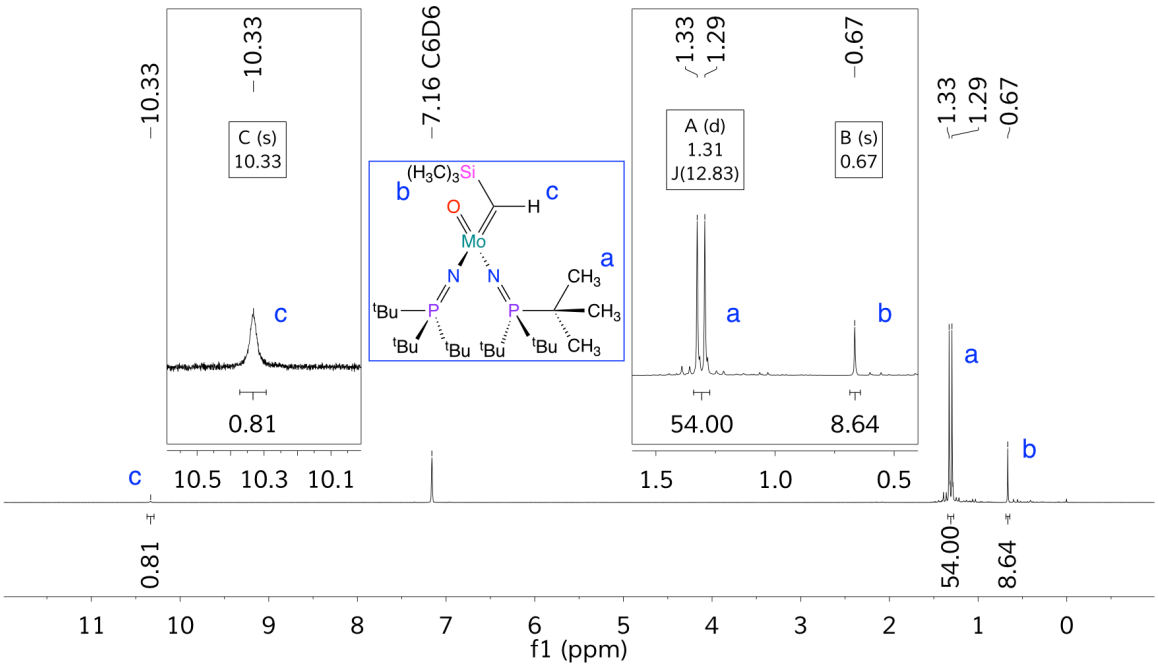

Figure 3.10: ^{1}H NMR spectrum of **3.1** in C_6D_6 (400 MHz)

The $^{31}P\{^{1}H\}$ NMR spectrum of **3.1** (Fig. 3.11) contains a singlet at 46.62 ppm, which indicates formation of a single product with chemically equivalent phosphinimide ligands when in solution.

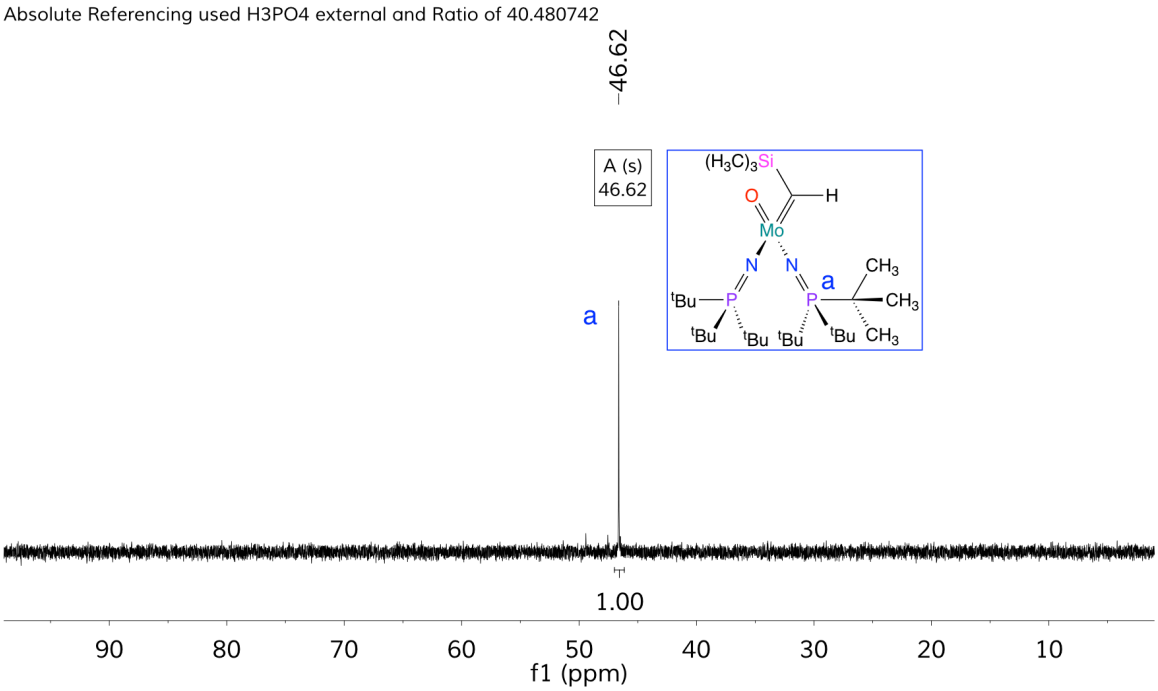

Figure 3.11: $^{31}P\{^{1}H\}$ NMR spectrum of **3.1** in C_6D_6 (162 MHz)

The $^{13}C\{^{1}H\}$ NMR spectrum of **3.1** (Fig. 3.12) exhibits all expected resonances except for the alkylidene carbon. The higher field trimethylsilyl singlet appears at 2.86 ppm, with the primary *tert*-butyl carbons at 29.57, and the expected ^{31}P-coupled doublet for the quaternary *tert*-butyl carbons at 41.77 ppm.

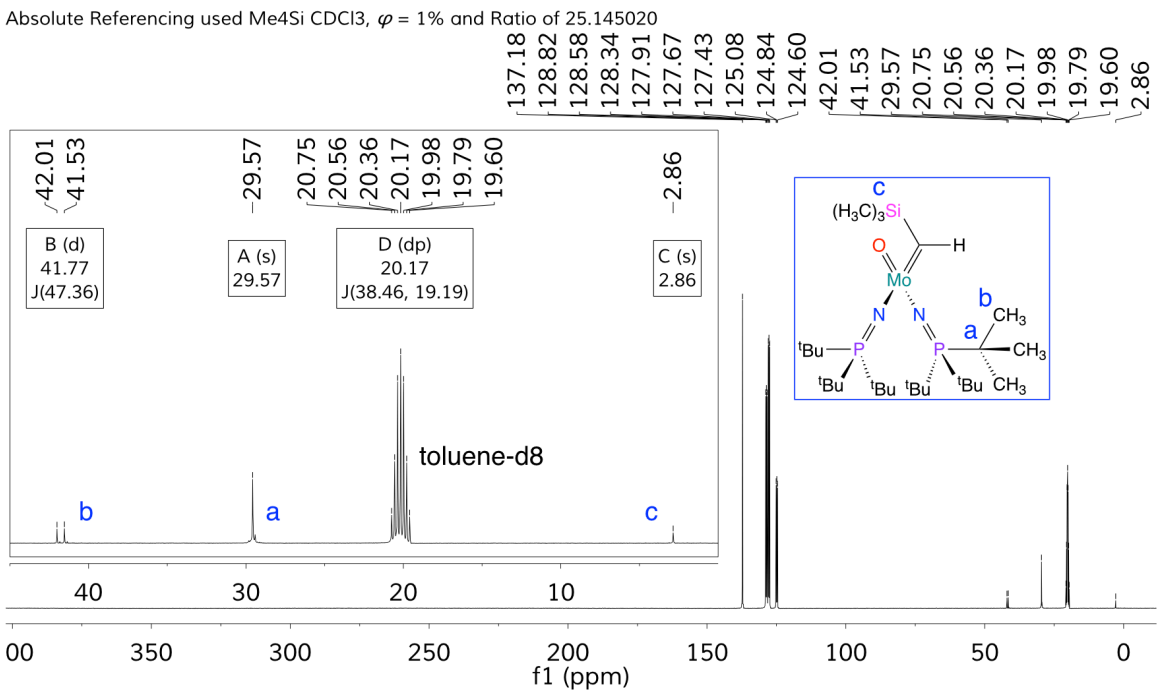

Figure 3.12: $^{13}C\{^{1}H\}$ NMR spectrum of **3.1** in toluene-d_8 (101 MHz)

The alkylidene carbon could not be resolved by 1-dimensional NMR even with a high sample concentration, decreased temperature, increased number of scans (2384), and an increased relaxation delay of 30 seconds. As such, alternative 2D NMR techniques were performed. Use of a 2D ^{1}H-$\{^{13}C\}$ band-selected heteronuclear single quantum coherence (HSQC) NMR experiment with adiabatic pulses enabled measurement of the alkylidene carbon signal (Fig. 3.13). The resonance is observed at 213.4 ppm, which is within the expected range for this type of ligand fragment.[12,16,17]

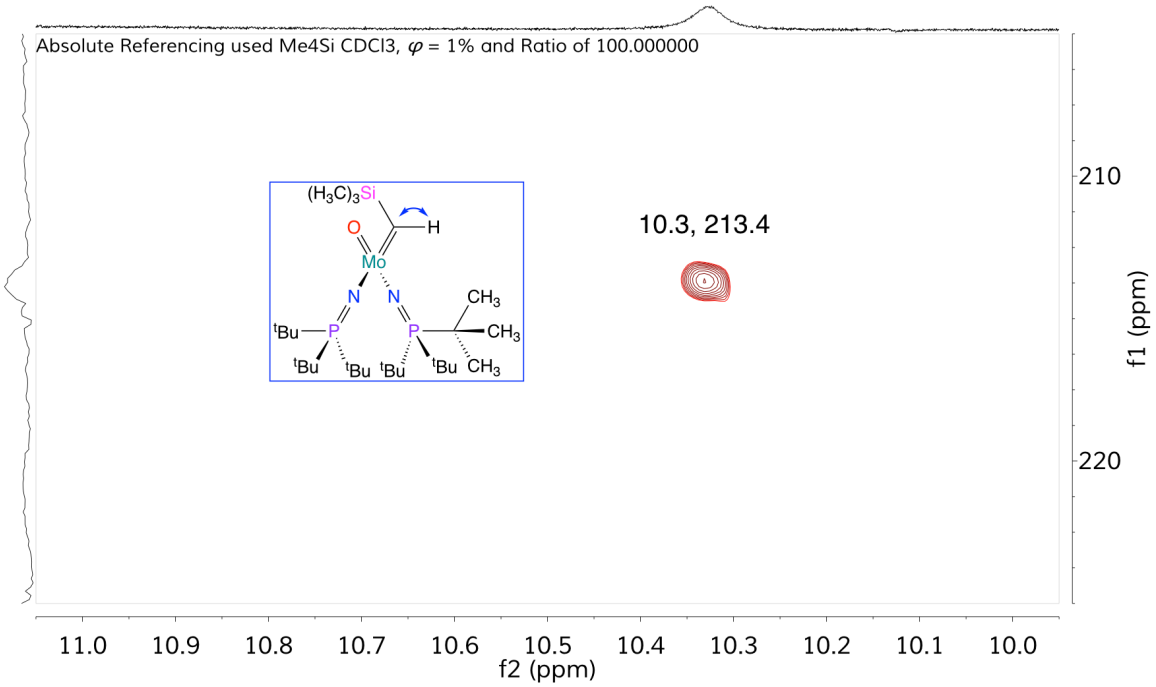

Figure 3.13: ^{1}H-{^{13}C} bsHSQCAD NMR spectrum of **3.1** in C_6D_6 (^{13}C decoupled during acquisition) (600 MHz, 151 MHz)

Additionally, the related ^{13}C-coupled HSQC experiment enabled measurement of the 120 Hz $^{1}J_{HC}$ coupling constant for the alkylidene CH fragment (Fig. 3.14), which is consistent with related Mo(VI) complexes.[16,18,19]

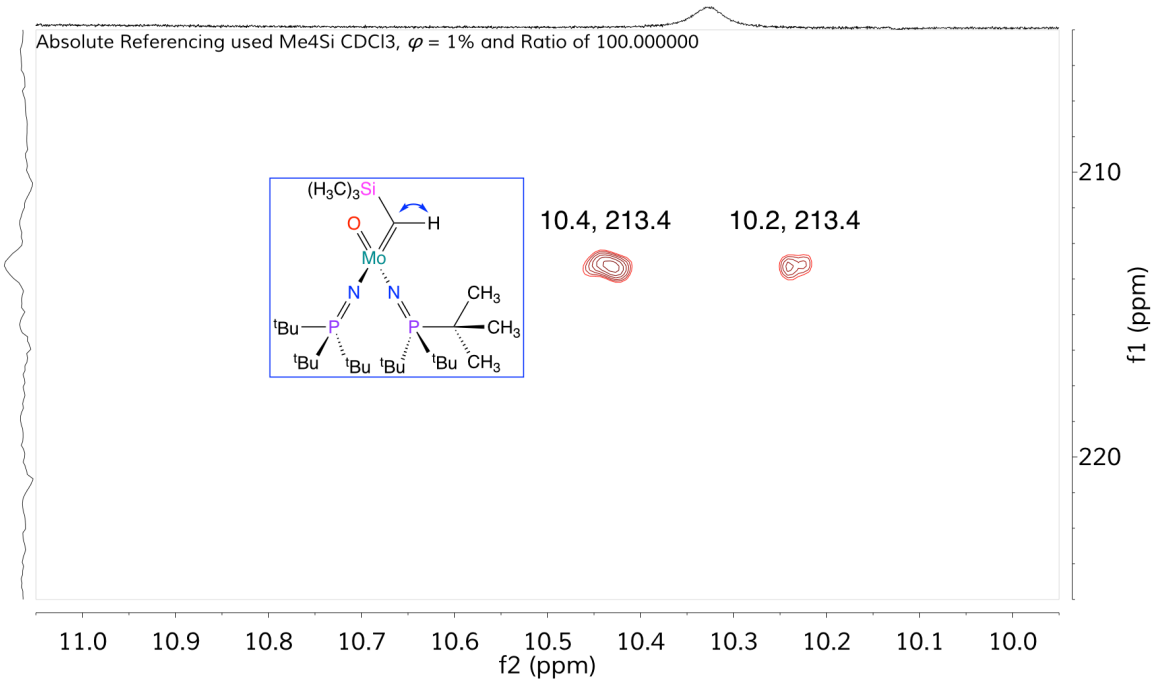

Figure 3.14: ^{1}H-^{13}C bsHSQCAD NMR spectrum of **3.1** in C_6D_6 (600 MHz, 151 MHz)

Complex **3.1** is the first reported neutral oxido-alkylidene molybdenum complex reported in the literature. As indicated earlier, there was only one previously reported oxido-molybdenum vinyl phosphonium adduct that could be viewed as a resonance form of the alkylidene species.[10,11]

In 2018, Schrock *et al.* reported the synthesis of oxido-alkylidene molybdenum complexes (**E**) that incorporated a bidentate *ortho*-methoxy benzylidene ligand (Fig. 3.15).[20] Interestingly, synthesis of these complexes involved initial reactions of benzylidyne-alkoxide complex (**F**) with water.

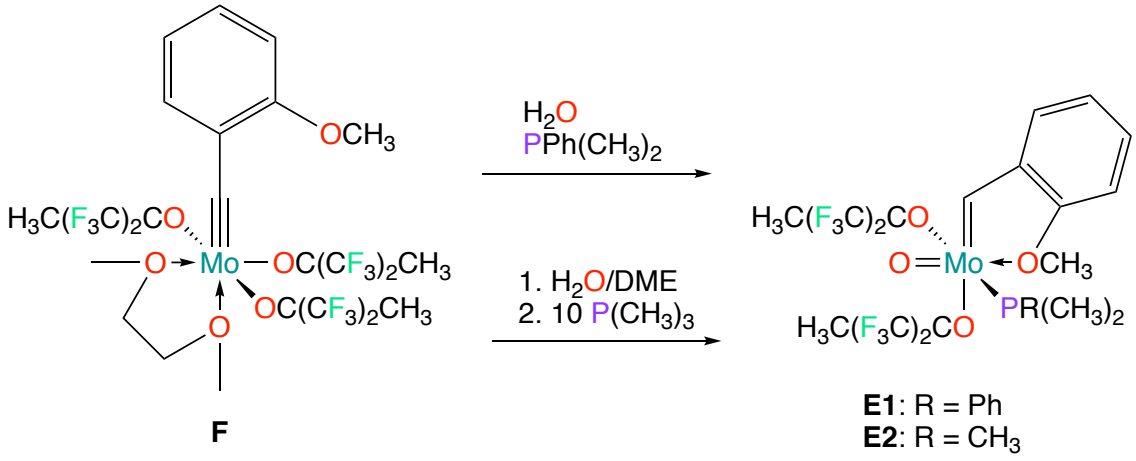

Figure 3.15: Generation of oxido-alkylidene molybdenum complex from reaction with water

Subsequent reactions of **E2** could generate the aryloxide derivative (**G**) (Fig. 3.16), which exhibited low catalytic metathesis activity for a range of substrates. However, addition of 1-2 equiv. of $B(C_6F_5)_3$ to **G** resulted in effective catalytic metathesis at room temperature. Catalytic activities of the precursor oxido-alkylidene complexes **E** were not reported.

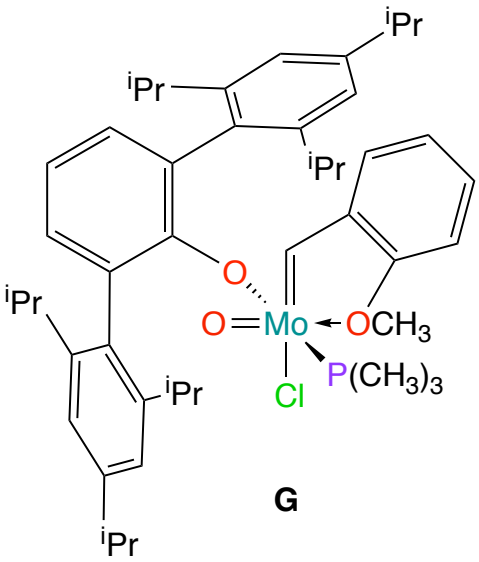

Figure 3.16: Aryloxide oxido-alkylidene complex

The synthesis of complex **3.1** also represents an important advance in the efficiency of generation of group 6 alkylidene complexes that are capable of metathesis reactivity.

Initial results for the synthesis of different types of alkylidene fragments, and varied phosphinimide derivatives, suggest that this synthetic approach may

be general. If these results are further validated, this methodology could enable efficient synthetic access to a new range of alkylidene complexes for study.

3.2.2 Imido-Alkylidene Complex

The related imido-alkylidene complex **3.2** was synthesized using similar methodology to **3.1**, with salt metathesis reactions to generate an intermediate dialkyl complex that subsequently eliminates tetramethylsilane to generate an alkylidene ligand, as illustrated in Fig. 3.17.

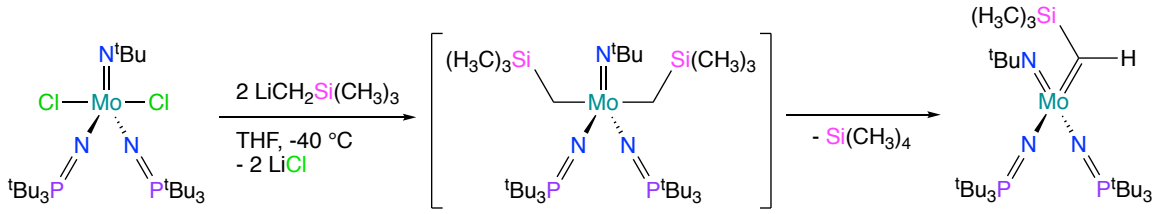

Figure 3.17: Synthesis of **3.2** by salt metathesis and alkane elimination

Complex **3.2** was characterized by NMR and single crystal XRD. Based on the XRD structure (Fig. 3.18), **3.2** is pseudo C_s symmetric with a plane of symmetry that contains the imido-N, Mo, and alkylidene-C atoms. The inner coordination sphere of the complex also exhibits pseudo-tetrahedral geometry about the molybdenum atom, with a τ'_4 value of 0.95.

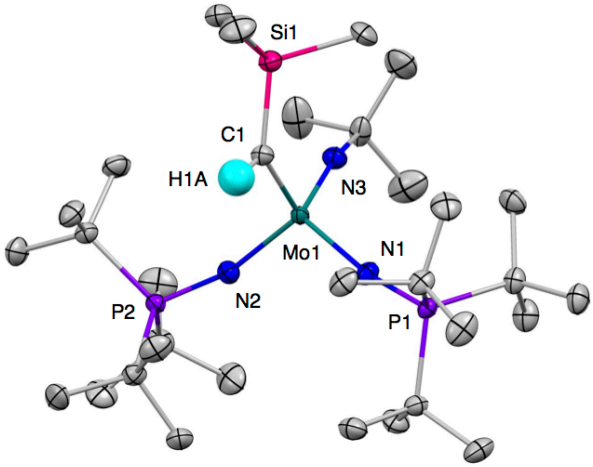

Figure 3.18: Thermal ellipsoid plot (50% probability) of complex **3.2**. Non-alkylidene hydrogen atoms have been omitted for clarity

Visualization of the space-filling model of the XRD structure of **3.2** shows greater steric protection near the alkylidene fragment (Fig. 3.19) than in the oxido-alkylidene complex **3.1**.

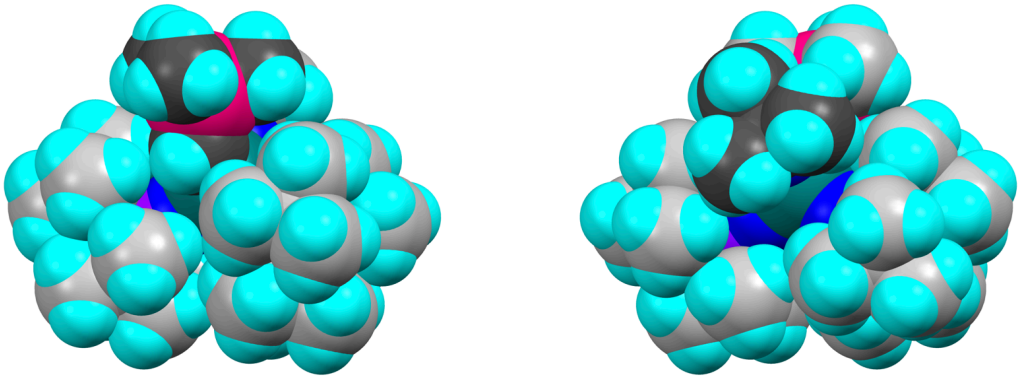

Figure 3.19: Space-filling model of complex **3.2** focused on alkylidene ligand (left, alkylidene carbon atoms indicated in dark grey) and imido ligand (right, imido carbon atoms indicated in dark grey)

The bond distances for **3.2** (Table 3.4) indicate very similar distances for both nitrogen donors on the phosphinimide ligands to the central molybdenum ion (Mo-N), and a slightly longer alkylidene bond (Mo=C) relative to **3.1**. The alkylidene-silicon (C1-Si1) bond is however, slightly shorter than the analogous bond in **3.1**.

Table 3.4: Selected XRD Bond Distances for Complex **3.2**

Atoms	Length (Å)	Atoms	Length (Å)
Mo1-C1	1.926(3)	C1-Si1	1.820(4)
Mo1-N1	1.890(3)	P1-N1	1.569(3)
Mo1-N2	1.899(3)	P2-N2	1.561(3)
Mo1-N3	1.748(3)	-	-

The bond angles (Table 3.5) containing the Mo-N-P fragments of **3.2** are both relatively linear, with angles above 162°, which are slightly more linear than the analogous bond angles in complex **3.1**. The more linear phosphinimide coordination is likely an effect of the increased steric bulk from the *tert*-butylimido ligand.

Table 3.5: Selected XRD Bond Angles for Complex **3.2**

Atoms	Angle (°)	Atoms	Angle (°)
Mo1-N1-P1	168.31(19)	N1-Mo1-N2	108.41(12)
Mo1-N2-P2	162.66(19)	C1-Mo1-N3	103.94(14)
N1-Mo1-N3	113.61(13)	Si1-C1-Mo1	128.72(19)
N2-Mo1-N3	112.43(13)	-	-

The phosphinimide ligands are oriented along different torsion angles relative to the central molybdenum (generally N3-Mo-N-P), with most of the bulk

of the phosphinimide ligands oriented slightly toward the alkylidene fragment (Table 3.6).

Table 3.6: Selected XRD Torsion Angles for Complex **3.2**

Atoms	**Angle (°)**	**Atoms**	**Angle (°)**
N3-Mo1-N1-P1	76.2(9)	N1-Mo1-N2-P2	130.0(7)
N3-Mo1-N2-P2	-103.6(7)	N2-Mo1-N1-P1	-158.1(9)
N3-Mo1-C1-Si1	-7.1(3)	-	-

The ^{1}H NMR spectrum (Fig. 3.20) of **3.2** indicates formation of a major product that corresponds closely to the spectral data for **3.1**, including a singlet trimethylsilyl resonance at 0.60 ppm, a ^{31}P-coupled phosphinimide doublet at 1.34 ppm, and a downfield alkylidene triplet at 10.28 ppm that is identified as long-range ^{31}P coupling ($^{4}J_{PH}$ = 2.2 Hz) to the phosphinimide phosphorus atoms based on 2D NMR spectral data for the related complex **3.3** (vide infra).

In addition to the major product signals, there is evidence of a minor product. The identity of this minor product is most strongly indicated by an additional downfield alkylidene singlet at 12.19 ppm, with an approximate 0.13 ratio to the major product, which suggests an alternate alkylidene isomer.

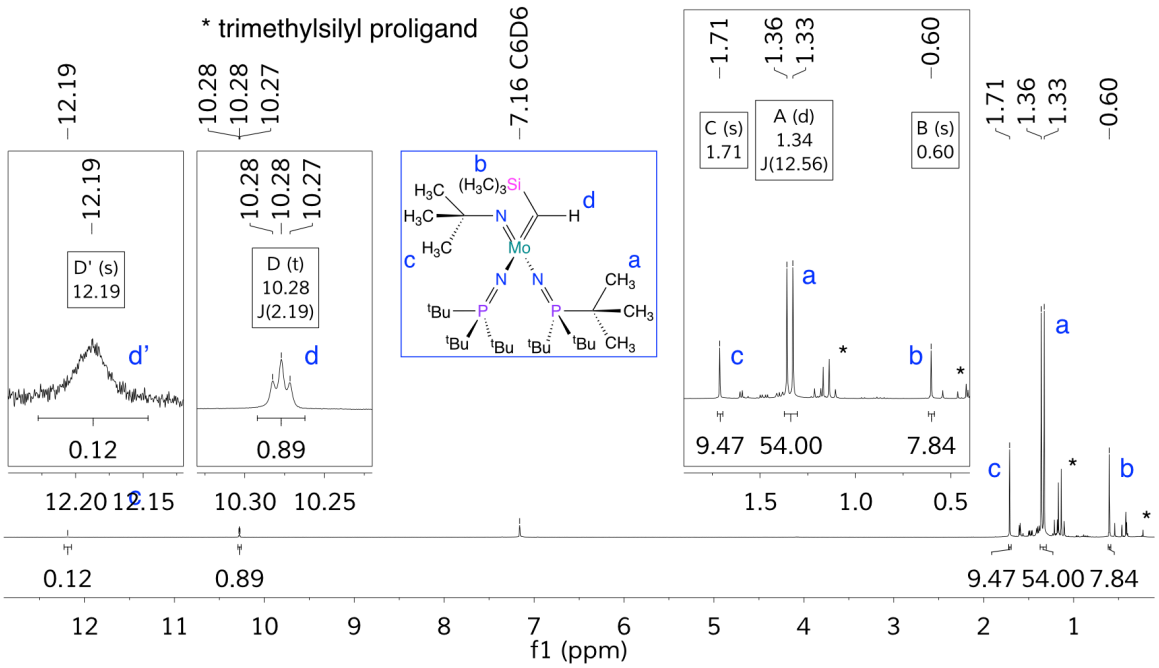

Figure 3.20: ^{1}H NMR spectrum of **3.2** in C_6D_6 (400 MHz)

The ^{1}H-decoupled ^{31}P NMR spectrum of **3.2** (Fig. 3.21) contains a major product singlet at 42.78 ppm, which indicates a complex with chemically equivalent phosphinimide ligands when in solution. A minor product is also observed at a higher chemical shift of 50.66 ppm. This resonance is interpreted to be the phosphinimide ligands for the *anti* isomer of **3.1**, primarily due to the relative ratio of the minor and major peaks in relation to the alkylidene proton signals from the ^{1}H NMR spectrum.

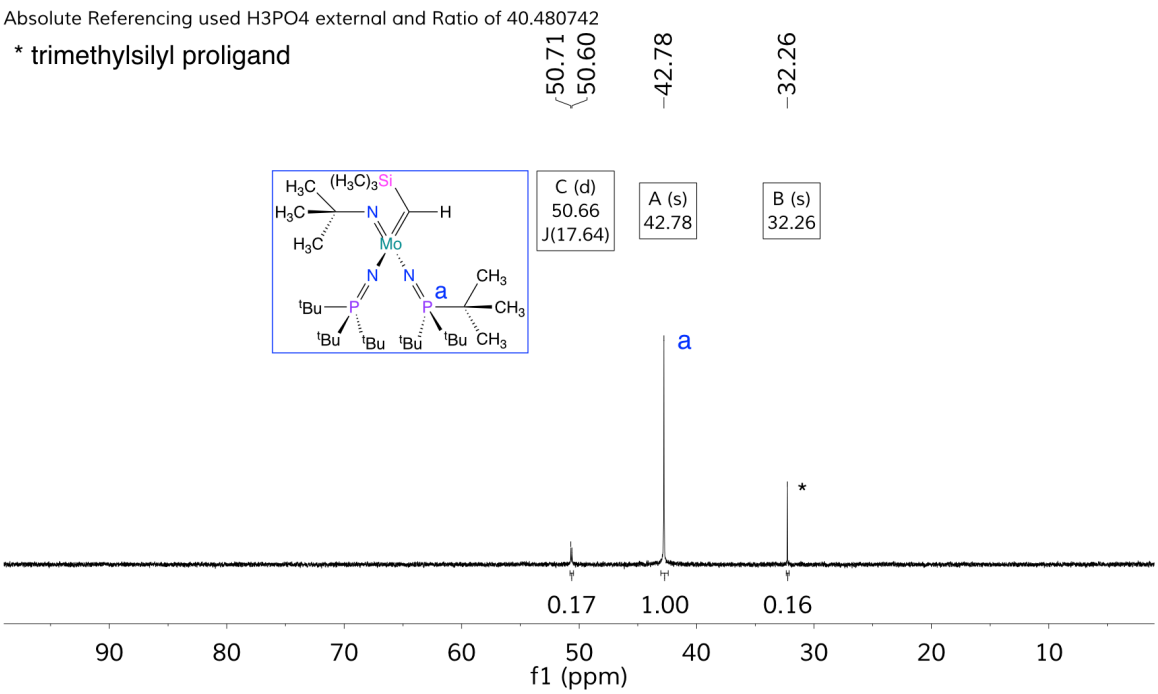

Figure 3.21: $^{31}P\{^{1}H\}$ NMR spectrum of **3.2** in C_6D_6 (162 MHz)

3.2.3 Oxido-Alkylidene Borane Complex

Given the unusual exposed oxido ligand in **3.1**, we were interested in potential modulation of steric and electronic properties at the Mo center through Lewis acid coordination. As shown in Fig. 3.22, **3.1** can be combined with tris(pentafluorophenyl)borane to generate a novel oxido-borane adduct complex **3.3** in 98 % isolated yield. Based on the XRD structure (Fig. 3.23), **3.3** is pseudo C_s symmetric with a plane of symmetry that contains the oxido-O, Mo, and alkylidene-C atoms. In addition, the core coordination sphere around the Mo is pseudo-tetrahedral with a τ'_4 of 0.95.

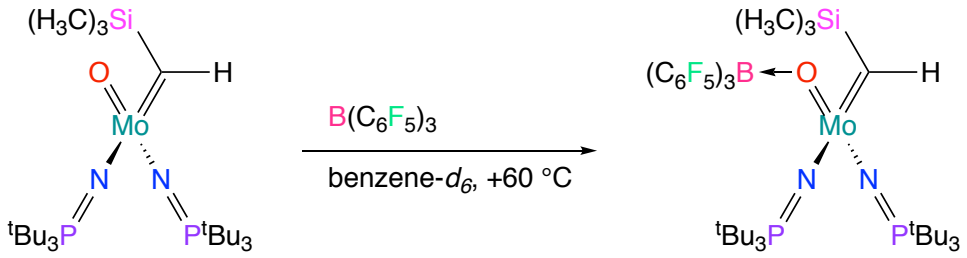

Figure 3.22: Synthesis of **3.3** by $B(C_6F_5)_3$ coordination

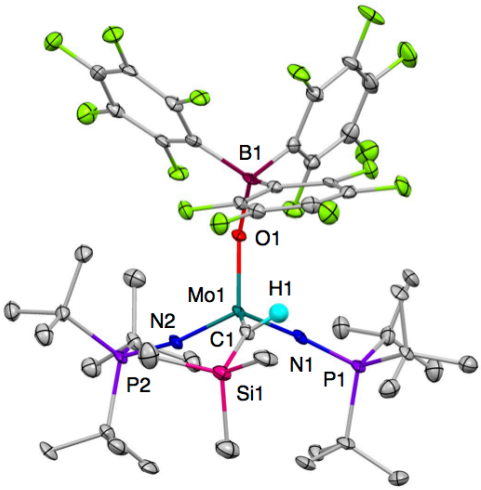

Figure 3.23: Thermal ellipsoid plot (50% probability) of complex **3.3**; non-alkylidene hydrogen atoms have been omitted for clarity

Visualization of the space-filling model of the XRD structure of **3.3** reveals a sterically protected oxido fragment in the complex (Fig. 3.24), and an alkylidene fragment that is forced out of a *syn* conformation by the presence of the borane.

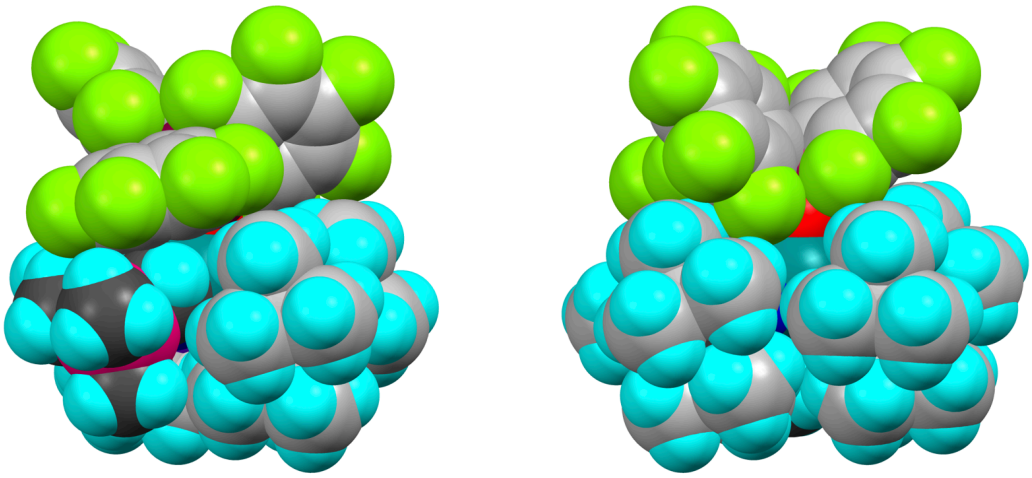

Figure 3.24: Space-filling model of complex **3.3** focused on the alkylidene ligand (left) and oxido ligand (right), alkylidene carbon atoms indicated in dark grey

The presence of tris(pentafluorophenyl)borane leads to some dramatic structural differences relative to the borane-free complex **3.1**. In comparison, **3.3** exhibits a molybdenum-oxido (Mo1-O1) bond distance increase of 0.143(6) Å, an alkylidene bond distance (Mo1-C1) decrease of 0.025(9) Å, and the phosphinimide N-donor (Mo1-N) bond distances decrease by an average of 0.050(5) Å (Table 3.7). Each of these metrical parameter differences supports the expected strong electron withdrawing effect of the coordinated borane.

Table 3.7: Selected XRD Bond Distances for Complex **3.3**

Atoms	Length (Å)	Atoms	Length (Å)
Mo1-C1	1.895(7)	C1-Si1	1.863(8)
Mo1-O1	1.843(5)	P1-N1	1.594(6)
Mo1-N1	1.865(6)	P2-N2	1.628(6)
Mo1-N2	1.799(6)	B1-O1	1.489(9)

The O1-Mo-C1 bond angle is slightly larger in **3.3** than **3.1**, possibly due to increased steric repulsion of the borane with the alkylidene fragment (Table 3.8). Phosphinimide bond angles to the more electropositive molybdenum atom (generally Mo-N-P) as compared to the borane-free complex **3.1** are decreased by an average of 1.95(35)°. The Mo-O1-B1 angle of 155.3(5)° in **3.3** suggests that the Mo-O bond has more single-bond character than in **3.1**.

Table 3.8: Selected X-ray diffraction model bond angles of **3.3**

Atoms	Angle (°)	Atoms	Angle (°)
Mo1-N1-P1	158.7(4)	N1-Mo1-N2	111.5(3)
Mo1-N2-P2	164.5(4)	O1-Mo1-C1	108.0(3)
O1-Mo1-N1	108.0(2)	Mo1-C1-Si1	148.7(4)
O1-Mo1-N2	113.8(3)	Mo1-O1-B1	155.3(5)

The alkylidene fragment of **3.3** has a torsion angle of 127.7(8)° and is rotated significantly in comparison to **3.1** by 127.4(11)°, placing the alkylidene ligand into an intermediate configuration between *syn* and *anti* (Table 3.9).

Table 3.9: Selected XRD Torsion Angles for Complex **3.3**

Atoms	**Angle (°)**	**Atoms**	**Angle (°)**
O1-Mo1-N1-P1	115.0(11)	N1-Mo1-N2-P2	-82.5(15)
O1-Mo1-N2-P2	39.9(16)	N2-Mo1-N1-P1	-119.4(11)
O1-Mo1-C1-Si1	127.7(8)	B1-O1-Mo1-C1	19.3(12)

Synthesis of **3.3** in the presence of 1-octene generates a single conformer of the product complex with a C_s symmetry, as indicated by ^{1}H, ^{19}F, and $^{31}P\{^{1}H\}$ NMR spectroscopy. Analysis of **3.3** by ^{1}H NMR spectroscopy (Fig. 3.25) gives rise to diagnostic resonances for all protons within the structure, including a higher field singlet at 0.25 ppm for the trimethylsilyl fragment and a ^{31}P-coupled doublet at 1.10 ppm ($^{3}J_{PH}$ = 13.7 Hz) for the phosphinimide protons. The alkylidene proton is identified at the much higher chemical shift of 9.49 ppm.

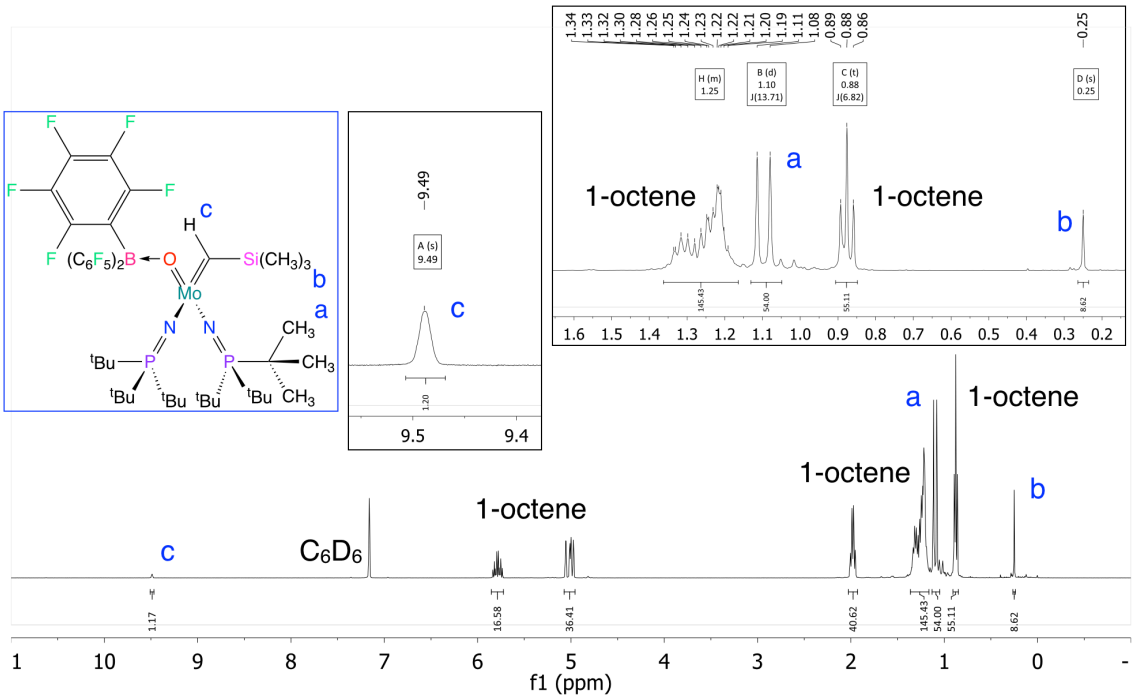

Figure 3.25: ^{1}H NMR spectrum of **3.3** with 1-octene in C_6D_6 (400 MHz)

The ^{1}H-decoupled ^{31}P NMR spectrum of **3.3** contains a singlet at 60.56 ppm (Fig. 3.26), which indicates formation of a single product with chemically equivalent phosphinimide ligands when in solution.

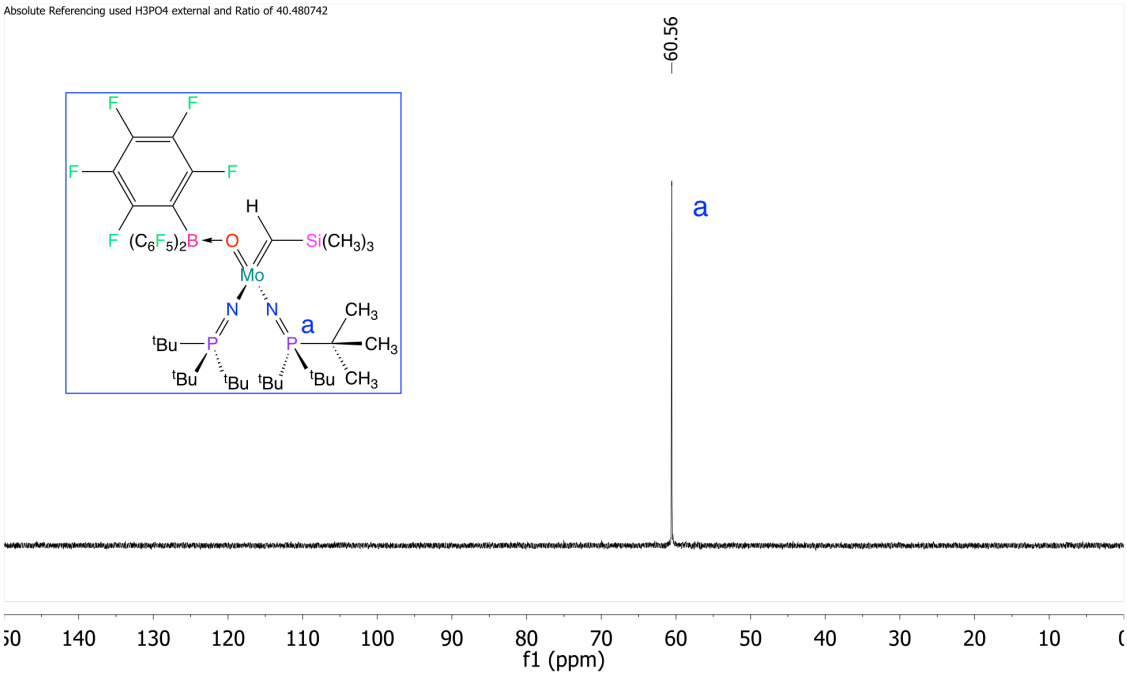

Figure 3.26: $^{31}P\{^{1}H\}$ NMR spectrum of **3.3** with 1-octene in C_6D_6 (162 MHz)

The ^{19}F spectrum of **3.3** (Fig. 3.27) reveals all expected resonances and coupling for the fluorine atoms within the borane fragment. A virtual triplet is observed at -165.67 ppm ($^{3}J_{FF}$ = 21.7 Hz) for the *meta*-fluoro groups, along with the expected triplet at -161.75 ppm ($^{3}J_{FF}$ = 20.6 Hz) for the *para*-fluoro. Finally, a doublet is observed at -130.34 ppm ($^{3}J_{FF}$ = 24.3 Hz) for the *ortho*-fluoro groups.

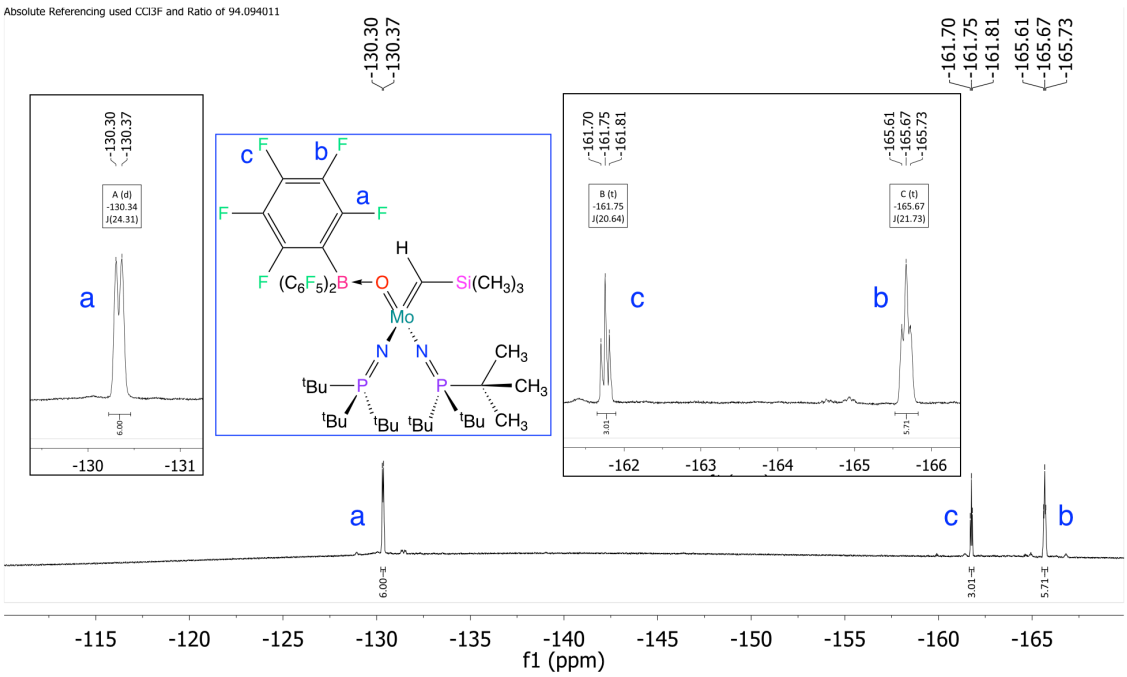

Figure 3.27: ^{19}F NMR spectrum of **3.3** with 1-octene in C_6D_6 (376 MHz)

Synthesis of **3.3** in the absence of 1-octene present leads to formation of an additional minor C_1 symmetric product relative to the main C_s complex previously described. Elemental analysis of this mixture indicates that the additional product is an isomer of **3.3**, and can be observed by ^{1}H, ^{19}F, and $^{31}P\{^{1}H\}$ NMR spectroscopy.

Analysis of **3.3** by ^{1}H NMR spectroscopy (Fig. 3.28) resolves an additional singlet that is assigned to the trimethylsilyl fragment in the C_1 isomer at 0.14 ppm, and ^{31}P-coupled doublets at 1.43 ppm ($^{3}J_{PH}$ = 13.9 Hz), and 1.55 ppm ($^{3}J_{PH}$ = 14.4 Hz) for the phosphinimide protons in the C_1 isomer. No alkylidene proton was identified by ^{1}H NMR spectroscopy for the C_1 isomer.

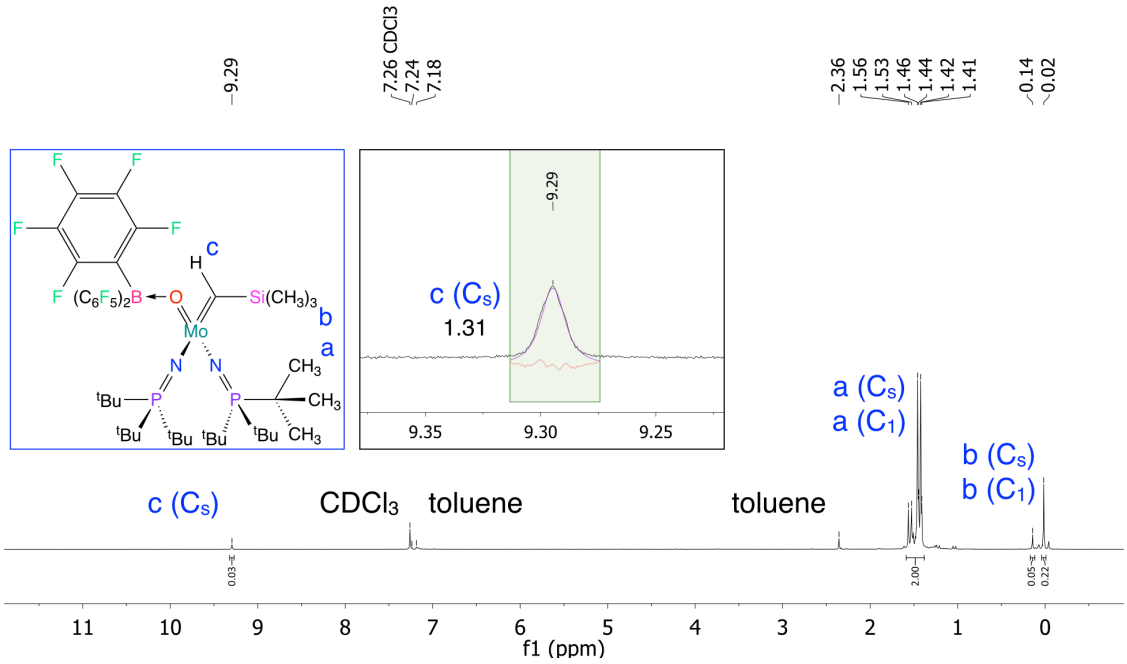

Figure 3.28: ^{1}H NMR spectrum of **3.3** in $CDCl_3$ (400 MHz)

The ^{1}H-decoupled ^{31}P NMR spectrum of **3.3** (Fig. 3.29) clearly shows the major C_s product, along with two singlets for the C_1 isomer at 61.18 ppm and 68.05 ppm.

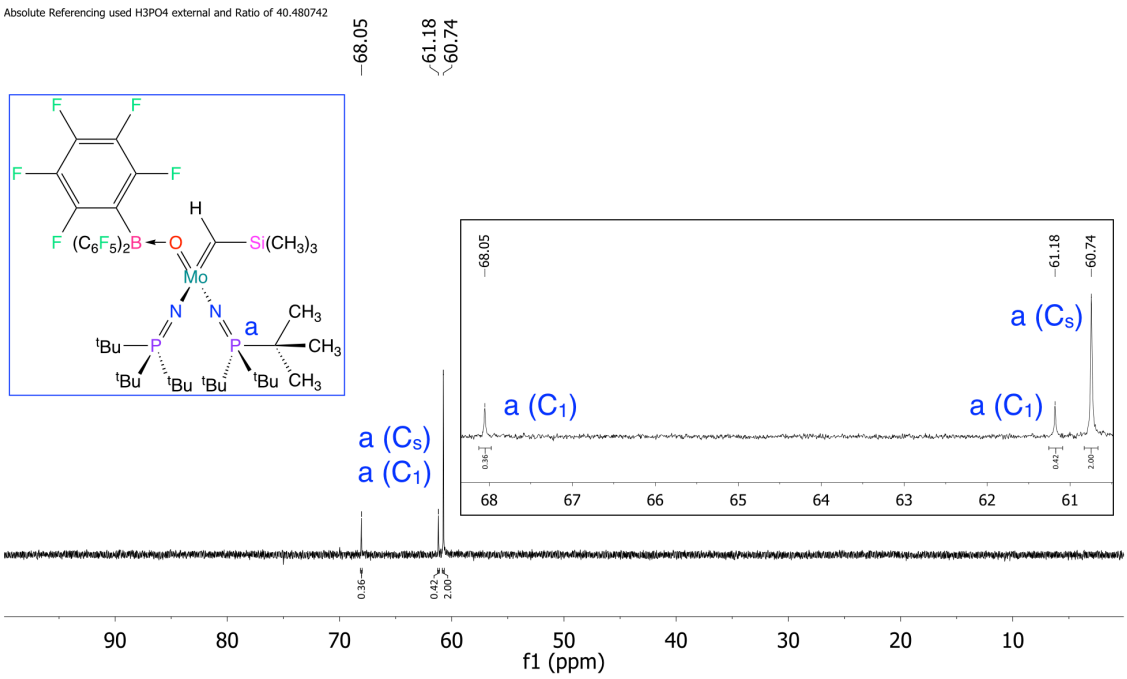

Figure 3.29: $^{31}P\{^{1}H\}$ NMR spectrum of **3.3** in $CDCl_3$ (162 MHz)

The ^{19}F NMR spectrum of **3.3** (Fig. 3.30) contains a multiplet at -166.10 ppm, a triplet at -162.20 ppm, and a doublet at -131.01 ppm for the major C_s product. The C_1 isomer peaks include a multiplet at -165.31 ppm, two triplets at -161.51 and -160.31 ppm, and two doublets at -132.89 and -132.04 ppm. The expected additional *meta*-position fluorine peaks may coincide with the C_s isomer triplet near -166 ppm, and are not specifically assigned.

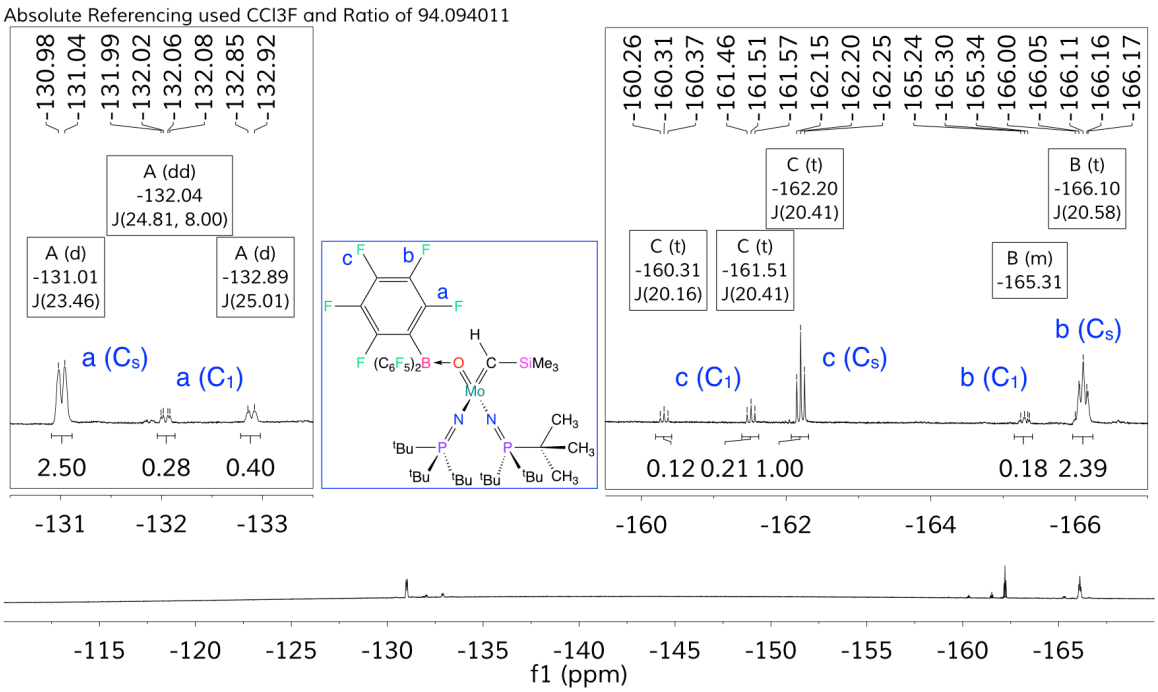

Figure 3.30: ^{19}F NMR spectrum of **3.3** in $CDCl_3$ (376 MHz)

Use of a 2D ^{1}H-{^{13}C} HSQC NMR experiment with adiabatic pulses enabled measurement of the alkylidene carbon signal for **3.3** (Fig. 3.31), where the resonance was found at 232.1 ppm, which is within the expected range for this type of ligand fragment, but substantially downfield shifted with respect to the resonance in the terminal oxido-alkylidene complex **3.1** at 213.4 ppm.

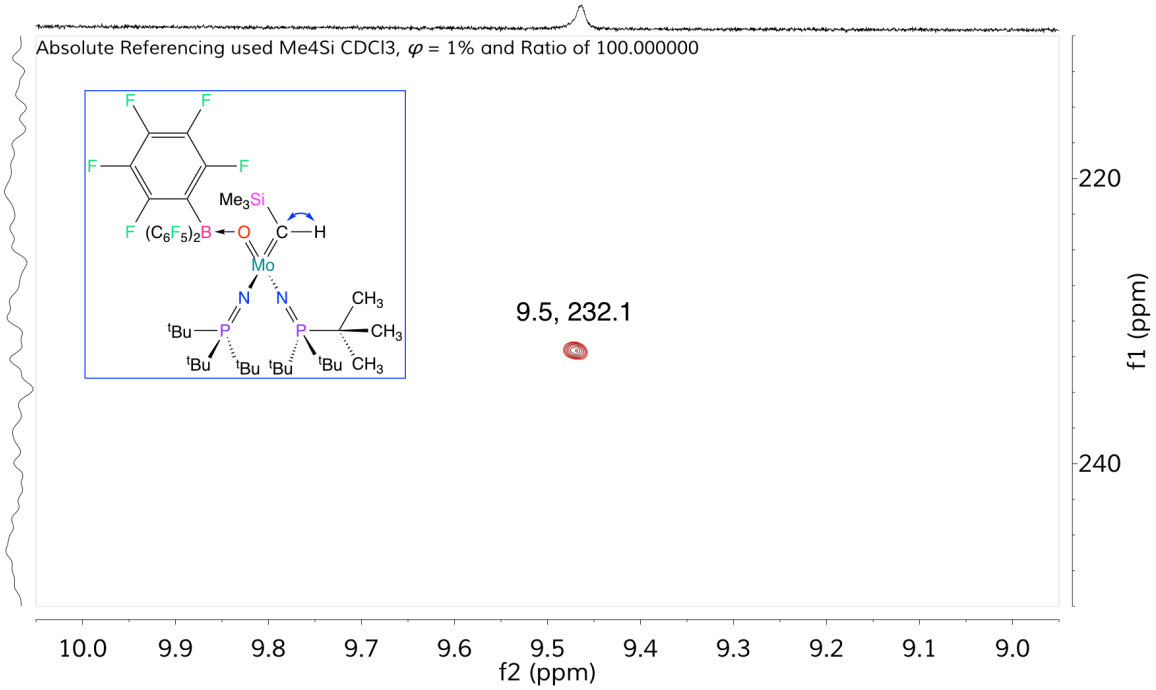

Figure 3.31: ^{1}H-{^{13}C} bsHSQCAD NMR spectrum of **3.3** in C_6D_6 (^{13}C decoupled during acquisition) (600 MHz, 151 MHz)

The related ^{13}C-coupled HSQC experiment enabled measurement of a 120 Hz $^{1}J_{HC}$ coupling constant for the alkylidene CH fragment which is identical to that measured for **3.1** (Fig. 3.32).

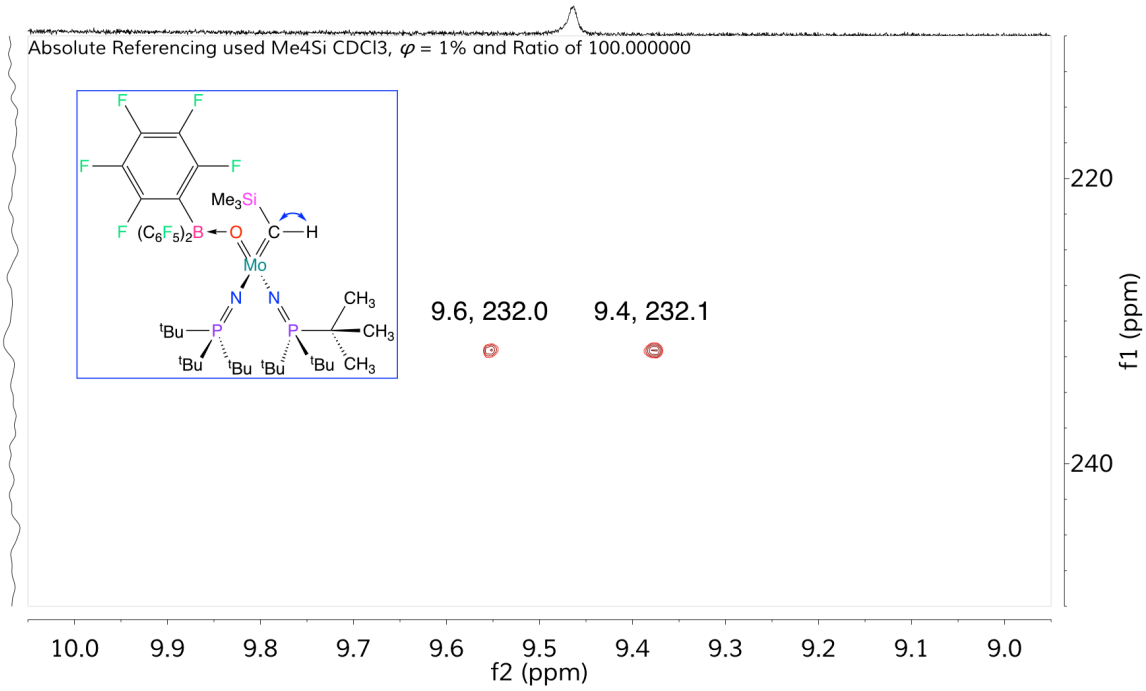

Figure 3.32: ^{1}H-^{13}C bsHSQCAD NMR spectrum of **3.3** in C_6D_6 (600 MHz, 151 MHz)

Use of a 2D ^{1}H-^{31}P gradient heteronuclear multiple bond correlation (gHMBC) NMR experiment enabled measurement of a cross peak that corresponds to 4-bond indirect dipole-dipole coupling (*J*-coupling) between the phosphinimide phosphorus atoms and the alkylidene proton (Fig. 3.33), which supports the clear triplet observed for imido complex **3.2** (Fig. 3.20) and likely influences the broadening of the alkylidene proton signals in oxido complexes **3.1** and **3.3** as well. The coupling constant is too small (~2 Hz) to be resolved by this 2D experiment and the cross peak appears as a singlet.

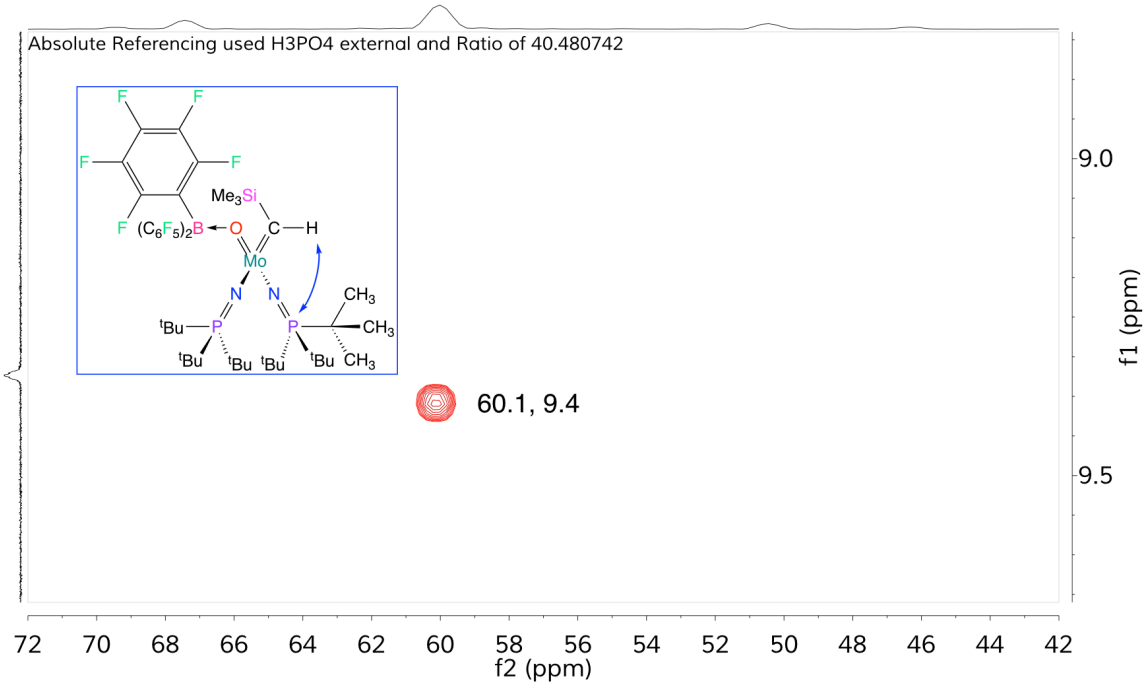

Figure 3.33: ^{1}H-^{31}P gHMBC NMR spectrum of **3.3** in C_6D_6 (400 MHz, 162 MHz)

3.3 Reactivity

Catalytic cross-metathesis reactivity was assessed for **3.3** with 1-octene as a substrate. No reactivity for **3.3** was observed when heated at 80 °C for 18 hours. Catalytic ring-opening metathesis polymerization (ROMP) was also assessed for **3.1** and **3.3** with norbornene as a substrate. Complex **3.1** at 10 mol % catalyst loading exhibits 18% conversion of norbornene to polynorbornene when heated at 80°C over 24 hours. This low conversion increases to 22% after more than 48 hours. In contrast, use of 10 mol % of complex **3.3** exhibits much higher catalytic performance with 84% conversion of norbornene when heated at 80°C for 17 hours.

Comparison of the catalytic differences between **3.1** and **3.3** indicates a number of key characteristics. Despite the good substrate accessibility to the metal center in **3.1**, actual catalytic reactivity appears to be limited by both the strongly electron donating phosphinimide ligands and the known lower reactivity of silyl alkylidenes.[17] Coordination of the borane to the oxido ligand in **3.3** clearly begins to reverse these reactivity-limiting effects. The marked improvement of **3.3** over **3.1** is attributed to the removal of electron density from the metal center, as substrate access is actually diminished by the presence of the sterically large borane.

Interesting aspects of complex **3.3** are that the catalyst appears to exhibit excellent stability at elevated temperatures, and may not be fully consumed during catalytic reactions, as unreacted **3.3** is observed after catalytic screens. These properties indicate that a much higher performance ROMP catalyst could be designed. Improved substrate access, and a more electropositive metal center, could be achieved with less bulky and more electron withdrawing phosphinimide ligands. A less bulky derivative of the alkylidene fragment could also increase reactivity.

Synthesis of alternative alkylidene fragments (methylidene and neopentylidene) were assessed, but never fully characterized or tested for catalytic performance. The more reactive alkylidene groups may prevent isolation of a stable product for characterization. However, it is possible good catalyst performance could be obtained by generating these complexes *in situ* to be used immediately for catalysis.

3.4 Conclusions

Alkylidene complexes supported by phosphinimide ligands were synthesized, characterized, and tested for preliminary catalytic metathesis reactivity. These complexes include the first reported neutral oxido-alkylidene on molybdenum, and the first reported borane adduct of an oxido-alkylidene molybdenum complex. The synthetic methodology used to generate these complexes is extremely atom-economic and high yielding, defining an efficient approach to synthesize useful molybdenum phosphinimide complexes with metal-carbon multiple bonds.

Future research in this area could focus on the development of more active metathesis catalysts, with evaluation of phosphinimide ligands with less steric bulk and more electron withdrawing groups. It would be important to evaluate if the thermal stability of complexes is impacted as steric bulk is decreased. However, based on the elevated temperature syntheses of precursor oxido-chlorido complexes described in Chapter 2, this may not lead to significant changes in stability. Use of alternative alkylidene ligands and other types of Lewis acids for coordination to the oxido ligand may affect catalytic performance as well. Other types of conversions could also be assessed, such as abstraction of the oxido ligand via trimethylphosphine to generate Mo(IV) alkylidene complexes for further study.

3.5 Experimental Section

General Experimental Procedures

Unless otherwise specified, all reactions and manipulations were performed under a dry oxygen-free atmosphere of dinitrogen in either a Vacuum Atmospheres NEXUS model drybox equipped with a 40CFM Dual Purifier NI-Train, or by using standard Schlenk techniques. Glassware was dried in an oven at 150 ºC overnight prior to use.

NMR spectra were collected using a Varian Inova 600 MHz NMR spectrometer with a 5 mm indirect detection probe, Varian VNMRS 500 MHz NMR spectrometer with a tunable 5 mm $^{1}H\{^{15}N\text{-}^{31}P\}$ PFG probe, Varian VNMRS 400 MHz spectrometer with an auto-tunable 5 mm Dual Broadband $^{15}N\text{-}^{31}P$ $\{^{1}H\}$ PFG probe optimized for broadband detection, or Oxford Mercury VX-300 300 MHz NMR spectrometer with a 5 mm 4-nuclei ($^{1}H/^{13}C/^{19}F/^{31}P$) auto-switchable PFG probe. Chemical shifts for ^{1}H, ^{11}B, ^{13}C, ^{19}F, ^{29}Si, and ^{31}P NMR spectra are reported in parts per million (ppm), and were referenced to residual solvent impurities, or when stated on the spectra with the absolute unified scale corresponding to the following standards using the relevant Ξ / % frequency ratios: ^{11}B, 32.083974 ($BF_3{\bullet}Et_2O$ $CDCl_3$, ϕ = 15 %); ^{13}C, 25.145020 ($Si(CH_3)_4$ $CDCl_3$, ϕ = 1 %); ^{19}F, 94.094011 ($FCCl_3$); ^{29}Si, 19.867187 ($Si(CH_3)_4$ $CDCl_3$, ϕ = 1 %); ^{31}P, 40.480742 (H_3PO_4 external).[21,22] All NMR spectral data were processed with the MestReNova 10.0.1 software package.

Elemental analyses were performed at Midwest Microlab LLC. Single crystal X-ray diffraction data were collected using a Bruker APEX2

diffractometer with a CCD area detector and graphite-monochromated Mo Kα radiation (λ = 0.71073 Å). Structural solution and refinement were accomplished using the APEX2, SAINT, SADABS, TWINABS, and SHELXL programs.[23–25] Details regarding data collection for each structure are provided in the individual CIF files.

The 2D NMR experiments used unmodified pulse sequences from the Agilent software package VNMRJ 4.2 with specific parameters reported for each compound. Relaxation delays for the 2D NMR experiments were optimized so that the recycle time equaled 1.3 times T_1 of the target proton resonances, with T_1 measured using INVREC NMR experiments with default parameters from VNMRJ 4.2.

Except where otherwise noted, reagents were purchased from commercial suppliers and used without further purification. Benzene-d_6, toluene-d_8, and chloroform-d, were purchased from Cambridge Isotope Laboratories (99.9%D) and were purified by storage over 4 Å molecular sieves under N_2 prior to use. Celite (Aldrich) and 4 Å molecular sieves (Aldrich) were dried under dynamic vacuum at 250 ºC for 48 h prior to use. 1-octene was purified using standard techniques.[26] $LiCH_2Si(CH_3)_3$ was purchased as an anhydrous 1.0 M solution in diethyl ether, and solvent was removed to give $LiCH_2Si(CH_3)_3$ as a white powder, which was used in the reactions described below. All solvents were purchased from commercial suppliers and dried and deoxygenated with the appropriate VAC Atmospheres Solvent Purifier modules and stored over activated 4 Å molecular sieves prior to use.

Synthesis of (^{t}Bu$_3$P=N)$_2$Mo(O)(=CHSi(CH$_3$)$_3$) (3.1): In a 25 mL suction flask, **2.4** (100.4 mg, 0.163 mmol) was dissolved in 4 mL of THF and cooled to -20 °C. A solution of LiCH$_2$Si(CH$_3$)$_3$ (31.5 mg, 0.334 mmol) in 2 mL of THF at -20 °C was slowly added to the solution of **2.4** while stirring. The reaction solution rapidly changed from transparent yellow to transparent dark red. Volatiles were removed under reduced pressure after one hour. The red oily material obtained was dissolved in hexanes and filtered through a pad of Celite. Highly crystalline (^{t}Bu$_3$P=N)Mo(O)(=CHSi(CH$_3$)$_3$) (**3.1**) was isolated (89.6 mg, 0.142 mmol, 87% yield) as a red solid after removal of hexanes under reduced pressure. Single crystals suitable for X-ray diffraction were obtained by slow evaporation of **3.1** in hexanes at -20 °C. ^{1}H NMR (400 MHz, benzene-d_6, 25.0 °C) δ = 0.67 (s, 9 H, Mo=CH(Si(CH_3)$_3$)), 1.31 (d, $^3J_{PH}$ = 12.8 Hz, 54 H, PC(CH_3)$_3$), 10.33 (s, 1 H, Mo=CH(Si(CH$_3$)$_3$)). ^{31}P{^{1}H} NMR (162 MHz, benzene-d_6, 25.0 °C) δ = 46.62 (s, 2 P, PC(CH$_3$)$_3$). ^{13}C{^{1}H} NMR (101 MHz, toluene-d_8, 15.0 °C) δ = 2.86 (s, Mo=CH(Si(CH$_3$)$_3$)), 29.57 (s, PC(CH$_3$)$_3$), 41.77 (d, $^1J_{PC}$ = 47.4 Hz, PC(CH$_3$)$_3$), alkylidene carbon could not be detected. Elemental analysis found: C, 52.89; H, 10.07; N, 4.28. C$_{28}$H$_{64}$MoN$_2$OP$_2$Si requires: C, 53.31; H, 10.23; N, 4.44.

Synthesis of (^{t}Bu$_3$P=N)$_2$Mo(=N^{t}Bu)(=CHSi(CH$_3$)$_3$) (3.2): In a 20 mL scintillation vial, **2.5** (195 mg, 0.228 mmol) was dissolved in 3 mL of THF and cooled to -40 °C. A solution of LiCH$_2$Si(CH$_3$)$_3$ (55 mg, 0.456 mmol) in 2 mL of THF at -40 °C was slowly added to the solution of **2.5** while stirring. The

reaction solution rapidly changed from transparent orange to transparent dark brown. Volatiles were removed under reduced pressure after one hour. The brown oily material obtained was dissolved in hexanes and filtered through a pad of Celite, and ($^{t}Bu_3P=N)_2Mo(=N^{t}Bu)(=CHSi(CH_3)_3$) (**3.2**) was isolated (146 mg, 0.213 mmol, 93% yield) as a oily brown viscous liquid after removal of hexanes under reduced pressure. Single crystals suitable for X-ray diffraction were obtained by slow evaporation of **3.2** in pentane at -30 °C. (Based on the ^{31}P NMR data, the *syn*:*anti* isomer ratio in solution was 1:0.17) ^{1}H NMR (400 MHz, benzene-d_6, 22.0 °C) δ = (*syn* isomer) 0.60 (s, 9 H, Mo=CH(Si(CH_3)$_3$)), 1.34 (d, $^{3}J_{PH}$ = 12.6 Hz, 54 H, PC(CH_3)$_3$), 1.71 (s, 9 H, Mo=N(CH_3)$_3$), 10.28 (t, $^{4}J_{PH}$ = 2.2 Hz, 1 H, Mo=C*H*(Si(CH$_3$)$_3$)); (*anti* isomer) 12.19 (s, 1 H, *trans*-Mo=C*H*(Si(CH$_3$)$_3$)). $^{31}P\{^{1}H\}$ NMR (162 MHz, benzene-d_6, 22.0 °C) δ = (*syn* isomer) 42.78 (s, 2 P, *P*C(CH$_3$)$_3$); (*trans* isomer) 50.66 (s, 2 P, *P*C(CH$_3$)$_3$).

Synthesis of ($^{t}Bu_3P=N)_2Mo(O\text{-}B(C_6F_5)_3)(=CHSi(CH_3)_3)$ (3.3): In a 20 mL scintillation vial, **3.1** (24.8 mg, 0.0393 mmol) was dissolved in 2 mL of benzene-d_6. A suspension of $B(C_6F_5)_3$ (20.2 mg, 0.0394 mmol) in 3 mL of benzene-d_6 was added dropwise to the solution of **3.1** at ambient temperature. The reaction solution rapidly changed from transparent red to dark brown, and was heated at 60 °C for 1 hour. Purple crystals of **3.3** (43.9 mg, 0.0384 mmol, 98 % yield) formed out of solution and were isolated after solvent removal under reduced pressure. Single crystals suitable for X-ray diffraction were obtained from a benzene-d_6 solution of **3.3** heated at +100 °C in a J. Young NMR tube.

Elemental analysis found: C, 48.40; H, 5.77; N, 2.37. $C_{46}H_{64}BF_{15}MoN_2OP_2Si$ requires: C, 48.35; H, 5.64; N, 2.45. (Based on the ^{31}P NMR data, the C_s:C_1 isomer ratio in solution was 1:0.39) ^1H NMR (400 MHz, chloroform-*d*, 0.0 °C, C_s isomer) δ = 0.02 (s, 9 H, Mo=CH(Si(CH_3)$_3$)), 1.44 (d, $^3J_{PH}$ = 13.7 Hz, 54 H, PC(CH_3)$_3$), 9.29 (s, 1 H, Mo=C*H*(Si(CH$_3$)$_3$)); (C_1 isomer) 0.14 (s, 9 H, Mo=CH(Si(CH_3)$_3$)), 1.43 (d, $^3J_{PH}$ = 13.9 Hz, 27 H, PC(CH_3)$_3$), 1.55 (d, $^3J_{PH}$ = 14.4 Hz, 27 H, PC(CH_3)$_3$), alkylidene proton could not be detected. $^{31}P\{^1H\}$ NMR (162 MHz, chloroform-*d*, 0.0 °C, C_s isomer) δ = 60.74 (s, 2 P, *P*C(CH$_3$)$_3$); (C_1 isomer) 61.18 (s, 1 P, *P*C(CH$_3$)$_3$), 68.05 (s, 1 P, *P*C(CH$_3$)$_3$). ^{19}F NMR (376 MHz, chloroform-*d*, 0.0 °C, C_s isomer) δ = -166.10 (m, (m-C*F*)), -162.20 (t, $^3J_{FF}$ = 20.4 Hz (p-C*F*)), -131.01 (d, $^3J_{FF}$ = 23.5 Hz, (o-C*F*)); (C_1 isomer) -166.10 (m, (m-C*F*)), -165.31 (m, (m-C*F*)), -161.51 (t, $^3J_{FF}$ = 20.4 Hz (p-C*F*)), -160.31 (t, $^3J_{FF}$ = 20.2 Hz (p-C*F*), -132.89 (d, $^3J_{FF}$ = 25.0 Hz (o-C*F*)), -132.04 (dd, $^3J_{FF}$ = 24.8 Hz, $^4J_{FF}$ = 8.0 Hz (o-C*F*)).

General Procedure for Catalytic Metathesis Screening: Complexes **3.1** and **3.3** were used in catalytic metathesis screening experiments with 1-octene and norbornene. Below is a representative procedure for **3.3** screened with norbornene as substrate:

Complex **3.3** (10.6 mg, 0.009 mmol) was dissolved in 1 mL of benzene-*d6*. Norbornene (8.0 mg, 0.085 mmol, 9.4 equiv.) was dissolved in 0.5 mL of benzene-*d6* and added to the solution **3.3** at ambient temperature. The resulting solution was transferred to a J. Young NMR tube, lowered into the

spectrometer and immediately monitored by ^{1}H NMR spectroscopy. Temperature adjustments up to 80 °C were initially made using the internal NMR spectrometer temperature controls. A silicone oil bath was used for heating the samples for longer duration at 80 °C. ^{1}H NMR spectra were collected periodically to monitor the reaction.

3.6 References

1. R. R. Schrock and A. H. Hoveyda, *Angew. Chem. Int. Ed.*, 2003, **42**, 4592–4633.
2. J. H. Wengrovius and R. R. Schrock, *Organometallics*, 1982, **1**, 148–155.
3. J. H. Wengrovius, R. R. Schrock, M. R. Churchill, J. R. Missert and W. J. Youngs, *J. Am. Chem. Soc.*, 1980, **102**, 4515–4516.
4. M. B. O'Donoghue, R. R. Schrock, A. M. LaPointe and W. M. Davis, *Organometallics*, 1996, **15**, 1334–1336.
5. D. V. Peryshkov and R. R. Schrock, *Organometallics*, 2012, **31**, 7278–7286.
6. M. P. Conley, V. Mougel, D. V. Peryshkov, W. P. Forrest, D. Gajan, A. Lesage, L. Emsley, C. Copéret and R. R. Schrock, *J. Am. Chem. Soc.*, 2013, **135**, 19068–19070.
7. J. Kress, M. Wesolek, J.-P. Le Ny and J. A. Osborn, *J. Chem. Soc. Chem. Commun.*, 1981, 1039–1040.
8. J. R. Kress, M. J. Russell, M. G. Wesolek and J. A. Osborn, *J. Chem. Soc. Chem. Commun.*, 1980, 431–432.

9. K. Amakawa, S. Wrabetz, J. Kröhnert, G. Tzolova-Müller, R. Schlögl and A. Trunschke, *J. Am. Chem. Soc.*, 2012, **134**, 11462–11473.
10. D. L. Hughes, K. Marjani and R. L. Richards, *J. Organomet. Chem.*, 1995, **505**, 127–129.
11. S. A. Fairhurst, D. L. Hughes, K. Marjani and R. L. Richards, *J. Chem. Soc. Dalton Trans.*, 1998, 1899–1904.
12. R. R. Schrock, J. S. Murdzek, G. C. Bazan, J. Robbins, M. DiMare and M. O'Regan, *J. Am. Chem. Soc.*, 1990, **112**, 3875–3886.
13. R. R. Schrock, S. Rocklage, J. H. Wengrovius, G. Rupprecht and J. Fellmann, .
14. J. M. Mayer, *Inorg. Chem.*, 1988, **27**, 3899–3903.
15. S.-H. Choi, Z. Lin and Z. Xue, *Organometallics*, 1999, **18**, 5488–5495.
16. J. H. Oskam, H. H. Fox, K. B. Yap, D. H. McConville, R. O`Dell, B. J. Lichtenstein and R. R. Schrock, *J. Organomet. Chem.*, 1993, **459**, 185–198.
17. L. N. Bochkarev, Y. E. Begantsova, V. I. Shcherbakov, N. E. Stolyarova, I. K. Grigorieva, I. P. Malysheva, G. V. Basova, A. L. Bochkarev, Y. P. Barinova, G. K. Fukin, E. V. Baranov, Y. A. Kurskii and G. A. Abakumov, *J. Organomet. Chem.*, 2005, **690**, 5720–5727.
18. A. Sinha and R. R. Schrock, *Organometallics*, 2004, **23**, 1643–1645.
19. T. S. Pilyugina, R. R. Schrock, A. S. Hock and P. Müller, *Organometallics*, 2005, **24**, 1929–1937.
20. K. V. Bukhryakov, R. R. Schrock, A. H. Hoveyda, C. Tsay and P. Müller, *J. Am. Chem. Soc.*, 2018, **140**, 2797–2800.

21. R. K. Harris, E. D. Becker, S. M. Cabral de Menezes, R. Goodfellow and P. Granger, *Pure Appl. Chem.*, 2001, **73**, 1795–1818.
22. R. K. Harris, E. D. Becker, S. M. Cabral de Menezes, P. Granger, R. E. Hoffman and K. W. Zilm, *Pure Appl. Chem.*, 2008, **80**, 59–84.
23. G. M. Sheldrick, *Acta Crystallogr. Sect. A*, 2015, **71**, 3–8.
24. G. M. Sheldrick, *Acta Crystallogr. Sect. C*, 2015, **71**, 3–8.
25. L. Krause, R. Herbst-Irmer, G. M. Sheldrick and D. Stalke, *J. Appl. Crystallogr.*, 2015, **48**, 3–10.
26. W. F. Armarego and C. L. L. Chai, *Purification of Laboratory Chemicals*, Elsevier, Waltham, MA, USA, 7th edn., 2013.

4 Molybdenum Oxido Bond 1,2-Addition and Cycloaddition Reactivity

4.1 Introduction

Reactive metal-element bonds are essential in the preparation of group VI complexes for use in homogeneous catalysis. Exploration of catalyst precursors and different synthetic approaches can result in the elucidation of new types of transformations or methods, and offers the opportunity to evaluate the impact of different ligand frameworks on precursor reactivity and catalyst performance.

Imido ligands bearing a Mo=N double bond can act as either reactive functionalities, or supporting ancillary groups on the metal center. One method for the generation of imido ligands on group VI complexes is through CO_2 elimination by a metathesis reaction between an oxido (Mo=O) ligand and an isocyanate reagent (R-N=C=O). In principal, this type of transformation may be possible with other types of heteroallenes, to generate other types of metal element multiple bonds (M=E). For instance, a ketene derivative could eliminate CO_2 and generate an alkylidene ligand (Fig. 4.1, E = CR).

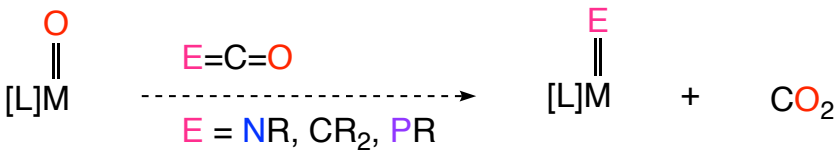

Figure 4.1: Generic metal-element multiple bond synthesis with heteroallenes and carbon dioxide elimination

A single previously reported example of a metathesis reaction between a rhenium-oxido group and diphenylketene ($Ph_2C=C=O$) showed that this reaction does not eliminate CO_2, and a bidentate ene-diolate ligand is generated, which incorporates a 4-membered dioxarhenacyclobutane (Fig. 4.2).[1]

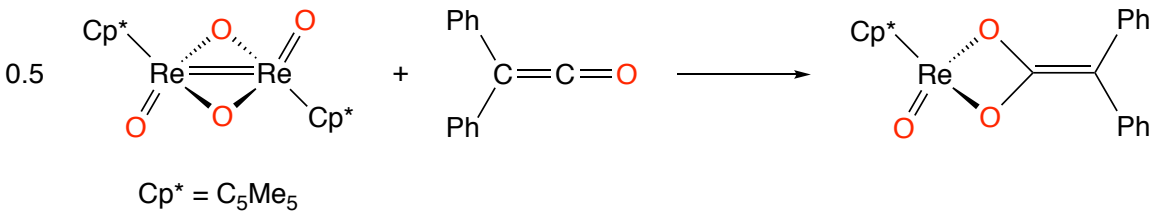

Figure 4.2: Ene-diolate ligand formation via ketene cycloaddition

While this example emphasizes potential difficulties in alkylidene generation from allene derivatives, other types of heteroallenes, with different electronic structures, may result in more desirable reactivity. Alkylidene formation could also be promoted by additional modification of the allene reagents, or the metal complex, to overcome electronic challenges to reactivity.

The potential for this type of reaction to create metal-element multiple bonds and eliminate CO_2 would be immense in terms of reaction efficiency and synthetic utility, and may be useful with other kinds of transition metals beyond

group VI. For group VI metals, this transformation could enable a highly effective synthetic route into catalysts that can generate polymers that incorporate heteroatoms, such as polymers containing P=C bonds. Current research on these materials is limited by difficult syntheses and low atom economy.

Isocyanates are commercially available reagents, and the chemistry to generate ketenes has been thoroughly studied.[2] In contrast, there has been limited research regarding the synthesis and properties of phosphaketenes, and the known methods all involve highly toxic reagents. As these hazardous reagents drastically limit our ability to study and use phosphaketenes, alternative methods to synthesize phosphaketenes were evaluated.

Similarly, the study of phosphaketene reactions with transition metals has been very limited, with one important example involving a group VI complex. In this case, 2,4,6-*tris*(*tert*-butyl)phenylphosphaketene was combined with $[WCl_2(P(CH_3)Ph_2)_4]$, where oxidative addition generates a terminal phosphinidene ligand and a metal-bound CO ligand (Fig. 4.3).[3] It is interesting to note that CO_2 elimination is not possible under these conditions.

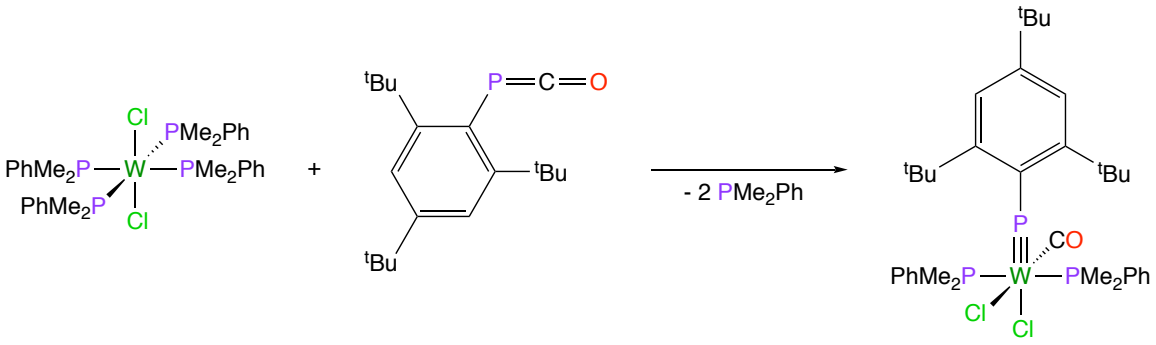

Figure 4.3: Terminal phosphinidene synthesis from phosphaketene oxidative addition

With this single example of transition metal based phosphaketene reactivity, it is unknown if other types of reactivity are possible with different transition metals, oxidation states, or ligand systems, making this an important area to investigate.

Chapters 2 and 3 described the development of the phosphinimide platform to support oxygen, nitrogen, and carbon multiple bonds in molybdenum complexes. Given this basis, and the interest in developing ways to catalytically generate phosphorus-containing polymers, which would require a catalyst with a Mo=P bond, this chapter focuses on the reactivity of phosphinimide ligand supported Mo=O bonds with reagents that can enable new approaches to generating reactive Mo=C and Mo=P bonds. In addition, new synthetic approaches to generate relevant organophosphorus compounds for use in Mo=O cycloaddition chemistry will be discussed.

4.2 Results and Discussion

4.2.1 Isocyanate Reactivity with Metal-Oxido Ligands

Isocyanates (R–N=C=O) are known to react with metal-oxido bonds, resulting in the formation of a metal-imido species with concomitant elimination of CO_2 as a byproduct (Fig. 4.4).[4,5]

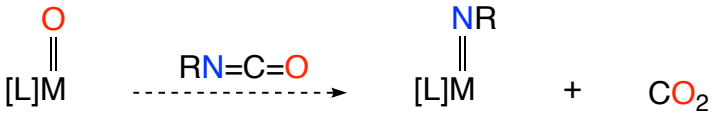

Figure 4.4: Generic imido ligand synthesis through [2+2] cycloaddition of organic isocyanates and metal-oxido species

This type of reactivity was assessed for some of the oxido complexes generated in Chapter 2, particularly the oxido-dichlorido **2.4** and dioxido complex **2.12**.

Complex **2.4** can be combined with 2,6-dimethylphenylisocyanate (2,6-Ph-N=C=O) to generate **4.1** through CO_2 elimination (Fig. 4.5), which can be observed by monitoring the ^{1}H-decoupled ^{31}P NMR spectrum of the reaction solution (Fig 4.6).

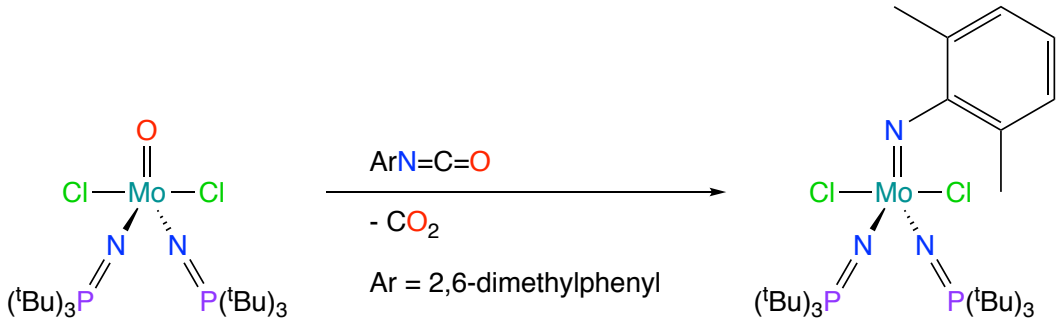

Figure 4.5: Synthesis of **4.1** from **2.4** and 2,6-dimethylphenylisocyanate

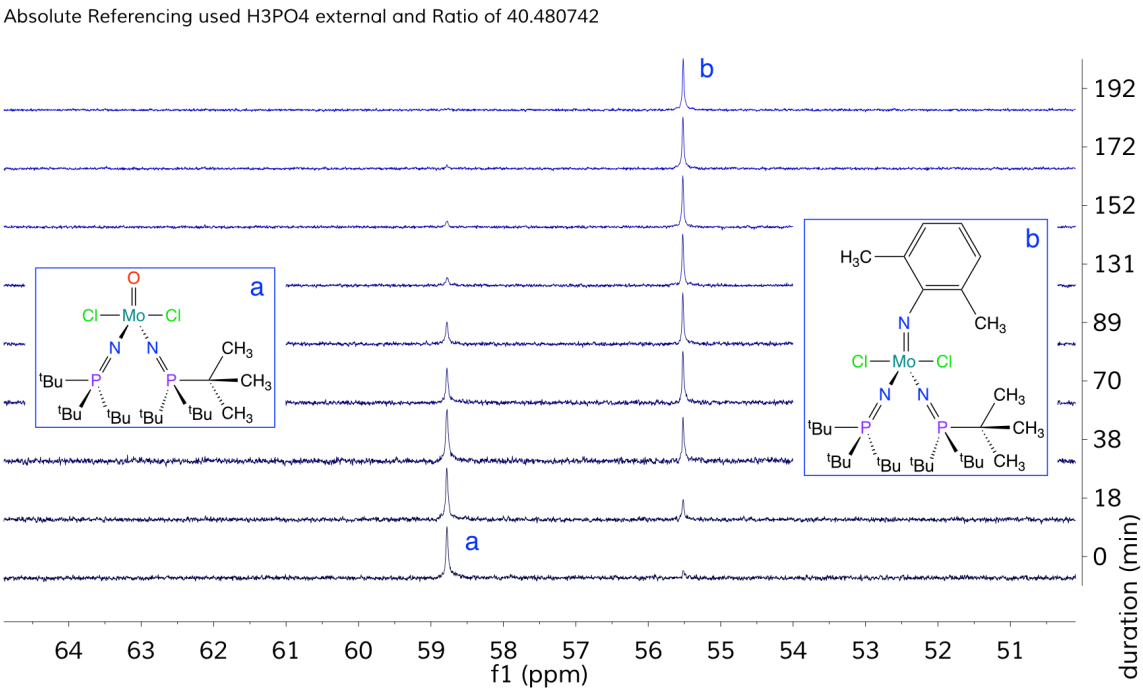

Figure 4.6: $^{31}P\{^{1}H\}$ NMR spectra of conversion of **2.4** (a) conversion to **4.1** (b) in C_6D_6 over 3.2 hours (202 MHz)

Complex **4.1** has been characterized by NMR spectroscopy, single crystal XRD. Based on the XRD structure, which is shown in Fig. 4.7, **4.1** is pseudo C_s symmetric with a trigonal bipyramidal (τ_5 = 0.91) ligand geometry about the metal center.

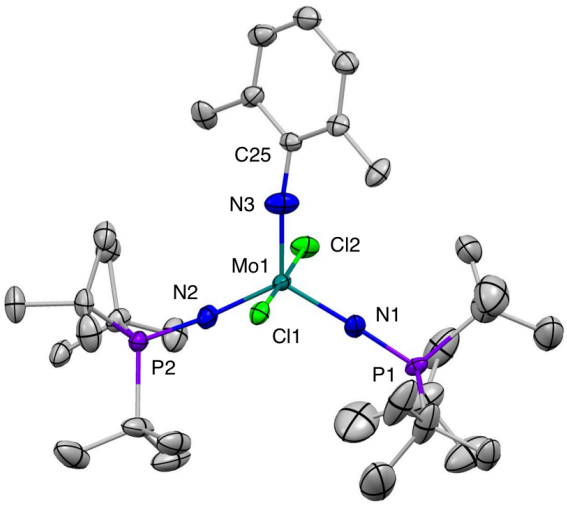

Figure 4.7: Thermal ellipsoid plot (50% probability) of complex **4.1**. Hydrogen atoms have ben omitted for clarity

Visualization of the space-filling model of the XRD structure of **4.1** shows a well-enveloped metal center, with close contacts between the phosphinimide *tert*-butyl groups and the methyl groups of the 2,6-dimethylphenylimido ligand (Fig 4.8).

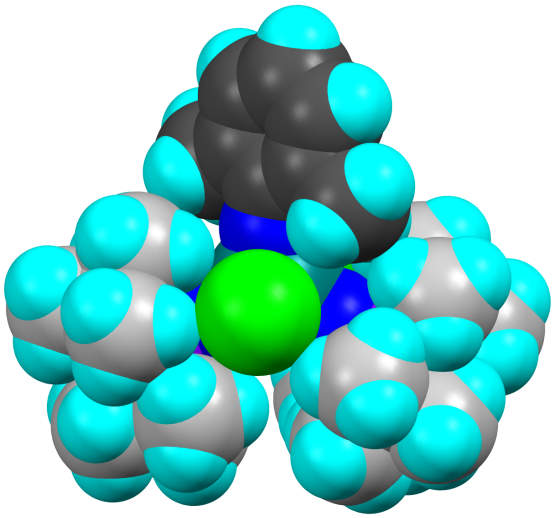

Figure 4.8: Space-filling model of complex **4.1** (van der Waals radii), imido carbon atoms indicated in dark grey

Comparison of **4.1** with the related *tert*-butyl imido complex **2.5** reveals the expected effects of the less electron donating 2,6-methylphenyl fragment relative to the *tert*-butyl fragment. The molybdenum-imido (Mo1-N3) bond distance in **4.1** is larger than in **2.5**, and all other coordinated bond distances are decreased to stabilize the slightly more positive metal center (Table 4.1).

Table 4.1: Selected XRD Bond Distances for Complex **4.1**

Atoms	**Length (Å)**	**Atoms**	**Length (Å)**
Mo1-Cl1	2.466(2)	Mo1-N3	1.769(8)
Mo1-Cl2	2.494(2)	P1-N1	1.602(7)
Mo1-N1	1.843(7)	P2-N2	1.602(7)
Mo1-N2	1.843(7)	N3-C25	1.37(11)

The imido ligand bond angle (Mo1-N3-C25) is more linear in **4.1** than **2.5**, which is likely a result of close steric interactions between the imido ligand methyl groups and the phosphinimide *tert*-butyl groups (Table 4.2). While the other bond angles in **4.1** are similar to **2.5**, the steric interactions indicated above can also be observed by a decrease in the bond angle between the phosphinimide ligands (N1-Mo1-N3) by 3.3(5)°.

Table 4.2: Selected XRD Bond Angles for Complex **4.1**

Atoms	**Angle (°)**	**Atoms**	**Angle (°)**
Mo1-N1-P1	171.6(5)	N1-Mo1-N2	122.8(3)
Mo1-N2-P2	171.6(5)	Cl1-Mo1-Cl2	177.63(7)
N1-Mo1-N3	119.6(4)	Cl1-Mo1-N3	90.6(3)
N2-Mo1-N3	117.6(4)	Cl2-Mo1-N3	87.1(3)
Mo1-N3-C25	171.1(8)	–	–

In solution, the ^{1}H NMR spectrum (Fig. 4.9) of **4.1** contains the expected phosphorus-coupled doublet for the phosphinimide *tert*-butyl groups at 1.47 ppm ($^{3}J_{PH}$ = 13.6 Hz), and a singlet for the arylmethyl protons at 3.06 ppm.

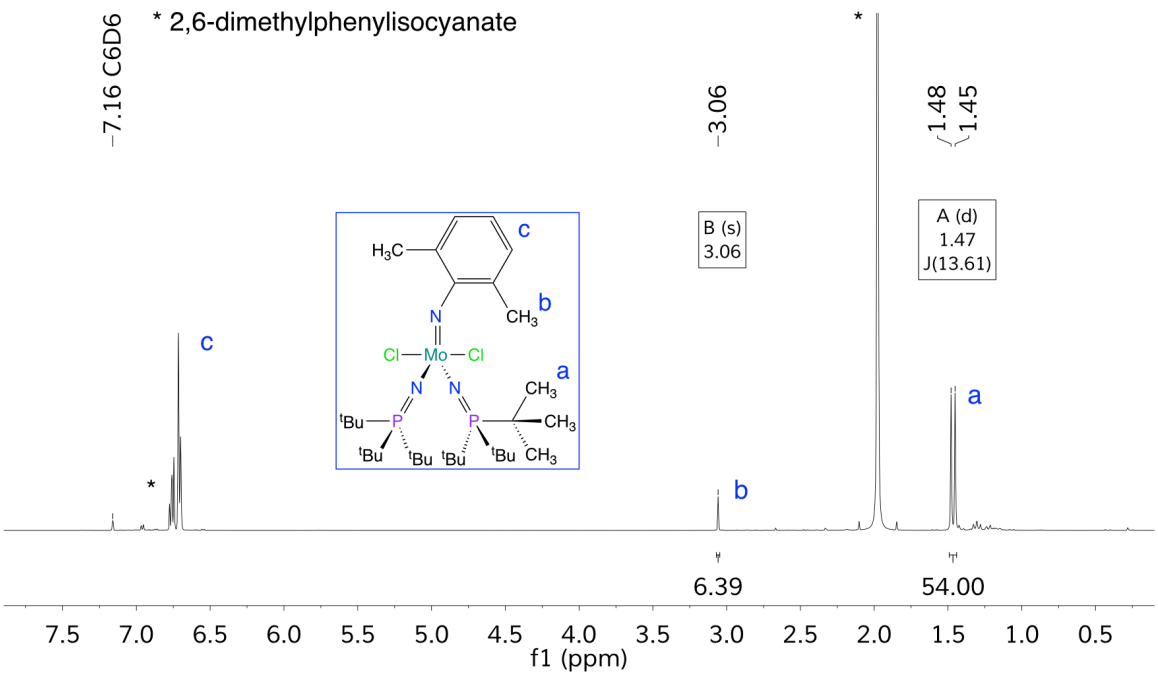

Figure 4.9: ^{1}H NMR spectrum of **4.1** in C_6D_6 with excess 2,6-dimethylphenylisocyanate (500 MHz)

Clean generation of the imido product is also supported by the $^{31}P\{^{1}H\}$ NMR spectrum (Fig. 4.10) of **4.1**, which contains a singlet at 55.52 ppm for the equivalent phosphinimide ligand environments.

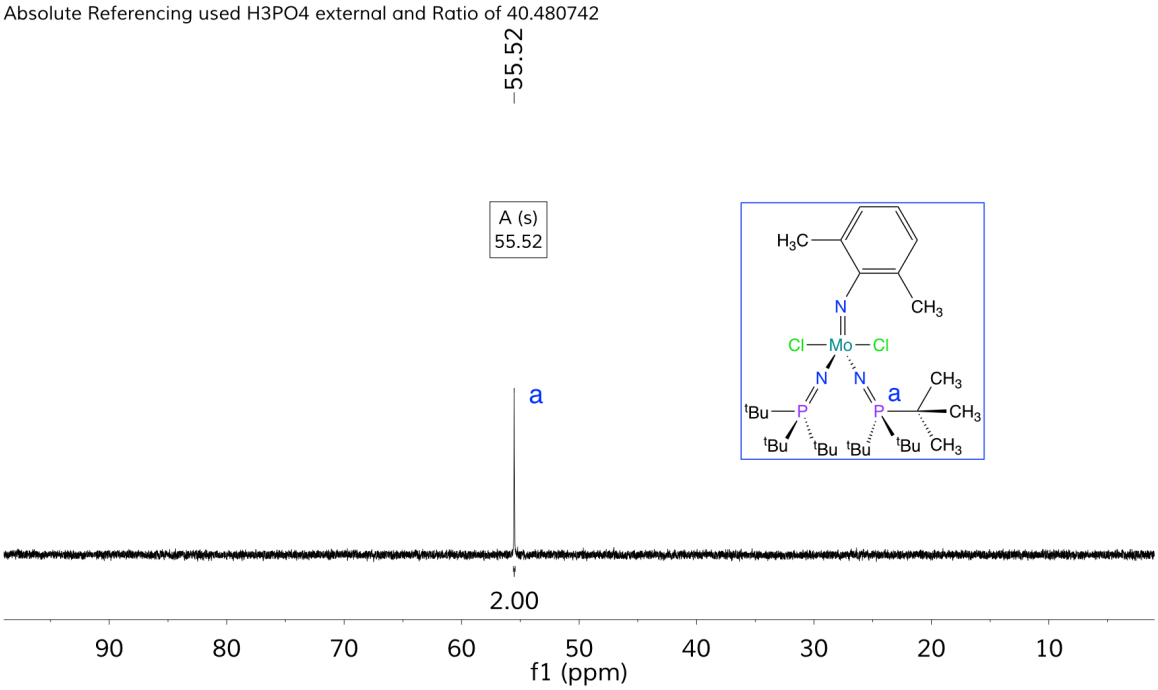

Figure 4.10: $^{31}P\{^{1}H\}$ NMR spectrum of **4.1** in C_6D_6 (202 MHz)

The analogous isocyanate reaction with **2.4** can be performed with phenylisocyanate (Ph-N=C=O), and also results in clean formation of the corresponding imido fragment in complex **4.2** (Fig. 4.11), which can be observed by monitoring the $^{31}P\{^{1}H\}$ (Fig. 4.12) and ^{1}H (Fig. 4.13) NMR spectra of the reaction solution.

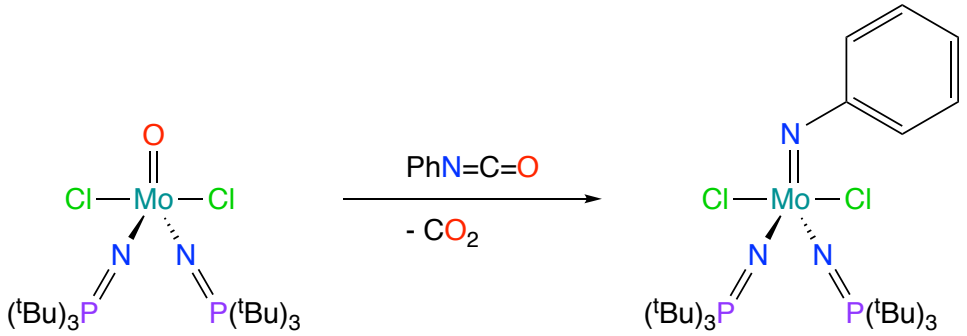

Figure 4.11: Synthesis of **4.2** through [2+2] cycloaddition of **2.4** phenyl isocyanate

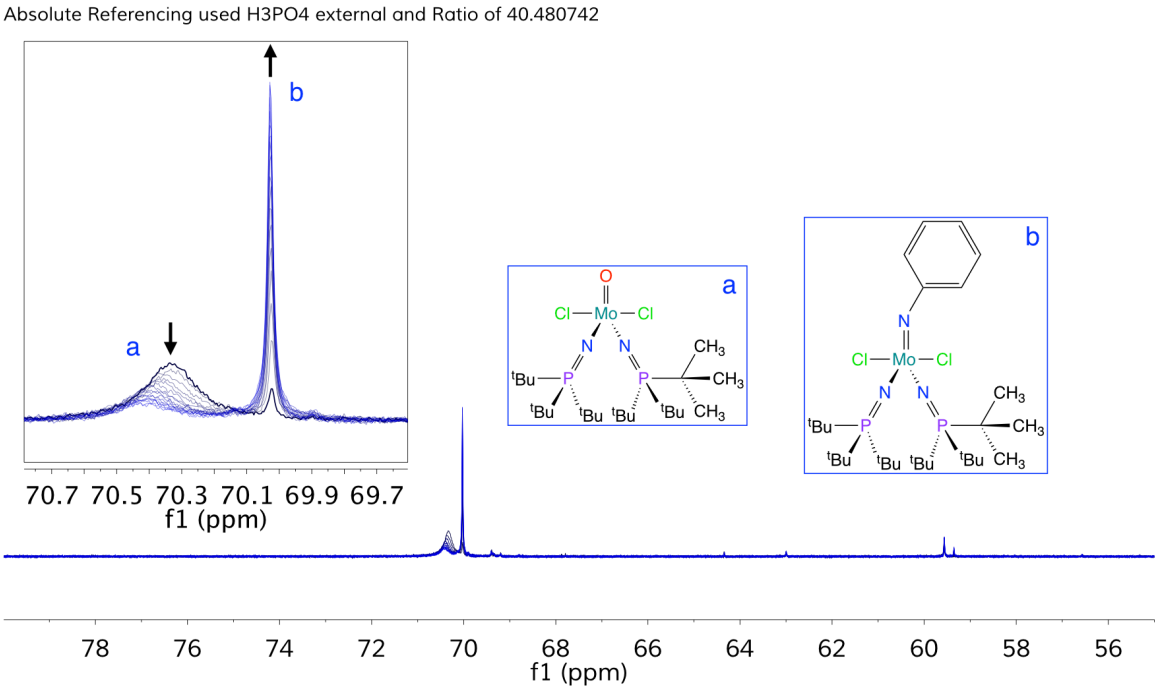

Figure 4.12: $^{31}P\{^{1}H\}$ NMR spectra of conversion of **2.4** (a) conversion to **4.2** (b) in C_6D_6 over six hours (162 MHz)

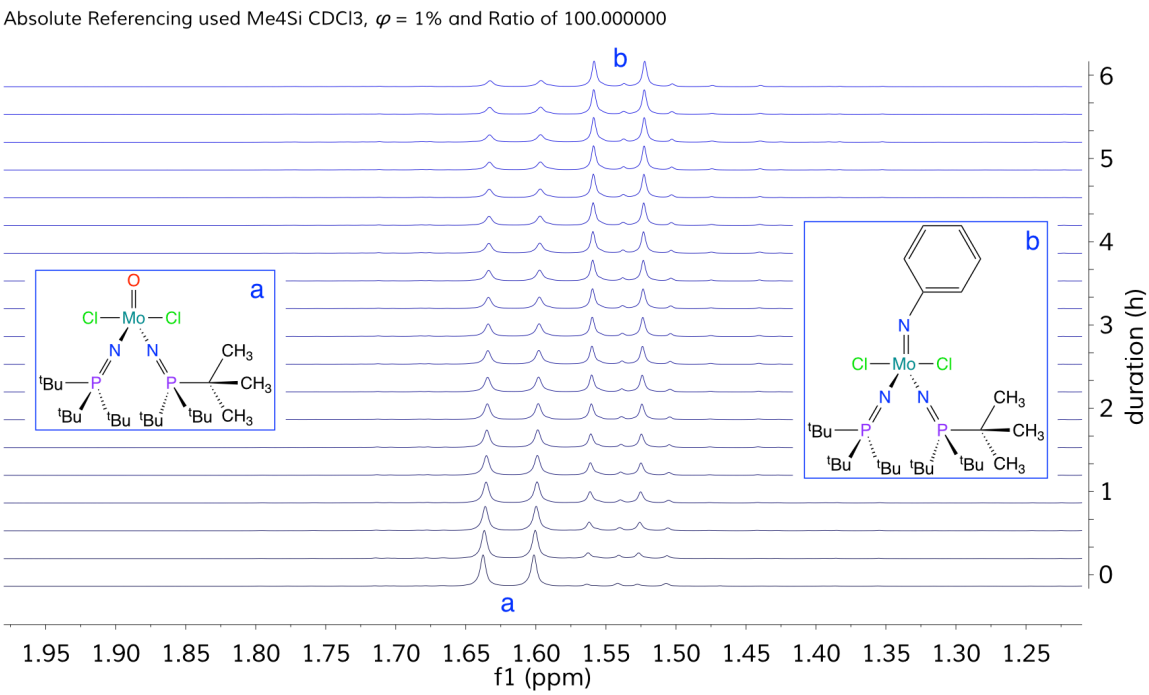

Figure 4.13: ^{1}H NMR spectra of conversion of **2.4** (a) conversion to **4.2** (b) in C_6D_6 over six hours (400 MHz)

The ^{1}H NMR spectrum of **4.2** contains the expected phosphorus-coupled doublet for the phosphinimide *tert*-butyl groups at 1.54 ppm ($^{3}J_{PH}$ = 14.4 Hz) (Fig. 4.14). The ^{1}H-decoupled ^{31}P{^{1}H} NMR spectrum of **4.2** contains a singlet at 70.03 ppm for the equivalent phosphinimide ligand environments (Fig. 4.15).

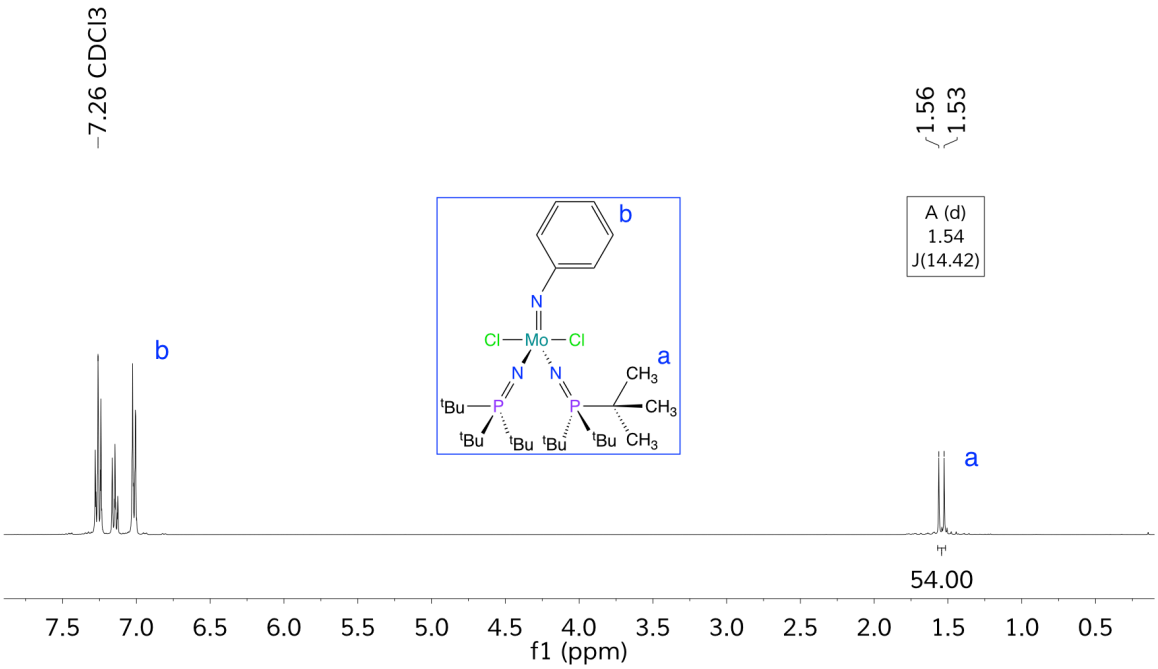

Figure 4.14: ^{1}H NMR spectrum of **4.2** in $CDCl_3$ (400 MHz)

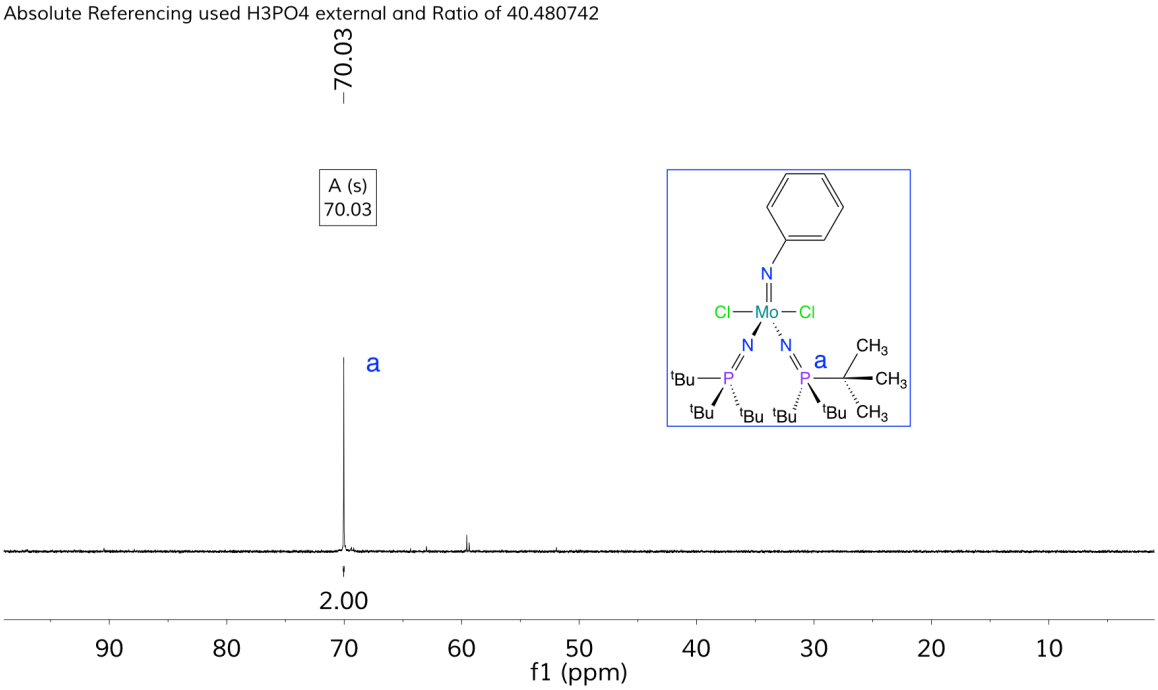

Figure 4.15: $^{31}P\{^{1}H\}$ NMR spectrum of **4.2** in in $CDCl_3$ (162 MHz)

4.2.2 Ketene Reactivity with Metal-Oxido Ligands

Given that it is theoretically possible to form alkylidene complexes through CO_2 elimination between ketenes and metal oxido species, and the dearth of information regarding this reaction, studies were undertaken to examine the reactivity of Mo=O bonds with the $R_2C=C=O$ fragment. Complex **2.4** can be combined with diphenylketene to generate the corresponding ene-diolate complex (Fig. 4.16) in high yield. This reaction is believed to proceed through the expected stepwise transformation, with initial formation of a red charge separated intermediate, followed by subsequent coordination of the ketene oxygen atom to form the dark green product complex. This product forms as a result of [2+2] cycloaddition of the terminal C=O bond with the Mo=O bond, rather than the internal C=C bond, which could result in CO_2 elimination.

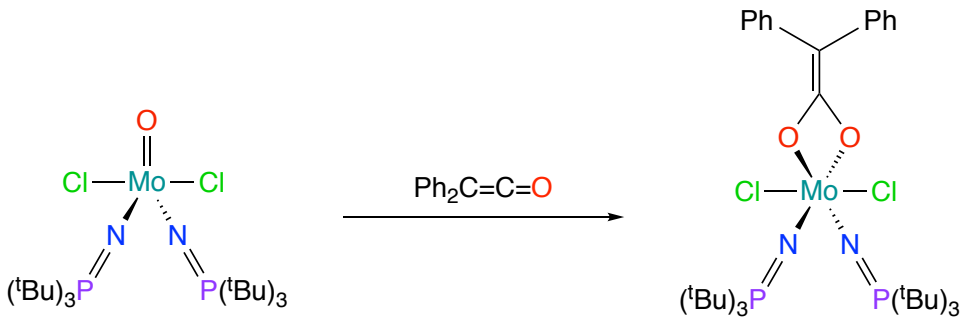

Figure 4.16: Synthesis of **4.3** through [2+2] cycloaddition of a Mo=O bond with diphenylketene

Complex **4.3** has been characterized by NMR, XRD, and EA. Based on the XRD structure, **4.3** is pseudo C_2 symmetric (or C_{2v} if the phenyl fragments can freely rotate), with a distorted octahedral core geometry due to the acute bite angle of the ene-diolate ligand (Fig. 4.17).

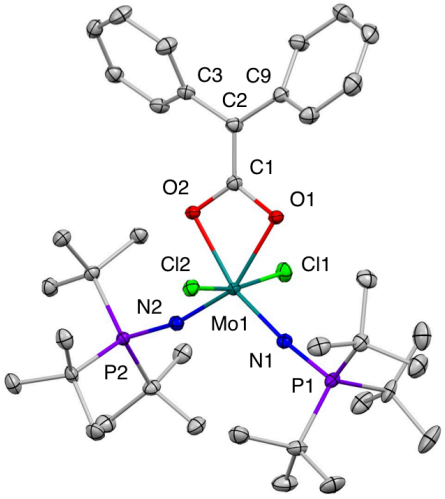

Figure 4.17: Thermal ellipsoid plot (50% probability) of complex **4.3**. Hydrogen atoms and dichloromethane molecules have been omitted for clarity

Visualization of the space-filling model of the XRD structure of **4.3** (Fig. 4.18) with solvent molecules present shows close interactions of dichloromethane around the ene-diolato metallacycle.

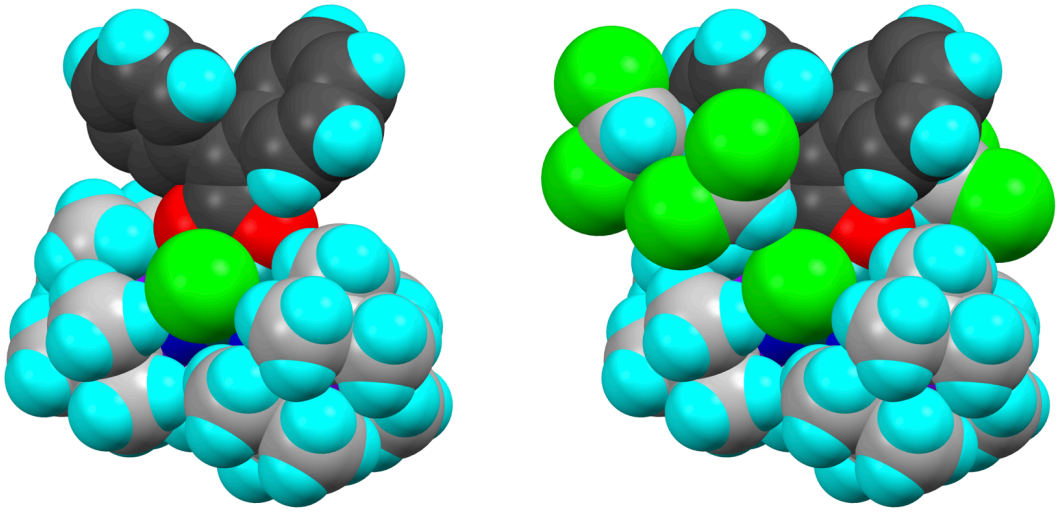

Figure 4.18: Space-filling model of complex **4.3** (van der Waals radii) with dichloromethane molecules omitted for clarity (left) and visible to show solvent interactions (right), ene-diolate carbon atoms indicated in dark grey

Compared with the reported rhenium complex, complex **4.3** has longer metal-oxygen bond lengths (Mo-O) (Table 4.3), which may be primarily an effect of the atomic radii differences between metals, or the lower oxidation state of the molybdenum ion (+6) versus the rhenium ion (+7). The metal-carbon (Mo1-C1) distance is slightly longer in **4.3** relative to the rhenium complex by 0.035(6) Å.

Table 4.3 Selected XRD Bond Distances for Complex **4.3**

Atoms	**Length (Å)**	**Atoms**	**Length (Å)**
Mo1-Cl1	2.4377(4)	Mo1-C1	2.5303(17)
Mo1-Cl2	2.4597(4)	C1-O1	1.331(2)
Mo1-N1	1.8221(14)	C1-O2	1.319(2)
Mo1-N2	1.8117(15)	C1-C2	1.386(2)
Mo1-O1	2.0779(12)	P1-N1	1.6320(14)
Mo1-O2	2.0776(11)	P2-N2	1.6373(15)

4.3 exhibits a more acute oxygen-metal-oxygen angle (O1-Mo1-O2) than the rhenium complex, yet has a less acute oxygen-carbon-oxygen angle (O1-C1-O2) than the ene-diolate ligand (Table 4.4). The opposite changes in these angles indicates that the carbon atom is closer to the two oxygen atoms in **4.3**, which is apparent in the observed bond distances and is consistent with weaker oxygen coordination to the metal center.

The ene-diolate metallacycle is oriented nearly orthogonally to the chlorido ligands with an average O-Mo-Cl bond angle of 85.69(2)°, where this angle is slightly less than 90° due to the chlorido ligands being tilted slightly toward the ene-diolate ligand.

Table 4.4: Selected XRD Bond Angles for Complex **4.3**

Atoms	Angle (°)	Atoms	Angle (°)
Mo1-N1-P1	170.35(9)	O1-C1-O2	110.11(14)
Mo1-N2-P2	165.33(9)	Cl1-Mo1-O1	83.76(4)
N1-Mo1-N2	110.07(6)	Cl1-Mo1-O2	89.29(4)
Mo1-O1-C1	93.23(10)	Cl2-Mo1-O1	85.12(4)
Mo1-O2-C1	93.61(9)	Cl2-Mo1-O2	84.58(3)
O1-Mo1-O2	63.05(5)	Cl1-Mo1-Cl2	168.817(17)

The ene-diolate ligand has a planar geometry with a O1-C1-C2-C3 torsion angle of 176.21(15)° (Table 4.5), which indicates that the C1-C2 bond has double bond character. This is further supported by the C1-C2 bond distance of 1.386(2) Å, which is well within the range for a C=C fragment.

Table 4.5: Selected XRD Torsion Angles for Complex **4.3**

Atoms	Angle (°)	Atoms	Angle (°)
Mo1-O1-C1-C2	-179.17(16)	N1-Mo1-N2-P2	-154.9(3)
Mo1-O1-C1-O2	0.13(13)	N2-Mo1-N1-P1	-152.2(5)
O1-C1-C2-C3	176.21(15)	–	–

The ^{1}H NMR spectrum of **4.3** (Fig. 4.19) shows a doublet at 1.68 ppm ($^{3}J_{PH}$ = 14.4 Hz) for the ^{31}P coupled phosphinimide ligands that are equivalent in

solution. Broad aryl signals are also present at 6.83 and 7.26 ppm for the ene-diolate ligand.

The $^{31}P\{^{1}H\}$ NMR spectrum of **4.3** (Fig. 4.20) exhibits a singlet at 71.70 ppm for the major product, again supporting equivalent phosphinimide ligand environments in solution for this system.

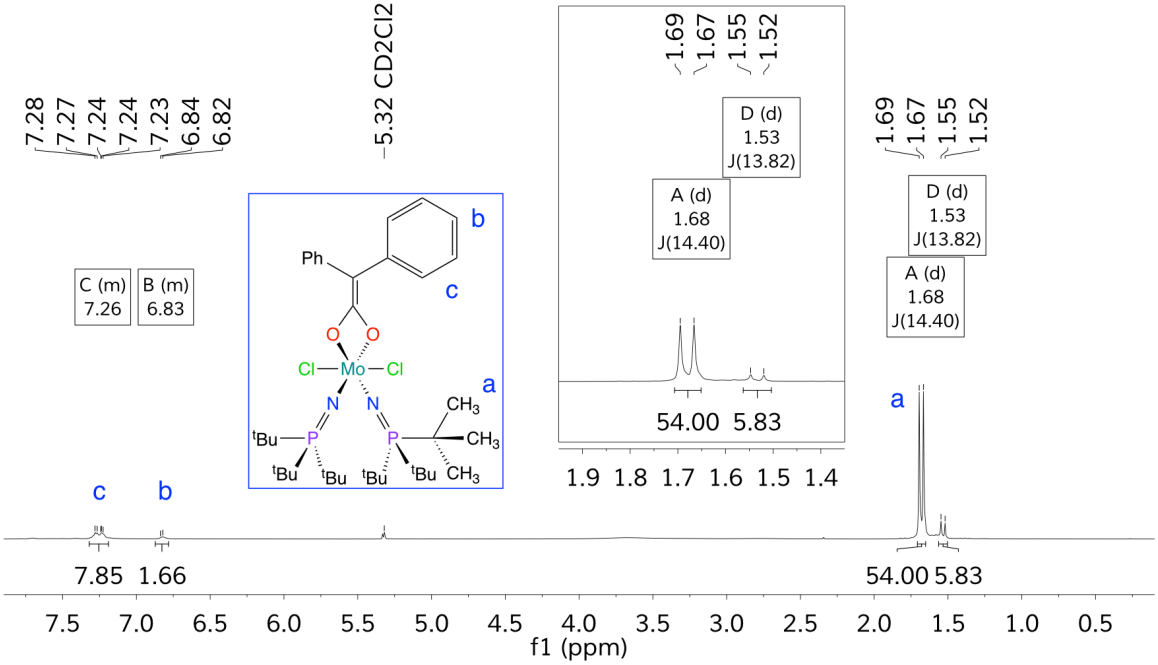

Figure 4.19: ^{1}H NMR spectrum of **4.3** in CD_2Cl_2 (500 MHz)

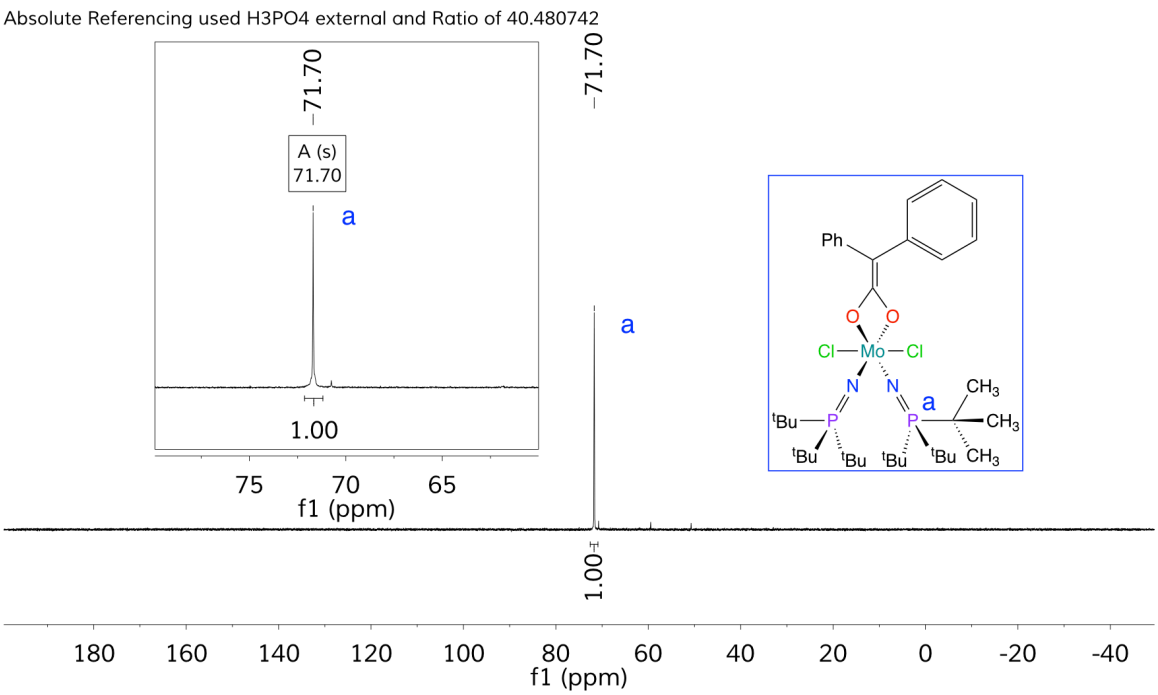

Figure 4.20: $^{31}P\{^{1}H\}$ NMR spectrum of **4.3** in CD_2Cl_2 (162 MHz)

The 2D gHMBCAD spectrum of **4.3** resolves a major cross-peak at 7.3 and 337.0 ppm for one of the alkene carbons of the ene-diolate ligand (Fig. 4.21). There are three additional cross-peaks of lower intensity at different ^{13}C chemical shifts, with one at 325.9 ppm, and further upfield cross-peaks at 273.7 and 262.8 ppm. These signals suggest slightly varied conformations of the ene-diolate fragment due to the far downfield chemical shifts observed, in a region that does not correspond with many molecular fragments, as well as a similar separation of peaks observed for complex **4.4** (Fig. 4.28).

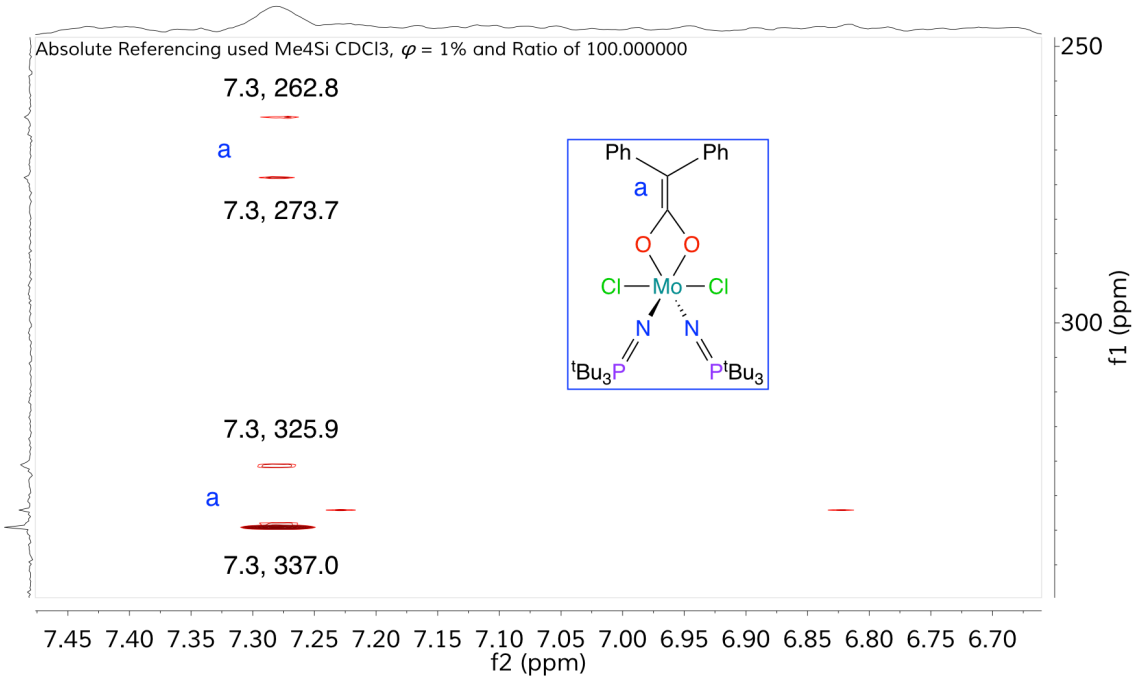

Figure 4.21: ^{1}H-^{13}C gHMBCAD NMR spectrum of **4.3** in CD_2Cl_2 (500 MHz, 126 MHz)

The ene-diolate ligand in **4.3** is thermally labile and **2.4** was regenerated by heating **4.3** at 50°C for 1 hour, resulting in phosphinimide ^{1}H and ^{31}P NMR signals that match **2.4**. Considering the relative stability of diphenylketene, and the robustness of the Mo=O bond, it is not surprising that the kinetic product is the ene-diolate species, and the thermodynamic product is the starting materials. Complex **4.3** can be further converted to the cationic borate complex **4.4** by reaction with a stoichiometric equivalent of sodium tetrakis[3,5-bis(trifluoromethyl)phenyl]borate, as shown in Fig. 4.22.

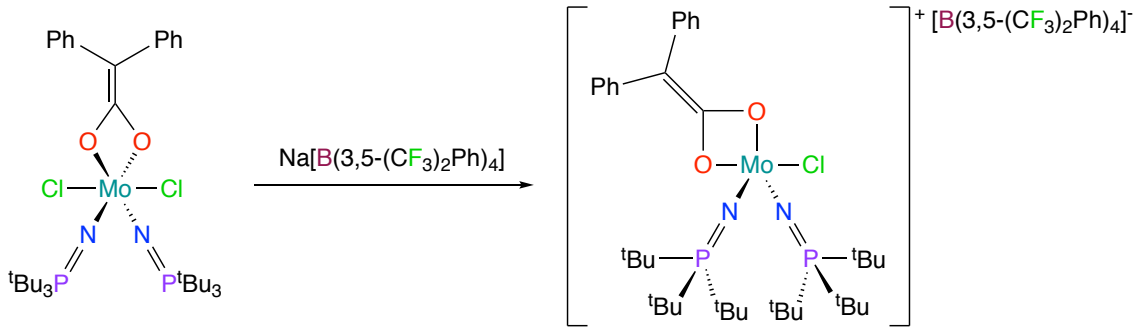

Figure 4.22: Synthesis of **4.4** by reaction of **4.3** with sodium tetra(3,5-bis(trifluoromethyl)phenyl)borate

At 25 °C, the ^{1}H NMR spectrum shows a doublet at 1.47 ppm ($^{3}J_{PH}$ = 14.5 Hz) for the ^{31}P coupled phosphinimide ligands that are equivalent in solution (Fig. 4.23). Broad aryl signals are also present at 7.30 ppm for the ene-diolate ligand, and at 7.59 and 7.75 ppm for the borate anion aromatic protons.

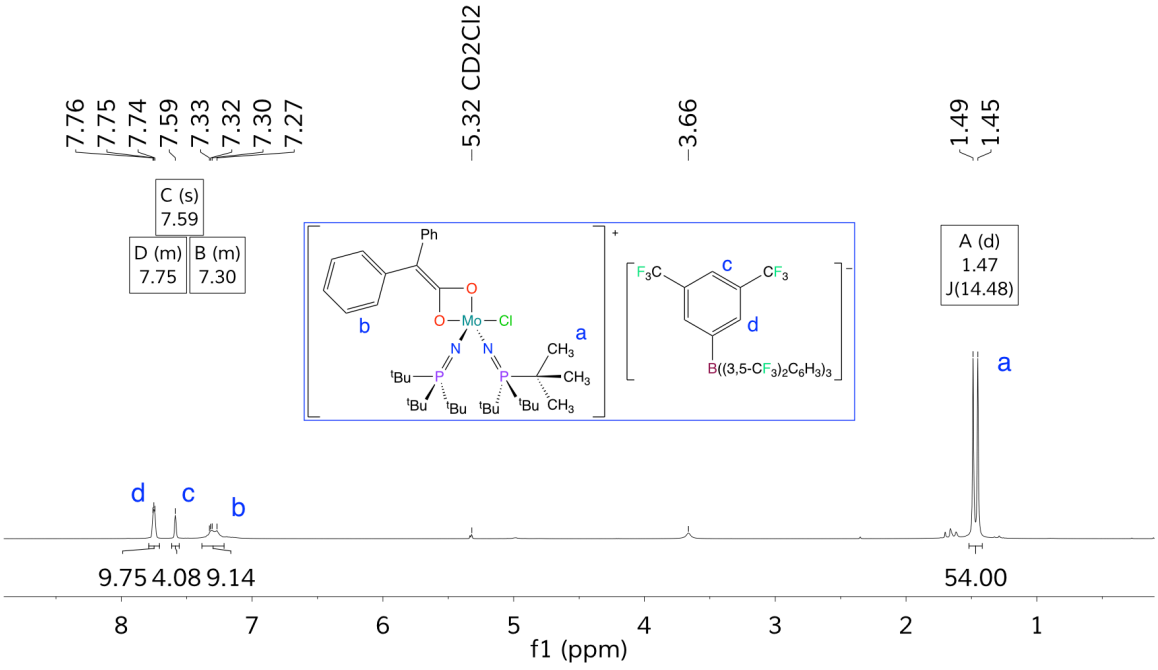

Figure 4.23: ^{1}H NMR spectrum of **4.4** in CD_2Cl_2 (400 MHz)

The $^{31}P\{^{1}H\}$ NMR spectrum of **4.4** is given in Fig. 4.24, and exhibits a singlet at 69.79 ppm for the major product, again supporting equivalent phosphinimide ligand environments in solution for this system. A minor peak was also located at 89.13 ppm, which is an unidentified side product, and is present in approximately 7% yield.

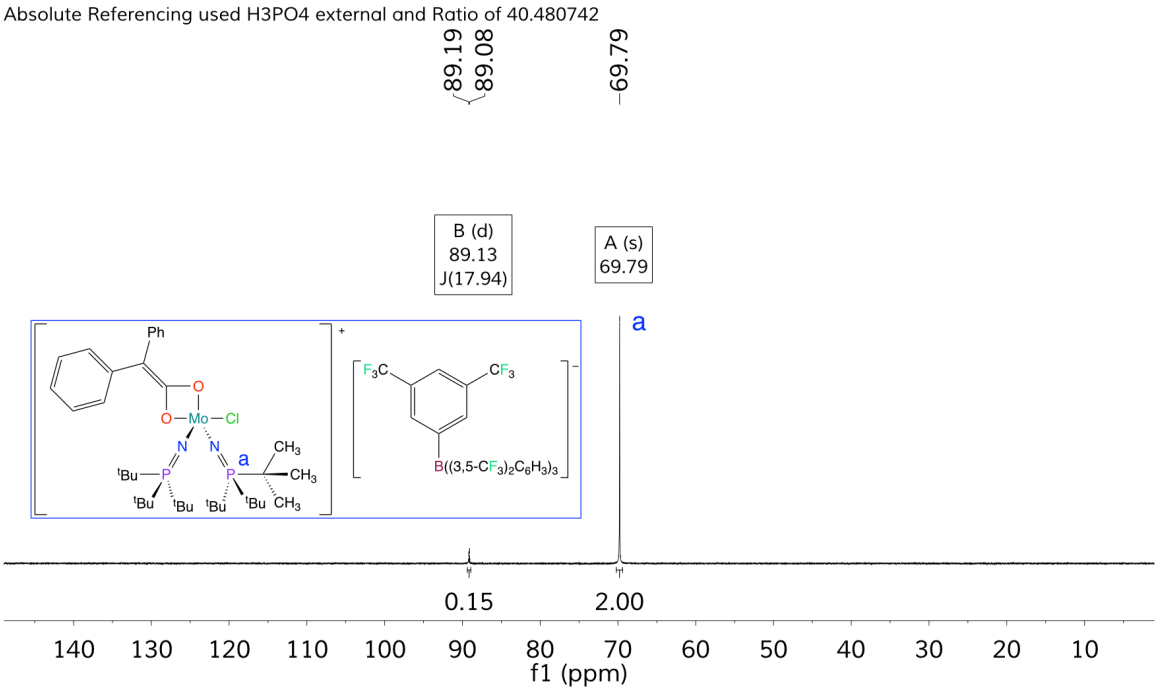

Figure 4.24: $^{31}P\{^{1}H\}$ NMR spectrum of **4.4** in CD_2Cl_2 (162 MHz)

The $^{13}C\{^{1}H\}$ NMR spectrum is shown in Fig. 4.25 and contains a *tert*-butyl singlet at 28.50 ppm, and a ^{31}P coupled *tert*-butyl quaternary carbon doublet at 39.23 ppm ($^{1}J_{PC}$ = 39.7 Hz) for the phosphinimide ligands. All expected signals for the borate counterion are present and observable, including a singlet at 117.42 ppm for the *para*-carbon relative to the boron center, a fluorine coupled quartet at 124.55 ppm ($^{1}J_{CF}$ = 272.3 Hz) for the trifluoromethyl groups, and resonances at 128.97 ppm for the CF_3-subsituted

arene, 134.74 ppm for the *meta*-carbon relative to the boron center, and 161.72 ppm ($^{1}J_{BC}$ = 49.9 Hz) for the *ipso*-carbon adjacent to the boron center, which is manifested as a quartet due to coupling to the spin 3/2 ^{11}B nucleus. The ene-diolate aryl signals overlap significantly and are observed in the multiplet peak centered at 128.97 ppm, while the two alkenyl carbon signals could not be detected using conventional one dimensional $^{13}C\{^{1}H\}$ NMR spectroscopy (vide infra).

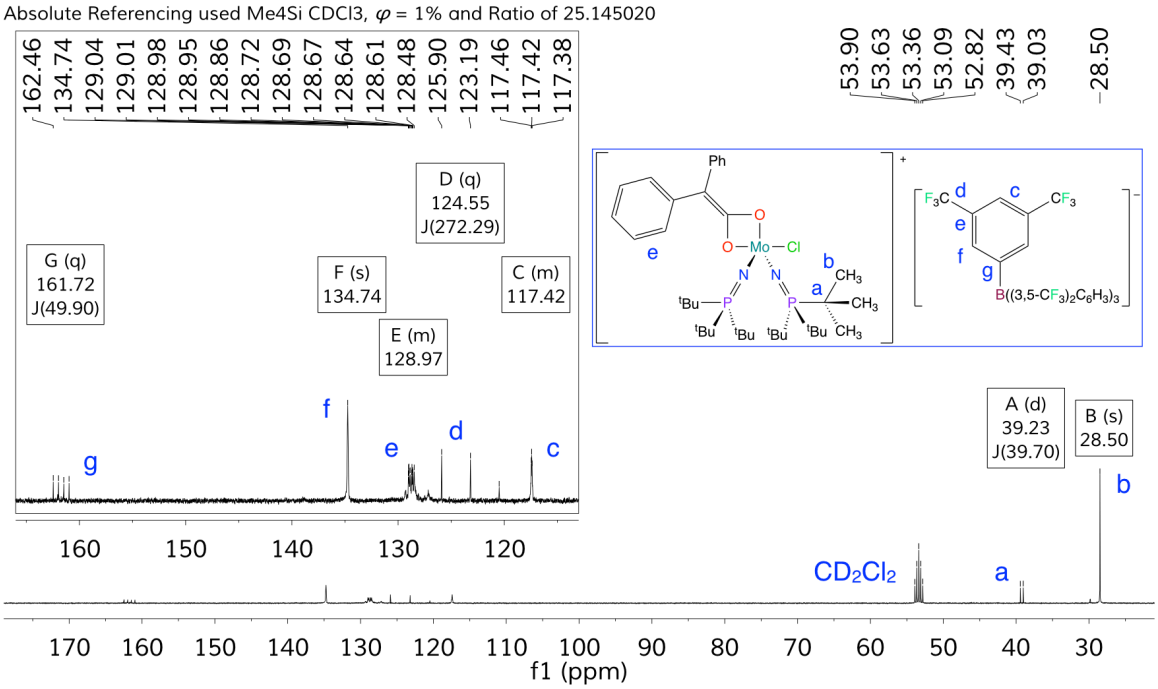

Figure 4.25: $^{13}C\{^{1}H\}$ NMR spectrum of **4.4** in CD_2Cl_2 (101 MHz)

The ^{19}F NMR spectrum shows the expected singlet at -62.81 ppm for the equivalent trifluoromethyl groups of the borate counterion (Fig 4.26), and the ^{11}B NMR spectrum supports the presence of a single B environment, with a

singlet at -6.61 ppm for the central boron atom of the borate counterion (Fig. 4.27).

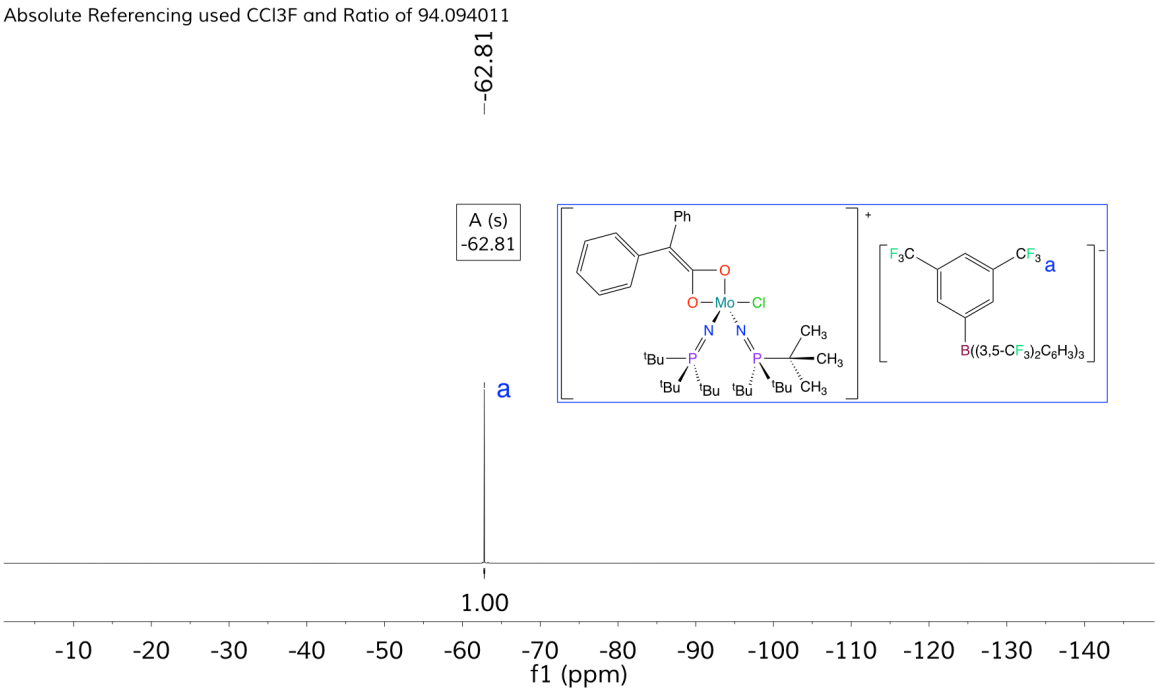

Figure 4.26: ^{19}F NMR spectrum of **4.4** in CD_2Cl_2 (376 MHz)

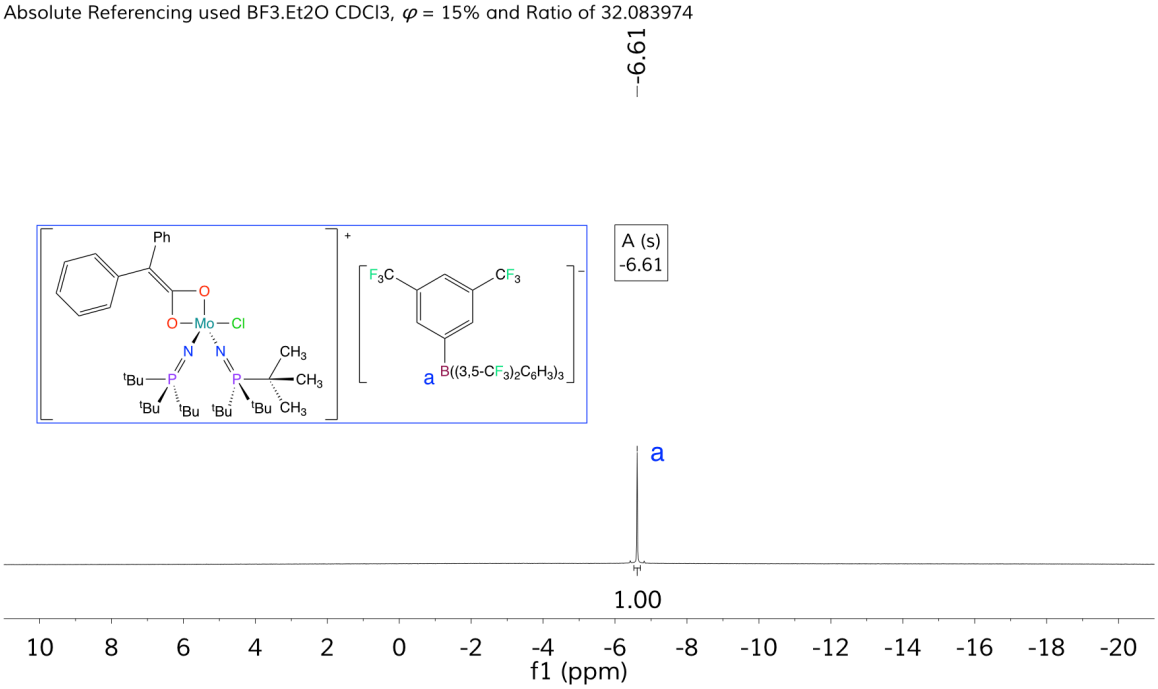

Figure 4.27: ^{11}B NMR spectrum of **4.4** in CD_2Cl_2 (128 MHz)

The 2D gHMBCAD spectrum of **4.4** resolves the two expected ^{13}C signals for the ene-diolate ligand (Fig. 4.28). The peaks are also assigned to specific carbons based on the difference in chemical shifts, and weak coupling (< 5 Hz) of the peak at 317.5 ppm in the ^{13}C channel which is believed to be 4-bond coupling to the phosphinimide ^{31}P nuclei, based on the similar magnitude of this coupling observed in complex **3.2**. The exact coupling constant is not defined, as the resolution of this spectrum cannot accurately quantify that value.

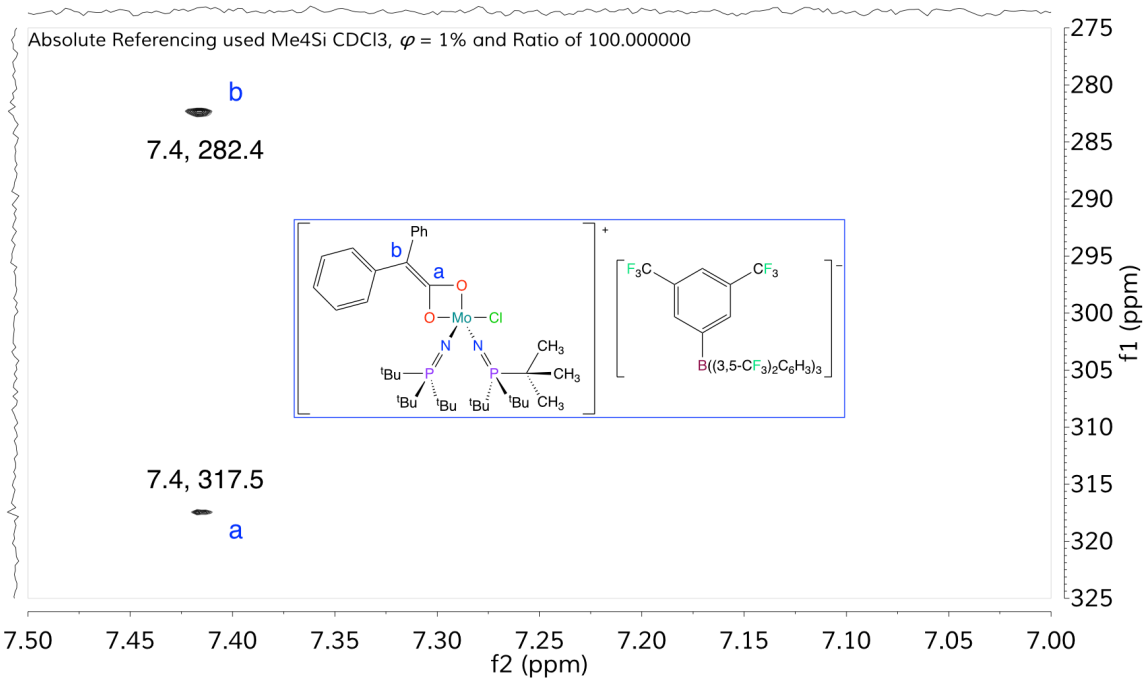

Figure 4.28: ^{1}H-^{13}C gHMBCAD NMR spectrum of **4.4** in CD_2Cl_2 (500 MHz, 126 MHz)

While the exact structure of **4.4** is not known, the analogous borate complex **4.5** generated from **2.4** was synthesized to verify that **4.4** does incorporate the diphenylketene within the complex (Fig. 4.29).

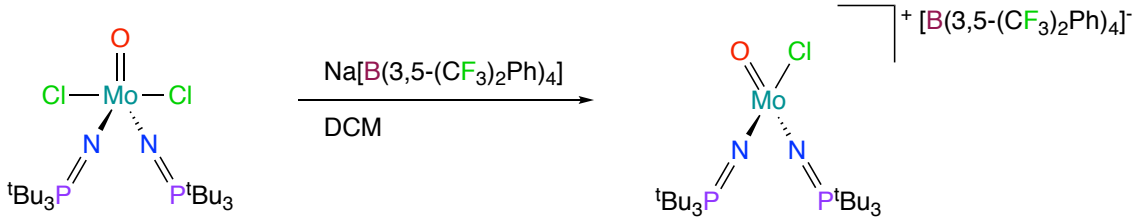

Figure 4.29: Synthesis of **4.5** by reaction of **2.4** with sodium tetra(3,5-bis(trifluoromethyl)phenyl)borate

The ^{1}H NMR spectrum of **4.5** exhibits the expected doublet at 1.54 ppm for the *tert*-butyl groups on the phosphinimide ligands, and two broad singlets at 7.55 and 7.71 ppm for the borate anion aryl protons (Fig. 4.30). The phosphinimide proton signals are substantially different than those observed for complex **4.4**, which indicates that **4.4** is not the same as **4.5** and that the diphenylketene is coordinated to the complex. The ^{1}H NMR chemical shifts for **4.5** are similar to the starting complex **2.4** when characterized in the same solvent, yet are shifted approximately 0.1 ppm upfield.

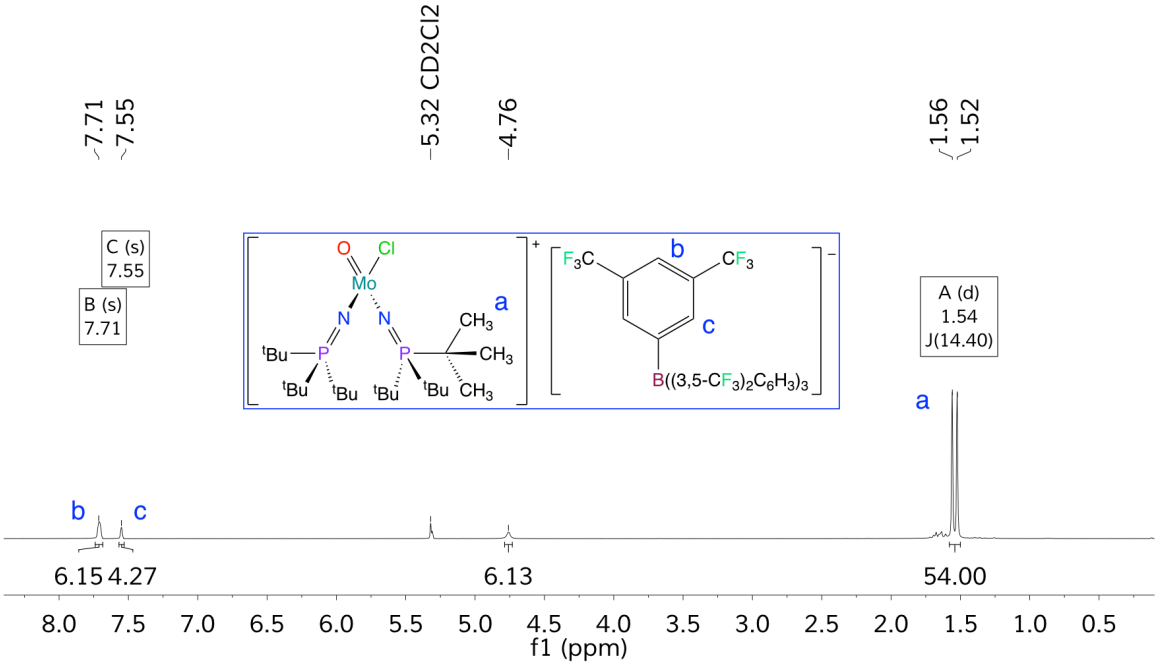

Figure 4.30: ^{1}H NMR spectrum of **4.5** in CD_2Cl_2 (400 MHz)

The ^{31}P{^{1}H} NMR spectrum **4.5** exhibits a singlet at 69.84 ppm, consistent with a single phosphinimide environment for the two ligands (Fig. 4.31). The chemical shift of this resonance is less than 1 ppm different than the analogous signal in **4.4**, and is almost identical to the analogous signal in **2.4**.

Based on the ^{1}H NMR spectra, the previously discussed 2D NMR data for **4.4**, and physical observations of color changes between the complexes and mass of materials isolated, it is reasonable each of these complexes is unique. Interestingly, despite the changes in coordination number and electronic structure, the ^{31}P NMR signals observed are relatively similar, which suggests these changes do not impact the phosphinimide chemical environment significantly, or the effects are balanced.

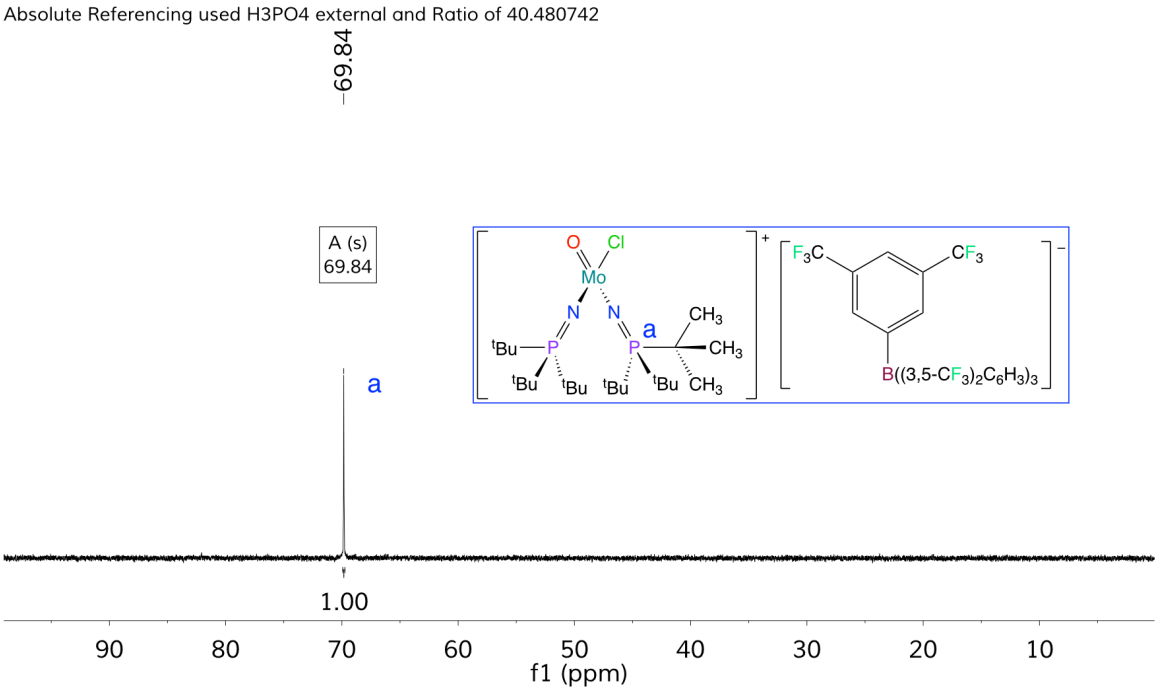

Figure 4.31: $^{31}P\{^{1}H\}$ NMR spectrum of **4.5** in CD_2Cl_2 (162 MHz)

The ^{19}F NMR spectrum of **4.5** contains the expected singlet for the trifluoromethyl groups on the borate anion at -62.91 ppm (Fig. 4.32), and the ^{11}B NMR spectrum of **4.5** likewise supports a single boron environment with a

singlet at -6.64 ppm for the borate anion (Fig. 4.33). Both of these measurements are within the expected range for this borate anion. The ^{19}F and ^{11}B NMR spectra differences between **4.5** and **4.4** are negligible, which is expected given the similar chemical environment of the outer sphere borate counterion.

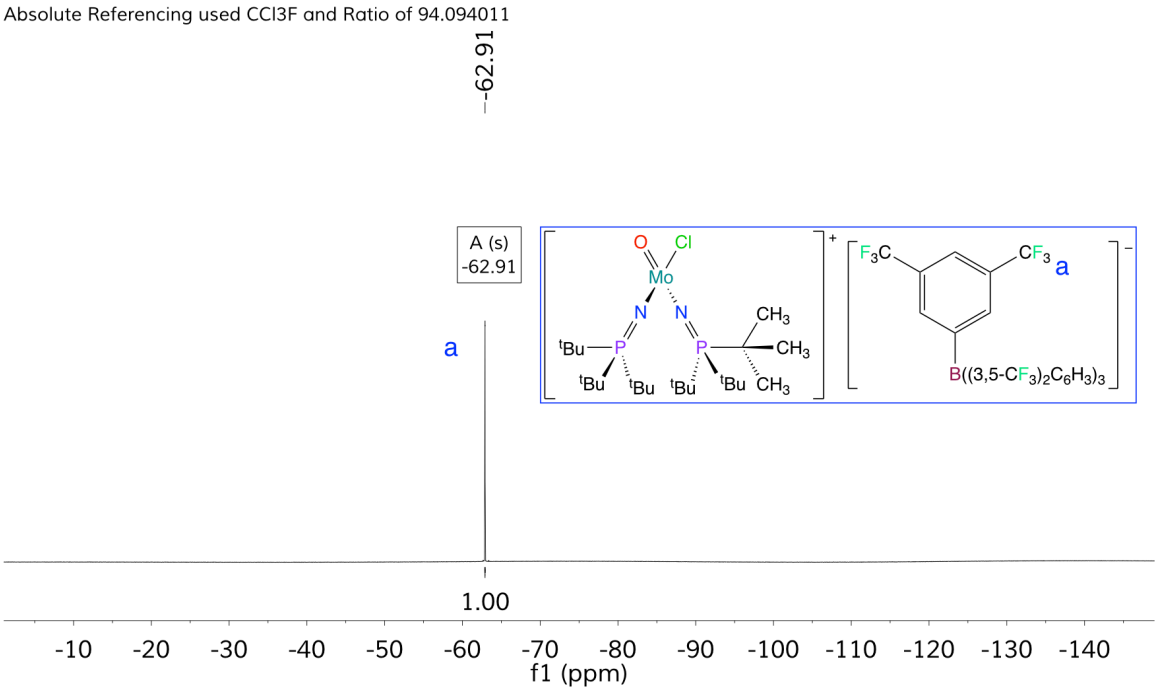

Figure 4.32: ^{19}F NMR spectrum of **4.5** in CD_2Cl_2 (376 MHz)

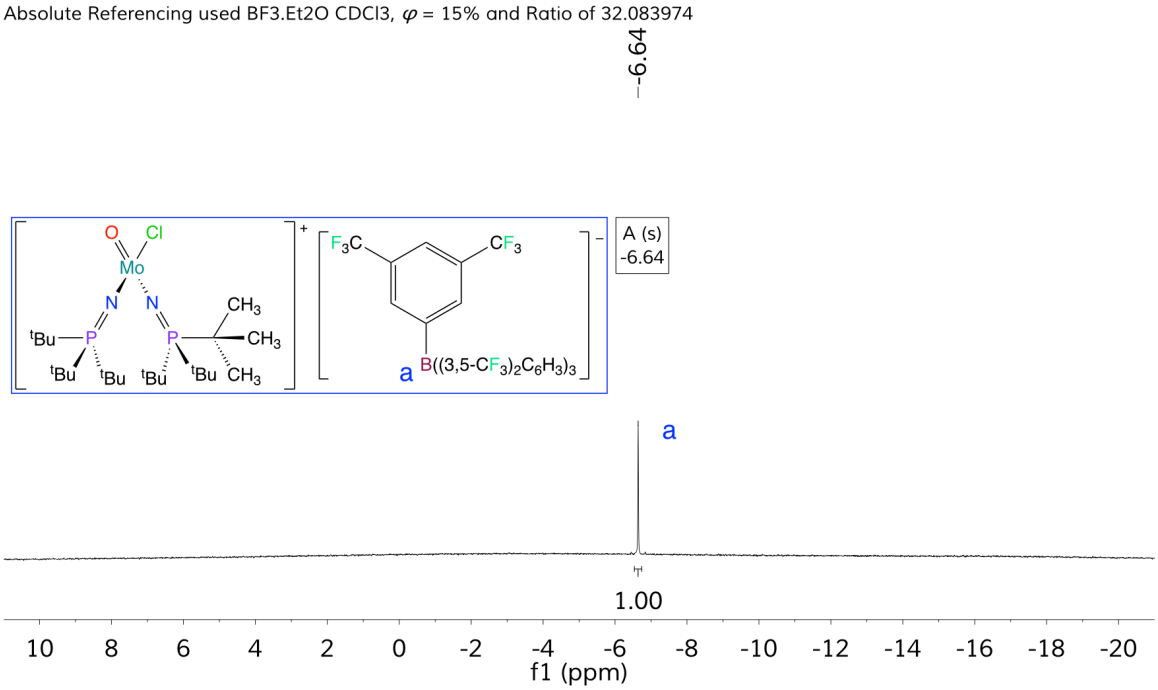

Figure 4.33: ^{11}B NMR spectrum of **4.5** in CD_2Cl_2 (128 MHz)

4.2.3 Ene-Diolate Reactivity and Formation of Alkylidyne

Ene-diolate complexes are very rare, and their reactivity has not been investigated. Considering **4.3** has two halide groups that can be readily substituted using a variety of chemical agents, we sought to examine the basic reactivity of this novel complex. To this end, **4.3** was reacted with 2 equiv. of (trimethylsilyl)methyllithium ($LiCH_2Si(CH_3)_3$), generating two distinct products in low yield (Fig 4.34). XRD analysis (Fig. 4.35) of a three-component crystal obtained from this material revealed the formation of the alkyl-alkylidyne complex $[(tBu_3P{=}N)_2Mo(\equiv CSi(CH_3)_3)(CH_2Si(CH_3)_3)]$ (**4.6**), and the trialkyl complex $[(tBu_3P{=}N)(tBu_2P{-}N{=})Mo(CH_2Si(CH_3)_3)_3]$ (**4.7**) where P-C bond scission has occurred within one of the phosphinimide ligands.

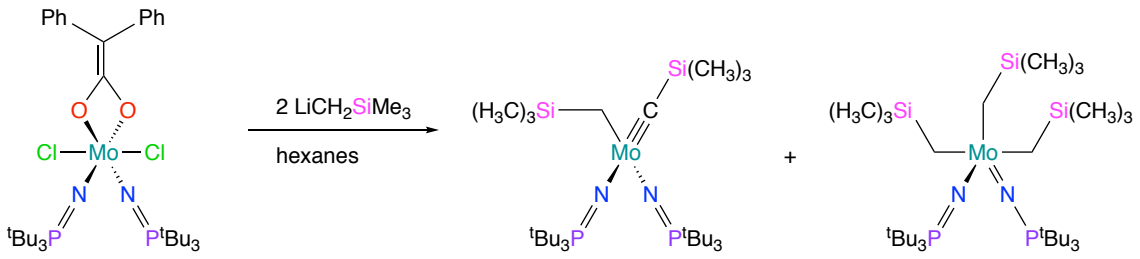

Figure 4.34: Reaction of **4.3** with (trimethylsilyl)methyllithium to generate **4.6** and **4.7**

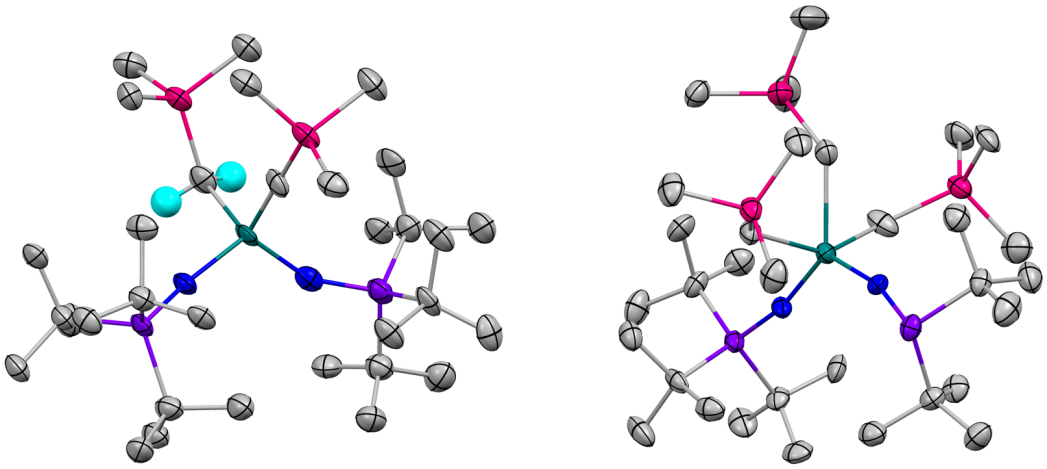

Figure 4.35: Lower quality XRD structures of **4.6** and **4.7**

These products were supported by solution phase spectroscopic evidence as well. The ^{1}H NMR spectrum of the product mixture contains a phosphorus-coupled doublet at 1.35 ppm ($^{3}J_{PH}$ = 12.6 Hz), and two singlets at 0.59 and 0.46 ppm, which correspond to **4.6** (Fig. 4.36). The ^{1}H NMR spectrum also contains two phosphorus-coupled doublets at 1.25 ($^{3}J_{PH}$ = 13.6 Hz) and 1.15 ppm ($^{3}J_{PH}$ = 13.5 Hz), and a singlet at 0.53 ppm, which correspond to **4.7**.

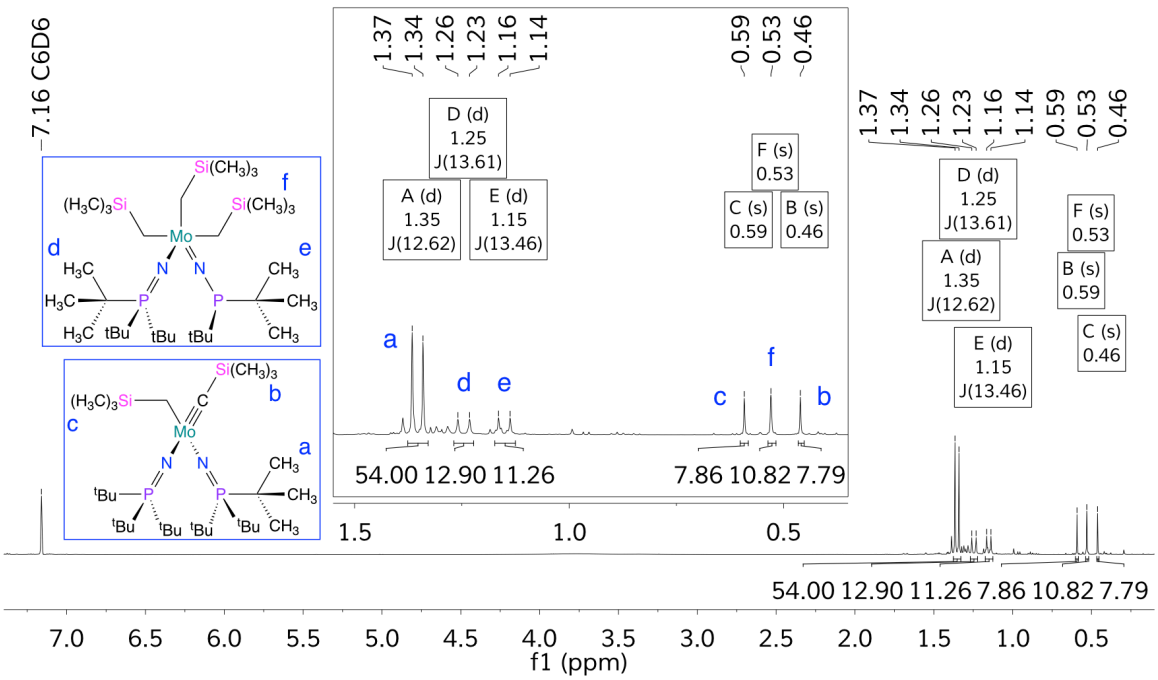

Figure 4.36: ^{1}H NMR spectrum of **4.6** and **4.7** in C_6D_6 (500 MHz)

The $^{31}P\{^{1}H\}$ NMR spectrum of the product mixture is given in Fig. 4.37 and contains the expected single resonance at 47.74 ppm for **4.6**, and two separate phosphorus resonances at 57.25 and 60.71 ppm for the distinct phosphinimide and imidophosphane ligands for **4.7**.

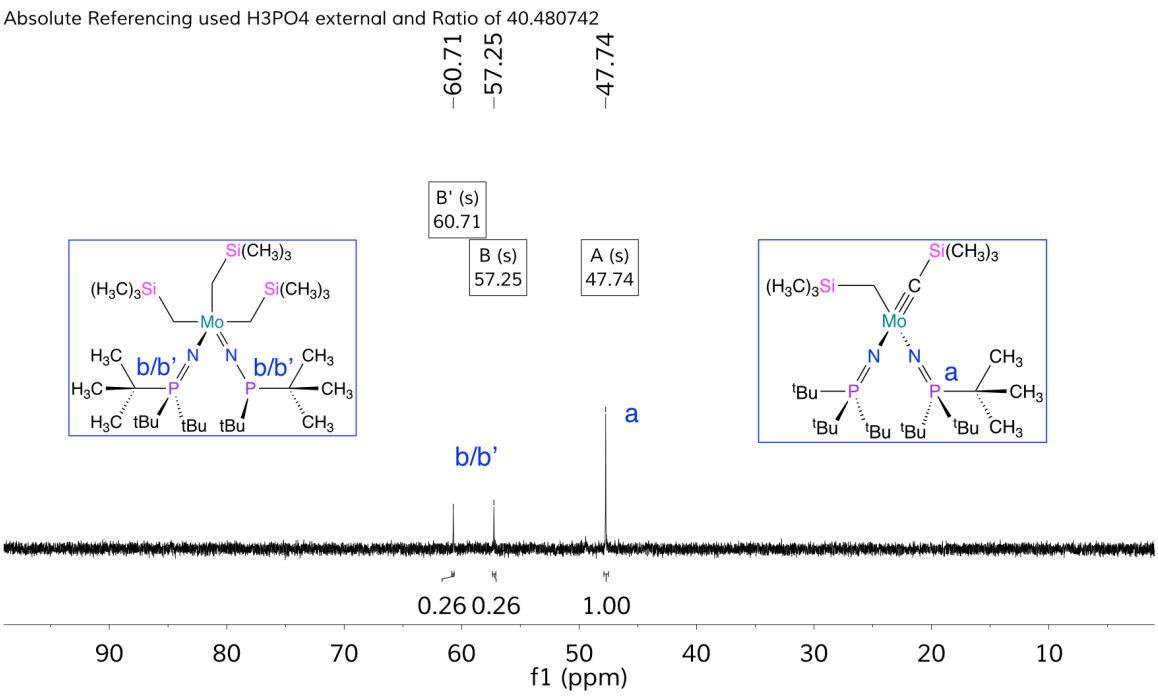

Figure 4.37: $^{31}P\{^{1}H\}$ NMR spectrum of **4.6** and **4.7** in C_6D_6 (202 MHz)

When the stoichiometry of the reagents are evaluated at 4 equivalents to (trimethylsilyl)methyllithium relative to **4.3**, the material isolated represents 90% conversion to both products, with a 4.17:1 ratio of generation of **4.6** to **4.7**.

Attempts to generate either **4.6** or **4.7** directly from the oxido-dichlorido complex **2.4** through reaction with 4 equiv. of $LiCH_2Si(CH_3)_3$ does not appear to proceed cleanly. The NMR data suggests that **4.7**, or the related complex where both phosphinimide ligands have converted to imidophosphane ligands, may have been generated in greater yield. However, there are other unidentified byproducts that do not correspond exactly with the alkyl-alkylidyne **4.6** or the oxido-alkylidene **3.1**. These results suggest that the ene-diolate ligand influences the decomposition pathways toward generation of **4.6** and **4.7**

instead of other byproducts, but may not be necessary for those kind of transformations to occur.

While not isolated, the fragmented complex **4.7** provides experimental support for one of the theoretical decomposition pathways for the phosphinimide ligand framework as proposed by Ziegler *et al*, where *tert*-butyl transfer to the metal center was determined to be the most favorable pathway for mono- and bisphosphinimide titanium complexes.[6] While **4.7** does not contain a *tert*-butyl ligand, this ligand may undergo elimination with one of the (trimethylsilyl)methyl ligands in the presumed tetraalkyl intermediate complex and result in formation of **4.7**.

In order to support our proposed mechanism involving a tetraalkyl intermediate, the alkyl-alkylidyne complex **4.6** was prepared through alkylation of the tetrabromido-molybdenum complex ($^{t}Bu_3P{=}N)_2MoBr_4$ (**4.8**). Complex **4.8** was synthesized by reaction of **2.4** with excess trimethylsilylbromide (Fig. 4.38) in quantitative yield. This transformation is proposed to eliminate hexamethylsiloxane through reaction with the oxido ligand, as well as eliminate trimethylsilylchloride through halogen exchange with the chlorido ligands.

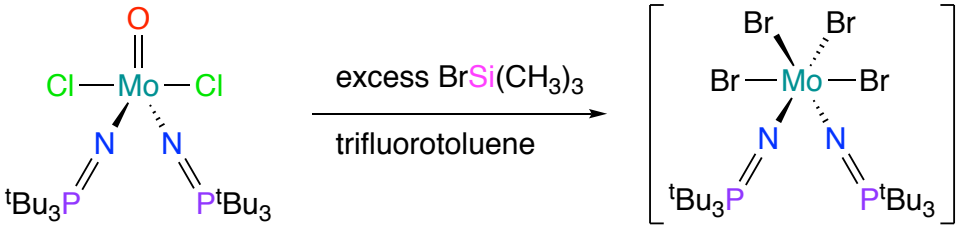

Figure 4.38: Synthesis of **4.8** by reaction of **2.4** with excess trimethylsilylbromide

Complex **4.8** has been characterized by NMR spectroscopy. Based on the NMR data, **4.8** appears to exist as a mixture of *cis* and *trans* isomers and is dependent on the solvent environment. The ^{1}H NMR spectrum in C_6D_6 contains the expected phosphorus-coupled doublet for the phosphinimide *tert*-butyl groups at 1.23 ppm, as well as an additional broad doublet at 1.04 ppm that appears to originate from a different phosphinimide ligand environment (Fig. 4.39).

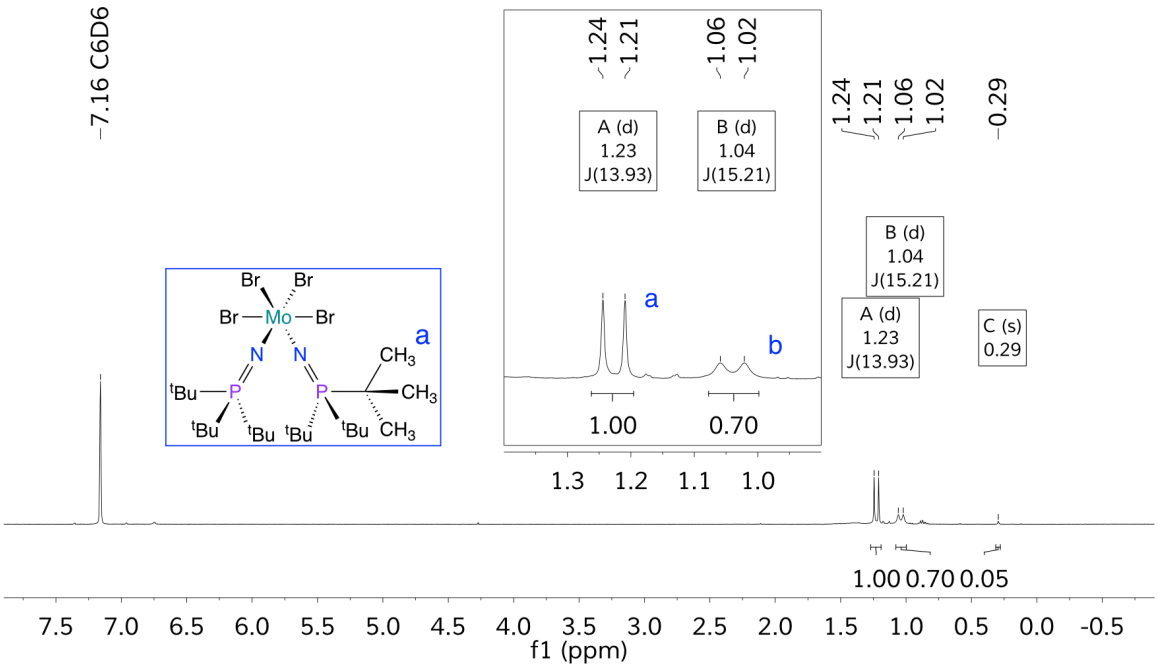

Figure 4.39: ^{1}H NMR spectrum of **4.8** in C_6D_6 (400 MHz)

The additional ^{1}H NMR doublet does not appear to be an effect of phosphinimide ligand asymmetry within a single isomer, as only one ^{31}P NMR resonance is observed at 70.76 ppm (Fig. 4.40).

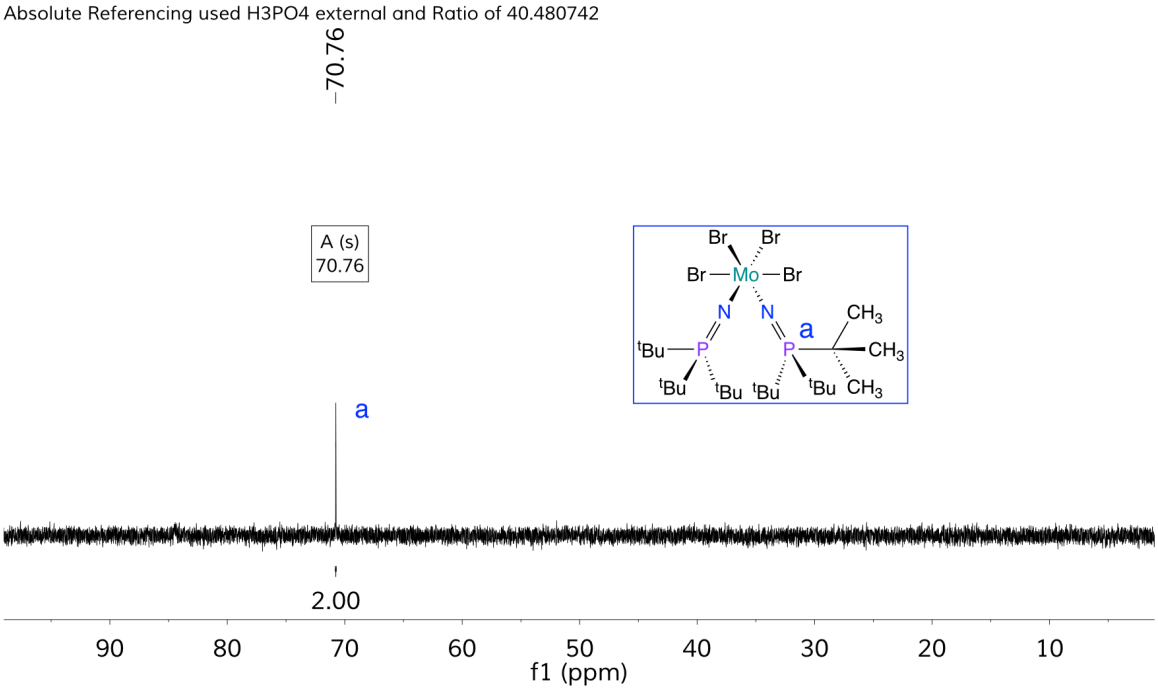

Figure 4.40: $^{31}P\{^{1}H\}$ NMR spectrum of **4.8** in C_6D_6 (162 MHz)

Complex **4.8** is more soluble in chloroform and the ^{1}H NMR spectrum in $CDCl_3$ shows a single phosphorus-coupled doublet at 1.80 ppm ($^{3}J_{PH}$ = 15.7 Hz) for the phosphinimide *tert*-butyl groups (Fig. 4.41). This result, coupled with the fact that the $^{31}P\{^{1}H\}$ NMR spectrum in $CDCl_3$ resolves to a single environment for the phosphinimide ligands at 98.33 ppm (Fig. 4.42), suggests that the two signals see in C_6D_6 arise from solubility differences between the two isomers and that the interconversion is very rapid under high solubility conditions, as seen in $CDCl_3$.

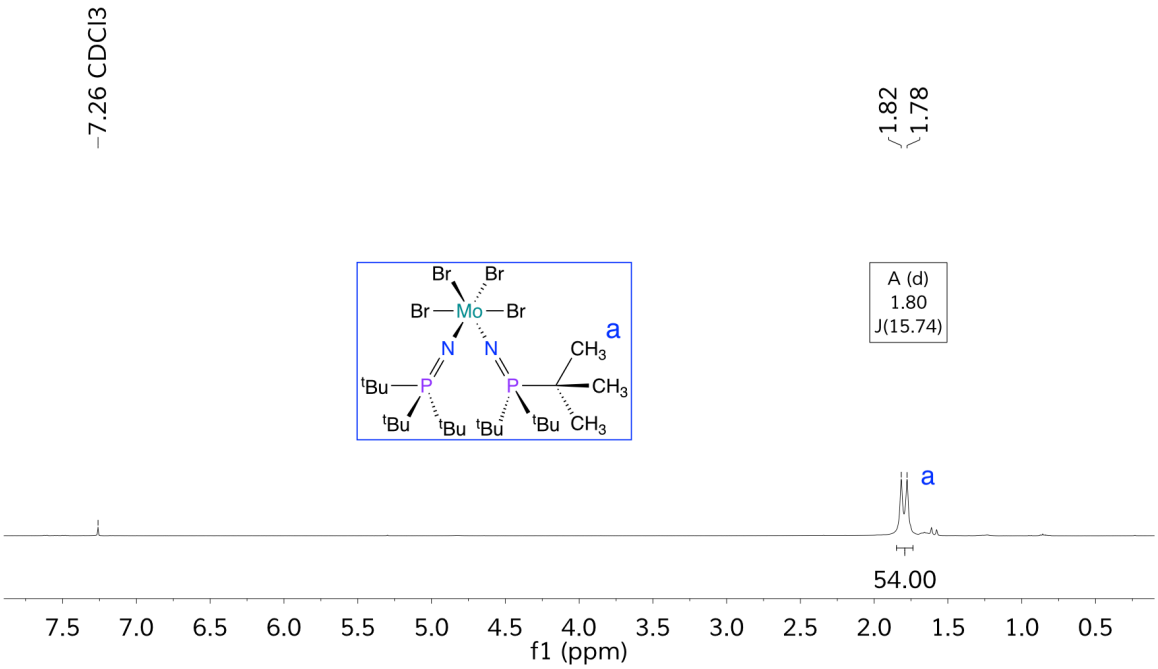

Figure 4.41: ^{1}H NMR spectrum of **4.8** in $CDCl_3$ (400 MHz)

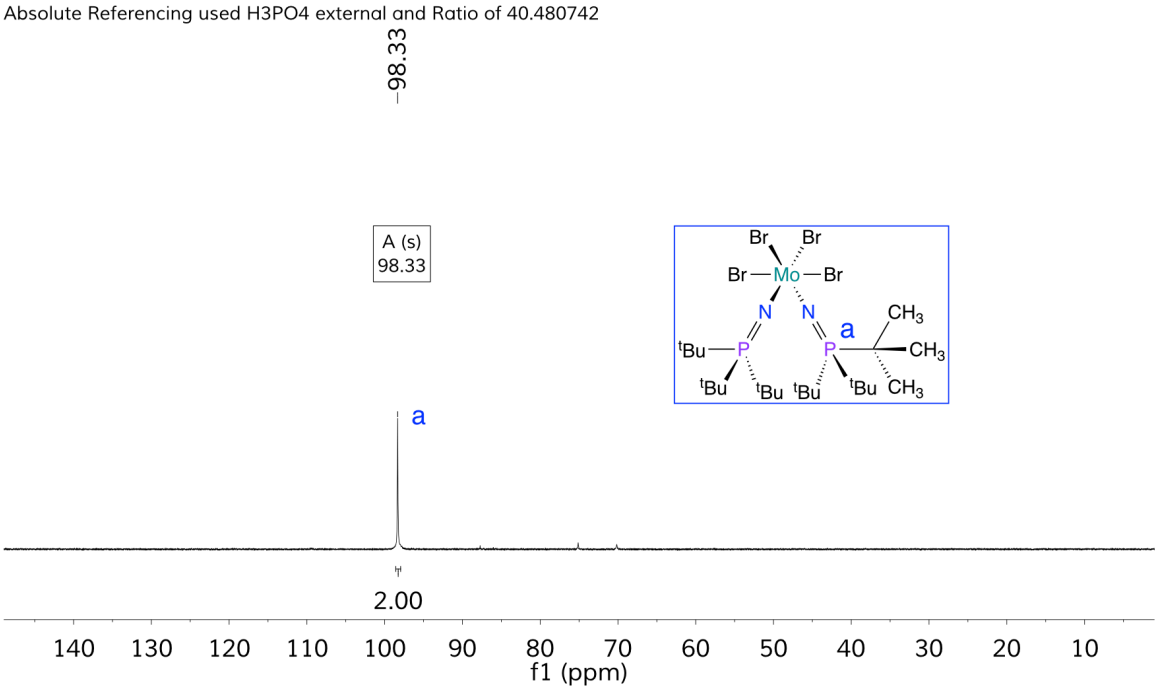

Figure 4.42: $^{31}P\{^{1}H\}$ NMR spectrum of **4.8** in $CDCl_3$ (162 MHz)

The ^{1}H-decoupled ^{13}C NMR spectrum in $CDCl_3$ is simple as anticipated, and shows a phosphorus-coupled doublet at 46.70 ppm ($^{1}J_{PC}$ = 28.9 Hz) for the quaternary carbons of the phosphinimide ligands, and a singlet for the primary methyl carbons at 30.62 ppm (Fig. 4.43).

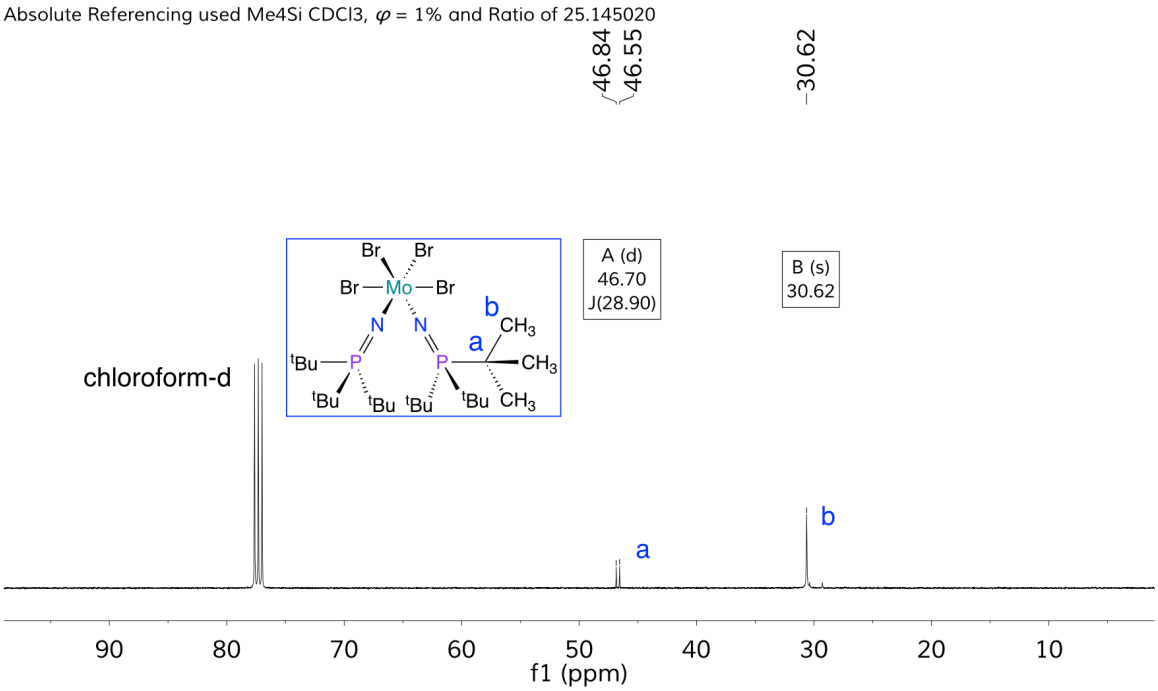

Figure 4.43: $^{13}C\{^{1}H\}$ NMR spectrum of **4.8** in $CDCl_3$ (101 MHz)

Synthesis of **4.8** offers a new highly efficient route for further installation of molybdenum-ligand multiple bonds, as there are no known molybdenum(VI) tetrabromido complexes available for synthesis. The only reported molybdenum(VI) tetrabromido complex is $Mo(=O)Br_4$ which has only been studied with gas-phase infrared spectroscopy and theoretical calculations.[7–10]

The analogous reaction of **2.4** with trimethylsilylchloride to generate the tetrachlorido analogue to **4.8** appears to proceed based on NMR spectroscopy

observations, yet at a slower rate than the reaction to generate **4.8**. Heating this reaction at 35 °C for 22 hours in dichloromethane results in approximately 63% conversion to the tetrachloride complex based on ^{1}H NMR spectroscopy integrations. Solvent polarity appears to be relevant for this conversion, as performing the same reaction in toluene at 60 °C for 22 hours only resulted in 26% conversion.

Complex **4.8** can be combined with four equivalents of (trimethylsilyl)methyllithium, to generate a presumable tetraalkyl intermediate complex that undergoes subsequent alkane elimination and proton rearrangement due to α-hydrogen abstraction processes, which results in formation of complex **4.6** (Fig. 4.44).

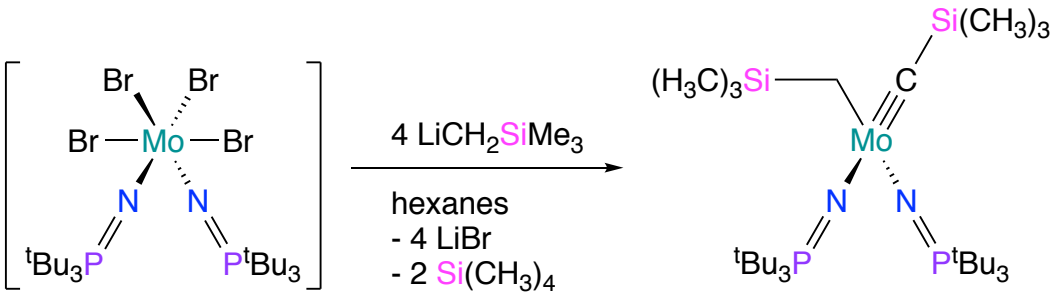

Figure 4.44: Synthesis of **4.6** by reaction of **4.8** with (trimethylsilyl)methyllithium

Complex **4.6** has been characterized by NMR spectroscopy and single crystal XRD. Based on the XRD structure, **4.6** is pseudo C_s symmetric with a plane of symmetry that contains the C1-Mo1-C5 nuclei, with a close to tetrahedral (τ'_4 = 0.94) core around the molybdenum atom (Fig. 4.45).

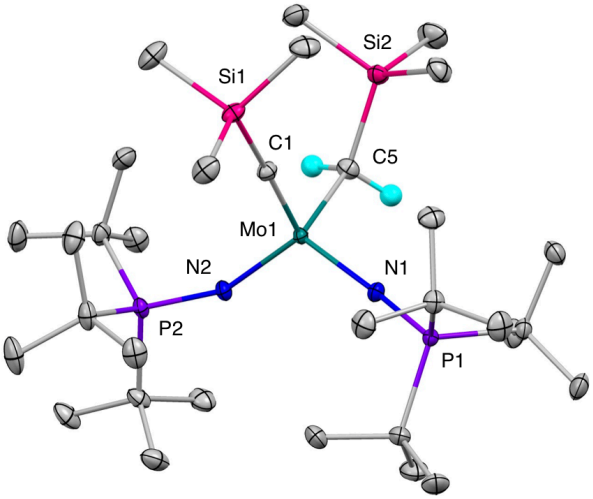

Figure 4.45: Thermal ellipsoid plot (50% probability) of complex **4.6**; non-methylene hydrogen atoms have been omitted for clarity

Visualization of the space-filling models of the XRD structure of **4.6** shows good steric protection near the alkylidyne ligand (Fig. 4.46), and greater steric accessibility to the metal-carbon bond of the alkylsilane ligand.

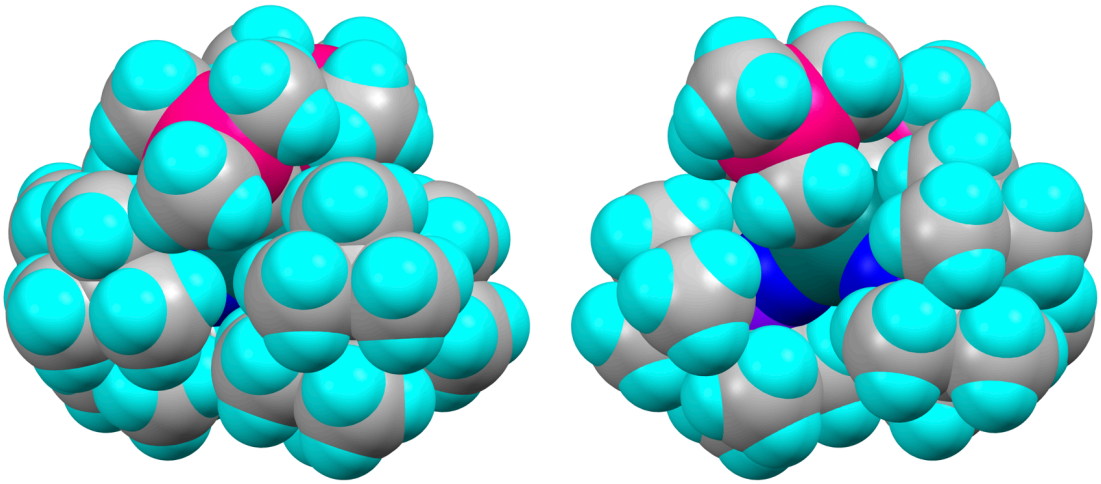

Figure 4.46: Space-filling model of complex **4.6** focused on the alkylidyne ligand (left, alkylidyne carbon atoms indicated in dark grey), focused on alkyl ligand (right, alkyl carbon atoms indicated in dark grey)

The molybdenum-carbon bond lengths (Table 4.6) for the alkylidyne (Mo1-C1) and alkyl (Mo1-C5) ligands show a dramatic difference of 0.390(1) Å. The bond lengths for the phosphinimide ligands are comparable to the structurally similar complexes in Chapter 3.

Table 4.6: Selected XRD Bond Distances for complex **4.6**

Atoms	**Length (Å)**	**Atoms**	**Length (Å)**
Mo1-C1	1.7724(7)	C1-Si1	1.8365(8)
Mo1-C5	2.1628(8)	C5-Si2	1.8496(8)
Mo1-N1	1.8799(6)	P1-N1	1.5739(7)
Mo1-N2	1.8925(6)	P2-N2	1.5775(6)

The alkylidyne bond angle (Mo1-C1-Si1) in **4.6** is nearly linear at 173.0(5)°, and the alkyl bond angle (Mo1-C5-Si2) is 120.49(4)°, which is reasonable for a carbon methylene fragment (Table 4.7). The phosphinimide coordination angles (Mo-N-P) have a difference of 15.10(5)° in the solid state structure, which is attributed to a crystal packing effect as this asymmetry is not observed in the solution-state NMR spectra. Both phosphinimide ligands are coordinated at a relatively linear angle, with an average of 161.39(3)°.

The bond angle between the phosphinimide ligands (N1-Mo1-N2) is larger than the same angle in the oxido-alkylidene complex **3.1** by 8.15(18)°. While **4.6** has more steric bulk from the alkylidyne and alkyl ligands than the oxido and alkylidene ligands in **3.1**, the bulk of the alkylidyne ligand is removed from the molybdenum center and the alkyl ligand has a more acute bond angle (than the alkylidene ligand in **3.1**), which also shifts steric bulk farther away from the phosphinimide ligands.

Table 4.7: Selected XRD Bond Angles for complex **4.6**

Atoms	**Angle (°)**	**Atoms**	**Angle (°)**
Mo1-N1-P1	168.94(4)	N1-Mo1-N2	114.72(3)
Mo1-N2-P2	153.84(4)	C1-Mo1-C5	103.32(3)
C1-Mo1-N1	111.28(3)	Mo1-C1-Si1	173.0(5)
C1-Mo1-N2	111.05(3)	Mo1-C5-Si2	120.49(4)

Analysis of **4.6** by ^{1}H NMR spectroscopy contains the ^{31}P-coupled doublet at 1.35 ppm for the phosphinimide *tert*-butyl protons, two singlets for the alkylidyne ligand at 0.46 ppm and the alkyl ligand at 0.59 ppm, and a singlet at 0.98 ppm for the methylene group of the alkyl ligand (Fig. 4.47).

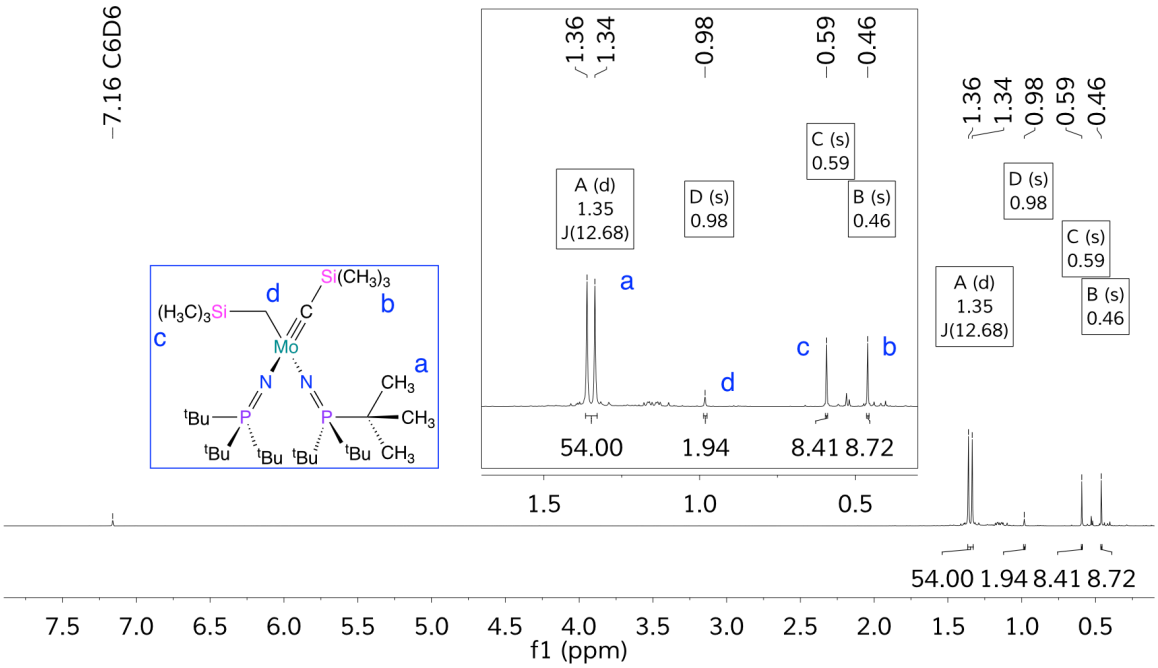

Figure 4.47: ^{1}H NMR spectrum of **4.6** in C_6D_6 (500 MHz)

There is a very minor amount of **4.7** formed during this reaction, which suggests that use of the ene-diolate complex **4.3** in this type of reaction is more prone to decomposition. The ^{31}P{^{1}H} NMR spectrum of **4.6** (Fig. 4.48) contains a singlet at 47.76 ppm, which indicates formation of a single product with chemically equivalent phosphinimide ligands when in solution, and is consistent with the results seen previously in Fig. 4.36.

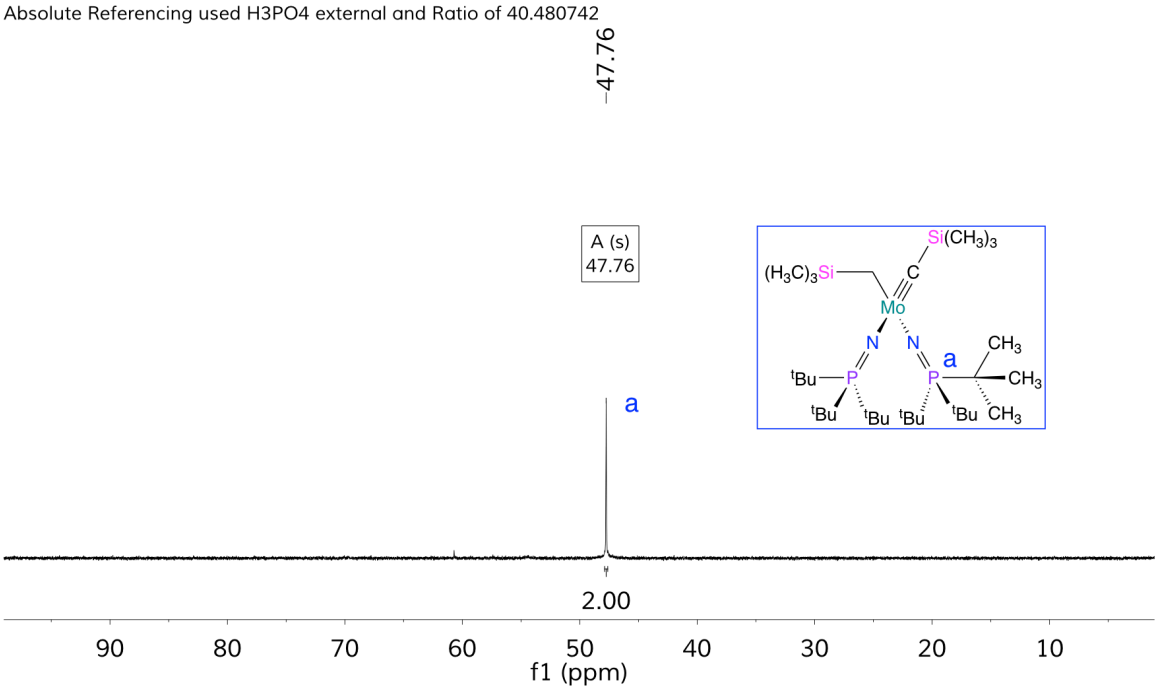

Figure 4.48: $^{31}P\{^{1}H\}$ NMR spectrum of **4.6** in C_6D_6 (162 MHz)

The 1D $^{13}C\{^{1}H\}$ NMR spectrum of **4.6** resolves all expected carbon resonances except for the alkylidyne carbon under these particular experimental conditions (Fig. 4.49). A phosphorus-coupled doublet is observed at 40.75 ppm for the phosphinimide quaternary carbon nuclei, a singlet is seen at 29.80 ppm for the phosphinimide primary methyl carbons, along with a singlet at 2.78 ppm for the trimethylsilyl fragment of the alkylidyne ligand, and two singlets for the alkyl ligand with one at 3.06 ppm for the trimethylsilyl fragment and one at 23.33 ppm for the methylene fragment.

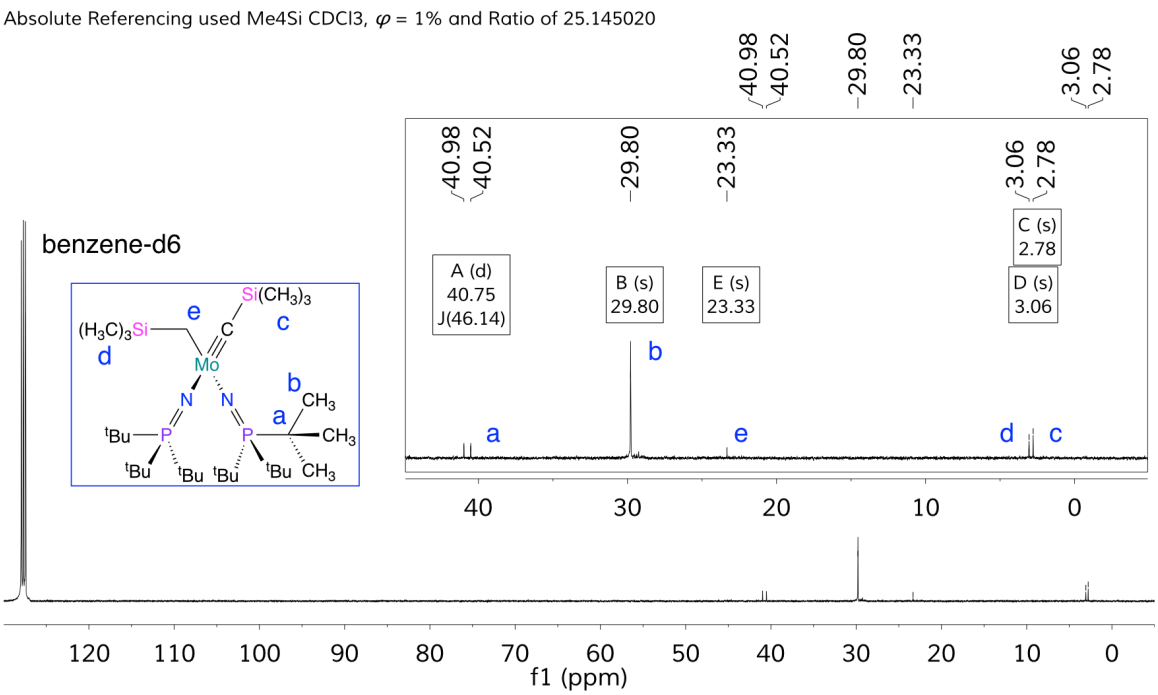

Figure 4.49: $^{13}C\{^{1}H\}$ NMR spectrum of **4.6** in C_6D_6 (101 MHz)

The alkyl methylene carbon resonance was further verified by multiple 2D NMR experiments. A ^{1}H-$\{^{13}C\}$ gHMBCAD experiment shows cross-peaks for the trimethylsilyl fragment to the methylene carbon and the methylene protons to the trimethylsilyl carbons (Fig. 4.50).

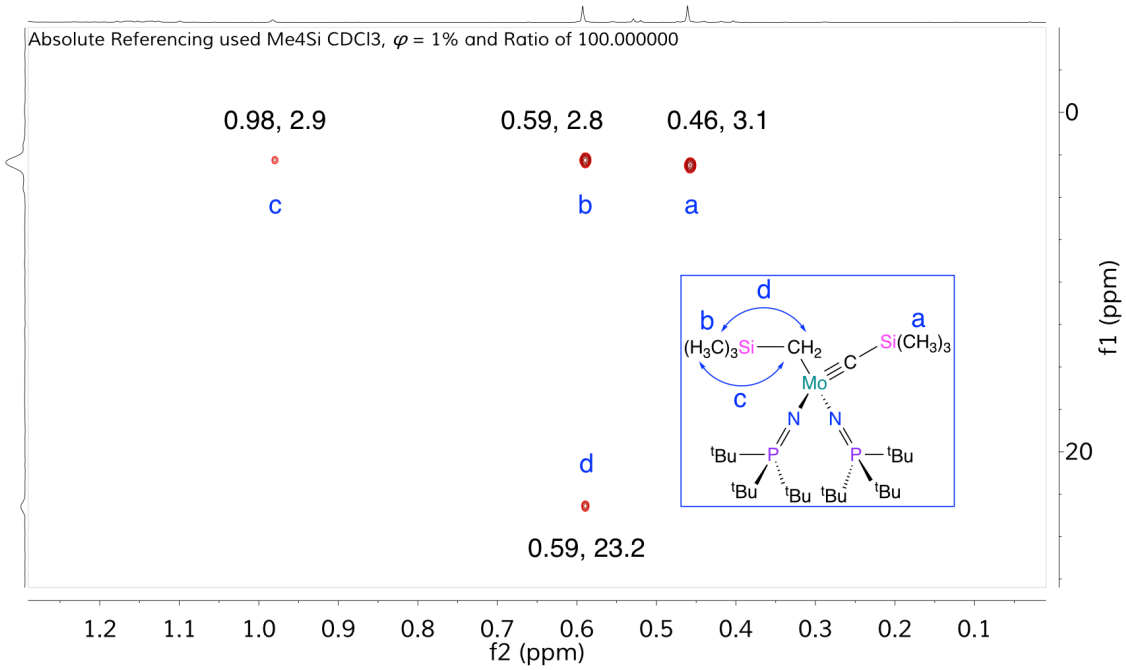

Figure 4.50: ^{1}H-{^{13}C} gHMBCAD NMR spectrum of **4.6** in C_6D_6 (^{13}C decoupled during acquisition) (500 MHz, 126 MHz)

A ^{1}H-{^{13}C} gHSQCAD experiment was also carried out, and clearly resolves the cross-peak for the directly bonded methylene fragment (Fig. 4.51), and a coupled ^{1}H-^{13}C gHSQCAD experiment resolves a doublet for the methylene fragment (Fig. 4.52). The one-bond coupling constant of 110 ppm for this resonance is similar to other CH_2 fragments bonded to molybdenum and tungsten.[11]

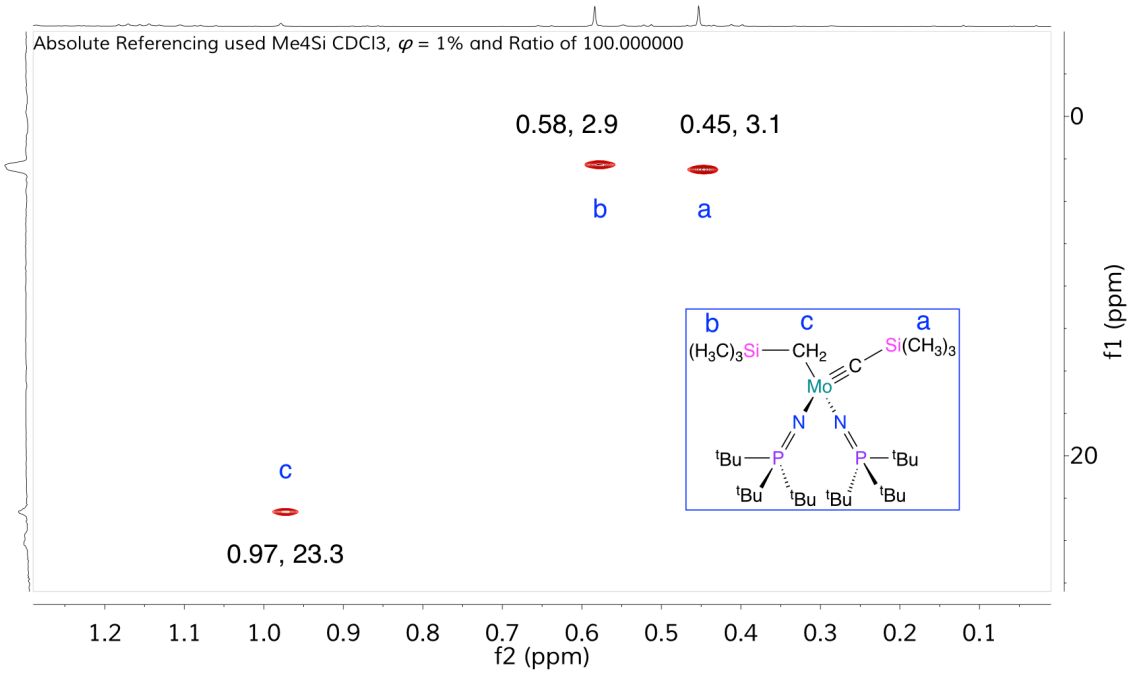

Figure 4.51: ^{1}H-{^{13}C} gHSQCAD NMR spectrum of **4.6** in C_6D_6 (^{13}C decoupled during acquisition) (500 MHz, 126 MHz)

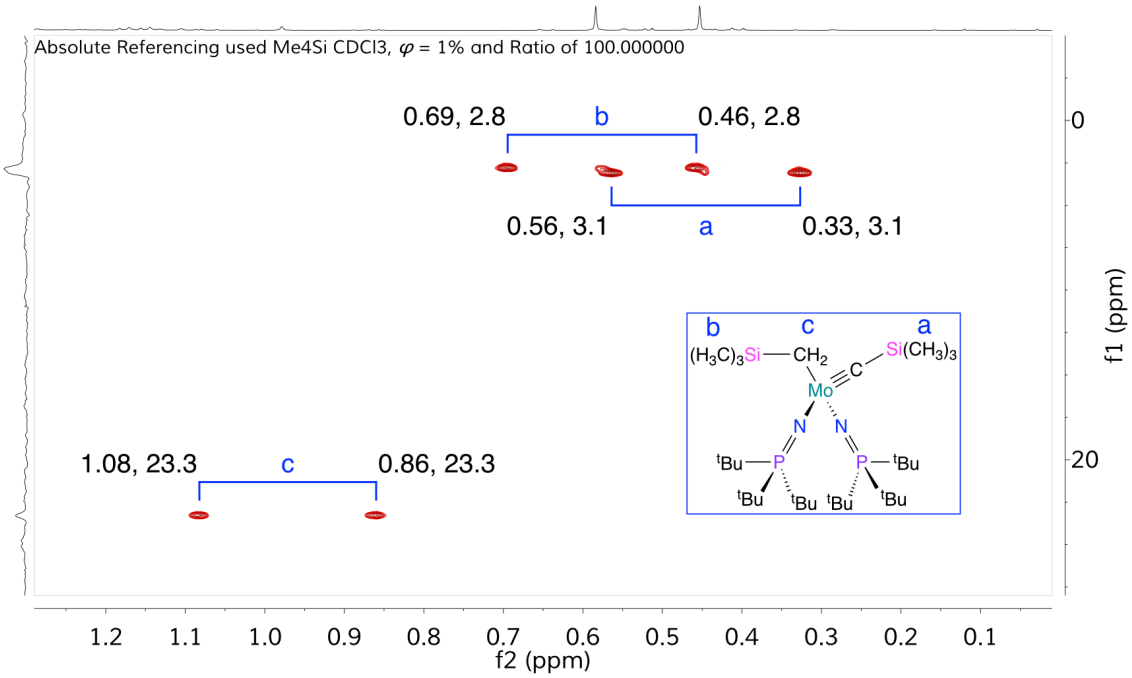

Figure 4.52: ^{1}H-^{13}C gHSQCAD NMR spectrum of **4.6** in C_6D_6 (500 MHz, 126 MHz)

^{13}C NMR resonances for M-CH_2 fragments in complexes with alkylidyne ligands have been previously reported further downfield in the range of 88-103 ppm, yet these are within complexes that are more electropositive than **4.6**. While structurally distinct, a tungsten complex with $P(CH_3)_3$ ligands shifts exhibits a W-CH_2 resonance at 53.5 ppm.[11]

As the alkylidyne carbon was not resolved by one dimensional NMR techniques, a 2D ^{1}H-{^{13}C} gHMBC NMR experiment was carried out to enable measurement of the alkylidyne carbon signal through a cross peak with the trimethylsilyl fragment of the alkylidyne ligand. The resonance is found at 325.1 ppm, which is within the expected range for this type of ligand fragment in related molybdenum and tungsten complexes (Fig. 4.53).[11–15]

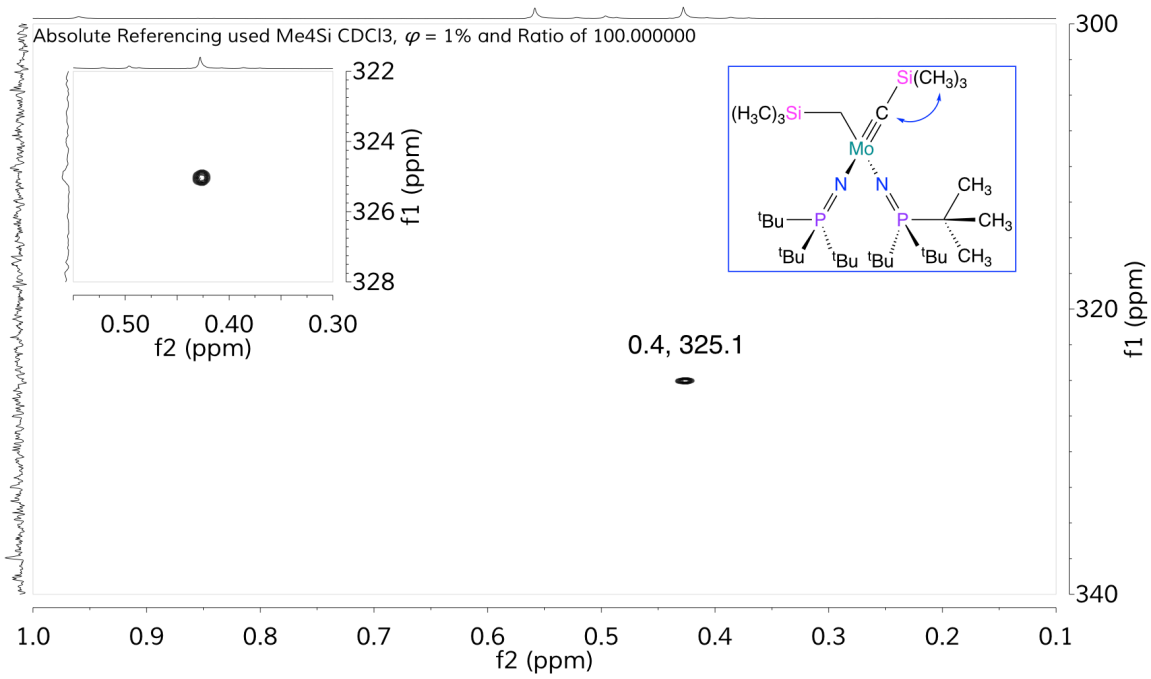

Figure 4.53: ^{1}H-{^{13}C} gHMBC NMR spectrum of **4.6** in C_6D_6 (^{13}C decoupled during acquisition) (500 MHz, 126 MHz)

4.2.4 Organophosphorus Chemistry

There are two known routes to synthesize phosphaketenes, which are severely limited by the use of extremely hazardous reagents. The primary hazardous reagents encountered in this chemistry are phosgene (Cl_2CO) and phosphine (PH_3). Both of these chemicals are highly toxic and reactive, and can only be produced in specialized laboratories.

The first synthetic route requires the use of phosgene, and generates a phosphaketene through chlorotrimethylsilane elimination reactions. This chloride elimination pathway has been reported for both supermesityl phosphine and *tert*-butyl phosphine (Fig. 4.54).

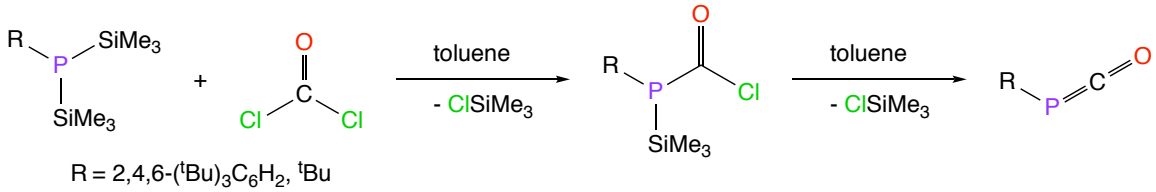

Figure 4.54: Phosphaketene synthesis with trimethylsilyl chloride elimination

Hydrogen chloride elimination has also been reported for trityl phosphine (Fig. 4.55). Both types of elimination were also reported for the *tert*-butyl derivative by starting with ^{t}BuPH(Si(CH$_3$)$_3$).

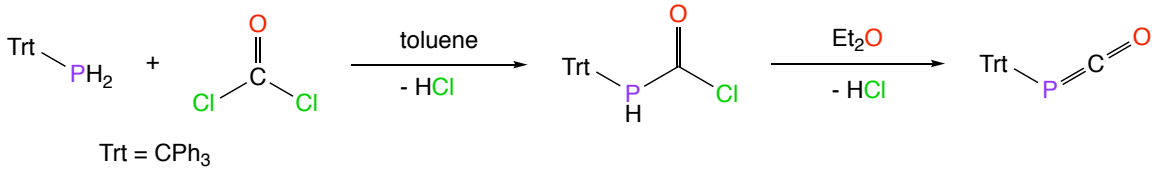

Figure 4.55: Phosphaketene synthesis with hydrogen chloride elimination

Another reported route is a synthesis specific to generating HPCO, and likely cannot be used effectively for the synthesis of more general molecules (Fig. 4.56). Synthesis of the starting NaPCO salt is difficult, and requires the use of phosphine (PH$_3$).

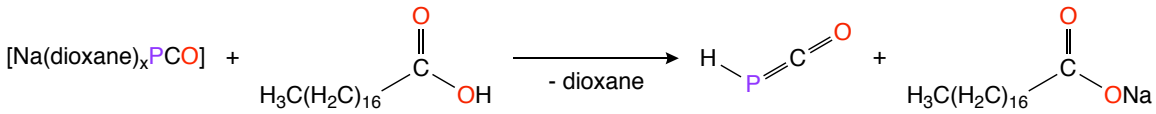

Figure 4.56: HPCO synthesis through salt metathesis

To improve on these existing methods, reactions similar to the synthesis of some types of ketenes were evaluated for their use in the synthesis of

phosphaketenes, with the overall goal being to use less hazardous reagents (vide infra).

4.2.5 Phosphaketene Reactivity with Metal-Oxido Ligands

Terminal phosphinidene ligands on metal complexes have been previously synthesized by salt metathesis methods or CO elimination methods. These synthetic approaches are labor intensive, have poor atom economy, and often use extremely hazardous reagents. To overcome all of these limitations of known techniques, a new synthetic approach was envisioned where CO_2 could be eliminated through cycloaddition of a phosphaketene species with a terminal metal oxido complex.

It has been previously shown that a terminal phosphinidene complex could be generated through oxidative addition of a phosphaketene proligand to a low oxidation state W center. The P=C bond undergoes fragmentation to eliminate one equivalent of CO, which coordinates to the phosphinidene complex (Fig. 4.3).

4.2.5.1 Phosphaketene Synthesis

Synthesis of the phosphaester compound **4.9** was achieved using a modified version of a reported synthesis, where hydrogen chloride is eliminated and neutralized by potassium carbonate (Fig. 4.57).

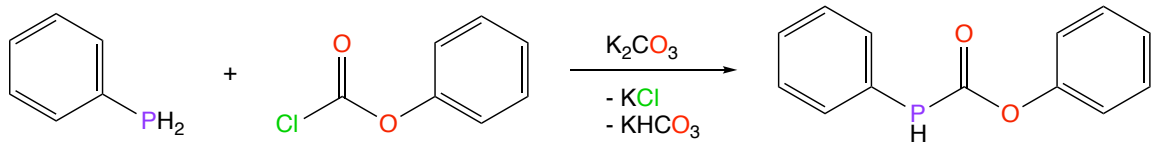

Figure 4.57: Phosphaester synthesis through reaction of phenylphosphine and phenylorthchloroformate

The ^{1}H NMR spectrum of **4.9** contains the ^{31}P-coupled doublet for the PH proton at 6.12 ppm ($^{1}J_{PH}$ = 236.1 Hz), a minimal signal for the precursor phenylphosphine at 3.83 ppm, and a number of unassigned aryl proton signals for the two phenyl groups of **4.9** that appear in the expected region from 6.8-7.5 ppm region (Fig. 4.58).

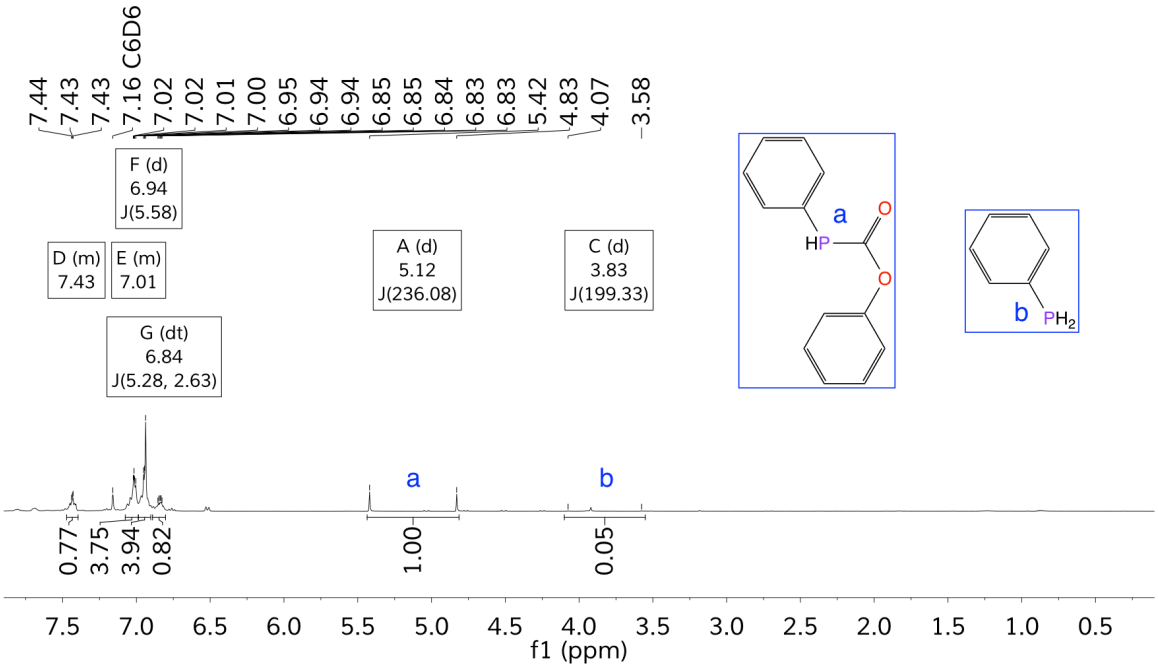

Figure 4.58: ^{1}H NMR spectrum of **4.9** in C_6D_6 (400 MHz)

The $^{31}P\{^{1}H\}$ NMR spectrum of **4.9** contains the expected singlet at -50.69 ppm (Fig. 4.59), and the ^{1}H-coupled ^{31}P NMR spectrum exhibits the expected doublet of triplets at -50.69 ppm ($^{1}J_{PH}$ = 235.9 Hz, $^{3}J_{PH}$ = 8.09 Hz) with strong coupling to the directly bonded proton and weaker 3-bond coupling to *ortho* protons in the phenyl fragment (Fig. 4.60).

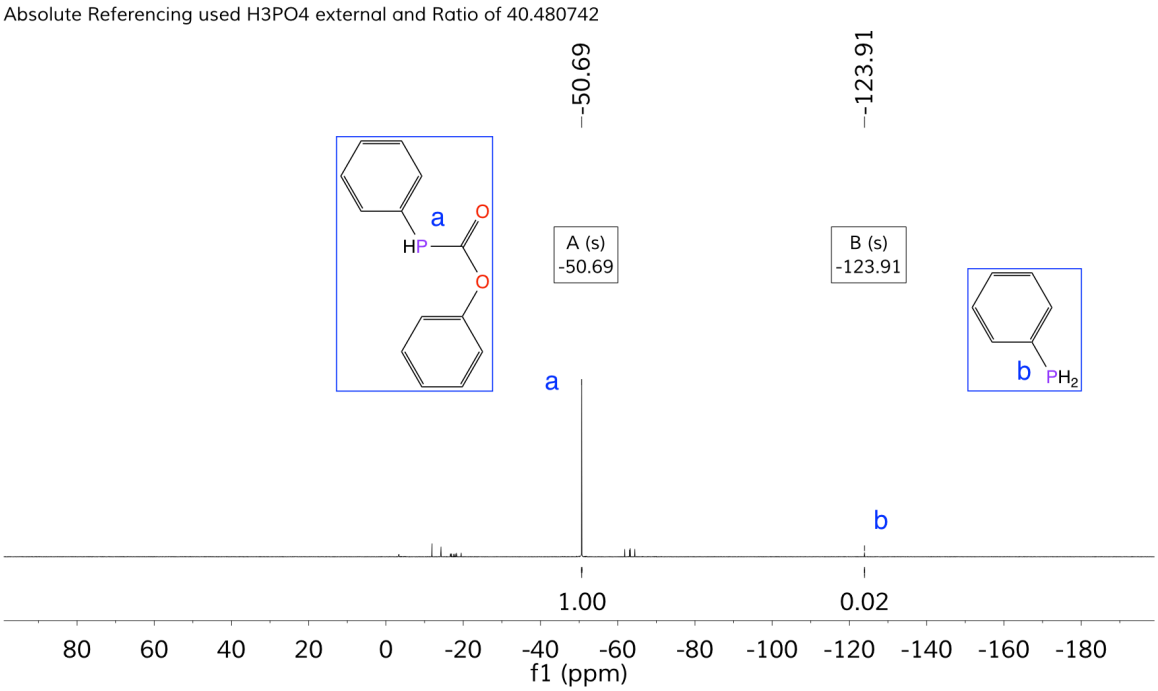

Figure 4.59: $^{31}P\{^{1}H\}$ NMR spectrum of **4.9** in C_6D_6 (162 MHz)

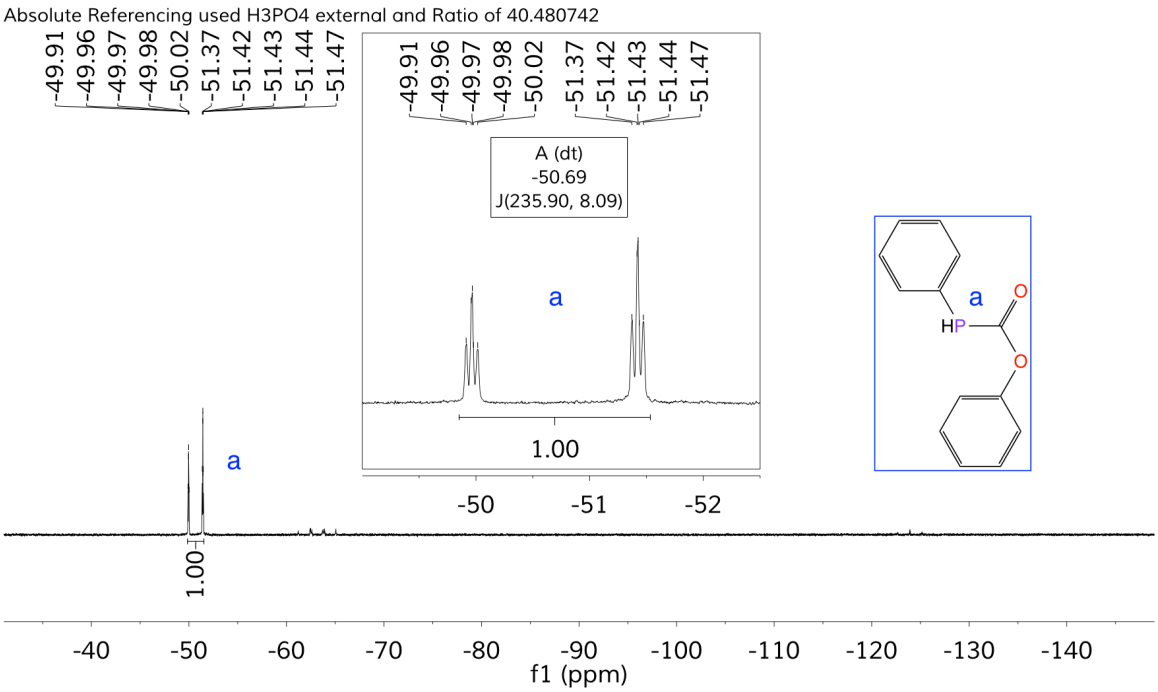

Figure 4.60: ^{31}P NMR spectrum of **4.9** in C_6D_6 (162 MHz)

Attempts were made to convert **4.9** to the corresponding phosphaketene derivative (**4.10**) through deprotonation with a suitable base and subsequent elimination of an aryloxide salt (Fig. 4.61).

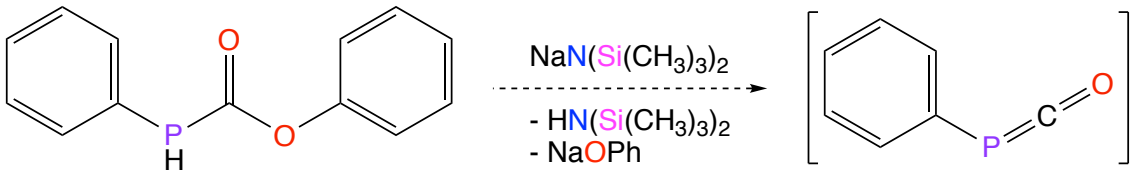

Figure 4.61: Attempted synthesis of **4.10** through deprotonation and aryloxide elimination

Formation of an orange product material indicates a reaction occurs between **4.9** and sodium bis(trimethylsilyl)amide. Rapid NMR analysis of the reaction solution reveals complete conversion of **4.9** as the P–H ^{1}H NMR doublet is not detected (Fig. 4.62) and the presence of bis(trimethylsilyl)amine, yet the remaining aryl protons do not provide much structural insight.

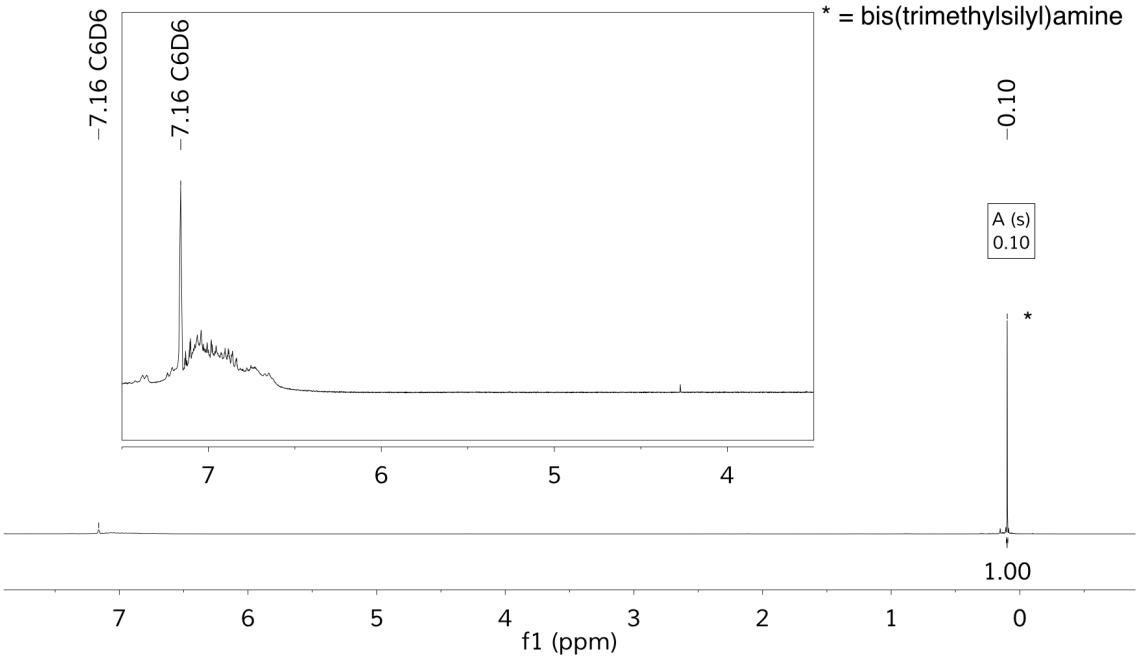

Figure 4.62: ^{1}H NMR spectrum of attempted synthesis of **4.10** in C_6D_6 (300 MHz)

The ^{31}P{^{1}H} NMR spectrum (Fig. 4.63) reveals signals at -48.23 ppm, -4.08 ppm which are assigned to P_xPh_x oligomers, and an unknown minor signal at 11.57 ppm.

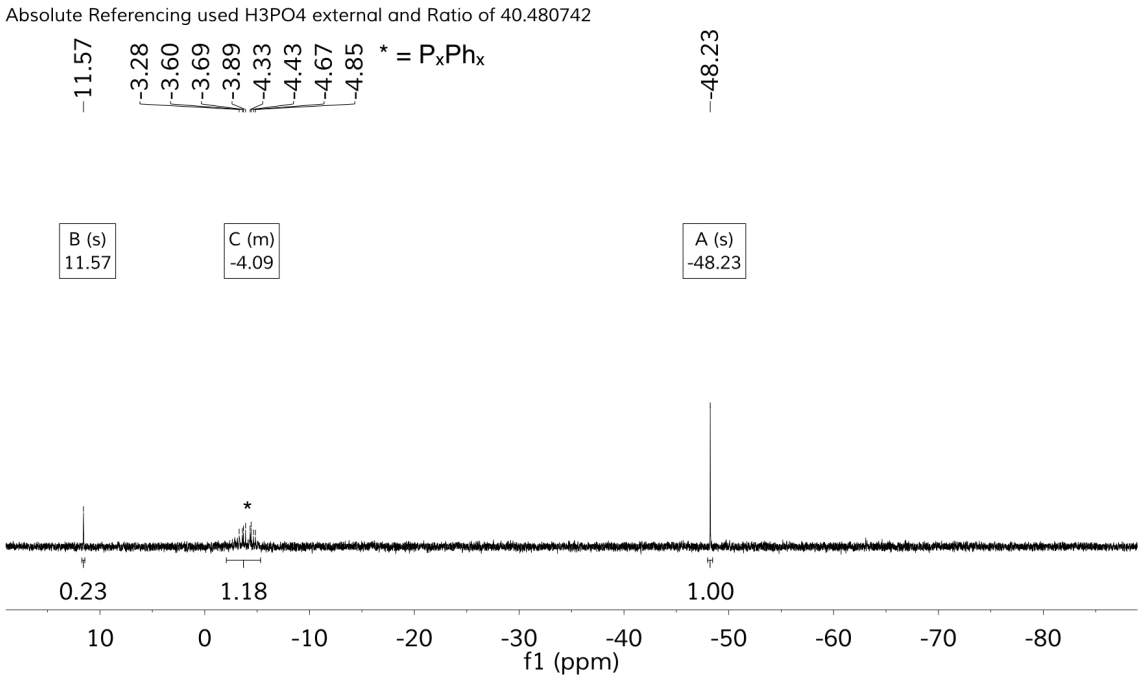

Figure 4.63: $^{31}P\{^{1}H\}$ NMR spectrum of attempted synthesis of **4.10** in C_6D_6 (121 MHz)

Attempts were made to isolate product material from this conversion, with the removal of salts through filtration. The NMR spectral data for this material is similar, with more decomposition observed (Fig. 4.64, Fig. 4.65) and interestingly the formation of a ^{31}P NMR signal further downfield at 157.91 ppm, which is tentatively assigned to the dimer of **4.10** (Fig. 4.66). The ^{1}H-coupled spectrum of this signal reveals a triplet with similar coupling to that observed in **4.9** (Fig. 4.67).

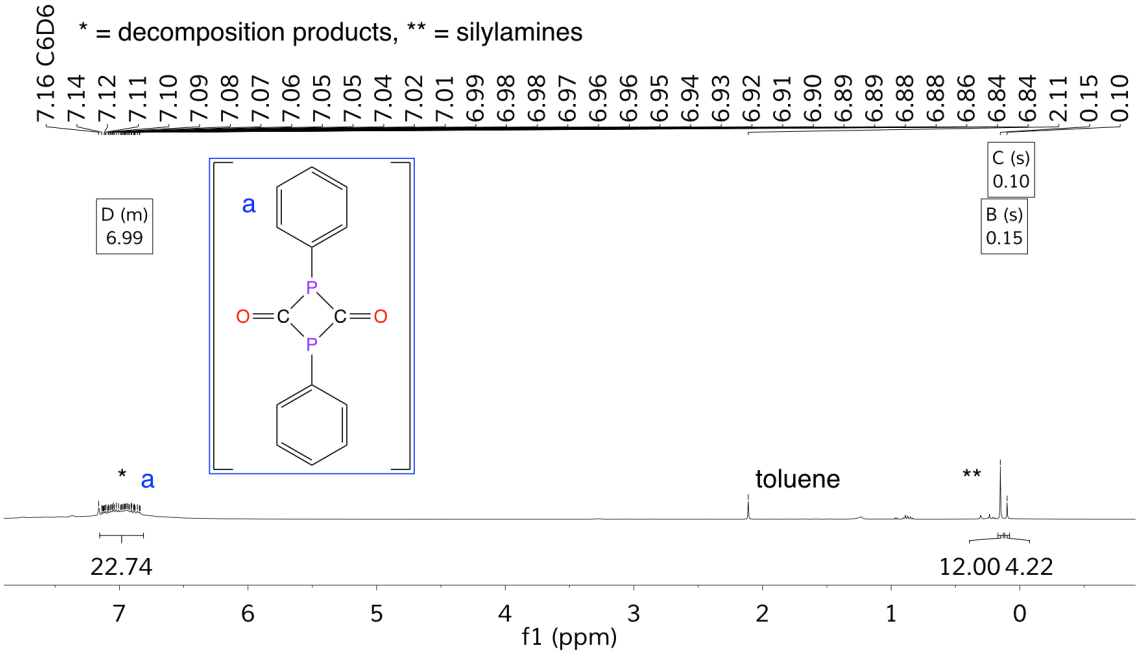

Figure 4.64: ^{1}H NMR spectrum of attempted isolation of **4.10** in C_6D_6 (400 MHz)

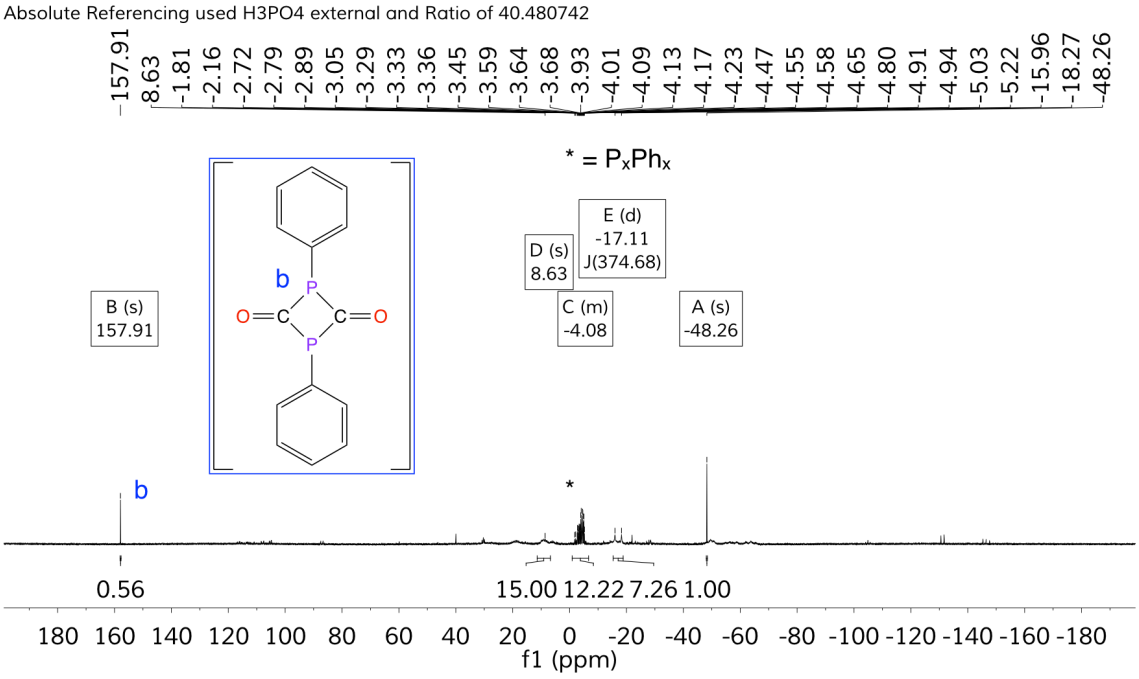

Figure 4.65: $^{31}P\{^{1}H\}$ NMR spectrum of attempted isolation of **4.10** in C_6D_6 (162 MHz)

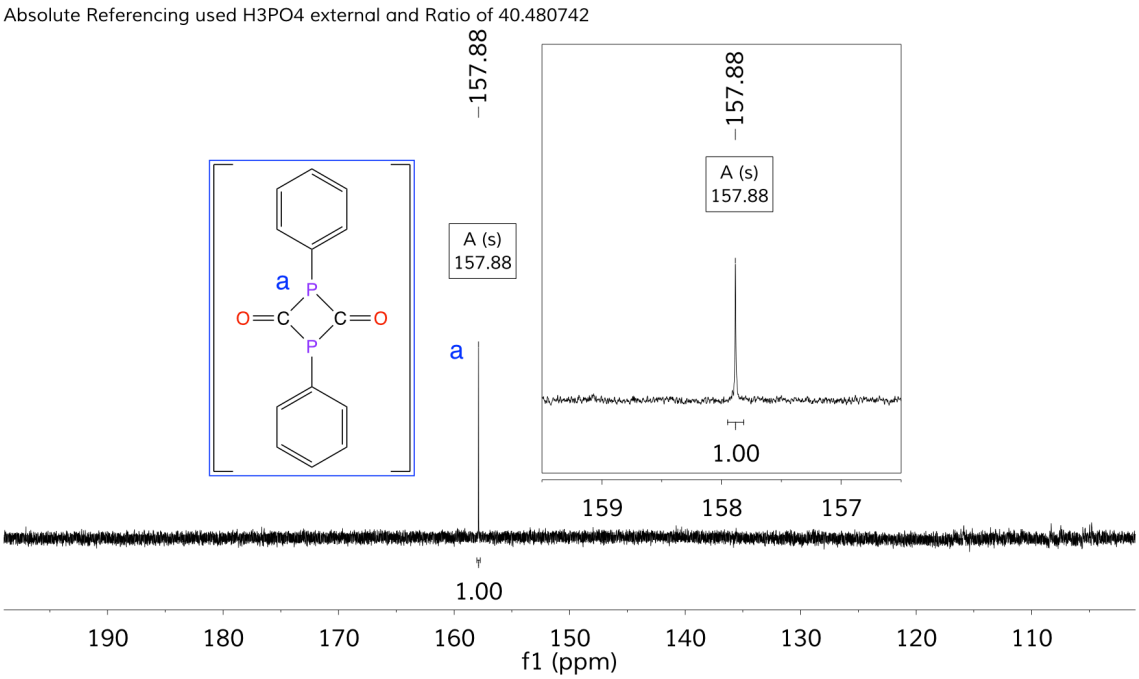

Figure 4.66: $^{31}P\{^{1}H\}$ NMR spectrum of attempted isolation of **4.10** in C_6D_6 focused downfield (162 MHz)

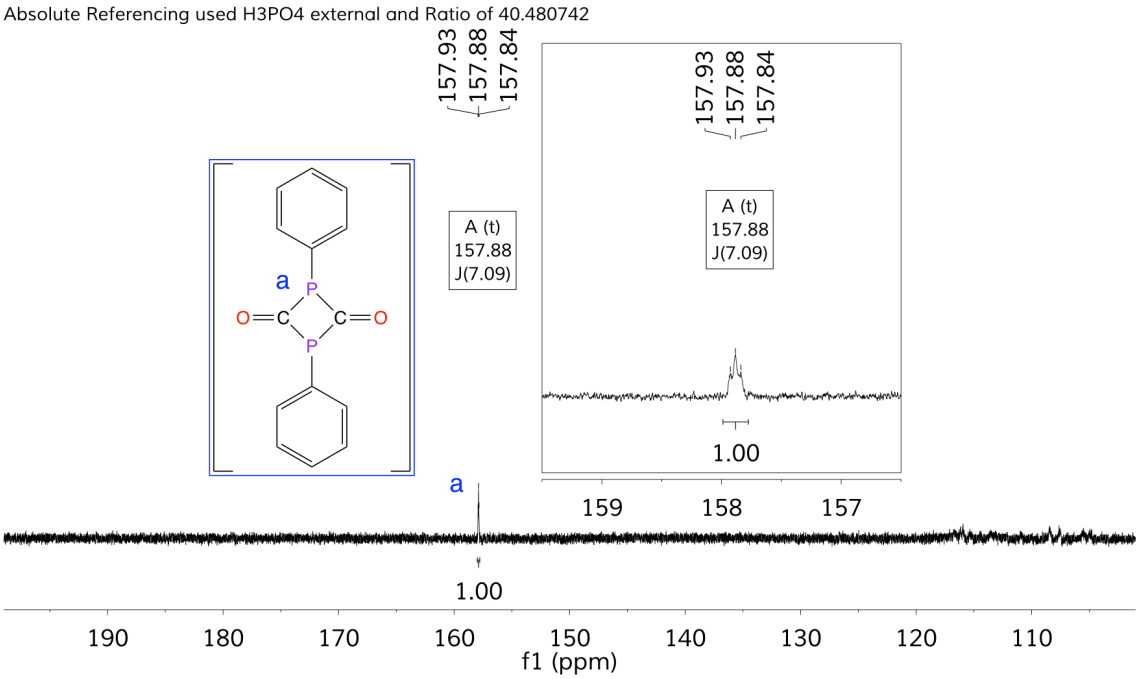

Figure 4.67: ^{31}P NMR spectrum of attempted isolation of **4.10** in C_6D_6 focused downfield (162 MHz)

Compound **4.10** has not been previously reported, and it is believed be thermally unstable based on the properties of other phosphaketenes with low steric bulk and likely forms a dimer. Density functional (DFT) calculations were carried out to provide additional support for the experimentally observed ^{31}P NMR peak at 157 ppm.

Use of compound **4.9** as the ^{31}P NMR chemical shift reference allows estimation of the ^{31}P NMR signals for **4.10** and both the *cis* (Fig. 4.68, left) and *trans* (Fig. 4.68, right) isomers (relative phenyl group orientation) of phenylphosphaketene dimer. Monomeric **4.10** was calculated to have a far upfield ^{31}P NMR chemical shift of -209.3 ppm, which was not observed experimentally (Table 4.8).

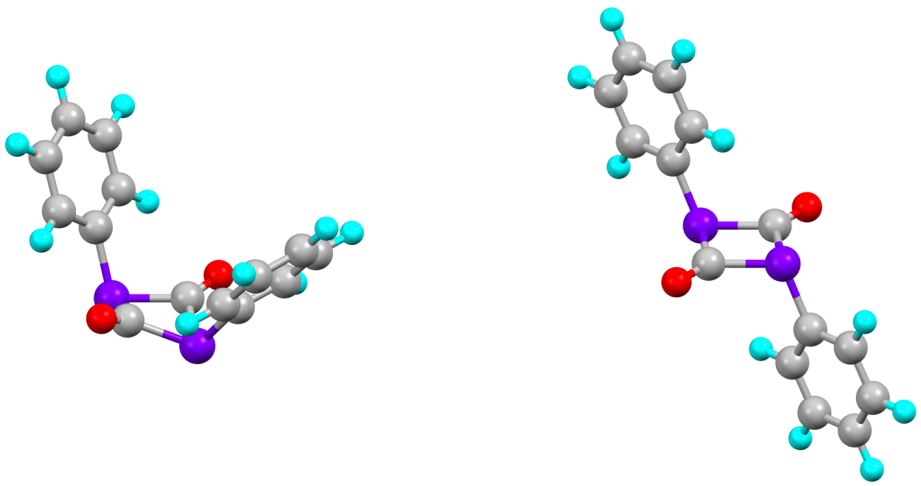

Figure 4.68: Calculated geometries of cis (left) and trans (right) isomers of phenylphosphaketene dimer (ORCA[16], PBE0[17] density functional with D3BJ[18,19] correction, def2-TZVPP[20] basis set)

The isomers of **4.10** dimer are calculated to have average ^{31}P NMR chemical shifts of 124.6 ppm (*cis*) and 93.4 ppm (*trans*). While both of these calculated values do not match the experimentally observed peak at 157.91 ppm, the calculations indicate the expected region for the phosphorus signals to be observed. Solvent interactions may impact the accuracy of these calculations, as the same type of calculations estimate the $PhPH_2$ ^{31}P NMR signal at -134.5 ppm, which is approximately 10 ppm lower than the experimentally observed resonance. This level of error is common in the literature for calculated ^{31}P NMR chemical shifts.

Table 4.8: Calculated and experimental ^{31}P NMR chemical shifts

Compound	Calculated (ppm)	Experimental (ppm)
4.10	-209.3	–
4.10 dimer (cis)	124.6	–
4.10 dimer (trans)	93.4	–
Phenylphosphine ($PhPH_2$)	-134.5	-123.91
Supermesitylphosphaketene (Mes*P=C=O)	-219.6	-207.4[21]
Phosphaketene (HP=C=O)	-349.7	-316.7[22]
Trimethylphosphine ($P(CH_3)_3$)	-68.2	-62[23]
Trimethylphosphine oxide ($O=P(CH_3)_3$)	22.3	36.2
Phosphine (PH_3)	-270.4	-240.6[22]

While the NMR spectral data suggests formation of **4.10** or a dimer, and there is reasonable correlation with the DFT predicted values, additional studies are required to definitively prove the synthesis of **4.10**. Synthesis of known phosphaketenes using this methodology should provide the most expedient validation. Reaction of **4.10** with a substrate to generate a more stable product could also help verify formation of **4.10**. Additional DFT studies could shed light on the identity of the compound that gives rise to the ^{31}P NMR signal observed at -48 ppm, such as analysis of other oligomeric forms based on **4.10**.

4.3 Conclusions

Molybdenum oxido bonds in phosphinimide complexes were assessed for reactivity with heteroallene molecules, including isocyanates and ketenes. A rare example of an ene-diolate complex was isolated from the reaction between diphenyl ketene and oxido-dichlorido complex **2.4**. Analysis of decomposition products derived from attempted alkylation reactions suggested the formation of low-coordinate phosphinimide complexes containing alkyl, alkylidyne, and imido-phosphane ligands. Synthesis of a novel tetrabromido complex enabled the mechanistic evaluation of an intermediate tetraalkyl species, which gives rises to an alkyl-alkylidyne complex. A new synthetic approach to the synthesis of phosphaketenes was evaluated and shows a path forward toward larger scale synthesis and use of phosphaketenes with less hazardous reagents and atom economic processes.

4.4 Experimental

General Experimental Procedures

Unless otherwise specified, all reactions and manipulations were performed under a dry oxygen-free atmosphere of dinitrogen in either a Vacuum Atmospheres NEXUS model drybox equipped with a 40CFM Dual Purifier NI-Train, or by using standard Schlenk techniques. Glassware was dried in an oven at 150 ºC overnight prior to use.

NMR spectra were collected using a Varian Inova 600 MHz NMR spectrometer with a 5 mm indirect detection probe, Varian VNMRS 500 MHz NMR spectrometer with a tunable 5 mm $^{1}H\{^{15}N\text{-}^{31}P\}$ PFG probe, Varian VNMRS 400 MHz spectrometer with an auto-tunable 5 mm Dual Broadband $^{15}N\text{-}^{31}P$ $\{^{1}H\}$ PFG probe optimized for broadband detection, or Oxford Mercury VX-300 300 MHz NMR spectrometer with a 5 mm 4-nuclei ($^{1}H/^{13}C/^{19}F/^{31}P$) auto-switchable PFG probe. Chemical shifts for ^{1}H, ^{11}B, ^{13}C, ^{19}F, ^{29}Si, and ^{31}P NMR spectra are reported in parts per million (ppm), and were referenced to residual solvent impurities, or when stated on the spectra with the absolute unified scale corresponding to the following standards using the relevant Ξ / % frequency ratios: ^{11}B, 32.083974 ($BF_3{\bullet}Et_2O$ $CDCl_3$, ϕ = 15 %); ^{13}C, 25.145020 ($Si(CH_3)_4$ $CDCl_3$, ϕ = 1 %); ^{19}F, 94.094011 ($FCCl_3$); ^{29}Si, 19.867187 ($Si(CH_3)_4$ $CDCl_3$, ϕ = 1 %); ^{31}P, 40.480742 (H_3PO_4 external).[24,25] All NMR spectral data were processed with the MestReNova 11.0.2 software package.

The 2D NMR experiments used unmodified pulse sequences from the Agilent software package VNMRJ 4.2 with specific parameters reported for

each compound. Relaxation delays for the 2D NMR experiments were optimized so that the recycle time equaled 1.3 times T_1 of the target proton resonances, with T_1 measured using INVREC NMR experiments with default parameters from VNMRJ 4.2.

Elemental analyses were performed at Midwest Microlab LLC. Single crystal X-ray diffraction data were collected using a Bruker APEX2 diffractometer with a CCD area detector and graphite-monochromated Mo Kα radiation (λ = 0.71073 Å). Structural solution and refinement were accomplished using the APEX2, SAINT, SADABS, TWINABS, and SHELXL programs.[26–28] Details regarding data collection for each structure are provided in the individual CIF files.

Except where otherwise noted, reagents were purchased from commercial suppliers and used without further purification. Benzene-d_6, chloroform-d, dichloromethane-d_2, and toluene-d_8, were purchased from Cambridge Isotope Laboratories (99.9%D) and were purified by storage over 4 Å molecular sieves under N_2 prior to use. Celite (Aldrich) and 4 Å molecular sieves (Aldrich) were dried under dynamic vacuum at 250 ºC for 48 h prior to use. All solvents were purchased from commercial suppliers and dried and deoxygenated with the appropriate VAC Atmospheres Solvent Purifier modules and stored over activated 4 Å molecular sieves prior to use.

Calculated molecular geometries were optimized using the PBE0[17] density functional with D3BJ[18,19] correction and def2-TZVP[20] basis set within the ORCA[16] software package. NMR chemical shifts were calculated using the

EPT/NMR module of ORCA, which uses Gauge Including Atomic Orbitals (GIAOs), with the def2-QZVPP basis set and def2/JK[29] auxiliary basis set.

Synthesis of [(^{t}Bu$_3$P=N)$_2$Mo(=N(2,6-(CH$_3$)$_2$C$_6$H$_4$))Cl$_2$] (4.1): A dichloromethane solution (5 mL) of [(tBu$_3$P=N)$_2$MoOCl$_2$] (**2.4**) (0.292 mmol) was prepared in a 20 mL scintillation vial. A dichloromethane solution (4 mL) of 2,6-dimethylphenylisocyanate (0.293 mmol) was prepared and added dropwise to the solution of **2.4** at ambient temperature. The yellow solution of **2.4** slowly grew darker after addition. After 24 hours, the solution is dark brown/red and volatiles were removed under reduced pressure, yet excess 2,6-dimethylphenylisocyanate could not be removed entirely. ^{1}H NMR (400 MHz, benzene-*d6*, 25°C) δ = 1.47 (d, $^3J_{PH}$ = 13.6 Hz, 54 H, PC(C*H*$_3$)$_3$), 3.06 (s, 6H, (o-C*H*$_3$)), (aryl signals overlapped with isocyanate) 6.71, 6.76, 6.96. ^{31}P{^{1}H} NMR (162 MHz, benzene-*d6*, 25°C) δ = 55.52 (s, 2 P, *P*C(CH$_3$)$_3$).

Synthesis of [(^{t}Bu$_3$P=N)$_2$Mo(=NPh)Cl$_2$] (4.2): A dichloromethane solution (5 mL) of [(tBu$_3$P=N)$_2$MoOCl$_2$] (**2.4**) (0.292 mmol) was prepared in a 20 mL scintillation vial. A dichloromethane solution (4 mL) of phenylisocyanate (0.293 mmol) was prepared and added dropwise to the solution of **2.4** at ambient temperature. The yellow solution of **2.4** turned red during the addition. After 24 hours, the solution is dark red and volatiles were removed under reduced pressure, yet excess phenylisocyanate could not be removed entirely. ^{1}H NMR (400 MHz, benzene-*d6*, 25°C) δ = 1.54 (d, $^3J_{PH}$ = 14.4 Hz, 54 H, PC(C*H*$_3$)$_3$),

(aryl signals overlapped with isocyanate) 7.02, 7.15, 7.25. $^{31}P\{^{1}H\}$ NMR (162 MHz, benzene-*d6*, 25°C) δ = 70.03 (s, 2 P, *P*C$(CH_3)_3$).

Synthesis of [(^{t}Bu$_3$P=N)$_2$Mo(O$_2$C=CPh$_2$)Cl$_2$] (4.3): A dichloromethane solution (5 mL) of [(tBu_3P=N)$_2$MoOCl$_2$] (**2.4**) (0.292 mmol) was prepared in a 20 mL scintillation vial and cooled to -30 °C. A dichloromethane solution (3 mL) of diphenylketene (0.293 mmol) was prepared, cooled to -30 °C, and added dropwise to the solution of **2.4**. The yellow solution of **2.4** immediately turned dark red during the addition, and slowly converted to dark green over 5 minutes. Volatiles were removed under reduced pressure after 1 hour, resulting in 220 mg (0.287 mmol, 98 % yield) of **4.3** as a dark green powder. Single crystals suitable for X-ray diffraction were obtained from a concentrated solution of dichloromethane at -30 °C. ^{1}H NMR (400 MHz, dichloromethane-*d2*, 25°C) δ = 1.68 (d, $^{3}J_{PH}$ = 14.4 Hz, 54 H, PC(C*H*$_3)_3$), 6.83 (m, 2H, (p-C*H*)), 7.26 (m, 8 H, (*o*-C*H*, *m*-C*H*)). $^{31}P\{^{1}H\}$ NMR (162 MHz, dichloromethane-*d2*, 25°C) δ = 71.70 (s, 2 P, *P*C$(CH_3)_3$). ^{1}H-^{13}C gHMBCAD NMR (dichloromethane-d_2, 25 °C) [(^{1}H, 500 Mhz), (^{13}C, 126 MHz)] δ = [7.3, 262.8] (s, *C*(O)$_2$=*C*(C$_6$*H*$_5$)), [7.3, 273.7] (s, *C*(O)$_2$=*C*(C$_6$*H*$_5$)), [7.3, 325.9] (s, *C*(O)$_2$=*C*(C$_6$*H*$_5$)), [7.3, 337.0] (s, *C*(O)$_2$=*C*(C$_6$*H*$_5$)). The ^{1}H-^{13}C gHMBCAD NMR experiment used a ^{1}H spectral window of 409.6 Hz, centered at 7.06 ppm, with a 0.156 s acquisition time (64 data points), and a 1.075 s relaxation delay; a ^{13}C spectral window of 25133.5 Hz, centered at 299.89 ppm; and 8 scans per time increment, 256 time increments, a J_{nxh} of 8 Hz, and non-uniform sampling density of 50%. Elemental

analysis found: C, 57.82; H, 8.42; N, 3.56. $C_{38}H_{64}Cl_2MoN_2O_2P_2$ requires: C, 56.37; H, 7.97; N, 3.46; which does not match given the observed thermal decomposition of this complex.

Synthesis of [(^{t}Bu$_3$P=N)$_2$Mo(O$_2$C=CPh$_2$)Cl][B(3,5-(CF$_3$)C$_6$H$_3$] (4.4): A dichloromethane solution (3 mL) of **4.3** (0.033 mmol) was prepared in a 20 mL scintillation vial and cooled to -30 °C. A dichloromethane solution (2 mL) of sodium tetrakis(3,5-bis(trifluoromethyl)phenyl)borate (0.033 mmol) was prepared, cooled to -30 °C, and added dropwise to the solution of **4.3**. The green solution of **4.3** became light transparent yellow over a few minutes, then converted to an opaque light green colored solution. After one hour, the solution was opaque turquoise in appearance, and the solution was filtered cold (-30 °C) through Celite. Volatiles were removed under reduced pressure, resulting in 46 mg (0.029 mmol, 88 % yield) of **4.4** as a turquoise powder. ^{1}H NMR (400 MHz, dichloromethane-d_2, 25.0 °C) δ = 1.47 (d, $^3J_{PH}$ = 14.5 Hz, 54 H, PC(CH_3)$_3$), 7.30 (m, 8 H, (ene-diolate *o*-C*H*, *m*-C*H*)), 7.59 (m, 4 H, (borane *p*-C*H*), 7.75 (m, 10 H, (ene-diolate *p*-C*H*; borane *o*-C*H*). ^{31}P{^{1}H} NMR (162 MHz, dichloromethane-d_2, 25.0 °C) δ = 69.79 (s, 2 P, *P*C(CH$_3$)$_3$). ^{13}C{^{1}H} NMR (101 MHz, dichloromethane-d_2, 25.0 °C) δ = 28.50 (s, PC(*C*H$_3$)$_3$), 39.23 (d, $^1J_{PC}$ = 39.7 Hz, P*C*(CH$_3$)$_3$), 117.42 (m, (borane *p*-C*H*)), 124.55 (q, $^1J_{CF}$ = 272.3 Hz, *C*F$_3$), 128.97 (m, (ene-diolate C*H*, *C*CF$_3$)), 134.74 (s, BC*C*), 161.72 (q, $^1J_{BC}$ = 49.9 Hz, B*C*), ene-diolate carbons not detected by 1D NMR. ^{11}B NMR (128 MHz, dichloromethane-d_2, 25.0 °C) δ = -6.61 (s, 1 B, *B*-aryl). ^{19}F{^{1}H} NMR (376 MHz

dichloromethane-d_2, 25.0 °C) δ = -62.81 (s, 20 F, CF_3). ^{1}H-^{13}C gHMBCAD NMR (dichloromethane-d_2, 25 °C) [(^{1}H, 500 Mhz), (^{13}C, 126 MHz)] δ = [7.4, 282.4] (s, $C(O)_2$=$C(C_6H_5)$), [7.4, 317.5] (s, $C(O)_2$=$C(C_6H_5)$). The ^{1}H-^{13}C gHMBCAD NMR experiment used a ^{1}H spectral window of 283.7 Hz, centered at 7.25 ppm, with a 0.902 s acquisition time (256 data points), and a 0.795 s relaxation delay; a ^{13}C spectral window of 25133.5 Hz, centered at 299.87 ppm; and 8 scans per time increment, 256 time increments, a J_{nxh} of 8 Hz, and non-uniform sampling density of 50%.

Synthesis of [(^{t}Bu$_3$P=N)$_2$Mo(=O)Cl][B(3,5-(CF$_3$)C$_6$H$_3$] (4.5): A dichloromethane solution (4 mL) of **2.4** (0.0812 mmol) was prepared in a 20 mL scintillation vial and cooled to -30°C. A dichlromethane suspension (3 mL) of sodium tetrakis(3,5-bis(trifluoromethyl)phenyl)borate (0.0812 mmol) at ambient temperature was added slowly to the solution of **2.4** while it returned to ambient temperature. The yellow solution of **2.4** became pale yellow/green and slightly opaque over a few minutes. After one hour, the solution was cooled to -30°C and filtered cold through Celite. Volatiles were removed under reduced pressure, resulting in 117 mg (0.0812 mmol, quantitative) of **4.5** as a light green oily solid. After storage of **4.5** at -30°C for a few days, the material was a crystalline light green powder. ^{1}H NMR (400 MHz, dichloromethane-d_2, 25.0 °C) δ = 1.54 (d, $^3J_{PH}$ = 14.4 Hz, 54H, PC(CH_3)$_3$), 7.55 (m, 4 H, (borane *p*-C*H*), 7.71 (m, 8 H, (borane *o*-C*H*). ^{31}P{^{1}H} NMR (162 MHz, dichloromethane-d_2, 25.0 °C) δ = 69.84 (s, 2 P, *P*C(CH$_3$)$_3$). ^{11}B NMR (128 MHz, dichloromethane-d_2, 25.0 °C) δ

= -6.64 (s, 1 B, *B*-aryl). $^{19}F\{^{1}H\}$ NMR (376 MHz dichloromethane-d_2, 25.0 °C) δ = -62.91 (s, 20 F, CF_3).

Synthesis of [(^{t}Bu$_3$P=N)$_2$MoBr$_4$] (4.8): A trifluorotoluene solution (3 mL) of **2.4** (0.187 mmol) was prepared in a 20 mL scintillation vial. A trifluorotoluene solution (4 mL) of trimethylsilylbromide (1.633 mmol) was added slowly to the solution of **2.4** at ambient temperature. The yellow solution became transparent red during the addition, and transitioned to an opaque orange after a few minutes. After 20 hours, volatiles were removed under reduced pressure, resulting in 153 mg (0.180 mmol, 96% yield) of **4.8** as an orange powder. ^{1}H NMR (400 MHz, benzene-d6, 25°C) δ = 1.04 (d, $^{3}J_{PH}$ = 15.2 Hz, 54 H (41%), PC(CH_3)$_3$), 1.23 (d, $^{3}J_{PH}$ = 13.9 Hz, 54 H (59%), PC(CH_3)$_3$). $^{31}P\{^{1}H\}$ NMR (162 MHz, benzene-d6, 25°C) δ = 70.76 (s, 2 P, *P*C(CH$_3$)$_3$). $^{13}C\{^{1}H\}$ NMR (101 MHz, benzene-d6, 25°C) δ = 28.86 (s, PC(*C*H$_3$)$_3$), quaternary carbons in phosphinimide ligand not resolved. ^{1}H NMR (400 MHz, chloroform-d, 0°C) δ = 1.80 (d, $^{3}J_{PH}$ = 15.7 Hz, 54 H, PC(CH_3)$_3$), 1.23 (d, $^{3}J_{PH}$ = 13.9 Hz, 54 H, PC(CH_3)$_3$). $^{31}P\{^{1}H\}$ NMR (162 MHz, chloroform-d, 0°C) δ = 98.33 (s, 2 P, *P*C(CH$_3$)$_3$). $^{13}C\{^{1}H\}$ NMR (101 MHz, chloroform-d, 0°C) δ = 30.62 (s, PC(*C*H$_3$)$_3$), 46.70 (d, $^{1}J_{PC}$ = 28.9 Hz, PC(*C*H$_3$)$_3$).

Synthesis of [(tBu$_3$P=N)$_2$Mo(≡CSi(CH$_3$)$_3$)(CH$_2$Si(CH$_3$)$_3$)] (**4.6**)**:** A hexanes (2 mL) suspension of **4.8** (0.0648 mmol) was prepared in a 20 mL scintillation vial

and cooled to 9°C. A hexanes solution (4 mL) of $LiCH_2Si(CH_3)_3$ (0.276 mmol) was added slowly to the solution of **4.8** while it returned to ambient temperature. The orange suspension of **4.8** transitioned to dark brown over a few minutes, and transparent red with fine colorless particles after 10 minutes. After two hours, the solution was filtered through Celite. Volatiles were removed under reduced pressure, resulting in 40 mg (0.0571 mmol, 89% yield) of **4.6** as a highly crystalline red solid. Single crystals suitable for X-ray diffraction were obtained from a concentrated solution of hexanes at 8°C. ^{1}H NMR (400 MHz, benzene-*d6*, 25°C) δ = 0.46 (s, 9H, ($CSi(CH_3)_3$), 0.59 (s, 9H, ($CH_2Si(CH_3)_3$), 1.36 (d, $^3J_{PH}$ = 12.7 Hz, 54 H, $PC(CH_3)_3$). ^{31}P{^{1}H} NMR (162 MHz, benzene-*d6*, 25°C) δ = 47.76 (s, 2 P, $PC(CH_3)_3$). ^{13}C{^{1}H} NMR (101 MHz, benzene-*d6*, 25°C) δ = 2.78 (s, $CSi(CH_3)_3$), 3.06 (s, $CH_2Si(CH_3)_3$), 23.33 (s, $MoCH_2Si(CH_3)_3$), 29.80 (s, $PC(CH_3)_3$), 40.75 (d, $^1J_{PC}$ = 46.1 Hz, $PC(CH_3)_3$), alkylidyne carbon could not be detected by 1D NMR. ^{1}H-{^{13}C} gHMBCAD NMR (benzene-d_6, 18.0 °C) (^{1}H, 500 MHz) δ = 0.5 (s, $MoCSi(CH_3)_3$)); 0.6 (s, $MoCH_2Si(CH_3)_3$)), 1.0 (s, $MoCH_2Si(CH_3)_3$)); (^{13}C, 126 MHz) δ = 2.8 (s, $MoCH_2Si(CH_3)_3$), 3.1 (s, $MoCSi(CH_3)_3$), 23.2 (s, $MoCH_2Si(CH_3)_3$). The ^{1}H-{^{13}C} gHMBCAD NMR experiment used a ^{1}H spectral window of 5506.6 Hz, centered at 4.53 ppm, with a 0.372 s acquisition time (2048 data points), and a 2.481 s relaxation delay; and a ^{13}C spectral window of 24509.8 Hz, centered at 82.53 ppm; 4 scans per time increment, and 512 time increments. ^{1}H-{^{13}C} gHMBCAD NMR (benzene-d_6, 25.0 °C) (^{1}H, 500 MHz) δ = 0.4 (s, $MoCSi(CH_3)_3$)); (^{13}C, 126 MHz) δ = 325.1 (s, $MoCSi(CH_3)_3$). The ^{1}H-{^{13}C} gHMBCAD NMR experiment used a ^{1}H spectral

window of 3742.5 Hz, centered at 3.75 ppm, with a 0.547 s acquisition time (2048 data points), and a 2.678 s relaxation delay; and a ^{13}C spectral window of 12566.8 Hz, centered at 299.91 ppm; 4 scans per time increment, and 256 time increments. ^{1}H-{^{13}C} gHSQCAD NMR (benzene-d_6, 22.0 °C) (^{1}H, 500 MHz) δ = 0.5 (s, MoCSi(CH_3)$_3$)); 0.6 (s, MoCH_2Si(CH_3)$_3$)), 1.0 (s, MoCH_2Si(CH_3)$_3$)); (^{13}C, 126 MHz) δ = 2.9 (s, MoCH_2Si(*C*H_3)$_3$), 3.1 (s, MoCSi(*C*H_3)$_3$), 23.3 (s, Mo*C*Si(CH_3)$_3$). The ^{1}H-{^{13}C} gHSQCAD NMR experiment used a ^{1}H spectral window of 4310.3 Hz, centered at 3.83 ppm, with a 0.238 s acquisition time (1024 data points), and a 2.987 s relaxation delay; and a ^{13}C spectral window of 8295.3 Hz, centered at 22.04 ppm; 8 scans per time increment, and 256 time increments. ^{1}H-^{13}C gHSQCAD NMR (benzene-d_6, 22.0 °C) (^{1}H, 500 MHz) δ = 0.5 (d, $^{1}J_{CH}$ = 115 Hz, MoCSi(CH_3)$_3$)); 0.6 (d, $^{1}J_{CH}$ = 115 Hz, MoCH_2Si(CH_3)$_3$)), 1.0 (d, $^{1}J_{CH}$ = 110 Hz, MoCH_2Si(CH_3)$_3$)); (^{13}C, 126 MHz) δ = 2.8 (s, MoCH_2Si(*C*H_3)$_3$), 3.1 (s, MoCSi(*C*H_3)$_3$), 23.2 (s, Mo*C*Si(CH_3)$_3$). The ^{1}H-^{13}C gHSQCAD NMR experiment used a ^{1}H spectral window of 4310.3 Hz, centered at 3.83 ppm, with a 0.238 s acquisition time (1024 data points), and a 2.987 s relaxation delay; and a ^{13}C spectral window of 8295.3 Hz, centered at 22.04 ppm; 8 scans per time increment, and 256 time increments.

Synthesis of PhP(H)C(=O)OPh (4.9): Phenyl phosphine (157 mg, 1.43 mmol) was weighed out and dissolved in 4 mL of toluene in a scintillation vial. Potassium carbonate (608 mg, 4.40 mmol) was added directly to the reaction solution. Phenyl chloroformate (216 mg, 1.38 mmol) was weighed out,

dissolved in 3 mL of toluene, and added to the reaction solution. The colorless transparent reaction solution was sealed and heated to +80°C while stirring. After 5 hours, NMR analysis indicates 73% conversion to **4.9**.

Attempted synthesis of PhP=C=O (4.10): 4.9 (83 mg, 0.36 mmol) was weighed out and dissolved in 2mL of THF in a scintillation vial. Sodium bis(trimethylsilyl)amide (67 mg, 0.37 mmol) was weighted out and suspended in 1 mL of THF in a separate vial. Both solutions were cooled to -30 °C. The sodium amide suspension was added dropwise to the phosphaester solution while warming to ambient temperature. The reaction solution immediately turned yellow, became yellow/orange during the addition, and returned to yellow (slightly opaque) by the end of the addition. The reaction solution was cooled to -30°C after one hour. Solvent was removed after 3 hours to obtain a light orange solid, which was filtered through Celite with toluene. Solvent was removed under vacuum to obtain a high viscosity orange liquid (which had almost no solubility in hexanes).

4.5 References

1. U. Küsthardt, W. A. Herrmann, M. L. Ziegler, T. Zahn and B. Nuber, *J. Organomet. Chem.*, 1986, **311**, 163–175.
2. T. T. Tidwell, *Ketenes II*, John Wiley & Sons, Inc., Hoboken, New Jersey, 2006.

3. A. H. Cowley, B. Pellerin, J. L. Atwood and S. G. Bott, *J. Am. Chem. Soc.*, 1990, **112**, 6734–6735.
4. G. Schoettel, J. Kress and J. A. Osborn, *Chem. Commun.*, 1989, 1062–1063.
5. R. R. Schrock, J. S. Murdzek, G. C. Bazan, J. Robbins, M. DiMare and M. O'Regan, *J. Am. Chem. Soc.*, 1990, **112**, 3875–3886.
6. T. Wondimagegn, K. Vanka, Z. Xu and T. Ziegler, *Organometallics*, 2004, **23**, 5737–5743.
7. B. G. Ward and F. E. Stafford, *Inorg. Chem.*, 1968, **7**, 2569–2573.
8. M. T. Benson, T. R. Cundari, S. J. Lim, H. D. Nguyen and K. Pierce-Beaver, *J. Am. Chem. Soc.*, 1994, **116**, 3955–3966.
9. T. Söhnel, W. Reichelt and H. Oppermann, *Z. Anorg. Allg. Chem.*, 1997, **623**, 1190–1200.
10. F. Wang and T. Ziegler, *Mol. Phys.*, 2004, **102**, 2585–2595.
11. D. N. Clark and R. R. Schrock, *J. Am. Chem. Soc.*, 1978, **100**, 6774–6776.
12. C. G. Young, E. M. Kober and J. H. Enemark, *Polyhedron*, 1987, **6**, 255–259.
13. M. Koy, I. Elser, J. Meisner, W. Frey, K. Wurst, J. Kästner and M. R. Buchmeiser, *Chem. Eur. J.*, 2017, **23**, 15484–15490.
14. R. P. Saint-Arroman, M. Chabanas, A. Baudouin, C. Copéret, J.-M. Basset, A. Lesage and L. Emsley, *J. Am. Chem. Soc.*, 2001, **123**, 3820–3821.
15. R. A. Andersen, M. H. Chisholm, J. F. Gibson, W. W. Reichert, I. P. Rothwell and G. Wilkinson, *Inorg. Chem.*, 1981, **20**, 3934–3936.

16. F. Neese, *Wiley Interdiscip. Rev. Comput. Mol. Sci.*, 2012, **2**, 73–78.
17. C. Adamo and V. Barone, *J. Chem. Phys.*, 1999, **110**, 6158–6170.
18. S. Grimme, J. Antony, S. Ehrlich and H. Krieg, *J. Chem. Phys.*, 2010, **132**, 154104.
19. S. Grimme, S. Ehrlich and L. Goerigk, *J. Comput. Chem.*, 2011, **32**, 1456–1465.
20. F. Weigend and R. Ahlrichs, *Phys. Chem. Chem. Phys.*, 2005, **7**, 3297.
21. R. Appel and W. Paulen, *Angew. Chem. Int. Ed.*, 1983, **22**, 785–786.
22. A. Hinz, R. Labbow, C. Rennick, A. Schulz and J. M. Goicoechea, *Angew. Chem. Int. Ed.*, 2017, **56**, 3911–3915.
23. R. Bosque and J. Sales, *J. Chem. Inf. Comput. Sci.*, 2001, **41**, 225–232.
24. R. K. Harris, E. D. Becker, S. M. Cabral de Menezes, R. Goodfellow and P. Granger, *Pure Appl. Chem.*, 2001, **73**, 1795–1818.
25. R. K. Harris, E. D. Becker, S. M. Cabral de Menezes, P. Granger, R. E. Hoffman and K. W. Zilm, *Pure Appl. Chem.*, 2008, **80**, 59–84.
26. G. M. Sheldrick, *Acta Crystallogr. Sect. A*, 2015, **71**, 3–8.
27. G. M. Sheldrick, *Acta Crystallogr. Sect. C*, 2015, **71**, 3–8.
28. L. Krause, R. Herbst-Irmer, G. M. Sheldrick and D. Stalke, *J. Appl. Crystallogr.*, 2015, **48**, 3–10.
29. F. Weigend, *J. Comput. Chem.*, 2008, **29**, 167–175.

Definitions

1D	1-Dimensional
2D	2-Dimensional
3D	3-Dimensional
ACM	Alkyne cross-metathesis
AD	Adiabatic
Ar	Aryl
Å	Angstrom
br	Broad
bs	Band-selected
C	Celsius
Cy	Cyclohexyl
d	Doublet
DCM	Dichloromethane
DFT	Density functional theory
E	Element
EA	Elemental analysis
Et	Ethyl
Equiv.	Equivalent
FID	Free induction decay
Fig.	Figure
FT	Fourier-transform
h	Hours

HMQC	Heteronuclear multiple-quantum correlation
HOMO	Highest occupied molecular orbital
HSQC	Heteronuclear single quantum correlation
HSAB	Hard-soft acid-base
Hz	Hertz
^{i}Pr	Isopropyl
IR	Infrared
J	Coupling constant
K	Kelvin
L	Ligand
LN_2	Liquid dinitrogen
LUMO	Lowest unoccupied molecular orbital
m	Multiplet
m	*Meta*
Me	Methyl
Mes	Mesityl
Mes*	Supermesityl
MHz	Megahertz
mL	Milliliter
mol	Mole
mmol	Millimole
NMR	Nuclear magnetic resonance
o	*Ortho*

OU	University of Oklahoma
p	*Para*
PFG	Pulsed field gradient
Ph	Phenyl
q	Quartet
R	Organic group
RCAM	Ring-closing alkyne metathesis
RCM	Ring-closing metathesis
ROAMP	Ring-opening alkyne metathesis polymerization
ROMP	Ring-opening metathesis polymerization
s	Singlet
s.u.	Standard uncertainty
t	Triplet
^{t}Bu	*Tert*-butyl
TFT	α,α,α-Trifluorotoluene
THF	Tetrahydrofuran
TMS	Trimethylsilyl
Tol	Tolyl
UV-Vis	Ultraviolet-Visible
XRD	X-ray Diffraction
v	Wavenumber, (cm^{-1})
°	Degree
°C	Degrees Celsius

δ	*Delta*, Chemical shift
Δ	*Delta*, Change in
Δ	*Delta*, Elevated temperature
Ξ / %	Frequency ratio